GEOPHYSICAL INVESTIGATION INTO THE GEOLOGY, GEOMETRY AND GEOCHRONOLOGY OF THE SOUTH AFRICAN PILANESBERG COMPLEX AND THE PILANESBERG DYKE SYSTEM

Sally-Anne Lee

School of Geosciences

Degree of Master of Science

A dissertation submitted to the Faculty of Science, University of the Witwatersrand, Johannesburg, in fulfilment of the requirements for the degree of Master of Science.

Johannesburg, 2016

DECLARATION

I declare that this Dissertation is my own, unaided work. It is being submitted for the Degree of Master of Science at the University of the Witwatersrand, Johannesburg. It has not been submitted before for any degree or examination at any other University.

Sally-Anne Lee

On the 6th day of November 2016.

ABSTRACT

The Mesoproterozoic Pilanesberg Complex, South Africa, is the world's largest alkaline intrusive complex. Mapped geological field relationships suggest the Complex has circular inward dipping layers. However, it is unclear how the dipping layers extend at depth. As a result, the 3D geometry of the Pilanesberg Complex is unknown. Modelling of the Pilanesberg Complex uses 2D forward models as well as 3D forward and inversion, gravity and magnetic data models, to set limits on the 3D geometry of the Pilanesberg Complex.

The 2D Bouguer gravity models and geology maps indicate that some of the Bushveld Complex Main Zone shifted to the west of the Pilanesberg Complex during emplacement. This, and a highly faulted country rock, accounts for a portion of how the host rock was able to accommodate the Pilanesberg Complex intrusion. The geometry of the Complex is explored with test gravity models where the model of outward dipping and vertically dipping cylinders are unable to match the Bouguer gravity signal over the Complex, but the inward dipping model matched the data to provide a possible solution for the geometry of the Complex. The Pilanesberg Complex geometry is modelled with 3D magnetic inversion, 3D forward gravity models and 2.5D gravity test profiles that were all constrained by the surface geology. The different models correlate so that best data fit for the Complex is represented by an overall inward dipping structure. Surface geological measurements indicate that the northern edge of the Complex dip out to the north. The 3D forward modelling was able to produce a positive solution that matched the gravity data with a northward dipping northern edge. The dipping northern edge is also observed on the University of British Columbia, UBC, 3D gravity inversion and the Euler deconvolution gravity profile solutions. The depth of the Pilanesberg Complex from 3D forward gravity modelling is estimated to be between 5 and 6 km. The Complex is suggested to have undergone block movement where the northern block and southern block are separated by the 30 km long Vlakfontein fault, which bisects the Complex from the north-east to the south-west. The image processing contact depth, Euler deconvolution solutions and the 3D Voxi inversion model suggest that the fresh bedrock is closer to surface in the north, while the southern block appears to be approximately 1km deeper than the northern block. The northern dip and block movement are explained by complicated structural events that include trap door graben settling which hinged on the northern edge as well as faulting and external block movement during a regional lateral extensional event.

The Pilanesberg Complex intruded during a larger system of alkaline intrusions, known as the Pilanesberg Alkaline Province. The intrusions are associated with the Province due to their ages and chemical affinity. This Province includes two dyke swarms that radiate to the north-west and south of the Pilanesberg Complex, as well as smaller circular clinopyroxenite intrusions throughout the Bushveld Complex.

The Pilanesberg dyke system and the circular clinopyroxenite intrusions are reversely magnetised with IGRF corrected values ranging between -150 to -320 nT compared to the normally magnetised 166 to 330 nT values of the Pilanesberg Complex. This suggests that a magnetic reversal occurred between the emplacement of the Pilanesberg Complex and the dyke System.

The age data of the Complex and dyke Swarm suggest a magnetic reversal could have occurred between the emplacement of the Pilanesberg Complex and the Pilanesberg dyke System. The Complex is dated at 1602 ± 38 Ma and 1583 ± 10 Ma, from two white foyaite samples from the southern edge (using $^{40}Ar/^{39}Ar$ amphibole spectrum analysis). These ages are vastly different from previously reported ages, which ranged between 1200 Ma and 1450 Ma (Harmer R., 1992; Hansen et al., 2006). The error analysis has improved considerably from the published dates making the proposed dates plausible for the intrusion of the Pilanesberg Complex as the first and main intrusion of the Pilanesberg Alkaline Province. The Pilanesberg dyke System intruded much later between 1219 ± 6 Ma to 1268 ± 10 Ma for the red syenite dyke samples (using $^{40}Ar/^{39}Ar$ on feldspars spectrum analysis) and 1139 ± 18 Ma obtained for the grey syenite dyke (using $^{40}Ar/^{39}Ar$ on amphiboles inverse isochronal analysis). The dyke Swarm dates are significantly younger than the previously published ages for the dykes, which were between 1290 Ma and 1330 Ma (Van Niekerk, 1962; Emerman, 1991).

ACKNOWLEDGEMENTS

The academic work achieved in this dissertation was made possible by the support, encouragement and assistance from incredible people, for which I am extremely grateful.

- Dr Susan Webb, my principal supervisor, for ever-positive outlooks and guiding support. Sue always made sure we were on track and working in the correct direction with many meetings and scientific contributions. Thanks for the financial assistance in the first year of the M.Sc.
- Thanks to Mike Jones for his editorial guidance.
- Thanks to Ray Durrheim for financial support in collaboration with the National Research Fund.
- Thanks for the work and financing on the geochronology data at the Norway Geological Survey, NGU, centre by Morgan Ganerød and Trond Torsvik.
- Acknowledgements and thanks to Geosoft for providing software and licences for making processing data possible as well as the fabulous 3D Voxel inversions.
- The Council for Geoscience for the magnetic and gravity maps of South Africa.
- University of British Columbia for providing access to the 3D inversion software.
- Patrick and Janine Cole – for producing and providing the 3D forward modelling package PyGMI.
- To Stephanie Enslin for assistance with programme and data management.
- Thanks for coffee break motivation from Ryan McIntosh, William Rankin and Cameron Penn-Clark
- Lastly but not least to my enchanting family for all the support and motivation. Especially you mom!

TABLE OF CONTENTS

LIST OF FIGURES

LIST OF TABLES

LIST OF SYMBOLS

nT - Nanotesla is equal to 10^{-9} tesla (T) which measures a magnetic field strength in SI units.

mT - Militesla is equal to 10^{-3} tesla (T) which measures a magnetic field strength in SI units.

mGal - MilliGal is equal to 10^{-3} of a Gal or Galileo, which is the measure of acceleration of gravity.

CHAPTER 1: INTRODUCTION

1.1 REGIONAL SETTING

1.1.1 Pilanesberg Geology

The Pilanesberg Complex was named after Pilane, a Tswana chief of the Mokatla tribe, who inhabited the mountainous area in the 19th century (Shand, 1923). The Pilanesberg Complex is located on the Kaapvaal Craton and is the world's largest known alkaline intrusion, with a diameter of 28 km and a surface area of 625 km^2 (Figure 1.1). It intruded into the gabbronorite of the Rustenburg Layered Suite and granite of the Lebowa Granite Suite in the western limb of the Bushveld Complex, South Africa (Hansen et al., 2006). The Pilanesberg Complex intruded between 1200 and 1450 Ma during the Mesoproterozoic Era due to an intraplate extension event (Michell and Liferovich, 2006; Retief, 1963). Brower, 1910 (Pantashi, 2006) first identified the Pilanesberg Complex after which it was classified based on different lithologies, element analysis as well as fault and fracture structure (Lurie, 1986).

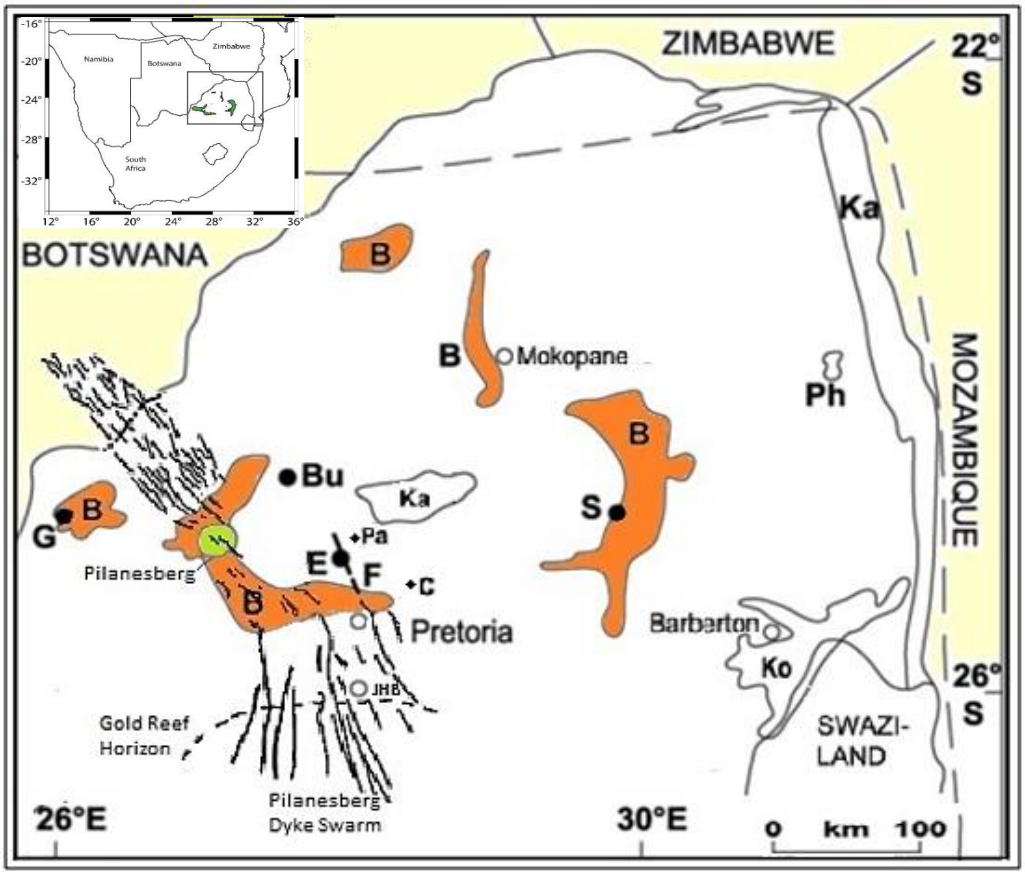

Figure 1.1 Regional setting of the Pilanesberg Complex and dyke Swarms in the western Bushveld Complex, modified from Emerman (1991), and Cawthorn (2006, 2012). Igneous bodies in the northern Kaapvaal Craton include Ko- Barberton komatiites, Ph- Phalaborwa Complex and B- Bushveld Complex. Ka- Karoo lavas, S-Spitskop, E-Elandskraal, F-Franspoort line of intrusions, G- Goudini Complex, Pa- Palmietgat kimberlite and C-Cullinan kimberlite.

The pyroclastic and lava flow successions resulted in an inward dipping structure around a preserved central core and plug (Olivo and Williams-Jones, 1999; Michell and Liferovich, 2006; Cawthorn et al., 2006). The Complex has a concentric appearance on the surface of a series of syenitic and foyaitic (nepheline syenites) intrusions as incomplete rings (McCaffrey, 1993; Cawthorn et al., 2012).

The Pilanesberg Complex is chemically and spatially associated with the Pilanesberg dyke System (Harmer, 1999) and other bodies in the Pilanesberg Province. These include the 1374 ± 10 Ma Ma Leeuwfontein Complex, 1341 ± 37 Ma Spitskop Complex (Rb-Sr method, 1341 ± 37 Ma (Harmer, 1999)), 1325 ± 11 Ma Stukpan Complex (Rb-Sr method, (Verwoerd et al., 1993)) and the clinopyroxenite pipes, at Elandskraal Volcano in the centre of the Bushveld Complex (Cawthorn et al., 2006; Emerman, 1991; C. R. Anhaeusser, pers. Comm, 2012). Other components of the Pilanesberg Province include necks, plugs, maars and smaller volcanic complexes.

1.1.2 Geology of the Pilanesberg Complex and dyke Swarms

The Pilanesberg Complex is comprised of distinctive roughly concentric inward dipping ring structures consisting of layers of syenite and red, white and green nepheline syenite (often referred to as foyaite). A thin layer of volcanic lava tuffs and coarse breccia partially cover the Complex (Figure 1.2). Erosion of some of the volcanic tuff has left the rest of the Complex partially unroofed, especially to the south (Shand, 1923; Shand, 1928; Hansen et al.; 2006, Cawthorn, 2015).

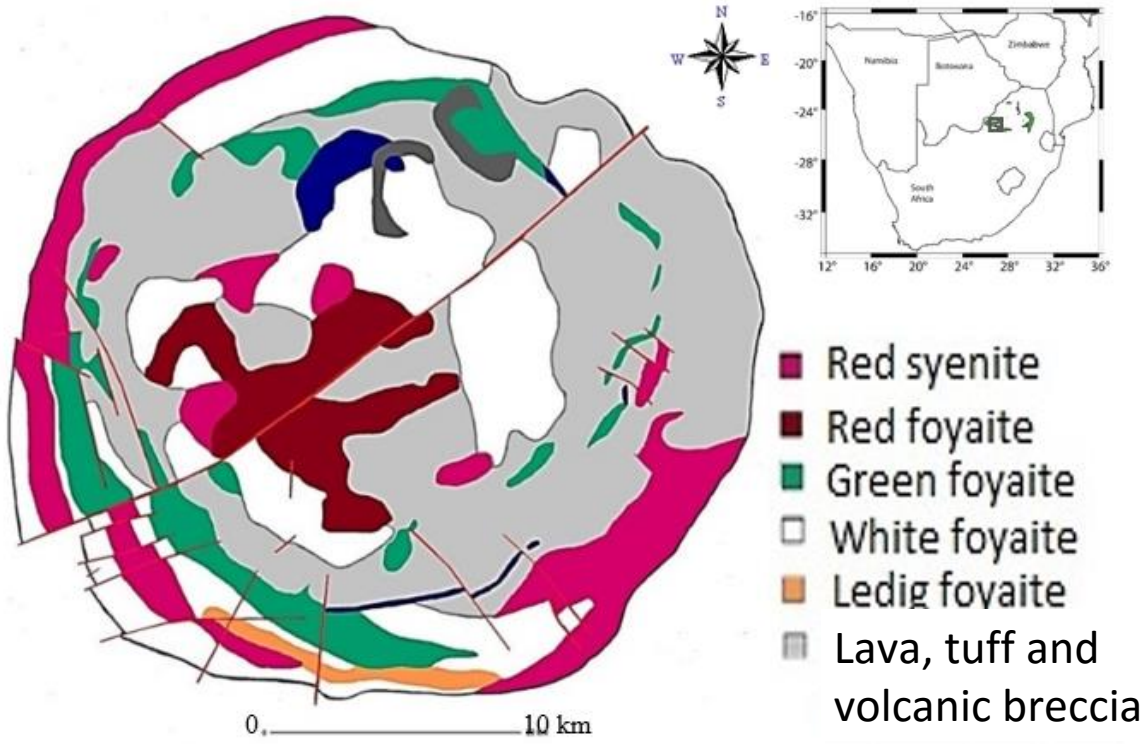

Figure 1.2 A schematic representation of the geology of the Pilanesberg Complex geology, modified from Lurie (1986), Cawthorn (1988), Cawthorn et al. (2006).

Trachytic pyroclastic units are formed by the alignment of fine to large grained crystals that are intruded by assorted nepheline syenite and tinguaite dykes as large cone sheets (Michell and Liferovich, 2006). Shand (1923) described the nepheline syenites as being red, white and green foyaites while Olivo and William-Jones (1999) described the rocks as red and white feldspathoidal syenite and green nepheline syenite. The oldest red feldspathoidal syenite forms the edge of the ring structure while the green nepheline syenite post-dates both the red and white nepheline syenite as the last to intrude in the centre of the ring structures (Figure 1.3).

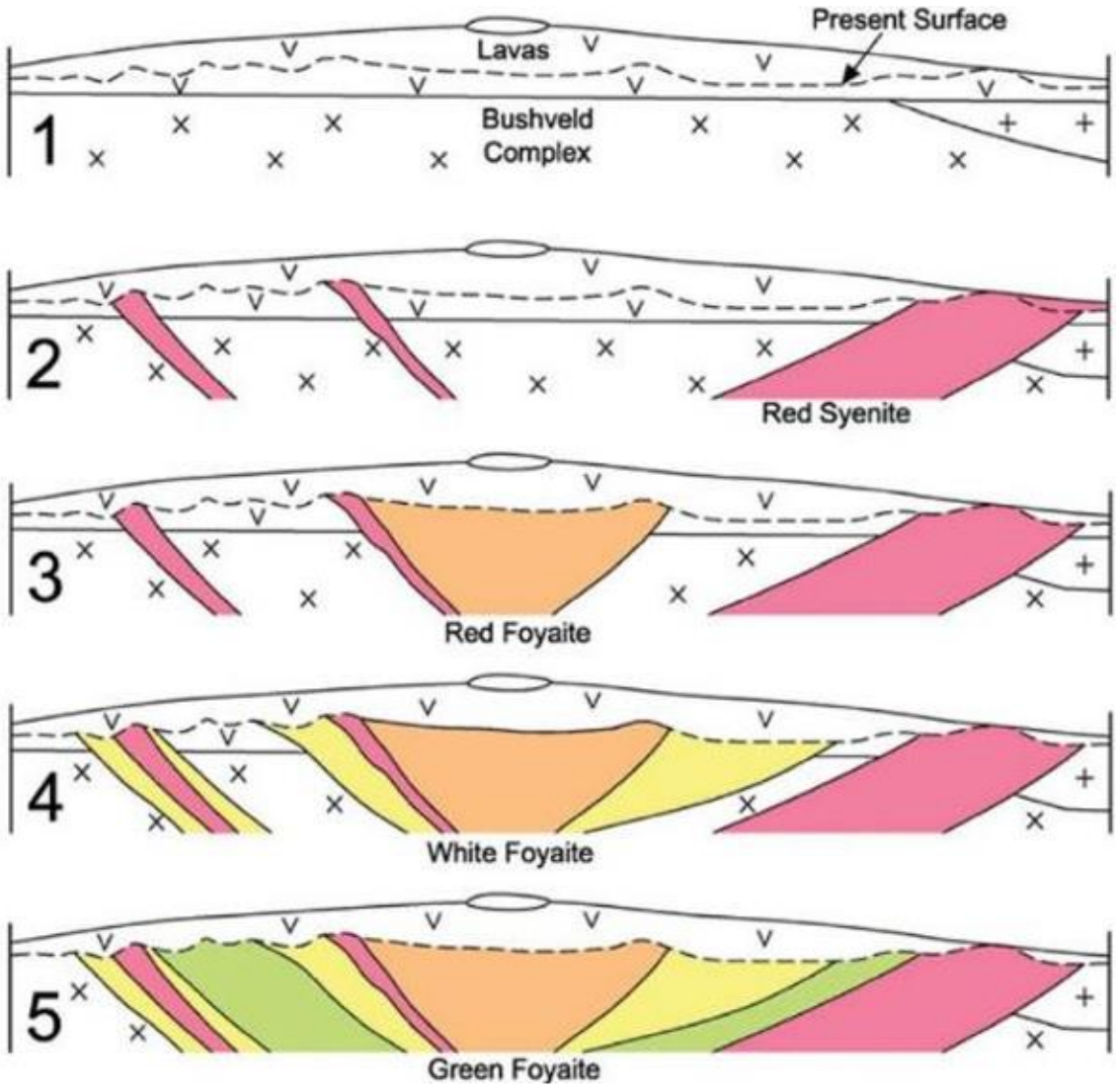

Figure 1.3 Schematic diagram of the 28 km diameter Pilanesberg Complex that is presented by Cawthorn (2015) to show the sequence of events as suggested by Lurie (1986). The inner and the outer red syenite intruded into the preceding lava (2), which was followed by red foyaite (3), white foyaite (4) and finally green foyaite (5). Profiles are from the west to east. From Cawthorn (2015). No depth scale is represented.

The ring structure dipped inward towards the centre of the Complex and was geologically mapped by Lurie (1986) to range from 35° in the south to 50° in the west and 45° in the east. Rocks in the north dip outwards at 35° towards the north.

The Pilanesberg Complex is cross cut by a major strike-slip fault, called the Vlakfontein fault, and smaller faults identified in Figure 1.4 and described by McCaffrey (1993) as a series of radial faults that cross cut the Pilanesberg Complex rings. The Vlakfontein fault was first identified as a major fault that continued below the sedimentary cover by Trofymczyk (1991) using an EM24-3 electromagnetic metre. The Vlakfontein fault bisects the Pilanesberg Complex which resulted in the outer red syenite ring being displaced by approximately 2 km on the south eastern edge due to the sinisterly horizontal displacement of the fault.

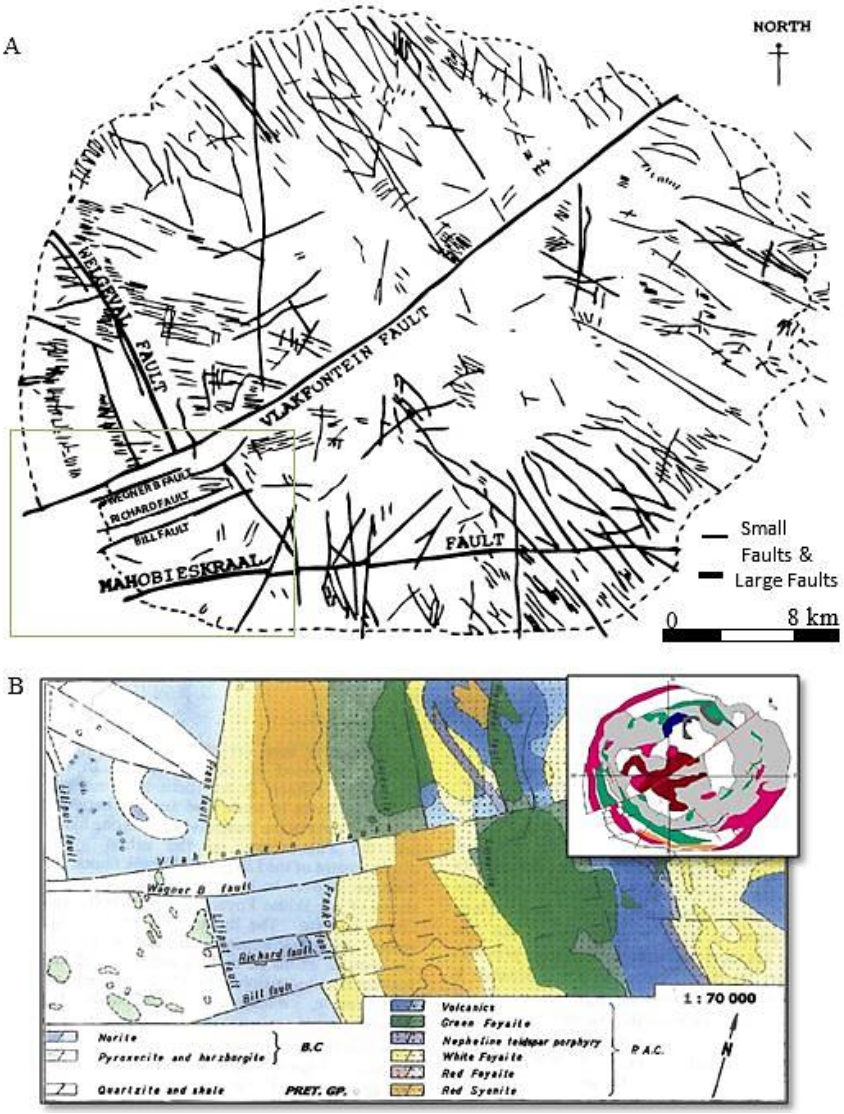

Figure 1.4 A) An overview of the faults, dykes and fracture lineation through the Complex. From McCaffey (1993). B) A schematic view of the Pilanesberg Complex south-west corner, which details the fault structure within the Pilanesberg Complex. Modified from Lurie (2008).

1.1.2.1 Geochemistry

Geochemistry data indicates that the rocks of the Pilanesberg Complex are rich in fluorine, strontium, niobium, tantalum, zirconium, hafnium, rare earth elements, thorium, yttrium and uneconomic uranium (Lurie, 1986; McCaffrey, 1993; Olivo and William-Jones, 1999). Further geochemical and petrographic analysis indicates that nepheline syenites were subject to widespread alteration and subsolidus equilibrium processes with a deuteric or altered Cl and Na-rich fluid phase. Replacement of primary alumina-silicates gave rise to the secondary minerals- rinkite, eudialyte and fluorapatite (Liferovich and Michell, 2006). The geochemistry of the Pilanesberg Complex has been compared to the Clinopyronenite intrusions and other intrusions in the Pilanesberg Province.

Recent work by Cawthorn et al. (2012) reveals circular clinopyroxenite pipes that are 1207 ± 200 Ma and approximately 8 km wide located in the centre of the Bushveld Complex (Figure 1.5). The pipes have an alkaline compositional affinity to intrusions such as Phalaborwa Complex, which suggests a relation to the Pilanesberg Province (Cawthorn et al., 2012).

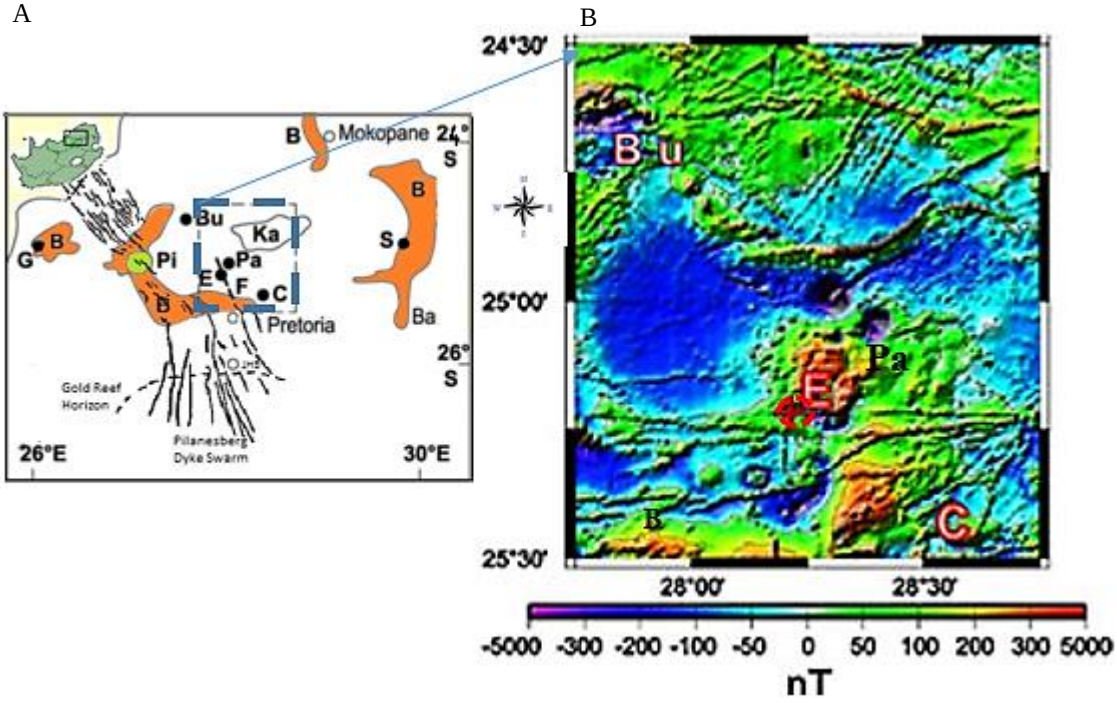

Figure 1.5 Occurrence of circular intrusions identified in the magnetic data that relates to the Pi - Pilanesberg Complex as well as the points in A) Bu-Buffleskraal, E-Elandskraal, C-Cullinan kimberlite and B, Bushveld Complex. Ka- Karoo lavas, S-Spitskop, E-Elandskraal and F- Franspoort line of intrusions, G- Goudini Complex, Pa-Palmietgat kimberlite. B) Corresponding magnetic map and labelled anomalies (Cawthorn et al., 2012)

1.2 GEOPHYSICS BACKGROUND

1.2.1 Pilanesberg Province Magnetics

The Pilanesberg dyke System (Jansen, 1977) is compositionally associated with the Pilanesberg Province intrusions. One swarm of syenite dykes trending north-west to south-east extends from the north-west of Pilanesberg Complex into Botswana. The second north-south trending swarm is traced through composition and magnetic correlation from the south of the Pilanesberg Complex into the Johannesburg Dome (Emerman, 1991) (Figure 1.6).The Pilanesberg dyke System ranges from 1290 ± 80 to 1330 ± 80 Ma (Van Niekerk, 1962; Emerman, 1991), which is comparable to dates for the Pilanesberg Province. The Pilanesberg ages range from 1250 ± 50 Ma (Olivo and William-Jones, 1999) to 1397 ± 47 Ma (Hansen et al., 2006; Cawthorn et al., 2012). The age data for the Pilanesberg Complex and the dykes suggest that they intruded during the same period from the same magma event. However, the airborne magnetic data associated with the dykes indicate strong negative anomalies which are opposite to the positive Pilanesberg Complex (Figure 1.6). Thus proposing a magnetic reversal occurred between the emplacement of the Pilanesberg and the dykes.

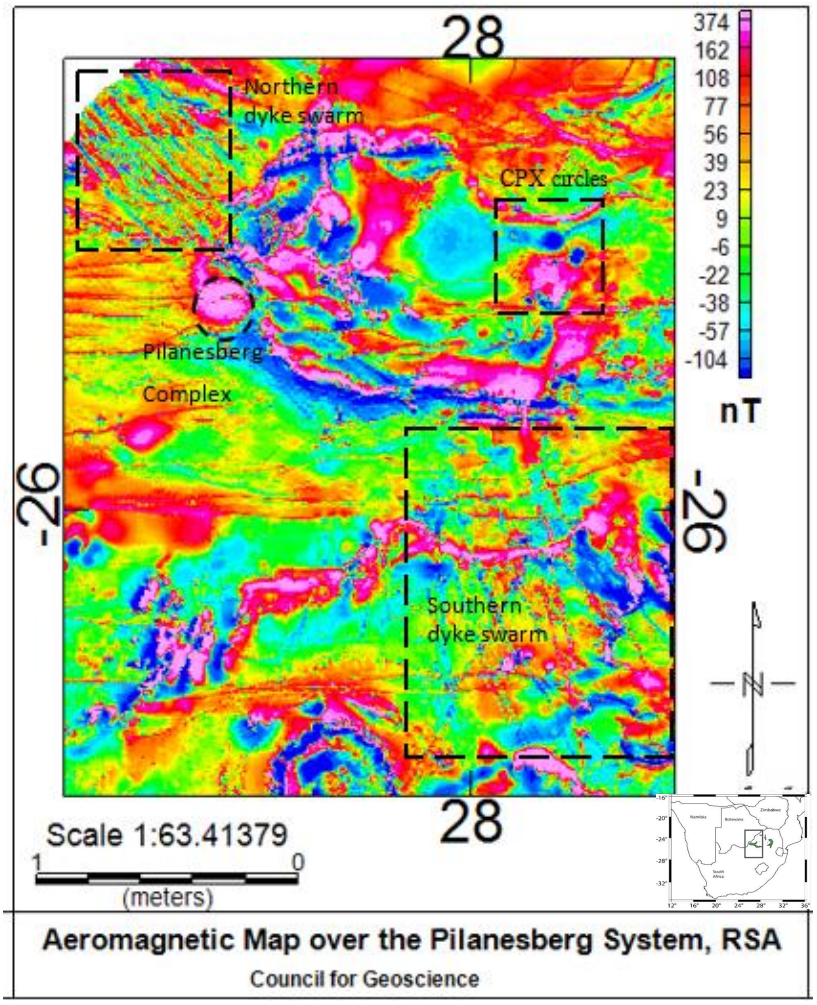

Figure 1.6 Magnetic data over the Pilanesberg Complex and Pilanesberg dyke swarms, from the Council for Geoscience. The magnetic map compares the positive anomaly of the Pilanesberg Complex with the negative anomalies from the dyke swarms.

The two dyke swarms have similar double-peaked reversed magnetic anomalies (Gough, 1958). The double peaked anomaly is the result of a two-staged emplacement dated at 1310 ±60 Ma (Emerman, 1991). First, a dolerite dyke intrudes into the country rock, after which a syenite dyke intrudes into the centre of the dolerite. This dyke is known as a composite dyke (Emerman, 1991. C. R. Anhaeusser, pers. Comm, 2012). The double-peaked magnetic anomalies from the composite dolerite-syenite dykes are observed in the northern dyke swarm in the south-east of Botswana (Figure 1.7), and extending 225 km south of the Pilanesberg Complex into the Wits Central Rand Gold mines along the gold reef (Hansen et al., 2006).

The compositions of the Pilanesberg dolerite dykes from the southern dyke swarm are tholeiitic and are comparable to basalts that are abundant in iron and silica with less aluminium (Hansen et al., 2006). Across both dyke swarms, the most common composition is the syenite dykes, which are identifiable by a single magnetic anomaly. The syenite dykes are sampled and examined as part of this thesis.

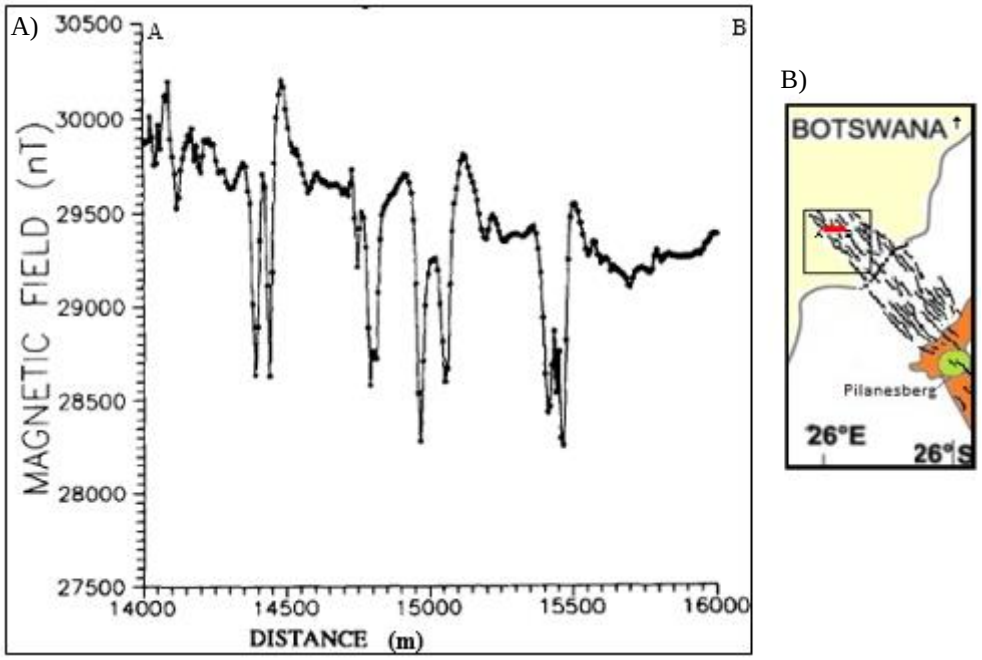

Figure 1.7 A) A profiles in Botswana of the total magnetic field across dykes of the northern dyke swarm, located south of the Monametsana River (Emerman, 1991). Each double-peak anomaly indicates a Pilanesberg dyke. B) Location of the profile across the dykes in Botswana.

1.2.2 Previous Paleomagnetic Data

Gough (1958) conducted early paleomagnetic studies on the southern dyke swarm using samples from deep mines or fresh quarries, thus avoiding iso-remnant magnetisation of the rocks due to lightning strikes. Gough (1958) sampled five Pilanesberg-aged dykes from the Central Rand Gold Mines. The

dykes sampled include the composite syenite-dolerite dykes from Libanon and Venterspost Gold Mines, the basic dykes at Robinson Deep and East Geduld Gold Mines, and a syenite dyke at the Simmer and Jack Gold Mine. Gough concluded that the dykes carried remnant magnetisation. There are some non-Pilanesberg normally magnetised dykes in the area (the 1120 ±45 Ma East Rand dykes), which are not related to the Pilanesberg Complex but are associated with the younger weakness zones. They should not be confused with the Pilanesberg dykes (Emerman, 1991).

The dyke samples used to calculate the mean magnetic pole orientation indicate that the dykes carried remnant magnetisation and a mean pole direction that defines a north-seeking magnetic pole. The paleomagnetic results indicated a correlation in the mean direction for a north-seeking magnetic pole with an inclination + 69.3° and azimuth N 24.0° E (Gough, 1958). Gough's mean north magnetic pole has a latitude of 7.5° N and longitude of 42.5° E and represents the pole position at the time of their emplacement. The accuracy of the pole assumes the rocks did not receive thermo-remnant magnetisation by a geocentric dipole field (Gough, 1958).

1.2.3 Gravity data

Gravity data over the Pilanesberg Complex and dyke swarms are sparse. The dots across Figure 1.8 depict the ground gravity sample sites for the gravity collected by the Council for Geoscience. The Pilanesberg Complex has a -102 mGal anomaly on the Bouguer gravity map. There is also a strong 30 mGal signal from the Bushveld Main Zone (Figure 1.8). On the gravity map, trends and internal structure are not identifiable at this resolution, as such the data will be image processed to detect any possible internal structure within the Pilanesberg Complex.

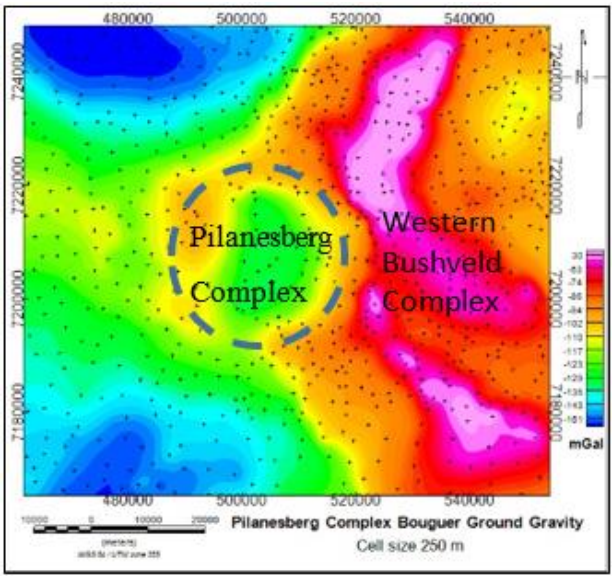

Figure 1.8 National Bouguer gravity data over the Pilanesberg Complex and Western Bushveld Complex with ground gravity stations plotted on top. The Pilanesberg Complex is outlined based the surface geology and the Bushveld Complex is represented by the 30 mGal high gravity is (data from the Council for Geoscience).

1.3 PREVIOUS AGE DATA

Dating of the Pilanesberg Complex is problematic, even though the rocks contain abundant Zr. The Zr associated is mostly with eudialyte rather than zircon. Eudialyte is not retentive of radiogenic Pb and is thus not suitable for geochronology (Olivo and Williams-Jones, 1999). It is unfortunate that there are no zircon grains as zircon dating would be an ideal method for dating these rocks.

Ages reported for the Pilanesberg Complex are between 1260 ± 50 Ma (K-Ar, Olivo and Williams-Jones, 1999) and 1397 ± 47 Ma (U-Pb on titanate, Hansen et al., 2006). These ages are considerably different from each other and are of poor precision. Therefore, the age of emplacement of the Complex is not well-constrained (Cawthorn et al., 2006). The age data compiled in Table 1.1 suggests that the Pilanesberg Complex was the first intrusion event of the Alkaline Province. Subsequent intrusions include the Leeuwfontein Complex and Spitskop Complex (1341 ± 37 Ma, Cawthorn et al., 2012). The age data from other intrusions in the Pilanesberg Alkaline Province includes the Spitskop Complex at 1341 ± 37 Ma (Rb-Sr, (Harmer, 1999)) and Stukpan at 1325 ± 11 Ma (Rb-Sr, Verwoerd et al., 1993). Gose et al. (2013) compiled a poler wander path for the Kaapvaal Craton which encompasses the above mentioned ages along a path that ranges from 1.4 Ga to 1.0 Ga (Figure 3.39).

The motivation for this study uses the observed difference in the magnetic anomalies between the Pilanesberg Complex and the Pilanesberg dyke System to suggest a gap in the ages related to a reversal of the Earth's magnetic field. Ages for the Pilanesberg dykes range from; 1290 ± 80 Ma, 1302 ± 80 Ma, 1310 ± 80 Ma (Robynson dyke) to 1330 ± 80 Ma (Gemspost, Venterspost Mine) (All from Rb-Sr on biotite, Van Niekerk, 1962., Emerman, 1991). These dates for the dykes fall within the range of ages obtained for the Pilanesberg Complex (Hansen et al., 2006).

The clinopyroxenite pipes in the centre of the Bushveld Complex at the Elandskraal Volcano are also similar in age to the other intrusions within the Pilanesberg Province. The drill core from the clinopyroxenite yielded an age of 1207 ± 200 Ma (Sm-Nd mineral isochron, Cawthorn et al. (2012)) (Figure 1.5).

The ages published for the intrusions in the Pilanesberg Province are summarised in **Table 1.1.**

Table 1.1 Published age dates for the Pilanesberg Complex and the Pilanesberg dykes to compare different dating results.

	Age ± error (Ma)	Method of Dating	Dated unit	Reference
Elandskraal Volcano	1207 ± 200	apatite–clinopyroxene pairs using Sm–Nd	olivine–magnetite–apatite clinopyroxenite body	Cawthorn et al. (2012)
Pilanesberg dykes	1290 ± 80	Rb-Sr on biotite		Van Niekerk, 1962., Emerman, 1991
	1302 ± 80	Rb-Sr biotite	Dolerite	Van Niekerk (1962), Schreiner and Van Niekerk (1958) from Hansen et al. (2006)
	1310 ± 80	Rb-Sr on biotite	Robynson dyke,	Van Niekerk, 1962., Emerman, 1991
	1330 ± 80	Rb-Sr on biotite	Gemspost, Venterspost Mine	Van Niekerk, 1962., Emerman, 1991
Pilanesberg Complex	1193 ± 98	Rb-Sr regressed isochron		Harmer (1992)
	1250 ± 50	K-Ar		Retief (1963) from Olivo and William-Jones (1999)
	1290 ± 180	Rb-Sr Stable Isotope dilution		Schreiner and Van Niekerk (1958)
	1330 ± 80	Rb-Sr Stable Isotope dilution		Van Niekerk (1962)
	1397 ± 47	SHRIMP U-Pb titanite	White nepheline syenite	Harmer R., Armstron R. (unpub) from Hansen et al. (2006)
Spitskop Complex	1341 ± 37	34-point whole-rock Rb–Sr isochron	Carbonitite ijolite, nepheline syenite.	Harmer, 1999
Leeuwfontein Complex	1374 ± 10	SHRIMP U–Pb zircon	Syenite	Harmer R., Armstron R. from Hansen et al. (2006)

A summary of published age data collected from the entire Pilanesberg Province, including the Pilanesberg Complex, Pilanesberg dykes and other intrusions in the Pilanesberg Province is presented in Figure 1.9. The comparison of all the intrusions emphasises how unprecise the ages are due to the difficulty of dating lithologies without zircons. The ages and errors for all the intrusions within the Pilanesberg Province are all within error analysis of each other between 1200 and 1400 Ma (Figure 1.9).

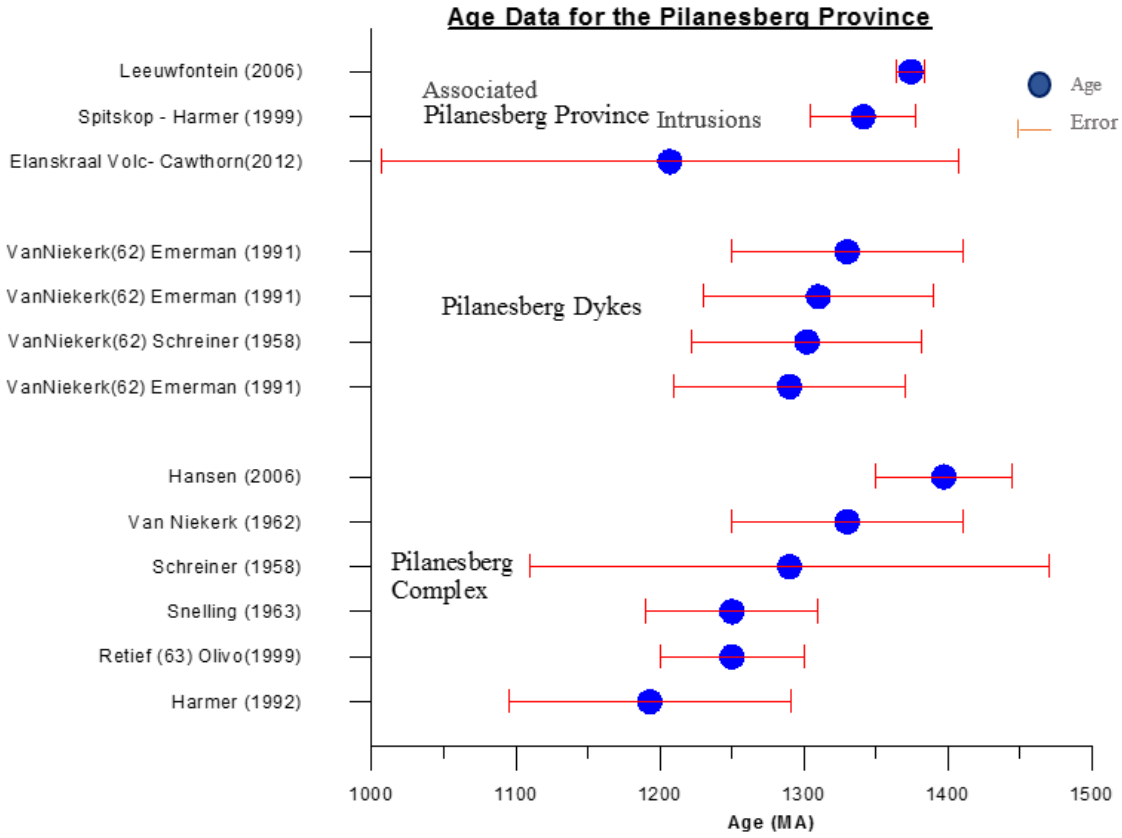

Figure 1.9 **Age data from the Pilanesberg Complex and associated bodies are summarised from oldest at the bottom to the most recent ages at the top. The first three points are dates from other complexes within the Pilanesberg Province. The next four data points are the published age dates for the Pilanesberg dykes System, and the remaining points display the different ages published for the Pilanesberg Complex between 1200 and 1400 Ma.**

1.4 GEOMETRY OF THE PILANESBERG COMPLEX

The shape of the Pilanesberg Complex is unknown at depth or in relation to any 3D geometry. Thus far, any suggested geometries for the Pilanesberg Complex have been based on the field observations on the surface alone. These geometries include a laccolith (Shand, 1928) and a funnel (Retief, 1963).

Lurie (1986) used surface dips to derive a geological model (Figure 1.10) of a cone, formed by inward-dipping ring dykes around a central plug with the vertical axis leaning to the south-east. In this model (Lurie, 1986) the internal dipping ring structure surrounds a central plug, with large faulted blocks resulting from a collapsed caldera formation (Figure 1.10). While surface dip measurements can constrain the surface geology, these measurements do not define the intrusion at depth. The apparent dip angle is 30° in the south, 40° in the west, and 30° in the east. The rocks in the north, however, dip northward at a 65° angle towards the north

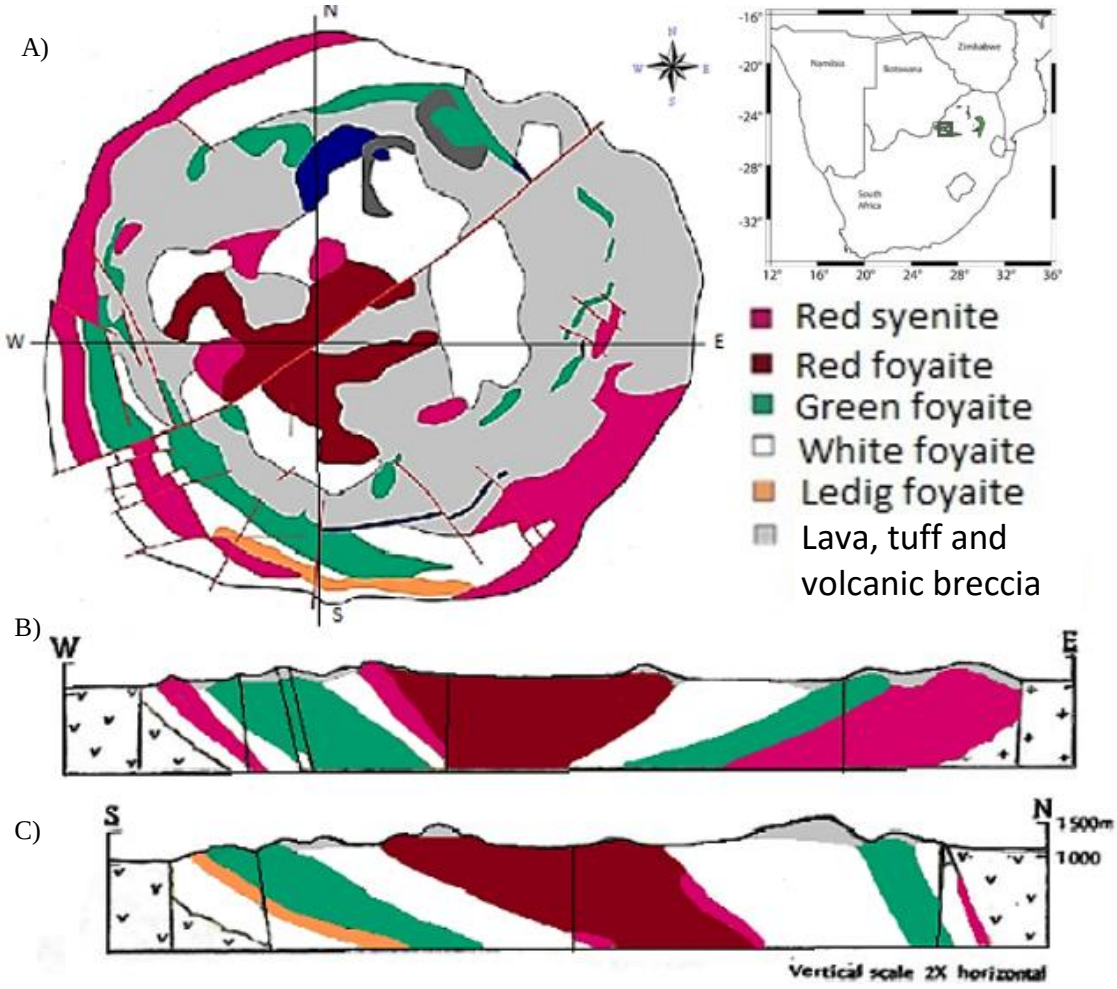

Figure 1.10 Geological overview of the Pilanesberg Complex in A) as well as schematical WE profile in B) and a SN profile through the Pilanesberg Complex in C). The profiles are extrapolated based on surface dip measurements. True depth is not represented Modified from Lurie (1986) and Cawthorn (1988).

Cawthorn (2009) proposed several models to account for the space required for the 28 km diameter intrusion that the host rock would need to accommodate when the Pilanesberg Complex intruded. The illustrative example in Figure 1.11 indicates how the host rock shifts, depending on the geometry and manner of intrusion.

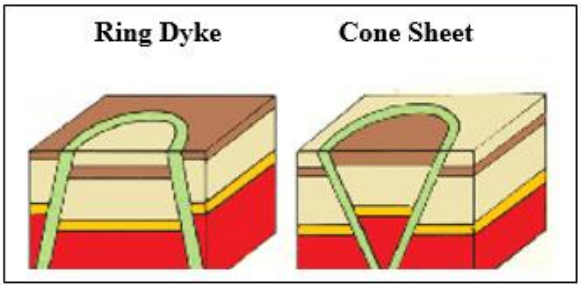

Figure 1.11. Two possible geometries explain the start of the intrusion process. The sequence examines how the host rock initially accommodates space for the intrusion of the Pilanesberg Complex. A ring dyke scenario would form either with subsidence of the host rock (left) or the formation of a cone sheet (right), modified from Cawthorn (2009). (No depth scale is represented.)

Cawthorn (2009) also discussed the possibility that the Complex emplaced as near-horizontal cone sheets that preceded centripetal subsidence. However, Cawthorn (2015) argues that the Complex is too large and coarse-grained to be either a ring dyke or a cone sheet, which are fine-grained intrusions. Moreover, such intrusions could not account for the elimination of the country rock into which it intruded. Cawthorn (2015) suggested that the Pilanesberg Complex is an inward-dipping sheet and later magma injections renewed an existing developing magma chamber (Figure 1.12). This particular model requires a level bottom to the Complex, such that the body does not extend to depth.

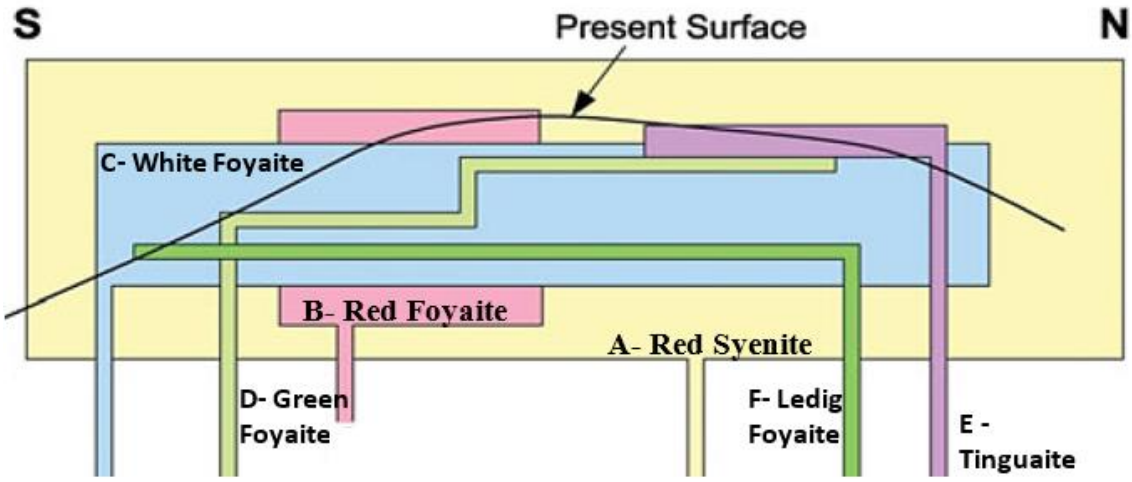

Figure 1.12. Cawthorn (2015) proposed the Pilanesberg Complex forms as an inward-dipping sheet with magma injections. The order of intrusion is as follows: A- Red Syenite, B- Red Foyaite, C- White Foyaite, D- Green Foyaite, E- Tinguaite and F- Ledig Foyaite. Modified from Cawthorn (2015). No depth scale is represented

1.5 PROSPECTUS

The prospectus outlines the stages involved in achieving the results required to solve the hypotheses about the Pilanesberg Complex presented herein. Some of the key concepts investigated include the internal and overall body geometry of the Pilanesberg Complex and how the Bushveld Complex accommodated the Pilanesberg Complex. The magnetic signatures and ages of the Pilanesberg Complex and the Pilanesberg dykes are also examined to see whether a reversal occurred between their emplacements

In Chapter 2, the data sets are introduced and reviewed as a background for the proceeding chapters. The data sets include the geology, terrain data, magnetic and gravity maps and the physical property data. The physical property data include Pilanesberg Complex rock information from the Council for Geoscience as well as physical property measurements made on the samples collected from the site locations for the Pilanesberg Complex and the dykes in this project. The profiles extracted from the gravity and magnetic maps are presented and will be reviewed with 2D and 2.5D models in the modelling chapter.

Chapter 3 is a geochronology analysis of two Pilanesberg dykes from the southern dyke swarm and two lithologies from the Pilanesberg Complex. Petrography and geochronology are used to examine the difference between the Pilanesberg Complex and the dykes. The geochronology uses the $^{40}Ar/^{39}Ar$ age dating method for the assessment of the samples.

Chapter 4 is the image-processing chapter. The gravity and magnetic data have different image processing techniques applied to them in order to highlight features utilised in the modelling and interpretation of the Pilanesberg geology. Image processing techniques examine the datasets for geological features used in modelling and the interpretation of inversion models. The magnetic map is reviewed with the following techniques: horizontal and vertical derivatives, analytic signal, sun shading and Euler deconvolution. Processed gravity maps include an automatic gain control, contact depth imaging and Euler deconvolution. A new geology map is presented for the Pilanesberg area based on the results from the image-processed maps.

The shape of the Complex at depth is investigated with gravity and magnetic 2D, 2.5D and 3D forward models and inversion models in Chapter 5. The modelling tests how the host rock accommodated the 28 km diameter intrusion to determine the correct geometry of the Complex. Profile models compare different geometries to test which best fit the potential field data. The suggested geometry is used to create a PyGMI 3D forward model to examine better the depth extent and host rock interaction. University of British Columbia (UBC) 3D inversion code models are used to confirm the geometry and host rock relationships while the Voxi inversion strictly examines the internal structure of ring and fault

behavioural patterns in the data. A series of schematic diagrams are produced to explain a possible intrusion history based on the forward and inversion modelling results with the geological data from previously published work.

Chapter 6 includes an interpretation summary to amalgamate all the chapters results including the image processing and geophysical modelling to define the shape of Pilanesberg Complex. The second part examines the geochronology to determine the age and see if there is a possibility for a magnetic reversal between the Complex and the Southern Dyke Swarm which could be followed up with a further study.

CHAPTER 2: DATA

The Pilanesberg Complex and the Pilanesberg dyke System data sets are image processed to find features relevant to the 2D and 3D modelling to assist with the interpretation of the Pilanesberg intrusion. Magnetic and gravity data grids discussed herein were obtained from the Council for Geoscience.

2.1 GEOLOGICAL DATA

The 2526 Rustenburg 1:250 000 geological map (Walraven, 1981) provides a necessary basis for models that attempt to show how the Pilanesberg Complex intruded into the gabbronorite of the Western Bushveld limb (Figure 2.1) and also constrains the gravity and magnetic models. From west to east, the geology changes from the Transvaal Super group to the Pilanesberg Complex and thence to the Bushveld granites. The north-south forward models start to traverse the Transvaal Super group, the northern Bushveld gabbro, the Pilanesberg Complex and into the Bushveld gabbro south of the Pilanesberg Complex. The map also displays Transvaal Silverton shale and Magaliesburg quartzite to the south-east of the Pilanesberg Complex. The Pilanesberg dykes intrude at north-south orientation to the south of the Pilanesberg Complex.

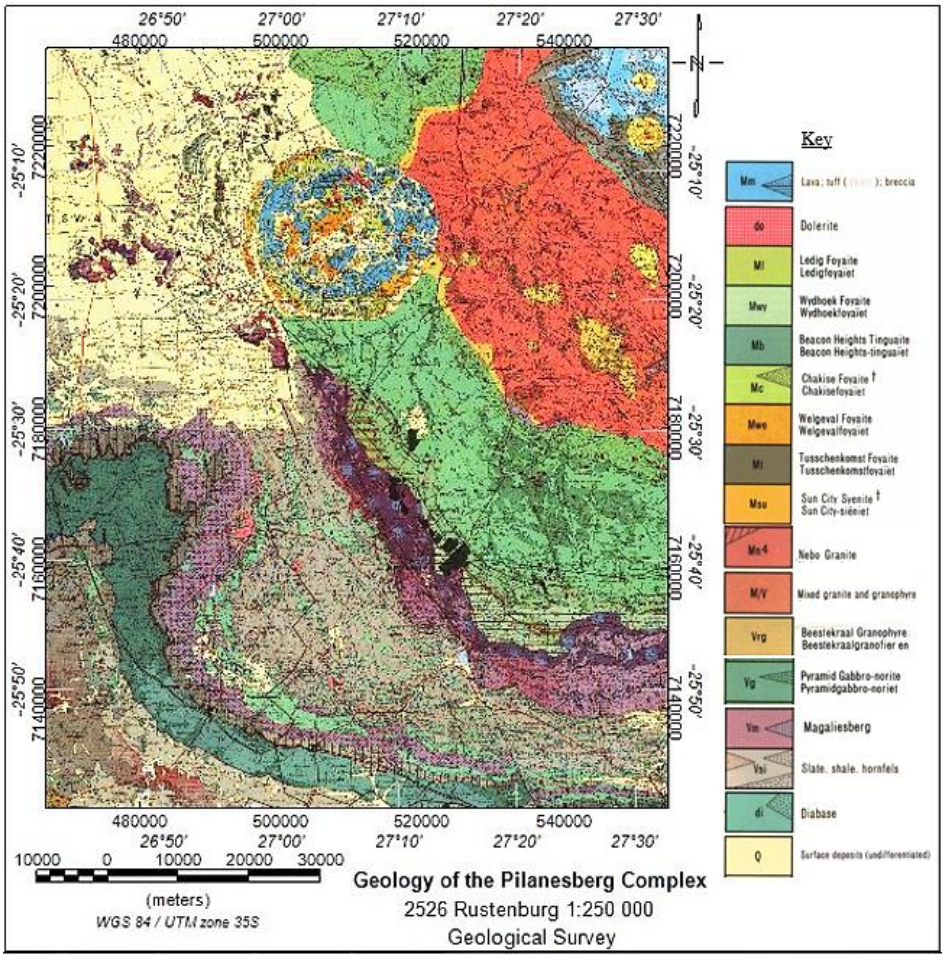

Figure 2.1 Rustenburg geological map, sheet 2526. The 1:250,000 map was cropped to display the Pilanesberg Complex and the pertinent surrounding rocks including the Bushveld Complex, and the Magaliesburg quartzite of the Transvaal Supergroup.

This map and the detail in Figure 2.2 indicate the internal geology of the Pilanesberg Complex, namely the 'ring' like symmetry that will be examined as part of the potential field modelling. The internal geology is examined as are the external relationships: these include the contact relationship of the Pilanesberg Complex such as the displaced Bushveld and Magaliesburg rocks on the west of the Pilanesberg Complex.

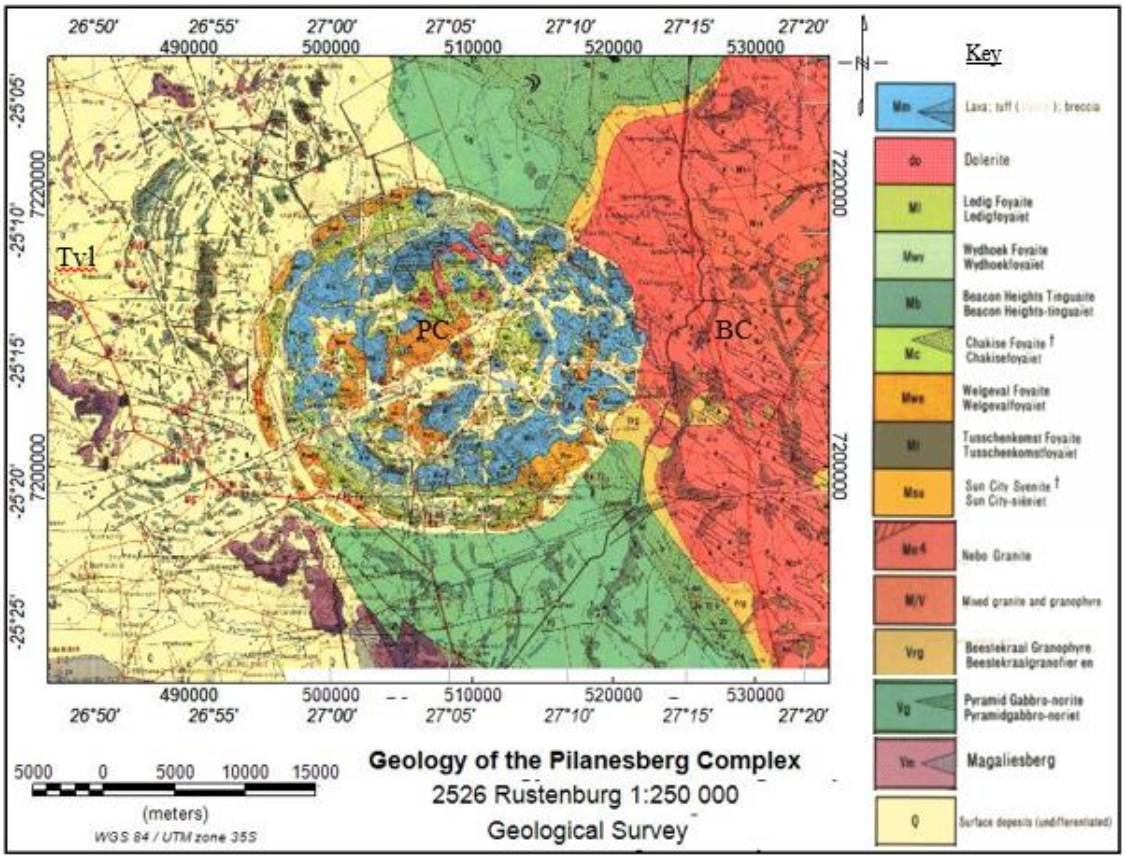

Figure 2.2. The circular Pilanesberg Complex geology situated in the Transvaal Supergroup (Tvl) and the Bushveld Complex (BC).

2.2 SAMPLING

Samples required to carry out the aim of this project include the grey syenite dyke and the red syenite dyke from the southern dyke swarm. Locations were identified from the features seen on the magnetic map. Google Earth images along with recommendations from Professor Carl Anhaeusser and Professor Grant Cawthorn suggested outcrop locations for the Pilanesberg Complex and the dykes (Figure 2.3).

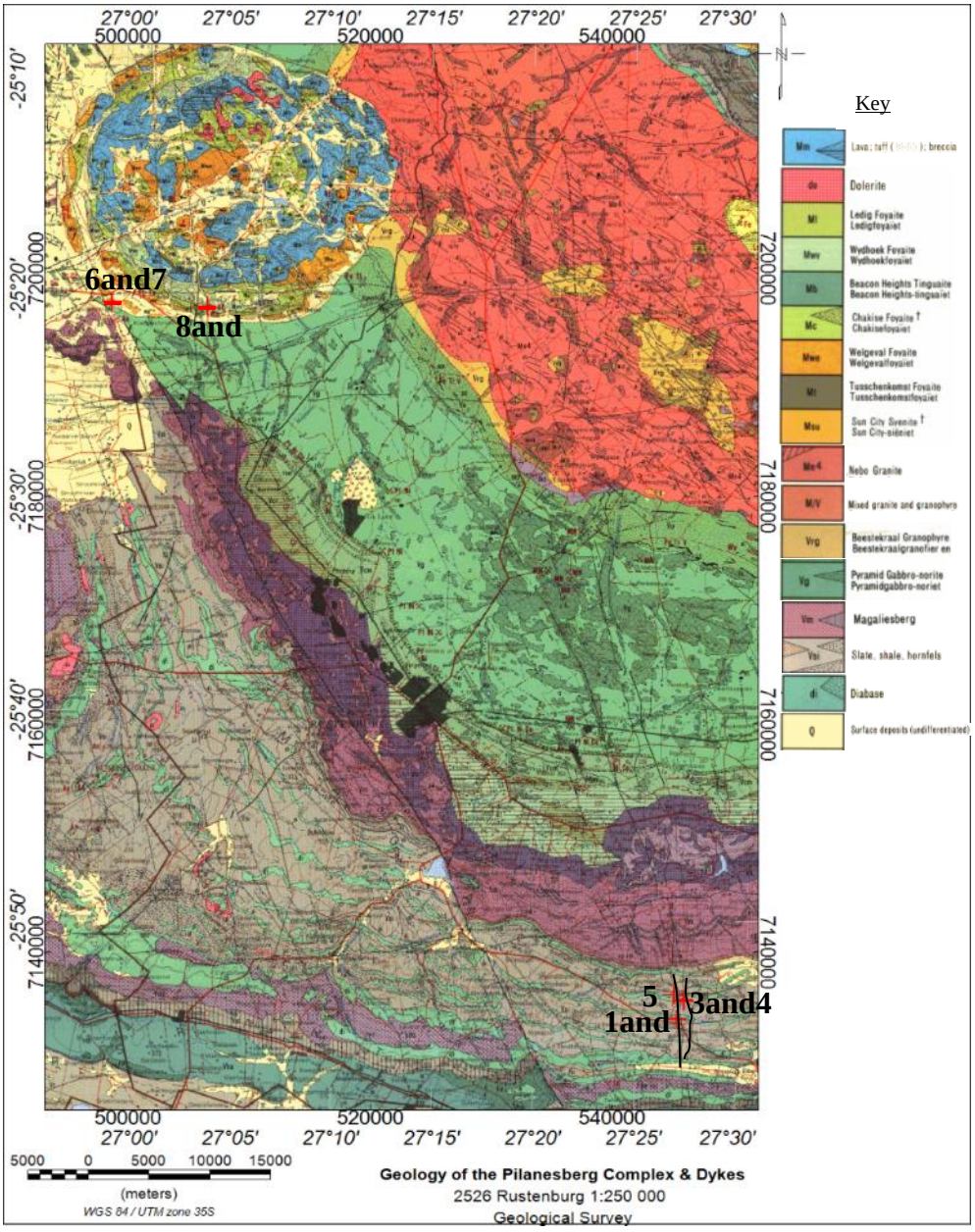

Figure 2.3 An overview setting from the grey and red syenite dyke sampled at 1 – 5 and seen below the Magaliesburg Quartzite. The Pilanesberg Complex is situated to the north with the white nepheline foyaite (6 and 7) and the green nepheline foyaite (8 and 9) sample locations located on the outer rings of the circular structure.

2.2.1 Field Sampling

Samples required to carry out the aim of this project include the grey syenite dyke and the red syenite dyke from the southern dyke swarm. Locations were identified from the features seen on the magnetic map. Google Earth images along with recommendations from Professor Carl Anhaeusser and Professor Grant Cawthorn suggested outcrop locations for the Pilanesberg Complex and the dykes (Figure 2.4).

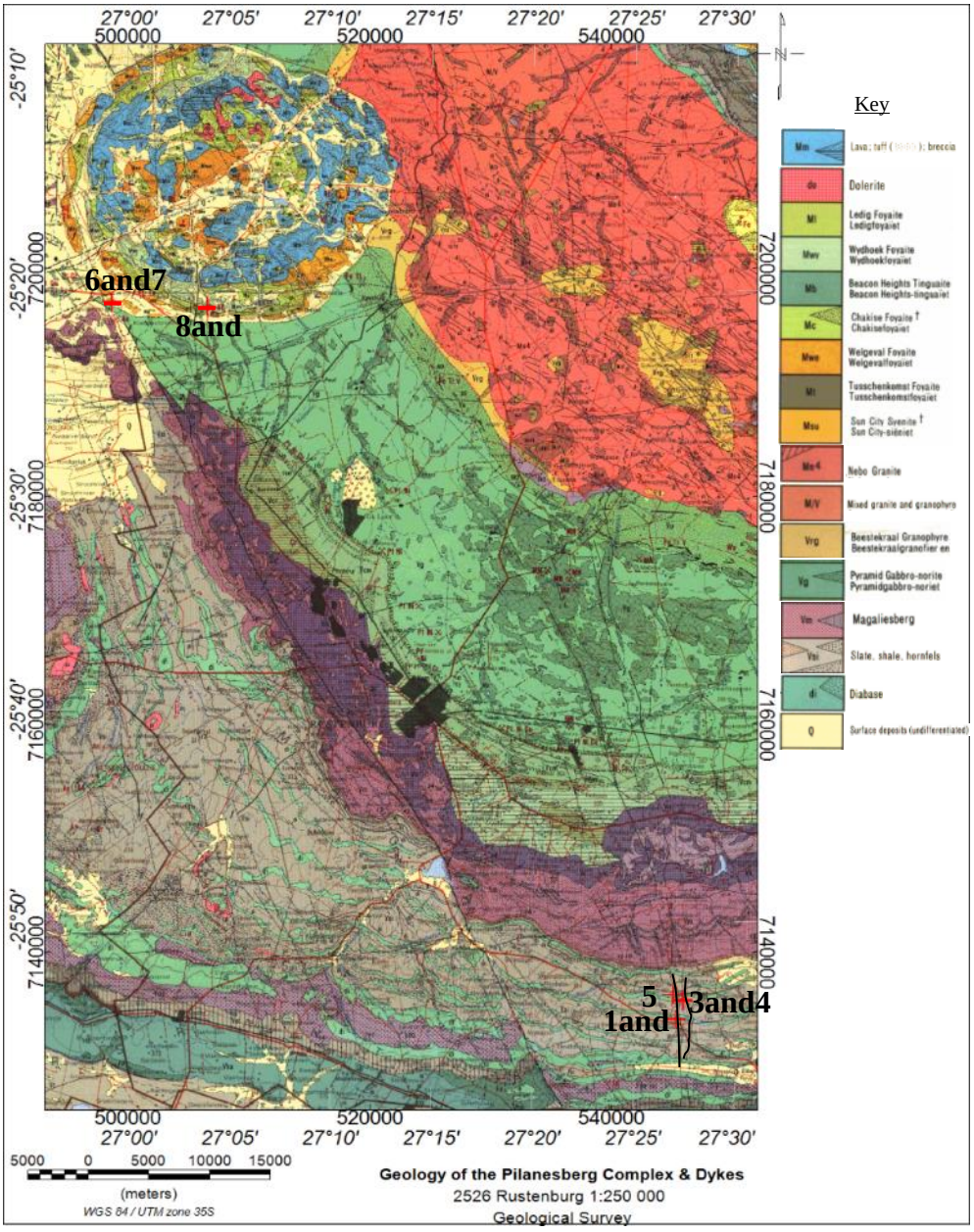

Figure 2.4 An overview setting from the grey and red syenite dyke sampled at 1 – 5 and seen below the Magaliesburg Quartzite. The Pilanesberg Complex is situated to the north with the white nepheline foyaite (6 and 7) and the green nepheline foyaite (8 and 9) sample locations located on the outer rings of the circular structure.

2.2.1.1 Methodology

Once the rocks had been identified as reliable outcrops, a clino-compass was used to orient the rocks at each site. Following which the true strike and dip measurement were recorded. The whole rock samples are oriented to both strike and dip before they are removed from the outcrop. The strike line is drawn across the outcrop and the dip is measured at 90° to the strike.

Standard procedure would recommend that drilling should take place in the field where a sun compass records the information in case the clino is influenced by the rocks magnetic properties. However, as the rocks are not significantly magnetic.

Whole rock samples were collected to be drilled in the lab. The core samples need to be approximately 6 cm long to allow for adequate analysis where they were then cut into discs with a height of 2 cm (Figure 2.5 A). Once drilled, the core is removed using a copper extractor, which averts any shock magnetism from occurring (Figure 2.5 B).

Figure 2.5 A) Red Syenite dyke whole rock sample 3 with strike lines drawn on during field measurements. The whole rock is drilled in the lab using nonmagnetic drill bits, which produce the circles. B) A copper extractor removes the white nepheline syenite core sample from the Pilanesberg Complex whole rock sample 6.

Core samples are marked with the strike orientation, dip direction and the sample number (Figure 2.6).

Figure 2.6 The core samples are marked with the strike and dip direction as well as sample labels. This sample is the green nepheline syenite 8.4 from the Pilanesberg Complex.

2.2.1.2 Sample Locations and Sample Collection

The samples, which are positively magnetised, were collected from the outer white foyaite and the green nepheline foyaite from the circular alkaline Pilanesberg system, and compares them with two dykes from the negatively magnetised southern Pilanesberg dyke swarm. A Google Earth image is compared to the corresponding magnetic map (Figure 2.7), where the dyke samples occur in the less magnetic material of -50 to -20 nT in the Transvaal Supergroup rocks. The Pilanesberg Complex samples are seen to correspond to a lower magnetic area with an approximate value of 26 nT, which is much lower than the remanent area related to the northern part of the Pilanesberg Complex, which ranges between 112 and 323 nT. The geochronology data and interpretation to follow, examine why the Complex and the dykes have different magnetisation properties.

A total of nine samples were collected for the study so results will be able to give an indication of pole positions, but many more samples would be required to create an apparent wander path. Samples were collected from two different syenite dykes, with samples 1, 2 and 5 obtained from the western grey dyke and samples 3 and 4 from the eastern red dyke. The remaining samples were collected from the Pilanesberg Complex with samples 6 and 7 obtained from an abandoned quarry of white nepheline syenite and samples 8 and 9 obtained outside the park gate on a river bed of green nepheline syenite (Figure 2.7). Samples collected are fresh rocks that are in-situ with the intruding body. The rocks appeared to be relatively altered when they were collected so data quality needs to be tested and the possibility that lightning may have hit these surface rocks needs to be examined.

In Figure 2.7, the location of the dyke samples collected below the Magaliesburg Quartzite is displayed with those from the Pilanesberg Complex samples of the circular intrusions southern edge.

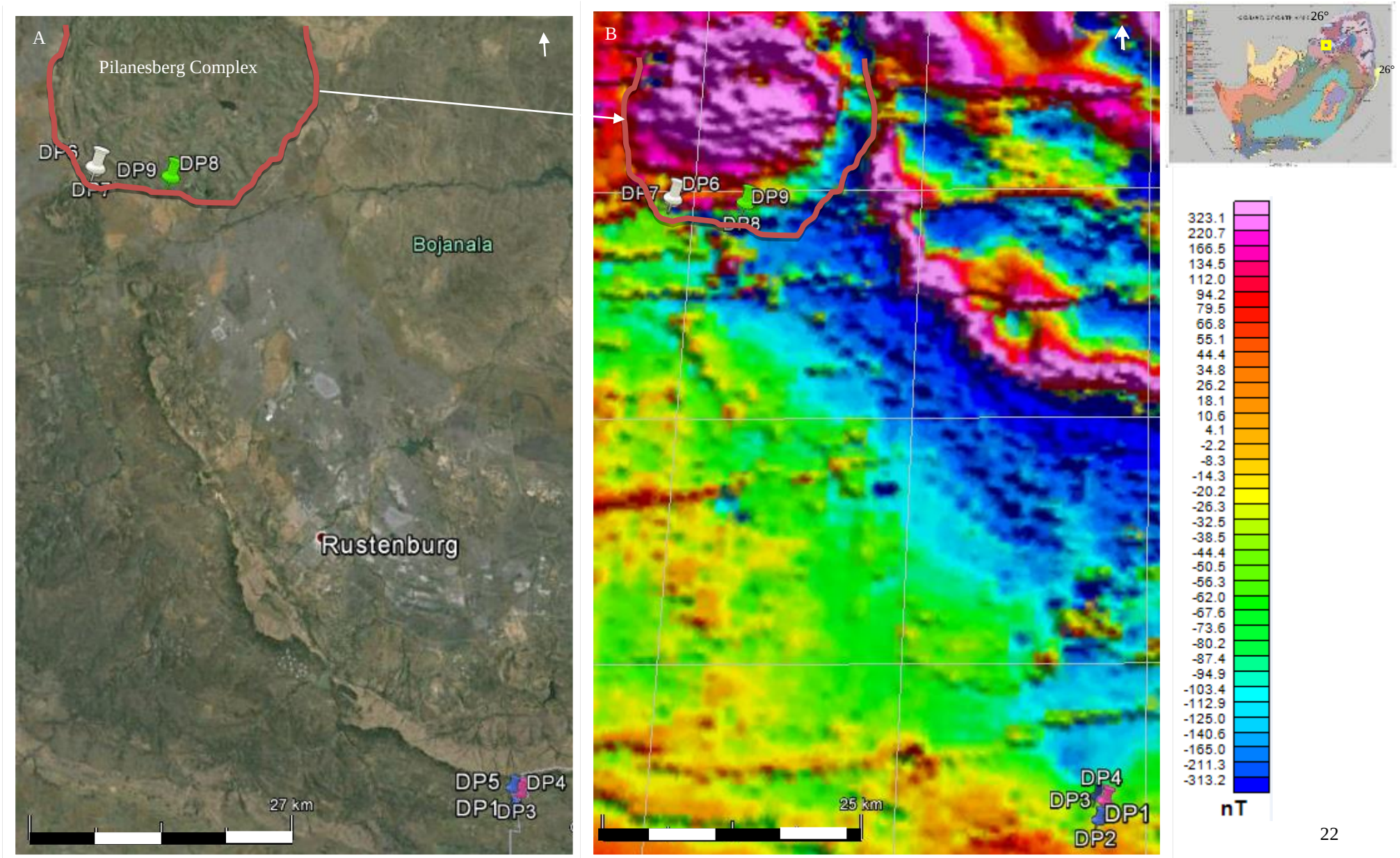

Figure 2.7 Google Earth image of the Pilanesberg System with sample locations and B) corresponding magnetic map of the Pilanesberg System.

The dykes are visible from Google Earth where the linear north, south trend is highlighted by the vegetation that grows along the dykes. The grey dyke has intruded on the western side seen in Figure 5.16 with samples 1 and 2 from the southern end and sample 5 is approximately 2.6 km north (Figure 2.8). Sample 3 and 4 are along the NS red dyke, which the vegetation highlights.

Figure 2.8 Collected samples 1, 2 and 5 are on the grey syenite dyke, while samples 3 and 4 from the red syenite dyke.

Site 1 and 2- Grey syenite dyke

Samples 1 and 2 obtained a southern syenite dykes (Figure 2.9) on a ridge that forms a prominent landscape feature standing a few metres tall and trending north towards the Pilanesberg Complex. Outcrops on the ridge should not be misidentified with the numerous boulders. The rocks in this area have the potential to be affected by lightning strikes due to the open area, higher elevation and Fe weathering. The samples 1 and 2 have been acquired from two small outcrop cliffs where the strike and dip orientation could be measured and the freshest rock samples could be obtained.

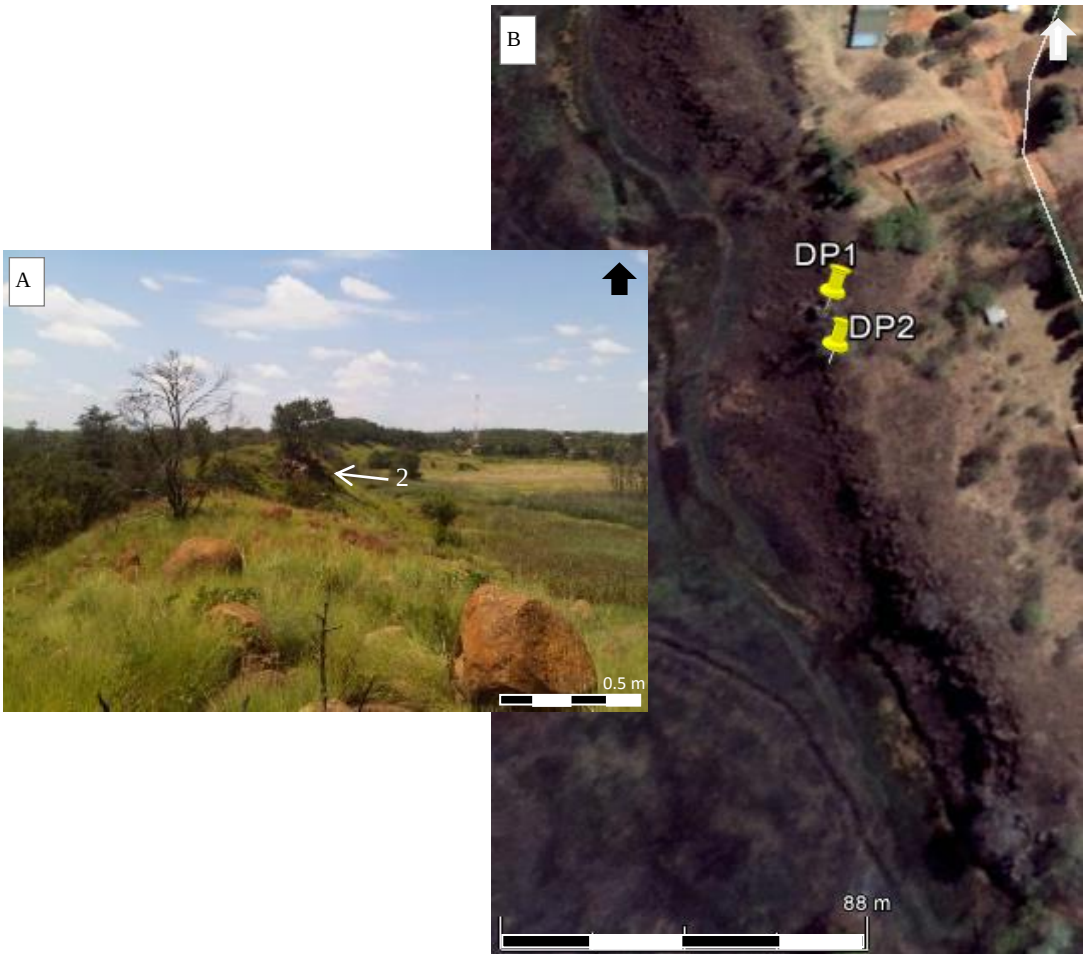

Figure 2.9 The syenite dyke forms a prominent ridge in the flat landscape of the Magaliesburg area as seen in image A) where the sample site 2 is on a small cliff. B) Displays the samples sites along the grey syenite dyke.

The grey dyke orientated whole rock samples were drilled in the Wits lab. The samples had a coating of brown weathering, underneath which is a grey syenite with large 1 cm phenocrysts and opaque minerals (Figure 2.10). The orientation lines indicating the strike and dip measurements is seen as the black line across the whole rock samples Figure 2.10.

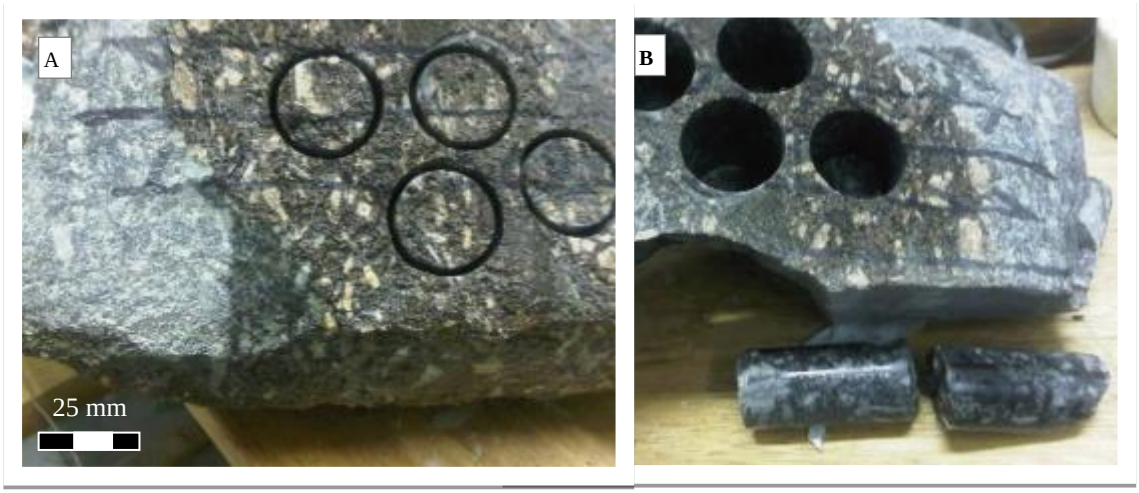

Figure 2.10 A) Syenite whole rock orientated and drilled sample 1 from site 1. B) The extracted core is grey in colour with large phenocrysts.

Site 2 is also sampled from the grey syenite dyke, as was site 1. The outcrop has a brown weathering layer beneath which is the grey rock containing large light coloured phenocrysts (Figure 2.11 B and C).

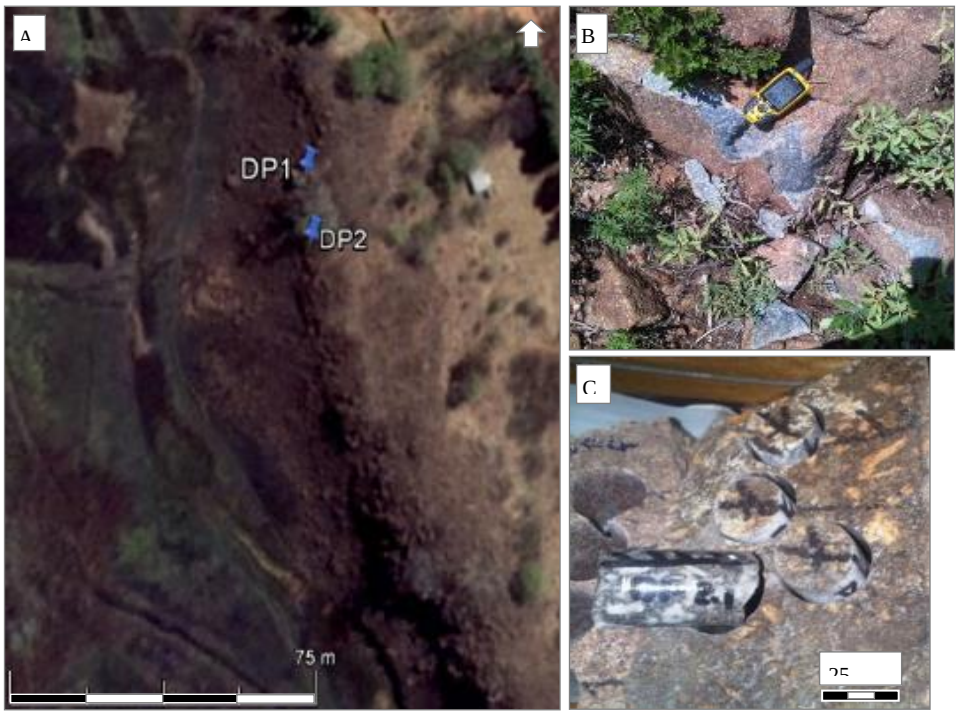

Figure 2.11 A) Site 2 along a grey syenite dyke. The whole rock sample is observed in B), and finally, the oriented core samples extracted for the physical property study in C)

Site 5- Grey syenite dyke

The samples from this site are from the grey syenite dyke closer to the Pilanesberg Complex and north of site 1 and 2. The sample was collected from an outcrop on the small ridge identified from the ridge extrapolated on Google Earth images (Figure 2.12).

Figure 2.12 A) The sites 1, 2 and 5 are observed from the grey syenite dyke running north-south on the Google Earth image. The red syenite dyke (samples 3 and 4) are parallel to the grey dyke. B) A closer view of site 5 on the ridge of the grey syenite dyke.

Site 3 and 4 – Red syenite dyke

The red syenite dyke was sampled at sites 3 and 4 (Figure 2.13) from the southern dyke swarm. The red syenite dyke runs parallel to the grey syenite dyke.

Figure 2.13 Sample 3 and 4 locations on the red Pilanesberg syenite dyke B) oriented whole rock sample C) and the drilled core sample of the distinct pink/red rocks.

In Figure 2.14, the drilled whole rock core sample indicates the red syenite dyke of site 4, which has a distinct pink/red colour in the hand sample with small black minerals and larger grey phenocrysts.

Figure 2.14 Sample 4.1 whole rock core sample from the red syenite dyke. The drilled oriented whole rock produced 25 mm diameter core used in the study.

5.3.3.1

Site 6 and 7- White foyaite

Site 6 and 7 are samples taken from a quarry of white nepheline syenite (Figure 2.15). The quarry is situated to the south-west of the Pilanesberg Complex game reserve outside of the game fence.

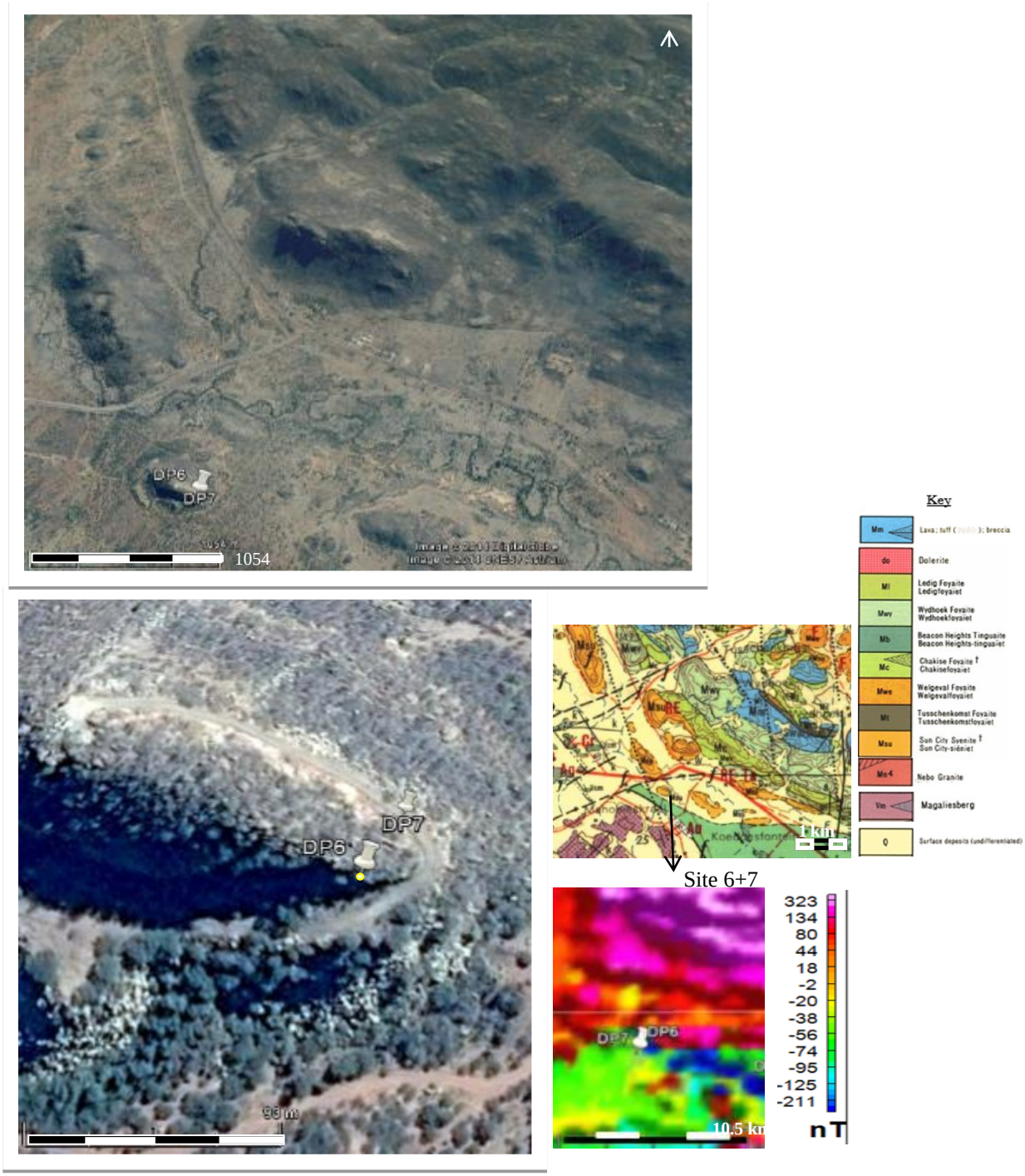

Figure 2.15 Samples 6 and 7 are white foyaite from the outer ring of the Pilanesberg Complex bottom left quadrant A). The quarried elevated hill is viewed in B). C and D identify where the sites are located on the geology and magnetic map respectively.

The samples examined for site 7 are also from the Pilanesberg Complex white nepheline syenite quarry (Figure 2.16).

Figure 2.16 The whole rock core samples of the Pilanesberg Complex white nepheline syenite. A) Drilled core extracted from the whole oriented rock. B) The wet core sample displays a slight green colouring.

5.3.3.2

Site 8 and 9- Green foyaite

The green nepheline syenite from the Pilanesberg Complex was sampled above a river located at the south gate of the game reserve (Figure 2.17). The outcrop is on a slope of the Ledig formation.

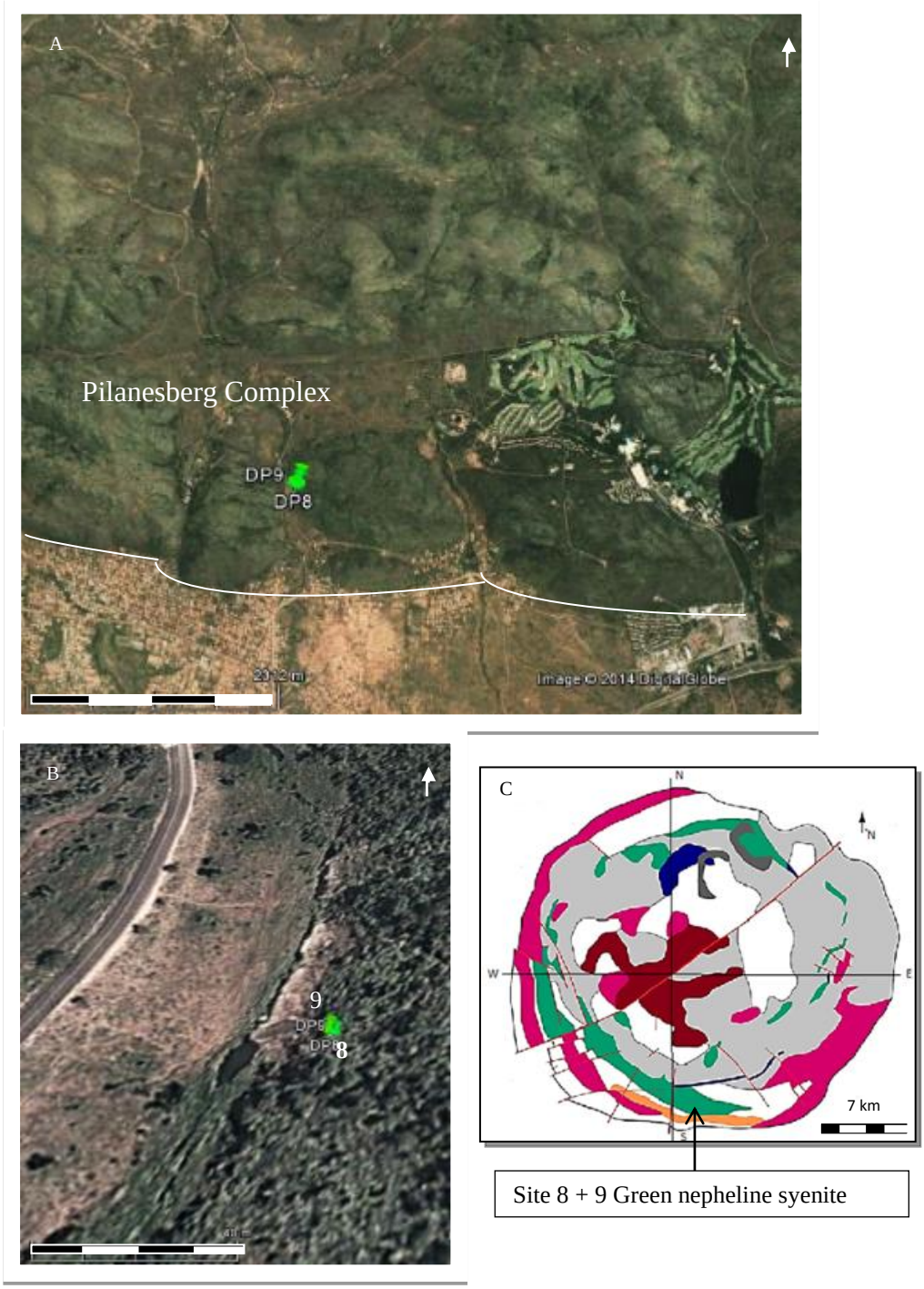

Figure 2.17 The green nepheline syenite samples observed in situ to the south of the Complex on an outcrop that is above a riverbed. A) Indicates the sampling locality with the surroundings B) indicates sites along the river and C) indicates the geological setting with colour references found in Figure 1.2.

The riverbed outcrop in Figure 2.18 A) has green colouring from the green nepheline syenite displayed on the freshly cut surface of image B), and D). The dark green-oriented core samples for sample 8 were drilled and extracted from the orientated bulk rock as displayed in C).

Figure 2.18 A) Green nepheline syenite in outcrop that will be used as oriented whole rock samples in B), oriented core sample 8.4 and 8.3 in C) and a display of the green colour of the rock sample in D).

Samples retrieved from the south of the Pilanesberg Complex are from the outer ring of the Complex. The white nepheline syenite quarry samples 6 and7 are from the outermost ring of the Complex (Figure 2.19) while samples 8 and 9 are from the riverbank outside the southern gate of the game reserve from the green nepheline syenite of the Ledig formation.

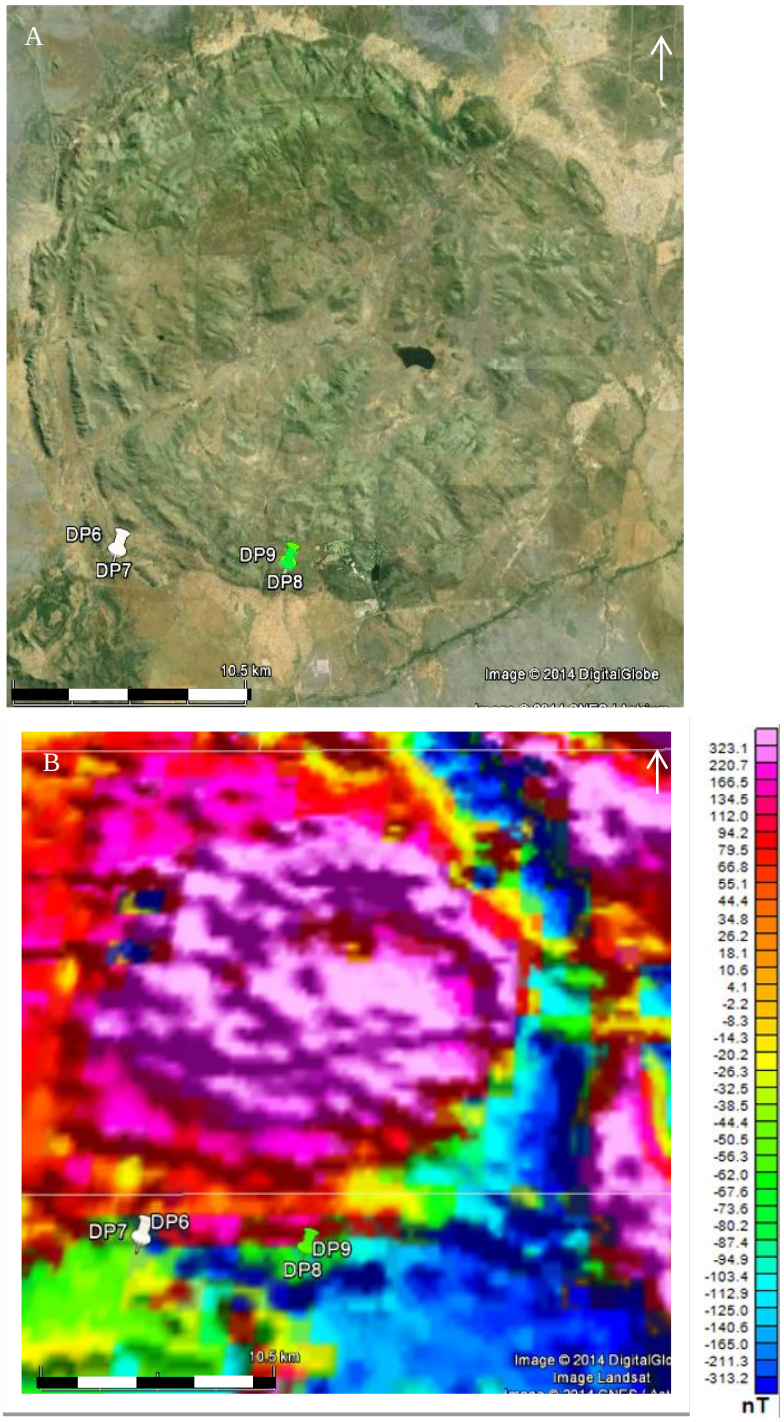

Figure 2.19 Samples 6 and 7 collected on the white marker and samples 8 and 9 situated at the green marker on the magnified magnetic map of the Pilanesberg Complex in B).

2.3 MAGNETIC DATA

The Council for Geoscience (CGS) collected the aeromagnetic data (Stettler et al., 1999) during the 1980s and the 1990s. The flight lines were flown in a north-south orientation with line spacing of 1 km and a sample spacing of ~ 60 m. The flight height of the survey was between 100 and 150 m. The properties of a magnetically normal field for the Earth (where the intensity is 28,500 nT, declination is −23° and inclination is −66°), was used to calculate the final aeromagnetic anomaly that has been corrected by the International Geomagnetic Reference Field, IGRF. The IGRF uses Gauss coefficients for a magnetic scalar potential that has been expanded using spherical harmonics. The final data map is a total magnetic intensity, TMI, map (Figure 2.20).

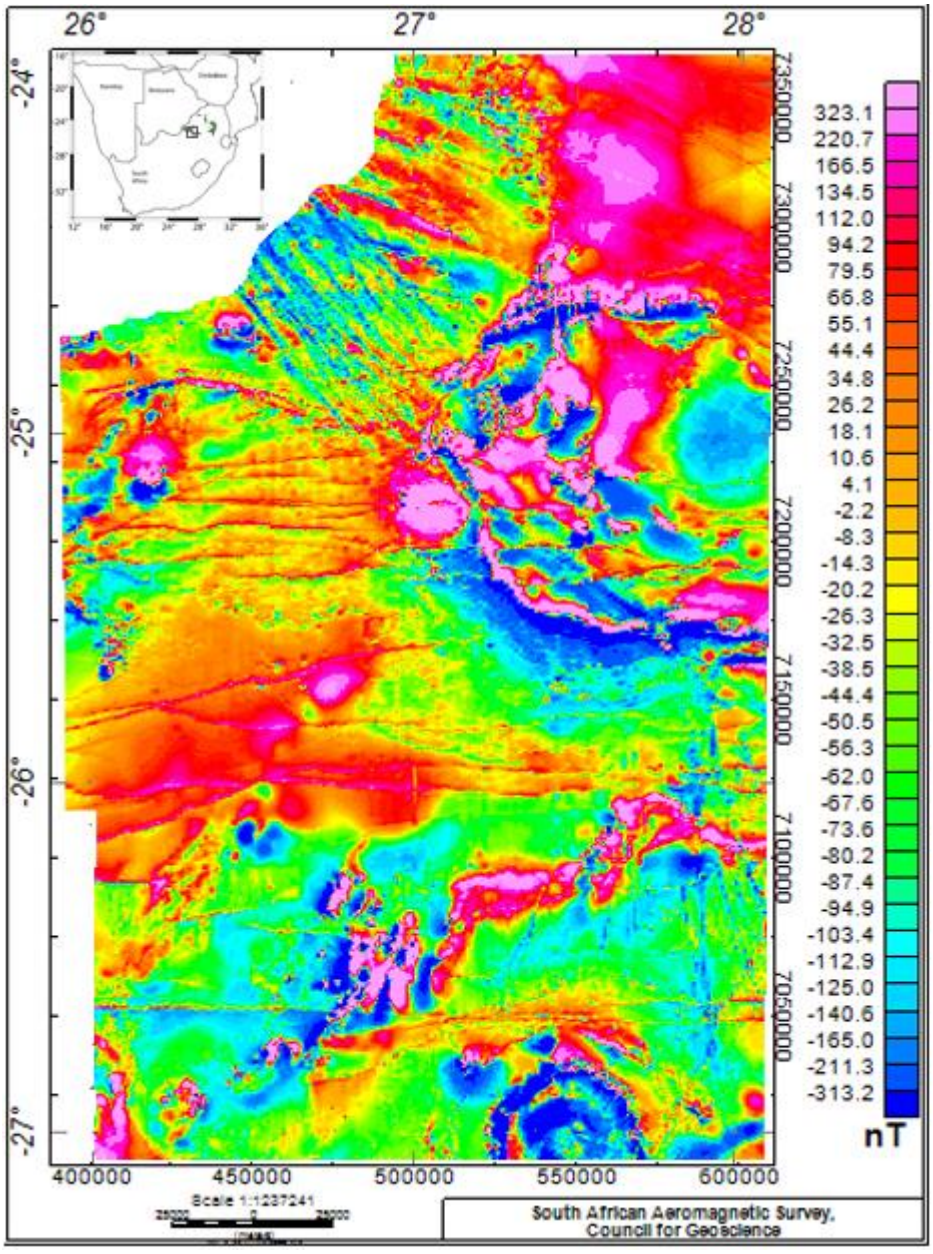

Figure 2.20 South African gridded aeromagnetic total magnetic intensity map with IGRF removed.

2.4 GRAVITY DATA

The gravity data collected by the CGS has a station spacing in this region of ~ 14 km. Ground gravity measurements were obtained along roads and at appropriate locations as part of a regional survey with 14559 stations being recorded by 1986. The data was initially referenced with International Gravity Standardization Net 1971. CGS subsequently processed the gravity data with the revised standard for reducing gravity data (Hinze et al., 2005). This method uses the terrestrial ellipsoid for the gravity stations height datum instead of using the geoid or sea level. The new ellipsoidal method does not change the local anomalies but does improve the interpretation of the regional anomaly. This is important to the Pilanesberg Complex as it encompasses a large area that will be influenced by regional trends. The resulting regional SA Bouguer gravity map is displayed in Figure 2.21. The Bouguer gravity has been calculated with the formulas discussed below.

The topographic model ETOPO1 has a resolution of 1 arcmin used for the calculation of the Bouguer anomaly assuming a crustal density of 2670 kg.m^{-3}. The Geodetic Reference System, GRS80, ellipsoid was used for the calculation which accounts for the mass, rotation and shape of the earth as the gravitational acceleration creates an ellipsoidal surface (Hinze et al., 2005). On this ellipsoid, the theoretical gravity g_T at latitude φ is:

$$g_T = \frac{g_e(1+k\sin^2\varphi)}{(1-e^2\sin^2\varphi)^{1/2}}, \quad (2.1)$$

where *ge* is the normal gravity at the equator with GRS80 reference ellipsoid, 978032.67715 mGal, *k is* a derived constant of 0.001931851353; and e^2 is 0.0066943800229, where *e* is the first numerical eccentricity.

The height correction is also affected because the height above the ellipsoid is used instead of the height above the geoid. Thus, a second order approximation is used about the ellipsoid, and with the GRS80 ellipsoid and an ellipsoid height of *h*, the height correction is:

$$\delta g_h = -(0.3087691 - 0.0004398\sin^2\varphi)h + 7.2125x10^{-8}h^2. \quad (2.2)$$

The Bouguer correction (BC) corrects for the gravitational attraction caused by a layer of the earth between the vertical datum. The traditional calculation assuming the earth between is represented by an infinite horizontal slab between the vertical datum and the earth is:

$$\delta gBC = 2\pi G\sigma h = 4.193 \times 10^{-5}\sigma h, \quad (2.3)$$

where G is the gravitational constant (6.673 ±0.001 × 10^{-11} $m^3.kg^{-1}.s^{-2}$), σ horizontal slab density (in kg.m^{-3}), and h is the station height (m) relative to the ellipsoid in this revised calculation.

The revised procedure accounts for the curvature effect of the earth. A closed-form formula for a spherical cap (SC) of radius 166.7 km is used so that

$$\delta gSC = 2\pi G\sigma(\mu h - \lambda R), \quad (2.4)$$

where μ and λ are dimensionless coefficients, R is earth's radius (R_o + h) at the station, R_o is the earth mean radius, h is height above the ellipsoid, and σ is the density of the material making up spherical cap.

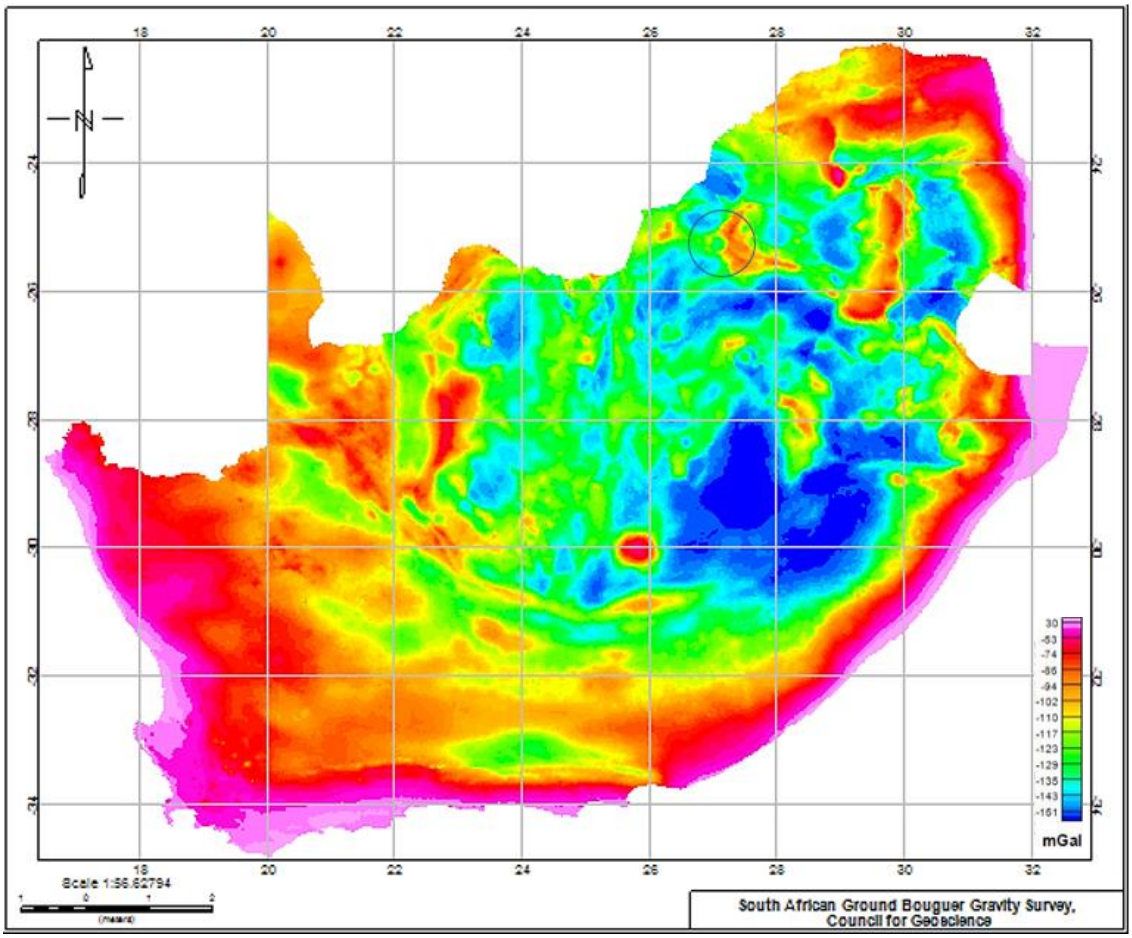

Figure 2.21 South Africa's Bouguer Gravity. The Pilanesberg Complex and Western Bushveld limb are circled.

In the national Bouguer gravity dataset from the CGS, the data has been gridded at 2 km where the Pilanesberg Complex has a gravitational signature of between -127 to -135 mGals. There is significant density contrast noted with the gravitational signal of -110 and +30 mGals in between the Bushveld Complex and the Pilanesberg Complex (Figure 2.21). Figure 2.5 also indicates that there is a large enough density contrast within the Pilanesberg Complex to make modelling profile data and creating 3D models a feasible way to examine the geometry of the Complex.

The feasibility of gravity modelling is examined by looking at the most detailed gravity map in Figure 2.22 where the coverage of the ground gravity stations is plotted for a qualitative analysis of the data. Figure 2.22 has been processed with a cell size of 250 m to indicate clearly detailed features.

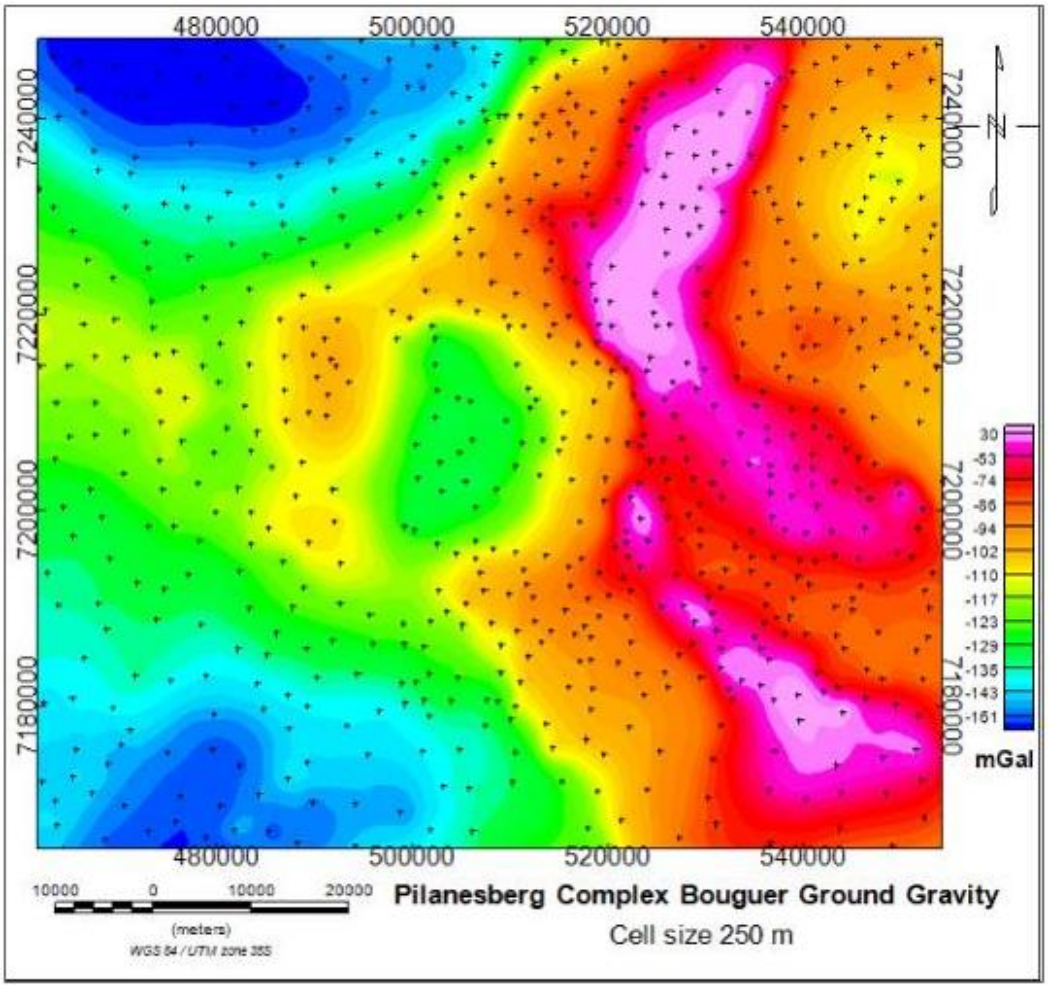

Figure 2.22 Council for Geoscience Bouguer gravity over the Pilanesberg Complex and Bushveld Complex stations shown as black crosses. Gridded to 0.25 km.

2.5 TERRAIN DATA

The Shuttle Radar Topography Mission (SRTM)**,** digital elevation model (DEM), is a high-resolution digital topographic database of the Earth collected by NASA and the USGS in 2005. The DEM has a resolution of 3 arc-seconds or 90 m at the equator (Jarvis et al., 2008). The SRTM data is used as the topography information for the Pilanesberg Complex (Figure 2.23). The DEM is used in the calculations of the 3D forward and inversion, gravity and magnetic models. It is clear that the Pilanesberg Complex has a prominent elevated surface compared to its host rocks.

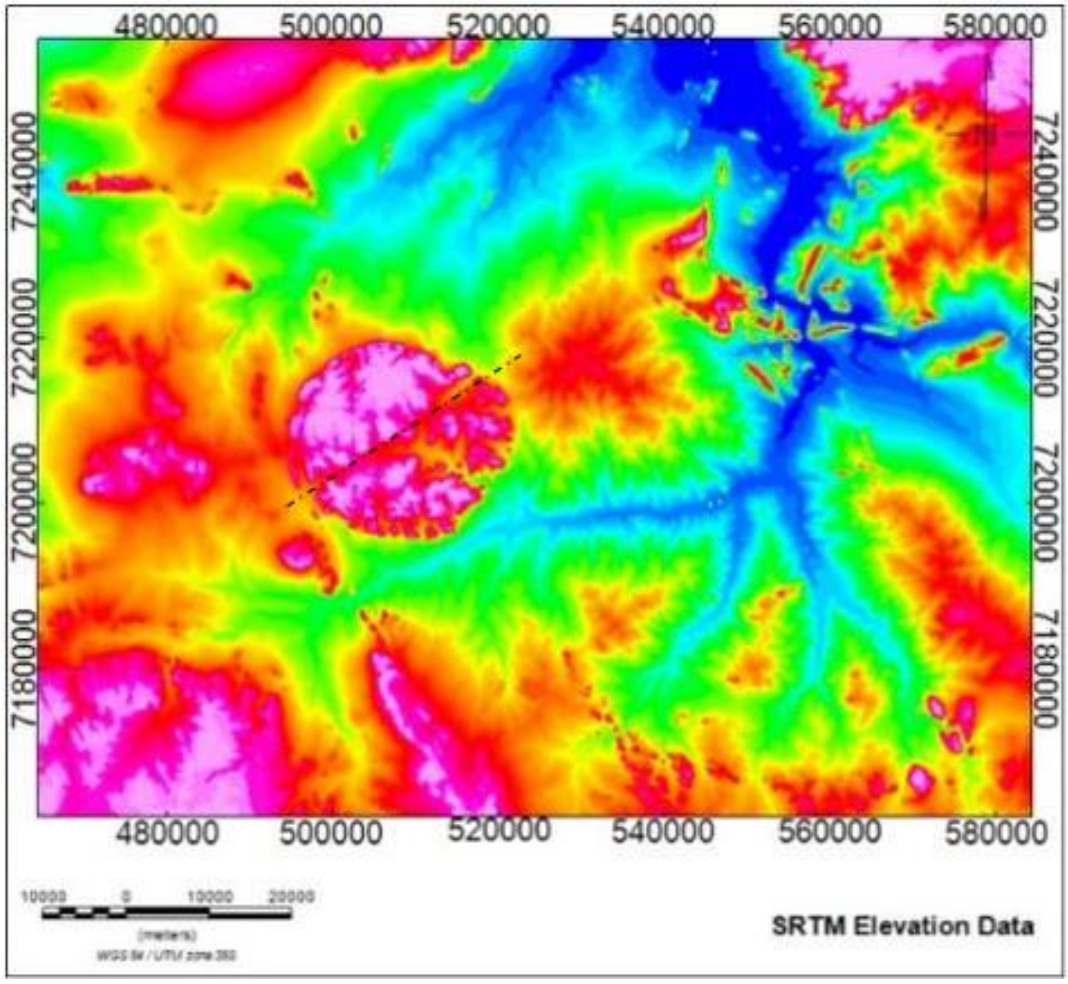

Figure 2.23 SRTM elevation data over the Pilanesberg Complex and surrounding Bushveld Complex. The Pilanesberg Complex has a high relief with the Vlakfontein fault seen as a prominent elevation feature. 90 m resolution.

The terrain and ring structure are displayed by a combined Landsat 7 and Landsat 8 image.

Landsat is a NASA satellite that continually images the earth. Landsat 7 has an Enhanced Thematic Mapper Plus (ETM) sensor at an altitude of 705 km and an 8-bit signal to noise ratio. The increased bands of the Landsat 8 use Operational Land Imager (OLI) and a Thermal Infrared Sensor (TIRS) with an improved 12-bit signal to noise ratio. Both images have a resolution of 30 m. The image displaying the Pilanesberg Complex is a combination of the Landsat 7 and Landsat 8 image (Figure 2. 24) on the 26th August 2013 (NASA and USGS, Landsat.usgs.gov, 7-9-2015).

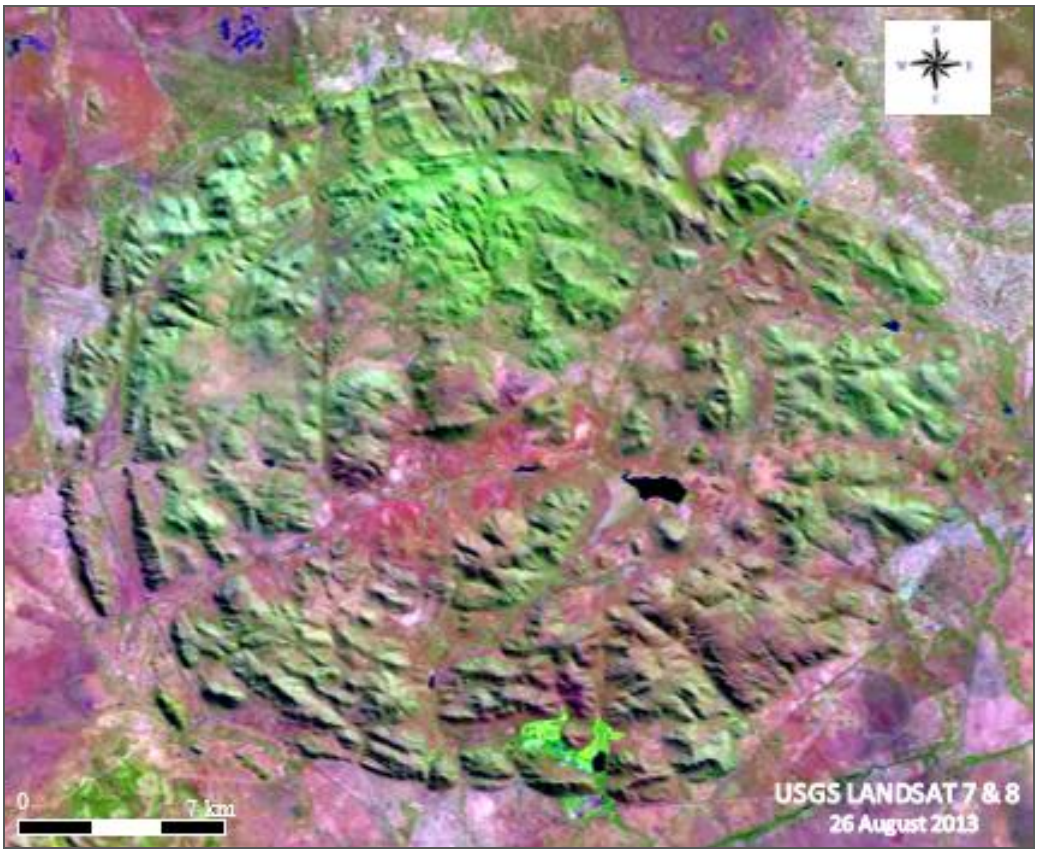

Figure 2. 24. The Pilanesberg Complex displayed with a combined Landsat 7 and 8-satellite image. The image is not a true colour image but the structural features are highlighted by combining both Landsat images (USGS, Landsat 7 and 8, 26 August 2013).

2.6 PHYSICAL PROPERTY DATA

Physical property data extracted from the Council for Geoscience database is used to estimate the density and magnetic susceptibility of each rock type for the geophysical modelling along the gravity and magnetic profiles. The estimates for rocks from the Pilanesberg Complex as well as the same rock types in different areas are listed in Table 2.1.

Table 2.1 Measured densities from the Council for Geoscience on relevant rocks from the Pilanesberg Complex and areas nearby.

Rock Type	Mean density $Kg.m^{-3}$	Min. density $Kg.m^{-3}$	Max density $Kg.m^{-3}$	Location	Latitude	Longitude
Alk-Feldspar Syenite	2680	Comment: Foyaite CGS Geol numb ref: 1417		Pilanesberg	-25.20	27.10
Syenite	2640	CGS Geol numb ref: 1418		Pilanesberg	-25.33	27.15
Syenite	2615	CGS Geol numb ref. 1557		Leeuwfontein		
Syenite	2684	CGS Geol numb ref. 1372		Richtersveld	-28.80	17.34
Syenite	2722	CGS Geol numb ref. 1452		Schiel Alkaline	-23.17	30.46
Average 2668.4						
Syenite dyke	2747	2733	2756	UP15	-25.88	27.88
Syenite dyke	2743	2738	2746	UP20	-25.93	27.88
Syenite dyke	2985	2963	2992	UP15	-25.96	27.92
Average 2825						
Lava	2740	2660	2910	Pilanesberg-1419	-25.22	-25.18
Lava	2900	2800	3000	Telford et al (1990)		
Average 2820						
Granite	2631	CGS Geol numb ref: 1086		Nebo	-24.05	28.75
Granite	2668	CGS Geol numb ref: 2003		Trompsburg	-29.89	25.60
Granite	2650	CGS Geol numb ref:505		Lebowa	-25.15	29.40
Granite	2640	2500	2810	Telford et al. (1990)		
Average 2647,25						
Gabbro	2912	CGS Geol numb ref:1446		Rustenburg Layered	-26.47	29.39
Gabbro	2858	CGS Geol numb ref:2256		Rustenburg Layered	-26.47	29.39
Gabbronorite	2898	CGS Geol numb ref:1083		Mapel Gabbronorite	-23.95	28.86
Gabbro	2831	CGS Geol numb ref:1083		Mapel Gabbronorite	-23.95	28.86
Gabbro	2987	CGS Geol numb ref:2003		Trompsburg	-29.94	25.61
Gabbro	3030	2700	3500	Telford et al. (1990)		
Average 2919,33						
Quartzite	2631	2633	2636	Magaliesburg Arenite	-25.72	27.81
Quartzite	2580	2320	2710	Johannesburg Arenite	-26.90	27.20
Quartzite	2664	2635	2696	Krugersdorp Arenite	-28.18	26.76
Quartzite	2720	CGS Geol numb ref:2656		Randfontein Arenite	-26.45	27.56
Quartzite	2600	2500	2700	Telford et al. (1990)		
Average 2639						
Transvaal	2564	CGS Geol numb ref:1652		Carbonate	-29.89	25.59
Transvaal	2703	CGS Geol numb ref:1652		Limestone	-29.89	25.59
Average 2633,5						

The average values ascertained for each rock type in Table 2.1 are used in Table 2.2 to determine the values to be used during 2D gravity modelling. For simplicity, an average geological density of 2.6 g.cm^{-3} is chosen as the background value (Table 2.2). The background density was subtracted from all the other geological units in the 2D profile models to give a density contrast to the Pilanesberg and Bushveld Complex.

Table 2.2 Measured densities from the Council for Geoscience and the background removed density values used in 2D gravity modelling. The background density of 2.70 g.cm^{-3} was used to provide adequate contrast between the Pilanesberg Complex, the background and the Bushveld Complex.

Rock Type	Mean density Kg.m^{-3}	Mean density g.cm^{-3}	Density contrast
Syenite	2668	2.67	-0.03
Lava	2820	2.82	0.12
Granite	2647	2.65	-0.05
Gabbro	2919	2.92	0.22
Quartzite	2639	2.64	-0.06
Transvaal Sg	2633	2.63	-0.07

The density measurements on the rocks collected from the Pilanesberg Complex and Pilanesberg dykes is in Appendix E. A summary of the results is provided in Table 2.3. The density is calculated by weighing each rock as well as measuring the rocks weight when submerged in water. Assuming the density of water is ~1 then

$$\frac{density\ of\ object}{density\ of\ fluid} = \frac{weight\ in\ air}{(weight\ in\ air) - (Weight\ in\ water)}. \qquad (2.5)$$

Table 2.3 Density measurement on the collected Pilanesberg samples using Archimedes Principal

Rock Unit	Average Density (g.cm^{-3})	Site	Site Density (g.cm^{-3})
Grey Syenite dyke	2.61	1	2.57
		2	5.63
		5	2.63
Red Syenite dyke	2.68	3	2.68
		4	2.69
Pilanesberg Complex White Foyaite	2.66	6	2.65
		7	2.66
Pilanesberg Complex Green Foyaite	2.92	8	2.99
		9	2.85

2.7 EXTRACTED PROFILE DATA

2.7.1 Gravity profiles

The Bouguer grid indicates that the gravitational signal of the Pilanesberg Complex is ~ 50 mGals lower than that of the Bushveld Complex (Figure 2.25). It is always valuable to investigate profile data to ascertain shape, dip and depth information about the geology (S. J. Webb, pers. comm. 06-2013). Three west-east profiles were extracted from the Bouguer gravity grid for modelling (Figure 2.25).

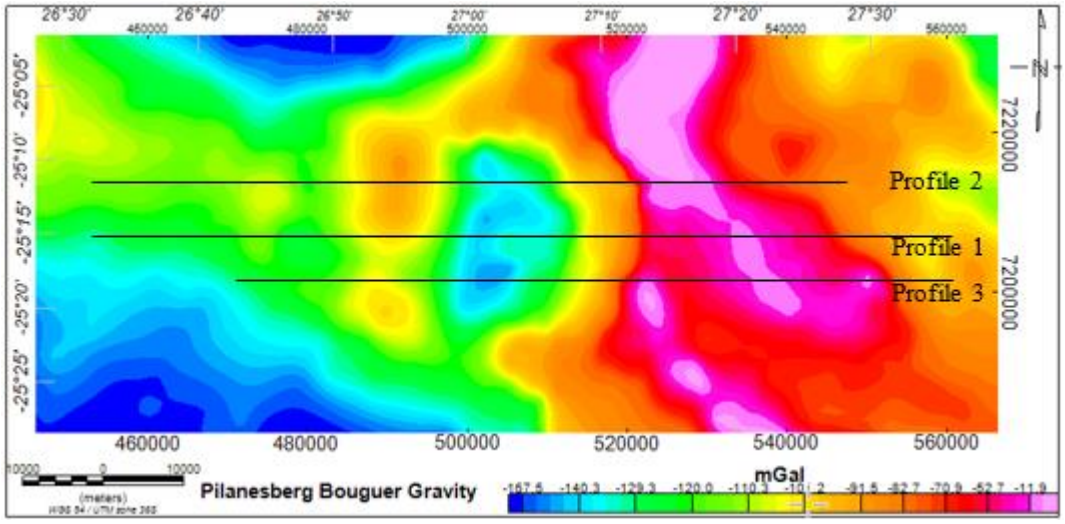

Figure 2.25 Location of the west-east profiles across the Bouguer gravity map of the Pilanesberg Complex.

Profile 1 overlain on the gravity map (Figure 2.26) shows that the central low of -130 mGals is due to the Pilanesberg Complex and the high of -80 mGals is due to the dipping Bushveld Complex with contacts and depth information required to model the signal represented by the overlying profile.

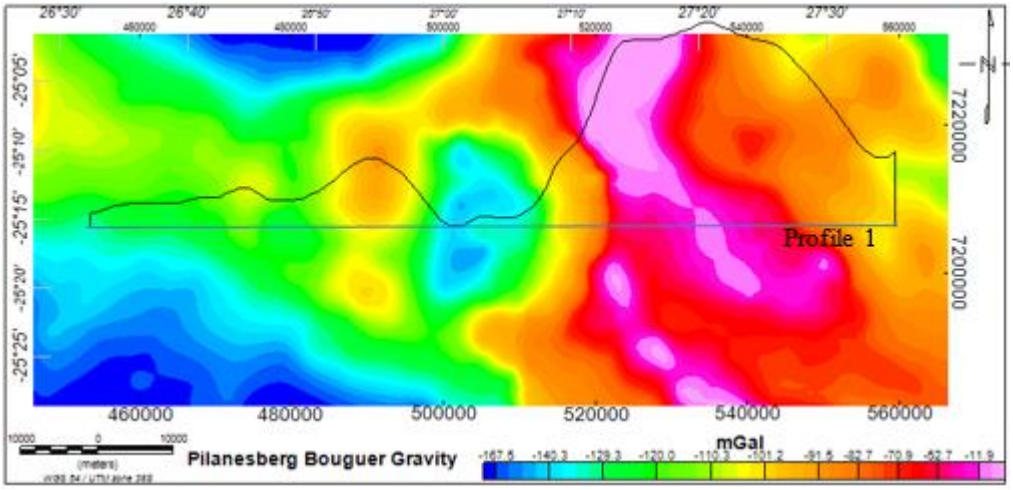

Figure 2.26 West-east profile1 with the Bouguer signal annotated on the Bouguer gravity over the Pilanesberg Complex and the Bushveld Complex

Profile 1 (Figure 2.27), profile 2 (Figure 2.28) and profile 3 (Figure 2.29) display the gravity profiles that will be examined through modelling. The WE profile 1 across the gravity data of the Pilanesberg Complex is through the middle of the Pilanesberg Complex (Figure 2.27). The low signal correlates with the Pilanesberg Complex and the 40 mGal higher signature is the western limb of the Bushveld Complex.

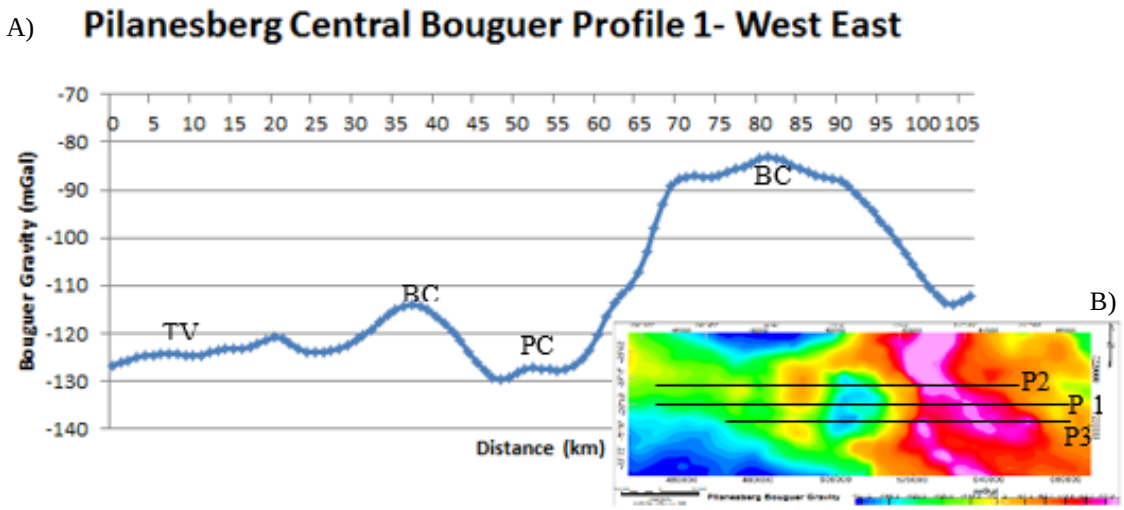

Figure 2.27 A) West-east profile 1 extracted from the Bouguer gravity gridded data in B) seen along P1. TVL- Transvaal Supergroup, BC- Bushveld Complex, PC- Pilanesberg Complex.

The northern traverse in a west-east direction is seen as profile 2 (Figure 2.28), which has the same overall pattern as profile 1 as the profiles move from Transvaal Supergroup over the Pilanesberg Complex and into the Bushveld Complex with some displaced Bushveld material to the west of the Pilanesberg.

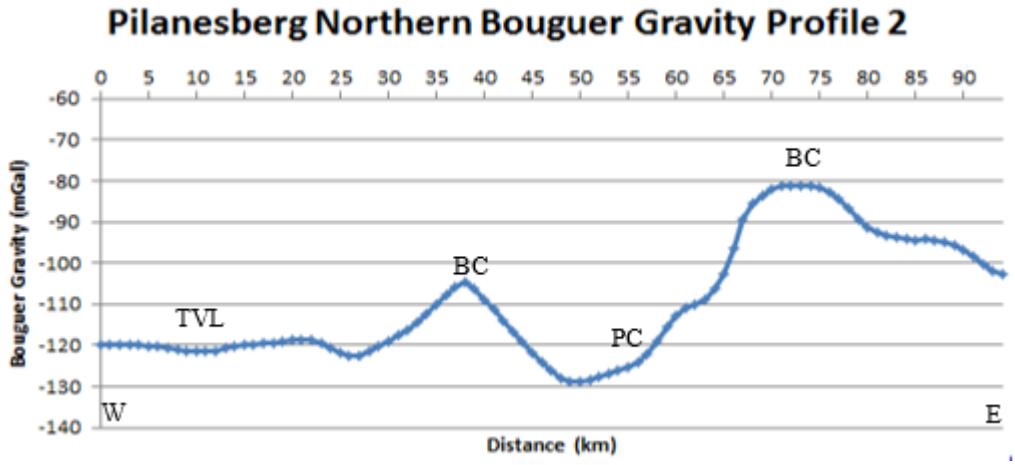

Figure 2.28 West-east profile 2 extracted from the Bouguer gravity gridded data. TVL- Transvaal Supergroup, BC- Bushveld Complex, PC- Pilanesberg Complex.

The third profile crosses the southern part of the Pilanesberg Complex from west to east, clearly defines the Bushveld to the east but there is less contrast with the Bushveld material to the west (Figure 2.29).

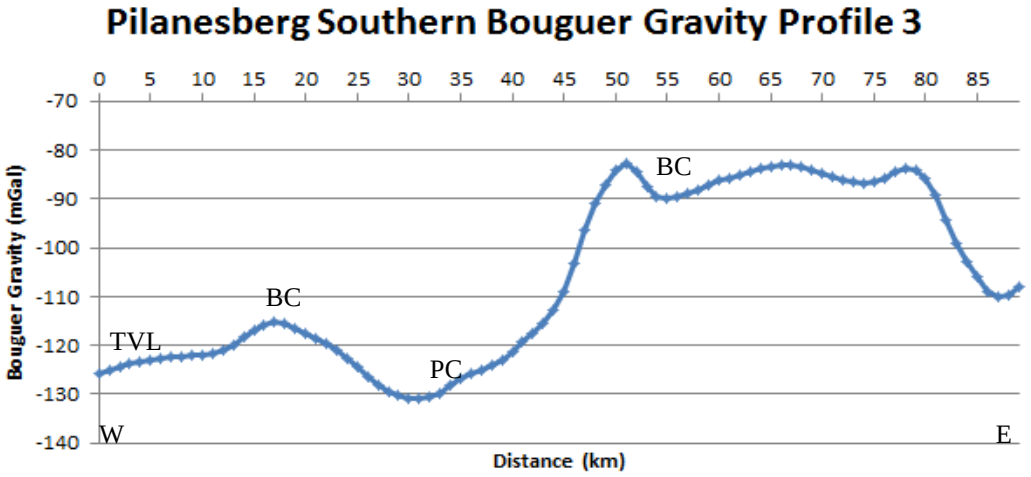

Figure 2.29 West-east profile3 extracted from the Bouguer gravity gridded data. TVL- Transvaal Supergroup, BC- Bushveld Complex, PC- Pilanesberg Complex.

Similarly, two north-south Bouguer gravity profiles have been extracted from the grid (Figure 2.30, Figure 2.31 and Figure 2.32). The north-south profile 4 is on the western side of the Pilanesberg Complex and profile 5 is on the east (Figure 2.30). These profiles cut across a greater amount of the Bushveld Complex on both the Northern and Southern contact with the Pilanesberg Complex.

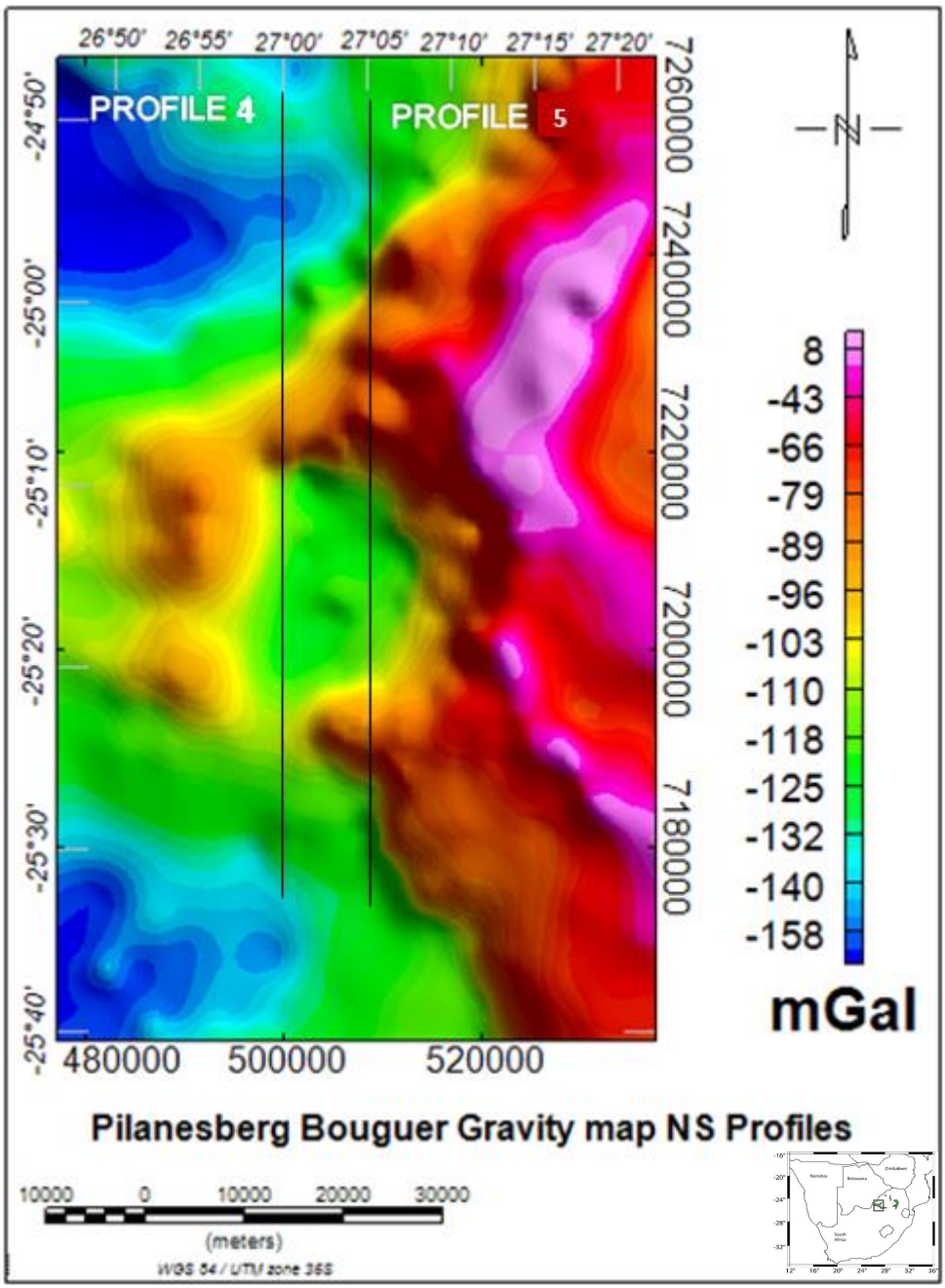

Figure 2.30 North-south profiles over the Bouguer gravity grid of the Pilanesberg Complex

Both north-south profiles reveal the signal is higher in the north at -110 mGals compared to the south at -120 mGals. The high to the north of the Pilanesberg Complex on profile 4 is substantial higher (Figure

2.31) than the northern high in profile 5 (Figure 2.32), which changes from a 12 mGal differerence to a 6 mGal difference between the northern and southern peak on the respective profile.

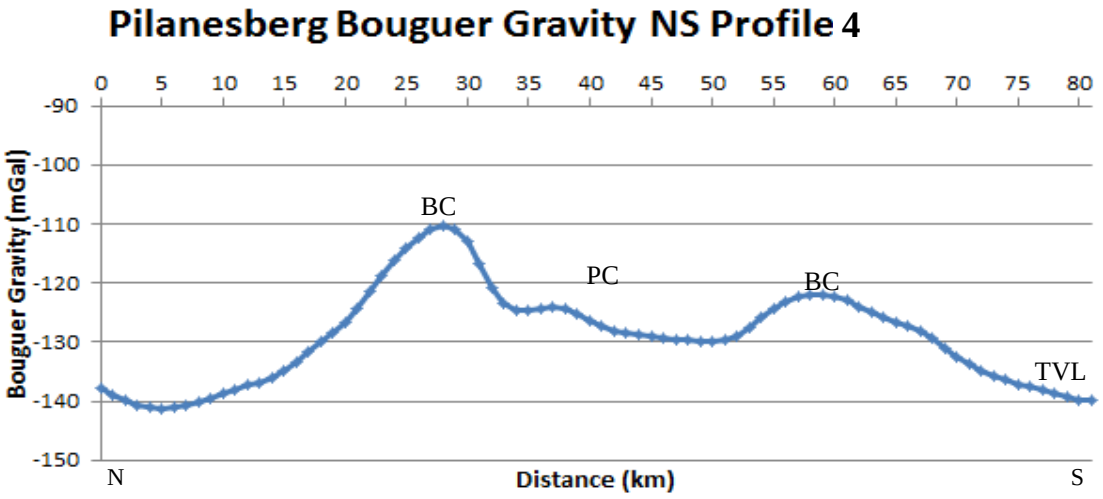

Figure 2.31 North-south profile 4 extracted from the Bouguer gravity gridded data. TVL- Transvaal Supergroup, BC- Bushveld Complex, PC- Pilanesberg Complex.

As profile 5 is east of Profile 4, this could suggest that as one moves east, we are getting closer to a denser body or that the body is closer to the surface. A similar feature is identified to the south of each profile is much broader in profile 4 and becomes sharper in profile 5 (Figure 2.32).

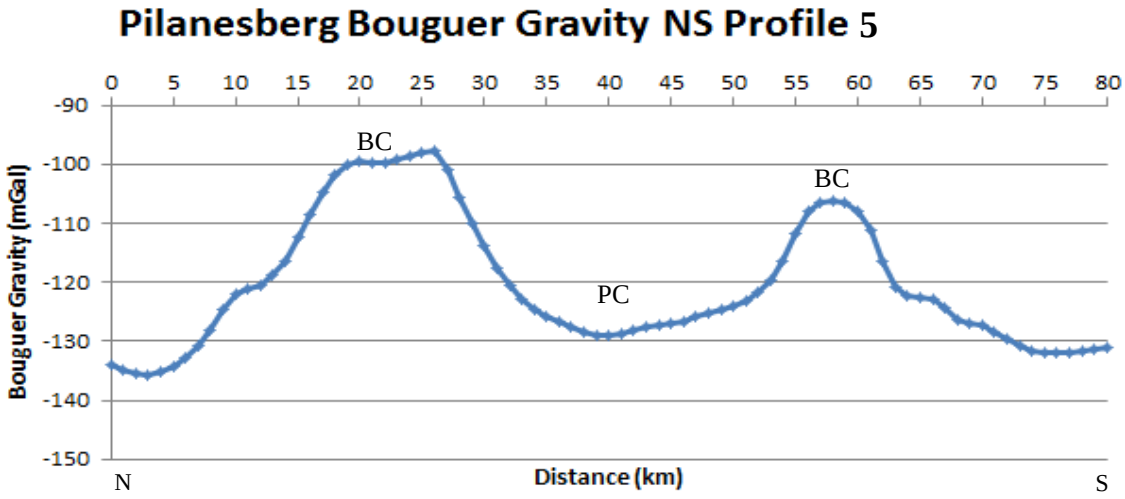

Figure 2.32 North-south profile 5 extracted from the Bouguer gravity gridded data. TVL- Transvaal Supergroup, BC- Bushveld Complex, PC- Pilanesberg Complex.

The high feature anomaly in the north of the Profile 4 and 5 is similar to the anomaly on the west of profile 1, 2, and 3 (Figure 2.27-Figure 2.29) which is associated with the Bushveld Complex on the geology map (Figure 2.2).

2.7.2 Magnetic data

Magnetic profile data over the Pilanesberg Complex and dykes derived from the TMI aeromagnetic survey over the country are shown in Figure 2.33. Image processing in Chapter 3 is used to examine and interpret the magnetic data. Following the examination of the Complex's geometry, the equivalent profiles the gravity profiles are extracted from the magnetic grid, namely profiles 1, 2 and 3 (Figure 2.33).

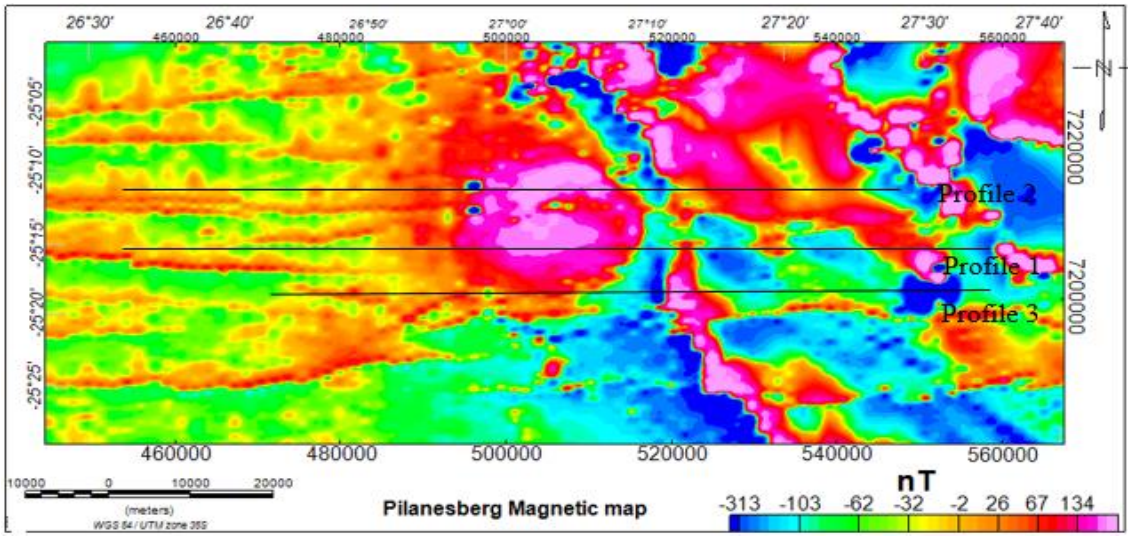

Figure 2.33 Magnetic map displaying the west-east magnetic profiles 1, 2 and 3 correlates with the gravity profile 1, 2 and 3. The magnetic profiles also move from the Transvaal Supergroup in the west through the Pilanesberg Complex and into the Bushveld Complex in the East.

The magnetic profiles reflect changes in magnetic susceptibility along the profiles. The central Pilanesberg Complex signal (Figure 2.34) is dome-shaped suggesting to a round or cylindrical geometry.

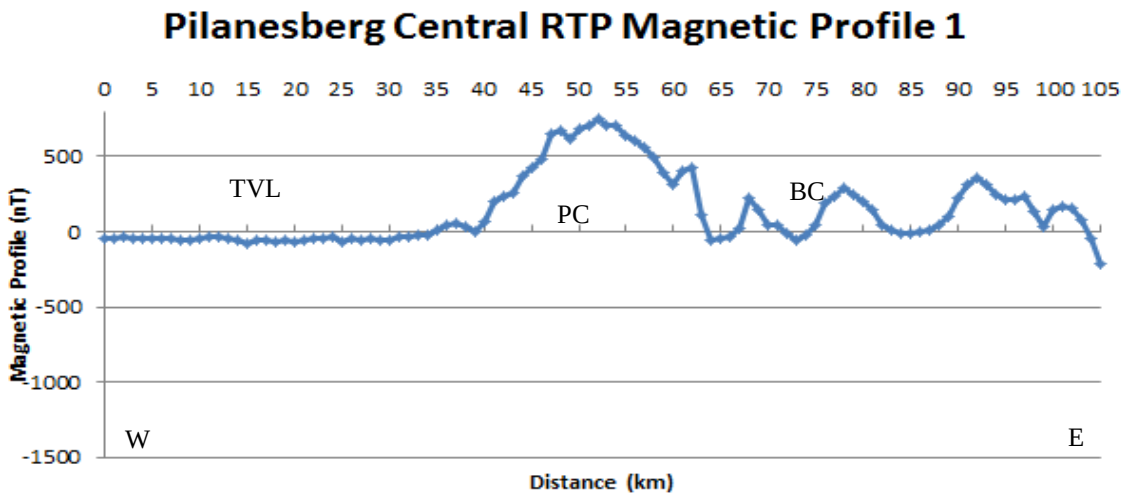

Figure 2.34 West-east magnetic data along Profile 1. TVL- Transvaal Supergroup, BC- Bushveld Complex, PC- Pilanesberg Complex.

Profile 2 in the north (Figure 2.35) cross cuts a negatively magnetised body west of the Complex as well as positive features in the east. The latter is likely to be associated with the Bushveld granite.

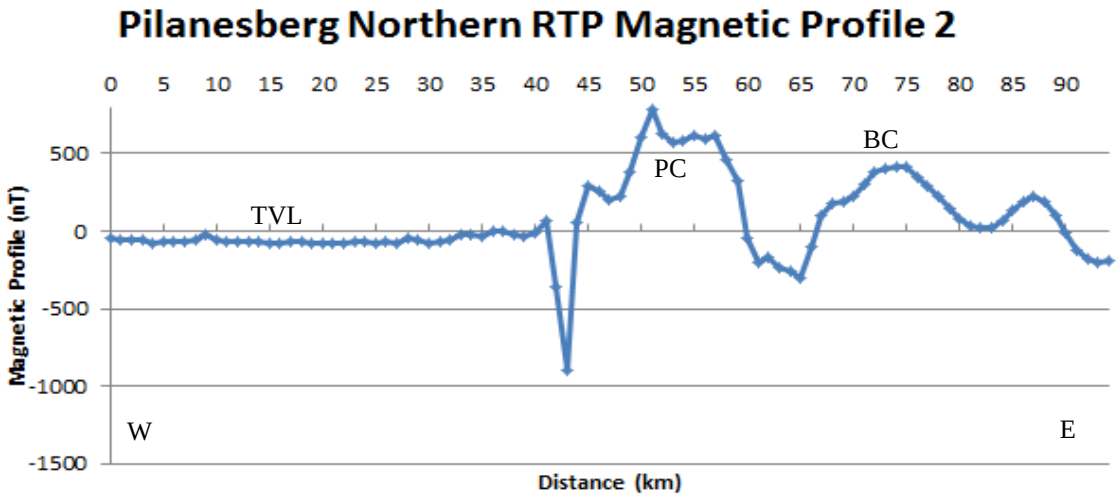

Figure 2.35 West-east magnetic data along Profile 2. TVL- Transvaal Supergroup, BC- Bushveld Complex, PC- Pilanesberg Complex.

Profile 3 (Figure 2.36) indicates a good amount of structural information over the Pilanesberg Complex. The Pilanesberg Complex has a broader anomaly in this profile compared to profile 1 and 2. There is a large negative spike between the Pilanesberg Complex and the Bushveld Complex, which may be due to an effect of remnant magnetisation between two positively magnetised bodies.

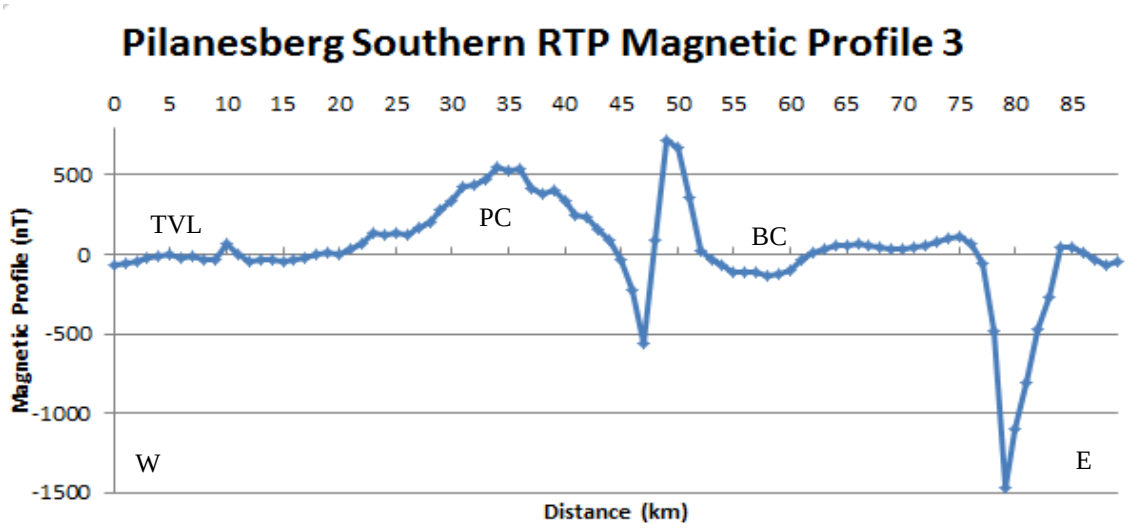

Figure 2.36 West-east magnetic data along Profile 3. TVL- Transvaal Supergroup, BC- Bushveld Complex, PC- Pilanesberg Complex.

Magnetic data profiles extracted in a north-south orientation, demonstrate how the Pilanesberg and Bushveld Complex signals interact. The data indicates a change between Profile 4, which has less contact with the Bushveld Complex, and Profile 5, which transects more of the Bushveld (Figure 2.37).

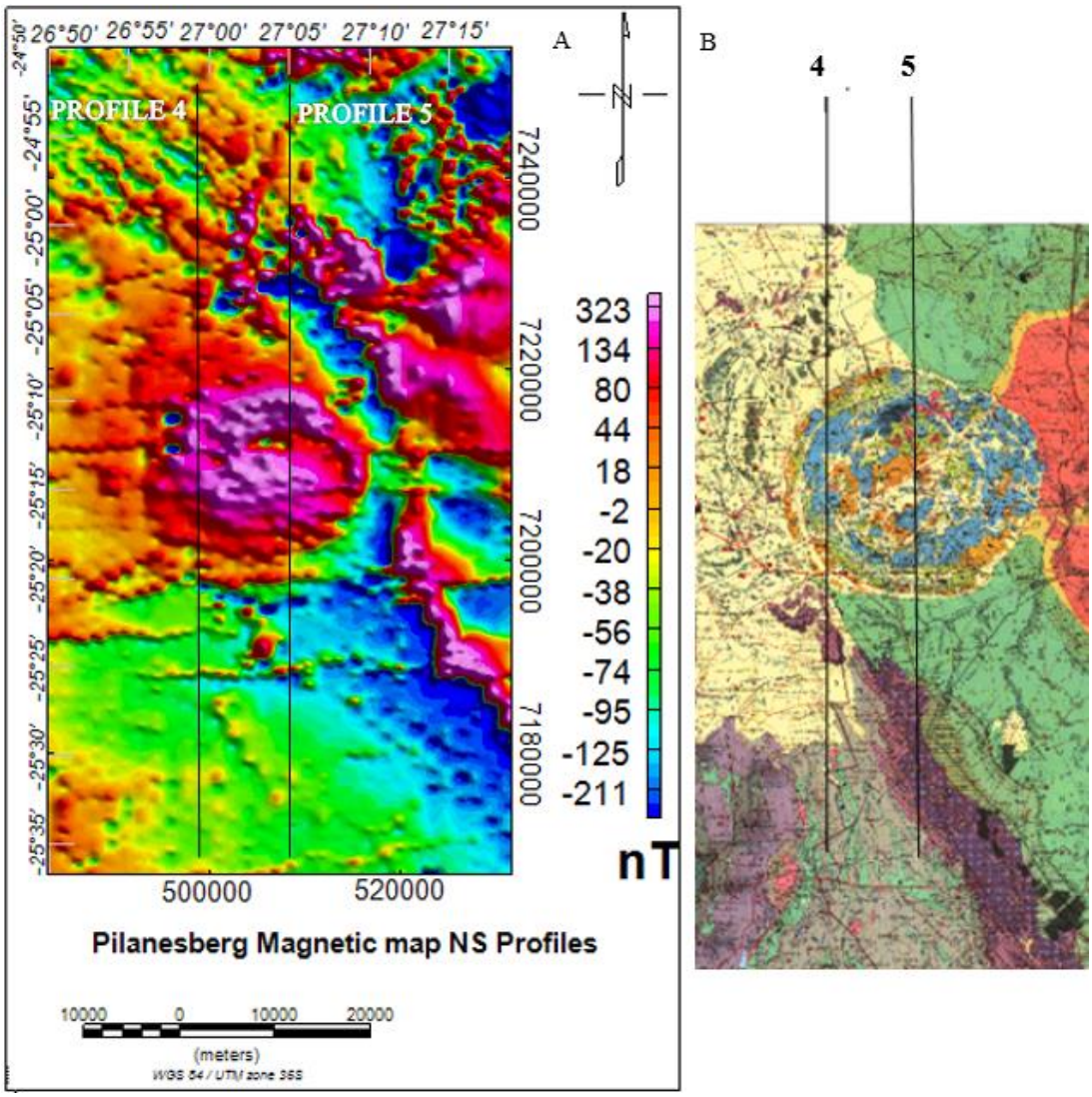

Figure 2.37 Magnetic map of the north-south profile 4 and 5 in A) and on the correlating geology map in B).

Profile 4 (Figure 2.38) identifies the Pilanesberg Complex as a broad anomaly in the centre of the profile. The short wavelength features over the Complex could be due to the internal ring structure. The north of the profile has irregular medium wavelength features correlated with an outcrop of the Bushveld and Magaliesburg quartzite fragments in the geology map (Figure 2.37).

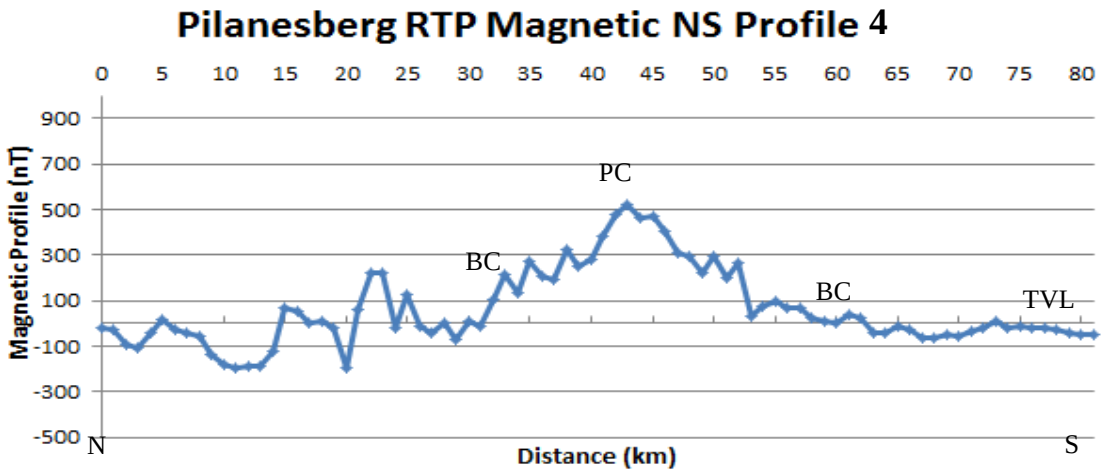

Figure 2.38 North-south magnetic data along profile 4. TVL- Transvaal Supergroup, BC- Bushveld Complex, PC- Pilanesberg Complex.

On profile 4 and profile 5 (Figure 2.39), the magnetic signature is comparable to both profiles for the southern area of the Pilanesberg Complex. However, the north of the Complex has a large positive spike possibly attributed to the contact with the Bushveld Complex. Further north there appears to be a double-peaked anomaly characteristic of the Pilanesberg dykes examined by Emerman (1991); this may indicate a Pilanesberg dyke intruding into the Bushveld Complex in the north.

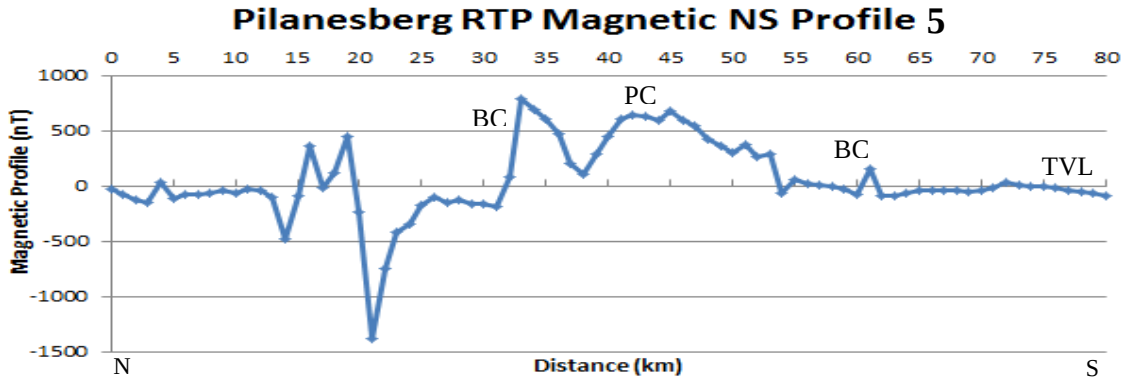

Figure 2.39 North-south magnetic data along Profile 5. TVL- Transvaal Supergroup, BC- Bushveld Complex, PC- Pilanesberg Complex.

The gravity and magnetic profiles will be used to model 2D profiles (Chapter 4) based on the physical properties of the rocks as well as the geology constraining the surface. The 2D profile models are used to test possible geometries for the shape of the Pilanesberg Complex. In order to produce and constrain the 2D profiles, the density and magnetic susceptibility value for each of the rock samples is measured.

2.8 SUMMARY

Multiple data sets over the Pilanesberg Complex have been used in this chapter, namely the geological map, the terrain map, the physical properties data and the geophysical magnetic and gravity data set. The data sets provide basic background information to understand how the data was collected.

The geology map shows how the Pilanesberg Complex intruded into the gabbronorite of the Western Bushveld limb such that it is bound by the norite on the north and southern contact. The Pilanesberg Complex has Transvaal Supergroup on the Western contact and Bushveld granite on the eastern contact.

Both the geology map and the terrain map show the sinistral Vlakfontein fault that bisects the positive elevation of the Pilanesberg Complex.

The magnetic map displays the positive magnetic signature of the Pilanesberg Complex that is compared with the negatively magnetised Pilanesberg dyke Swarm. The Pilanesberg Complex has a ~ 50 mGal lower gravity signature than the Bushveld Complex. The correlation continues in the physical property data, where the Pilanesberg syenite density is 2.67 $g.cm^{-3}$ compared to the Bushveld gabbronorite, which has a density of 2.92 $g.cm^{-3}$.

The gravity and magnetic data sets will be used to create 2D profile, 3D forward and inversion models. The geology and terrain data will be used as the surface constraints in any of the 2D or 3D models presented. The physical property data is imperative in the 2D profile modelling to construct geological bodies to create a realistic and relevant geological model that fit all the above data sets in both geology and structural geometry.

Processing of the magnetic and gravity data sets will follow in the next chapter.

CHAPTER 3: GEOCHRONOLOGY INVESTIGATION

The magnetic map over the north of South Africa shows a disparity between the rocks in the Pilanesberg System (Figure 1.6). The Pilanesberg System comprises of the Pilanesberg Complex, Pilanesberg dykes and the alkaline pipes in the centre of the Bushveld Complex granite (Van Niekerk, 1962). The disparity in question is the negative value of ~ 100 nT over the Pilanesberg dykes while the Pilanesberg Complex is completely opposite with a positive magnetic signature of ~ 370 nT. The Pilanesberg Complex and the Pilanesberg dykes are classified as part of the same system, suggesting that they intruded at roughly the same time. The opposite magnetic signature of the intrusions, however, suggests that they are not equivalent.

The Pilanesberg Complex and the Pilanesberg dykes are examined with geochronology and petrography to see if the intrusions differ in age. The samples collection information is documented in Table 3.1 and seen in Figure 3.1

Table 3.1 Sample collection and location information including measured density and susceptibility readings.

Sample No.	dyke/ Complex	Strike °	Dip°	Dip Orient.		Easting	Northing	Elevation (m)	Rock name	Rock colour	Average Density (g/cm^{-3})	Average Susceptibility (SI)
1	dyke1	285 °	80 °	N	35J	545252	7134121	1452	Syenite	Grey	2.57	0.038
2	dyke1	196 °	65 °	W	35J	545257	7134102	1449	Syenite	Grey	2.63	0.04
		30 °	10°									
5	dyke1	266 °	5 °	NW	35J	545047	7136294	1502	Syenite	Grey	2.63	0.018
3	dyke2	203 °	52 °	NW	35J	545856	7135710	1475	Syenite	Red	2.69	0.197
4	dyke2	23 °	5 °	E	35J	545808	7135811	1468	Syenite	Red	2.69	0.198
6	Complex	110 °	76 °	SW	35J	498638	7197097	1146	Foyaite	White	2.65	0.016
7	Complex	41 °	85 °		35J	498650	7197128	1154	Foyaite	White	2.66	-0.004
8	Complex	218 °	84°		35J	506485	7196666	1114	Foyaite	Green	2.99	0.032
9	Complex	298 °	27 °		35J	506487	7196665	1096	Foyaite	Green	2.85	0.048

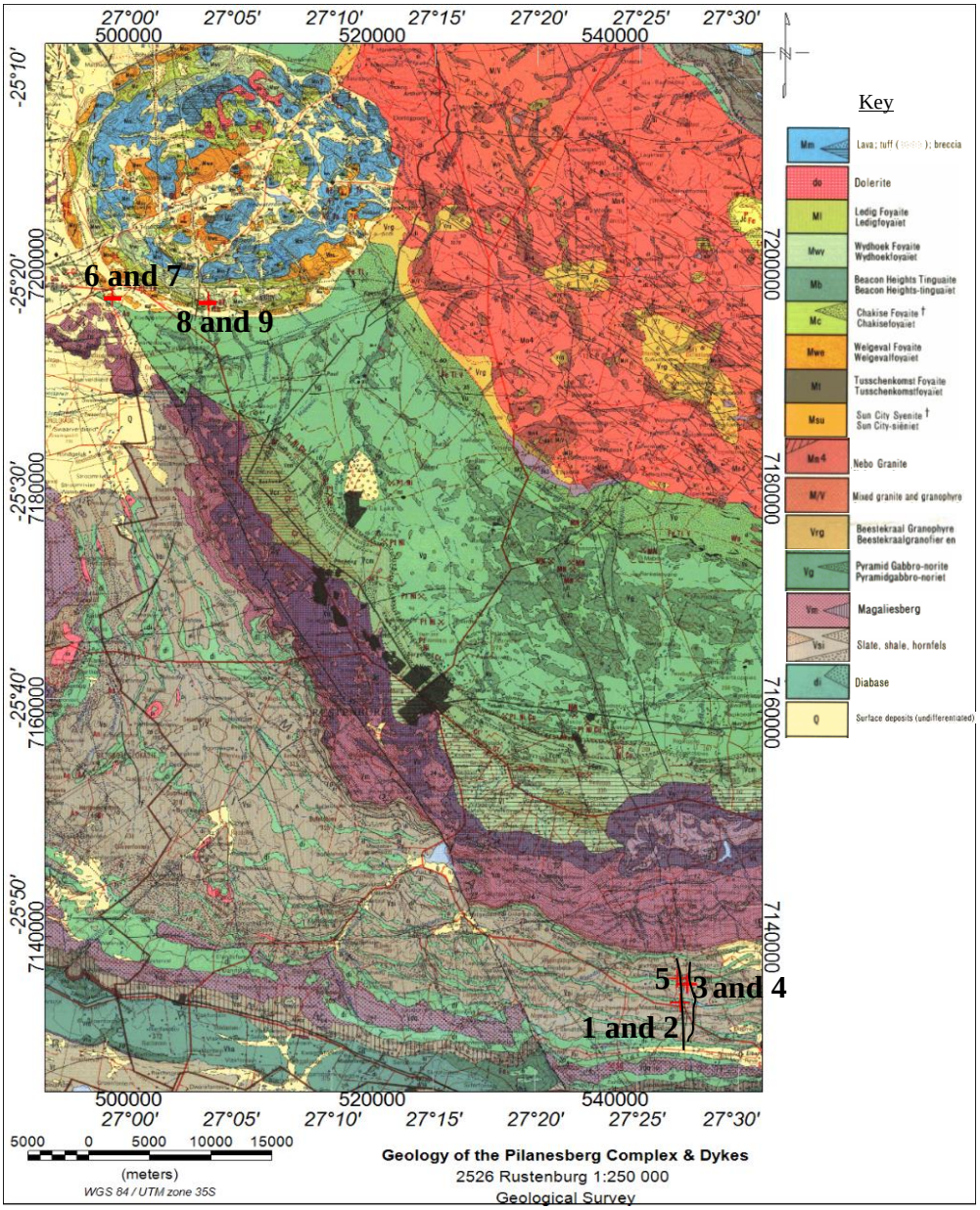

Figure 3.1 Geochronology sample and petrology samples are analysis from the grey and red syenite dyke of the southern Pilanesberg dyke swarm (samples 1-5), and the Pilanesberg Complex white foyaites (samples 6 and7) and green foyaite (samples 8 and 9).

3.1 PETROGRAPHY

The petrography aims to identify the mineralogy of the rocks in polished thin section and to identify the opaque mineralogy that is vital to explaining the geochronology. Polished thin sections were made for comparison of the different localities from the grey syenite dyke, red syenite dyke, Pilanesberg white foyaite and the Pilanesberg green foyaite.

3.1.1 Petrography of the grey syenite dyke – site 1, 2 and 5

The grey syenite dyke sampled at sites 1, 2 and 5 have large grains of plagioclase surrounded by a needle-like aegirine matrix (Figure 3.2). Sample 1 also contains more abundant magnetite than some of the other samples. In this case, minor intrusions or hypabyssal igneous intrusions form the Pilanesberg dyke swarm (MacKenzie and Adams, 1994), which can be expected to be medium grained which is seen in thin section.

Site 1 – grey syenite dyke

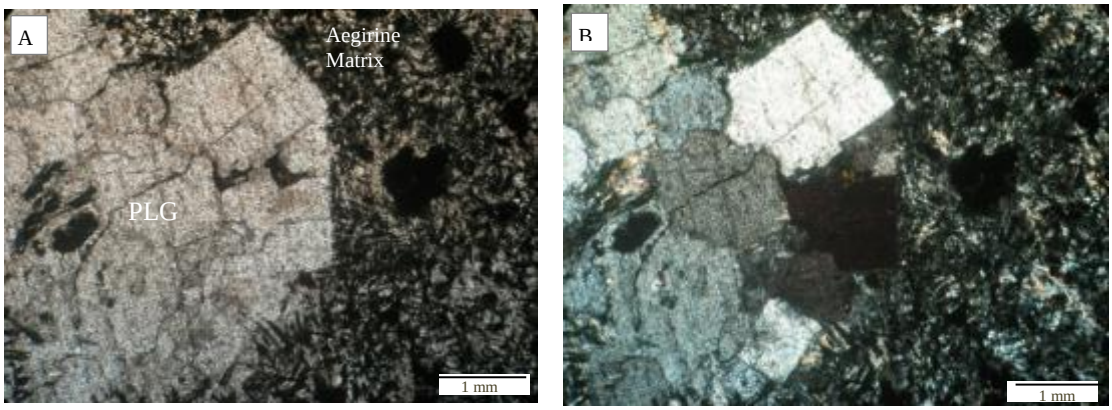

Figure 3.2 A) Sample 1.3A from the grey syenite dyke examined under plane polarised light (PPL) and B) under crossed polarised light (cross-polarised light (XPL) in transmitted light (TRS)) in B. The large plagioclase grains seen on the left while the rest of the matrix has a needle-like texture from aegirine surrounding medium sized opaque minerals likely to be magnetite (transmitted light).

The alteration and textures for the grey syenite dyke examined in thin section are indicated in Figure 5.48. Notable features are the aegirine overprinting of clinopyroxene grains (Figure 3.3 A and B), which themselves have a rim texture. The majority of the rock sample is composed of the needle sha ped aegirine (Figure 3.3 C and D). The aegirine is a large dark phenocryst (approximately 5 mm across) that is observed in E and F with alteration and rimming textures (Figure 3.3).

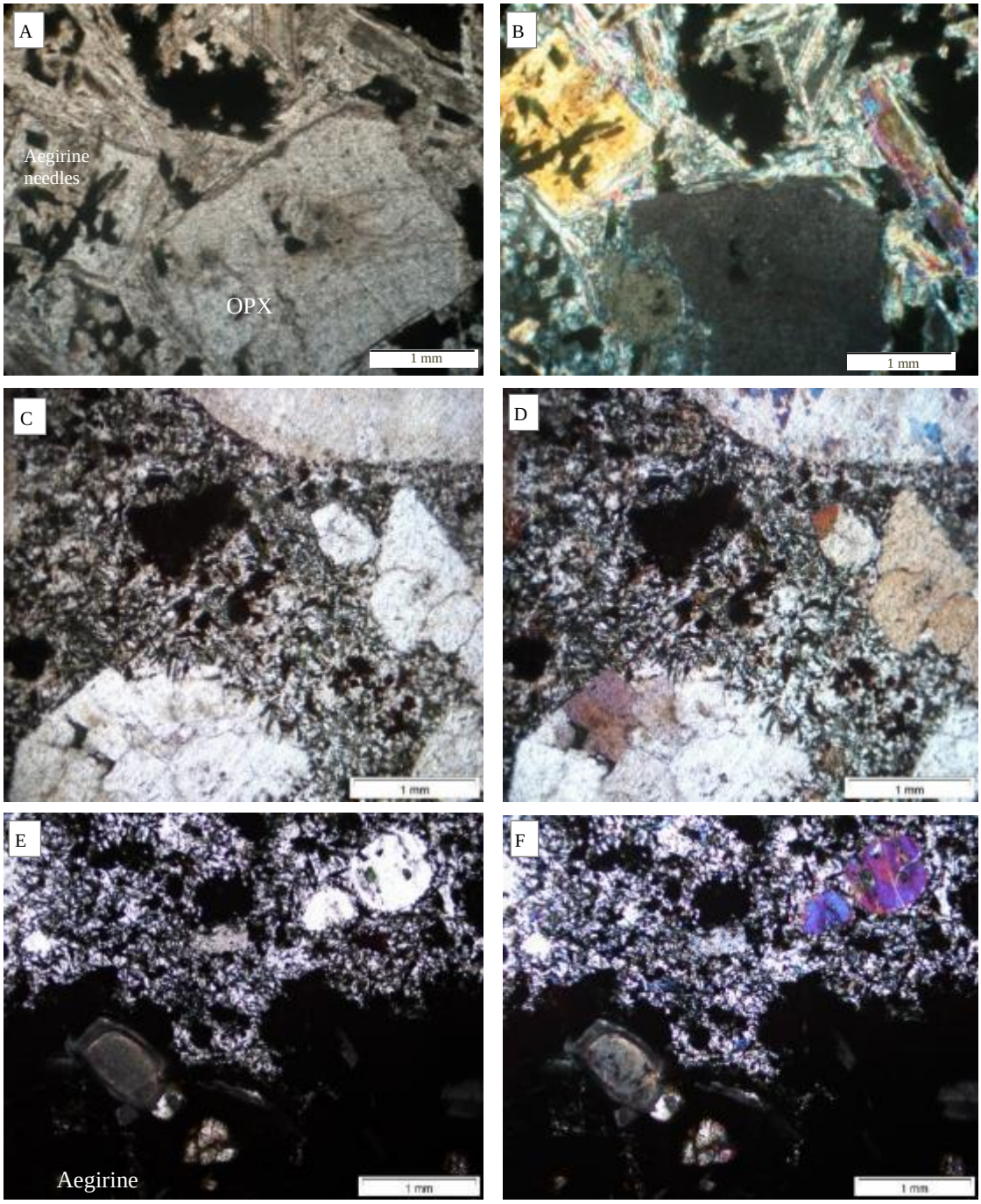

Figure 3.3 Sample 1.3A from the Pilanesberg grey syenite dyke under TRS PPL in image A, C and E and XPL in B, D and F. All of the above pictures display the fine needle texture of the groundmass surrounding large altered and zoned phenocrysts (E and F). The alteration zoning around clinopyroxene are prominent in images E and F while overprinting of the orthopyroxene by aegirine in image A and B is shown (4x magnification).

On a larger scale, in transmitted light, the opaque minerals are approximately 2 mm in sample 1.3A (Figure 3.4 A and B) while the opaque minerals are roughly the same size as the dark aegirine in sample 1.3B Figure 3.4 C and D). The large size difference between the opaque minerals suggests that they formed in early and late stages of cooling.

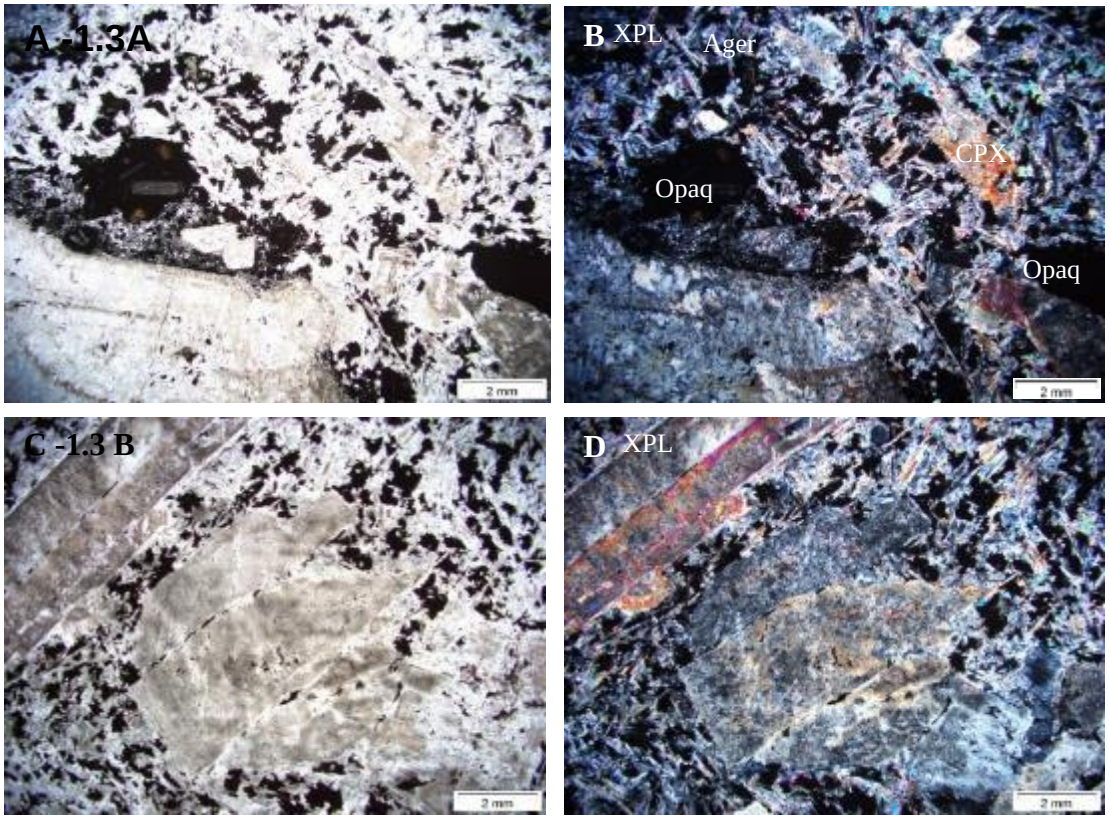

Figure 3.4 A and B, PPL and XPL images of sample 1.3A. C and D, PPL and XPL images from 1.3 B. 1.3A has coarser 2 mm opaque grains and other smaller grains while 1.3B only has smaller (0.5 mm) opaque minerals.

The opaque minerals that were identified in transmitted light have been examined with reflected light to determine their mineralogy and the potential importance to the susceptibility.

The grey syenite dyke is shown in transmitted PPL light (Figure 3.5 A) and reflected light (Figure 3.5 B). Sample 1.3 has a large aegirine phenocryst that is examined for opaque minerals in Figure 3.5 B. The aegirine contains small to medium whitish grey magnetite grains and some small yellow sulphides.

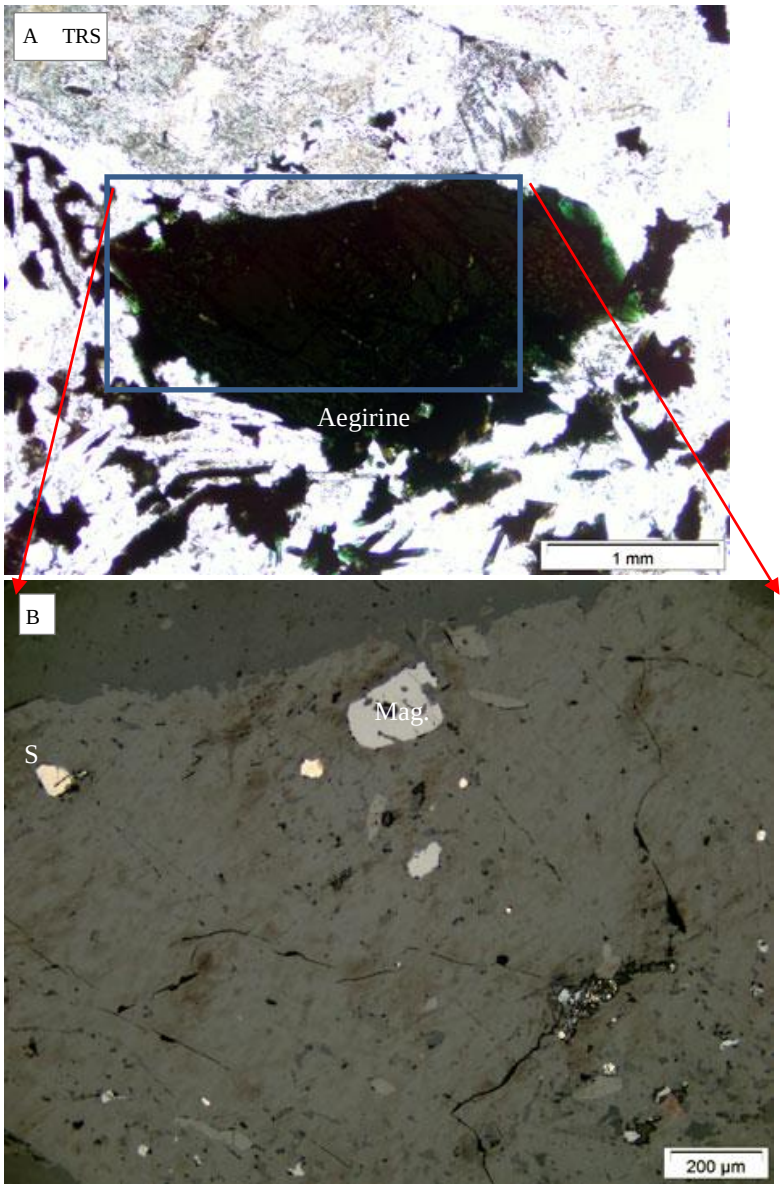

Figure 3.5 A) The transmitted light (TRS) section of sample 1.3 from the grey syenite dyke where the area demarcated over the aegirine grain in B) using reflected light. The light grey grains are magnetite (Mag) and the yellowish-white grains as pyrite(S).

A transition view is displayed for sample 1.3 A in Figure 3.6 B, where A) is transmitted light B) is a combination of transmitted light, and some reflected light and pure reflected light in C). This allows the opaque minerals to be identified while the silicates seen using transmitted light can be observed at the same time. In this case, the medium sized magnetite grain is associated with biotite, while the small magnetite grains occur with the aegirine needles in the matrix (Figure 3.6 C).

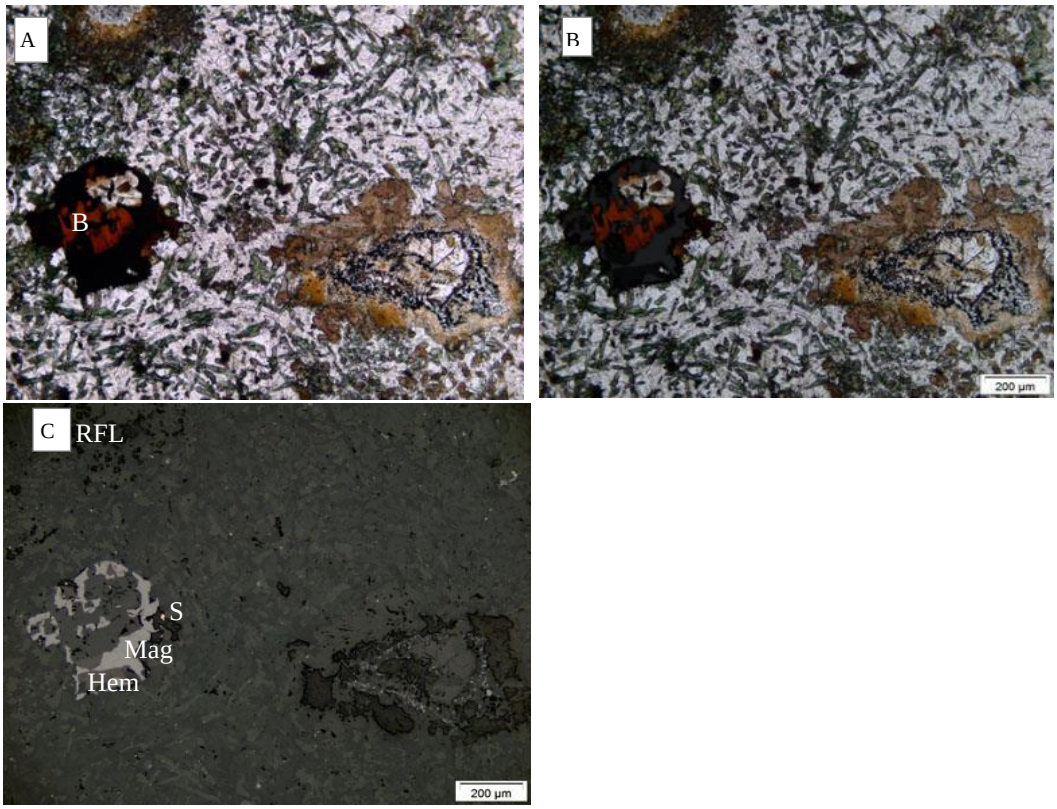

Figure 3.6 A) Transmitted light of sample 1.3 from the grey syenite dyke showing the opaque minerals associated with the large biotite grain and the aegirine needles in the matrix and as an alteration occurrence. B) Includes some reflected light to identify the opaque minerals in transmitted light. C) The different sizes of magnetite include medium sized magnetite grains associated with biotite (B), to small grains from a leaching process as well as part of the matrix. Sulphides (S) appear as yellowish grains. The 300 µm whitish grey magnetite grain has inclusions of late stage or secondary pinkish brown hematite (Hem).

Site 2 – grey syenite dyke

The grey syenite dyke is sampled at site 2, which is approximately 50 m from site 1 along the same dyke. The mineralogy of sample 2.1 includes the opaque minerals hosted in aegirine as well as biotite and perthitic potassium feldspar, which is examined in Figure 3.7 under plane and cross-polarised transmitted light.

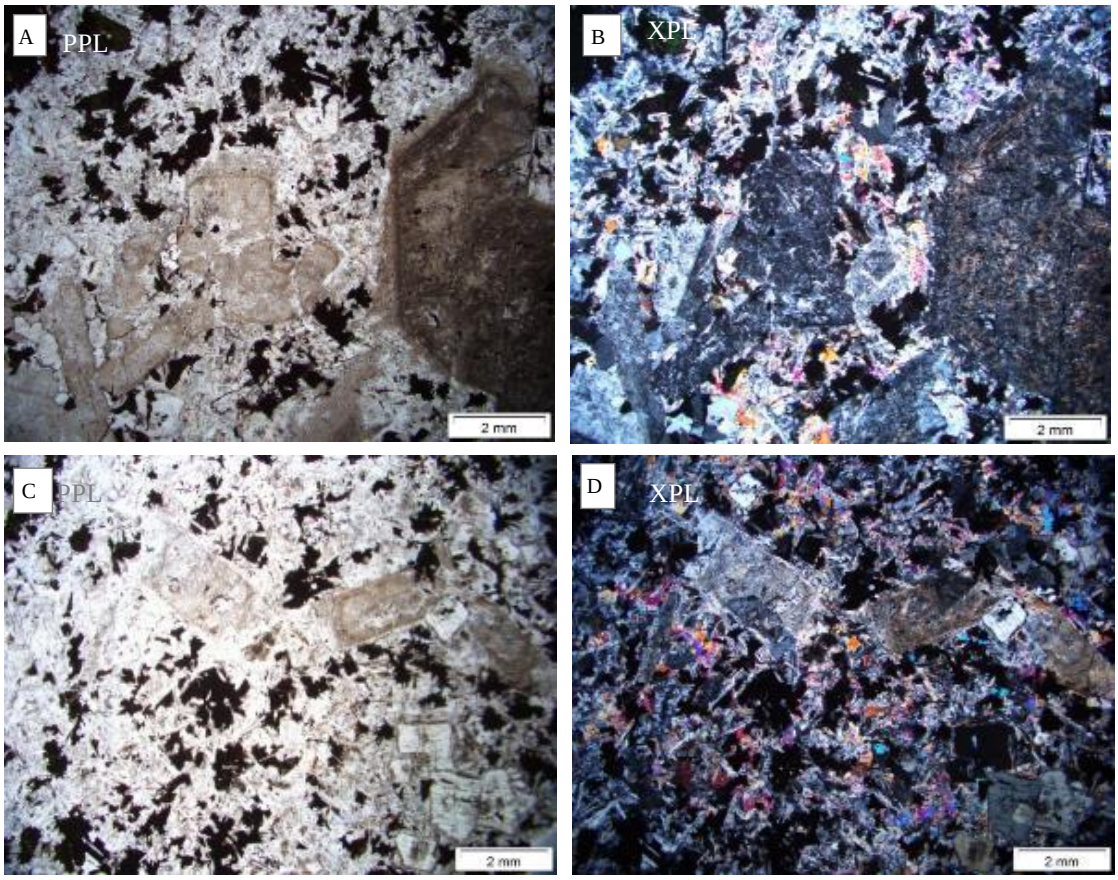

Figure 3.7 Thin section of sample 2.1 is investigated in two area. A) The large 2 – 4 mm grains of perthitic altered potassium feldspar (Kspar) with alteration rims (A and C), which are surrounded by aegirine, biotite, clinopyroxene CPX and minor opaque minerals (B and D). The opaque minerals are associated with agerine.

Similar mineralogy can be seen in another sample from the grey dyke at site 2 for sample 2.2 where the clinopyroxene forms a rim around the large phenocrysts of K-feldspar (Figure 3.8 A) and B)). The opaque minerals in this sample are also associated with aegirine and biotite in the matrix that surrounds phenocrysts of K-feldspar (Figure 3.8 C-F).

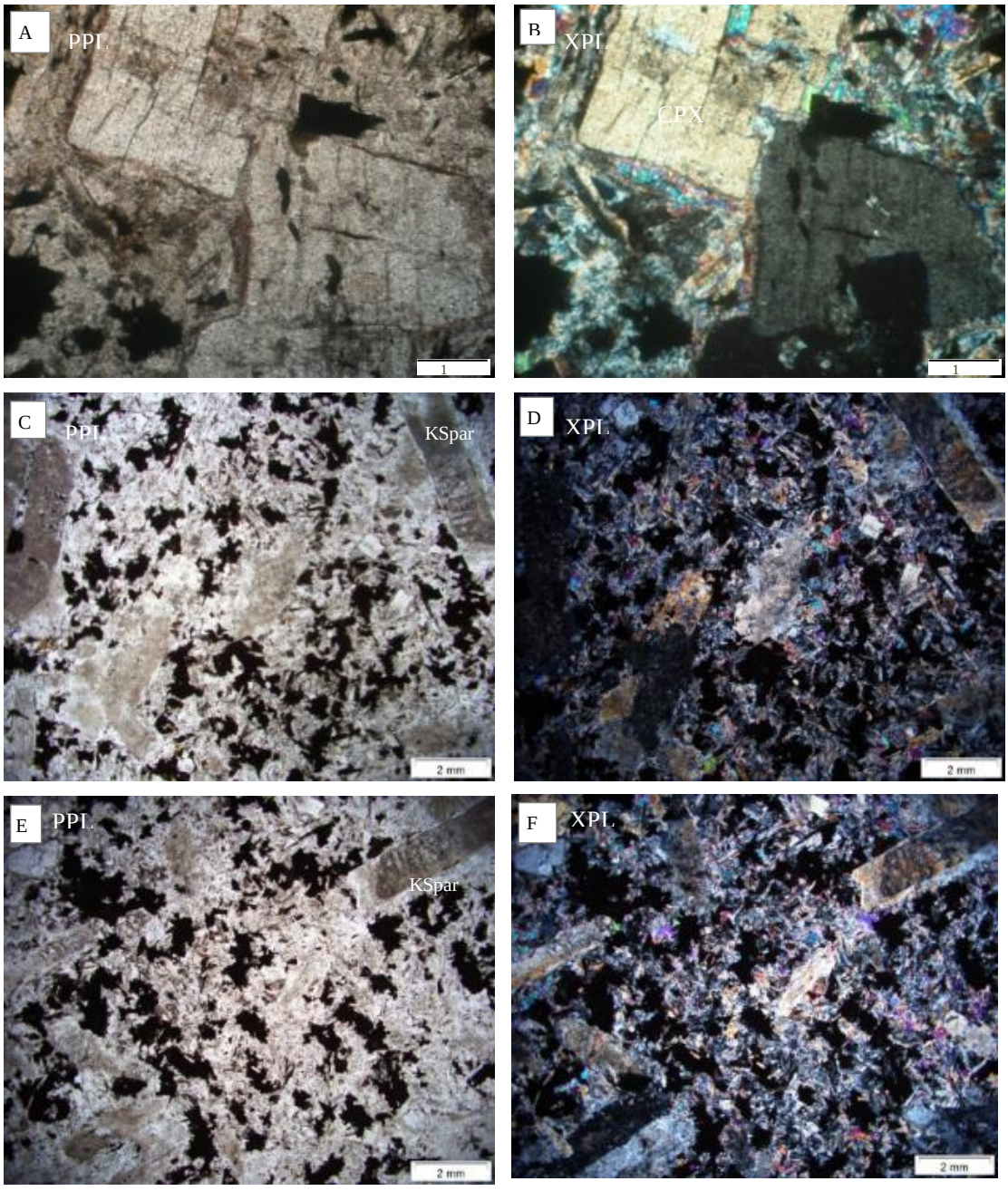

Figure 3.8 Sample 2.2. A and B) have a 4x magnification and indicate the well-developed grains of CPX rims and medium sized opaque minerals in transmitted light. The elongate grains are potassium feldspar with a perthitic texture (C-F). The rest of the rock samples are composed of aegirine, biotite, CPX, sanidine and opaque.

The opaque minerals for site 2, the grey dyke, occur as medium to large magnetite grains as well as medium grains that appear to be slightly broken up with some magnetite along alteration channels (Figure 3.9).

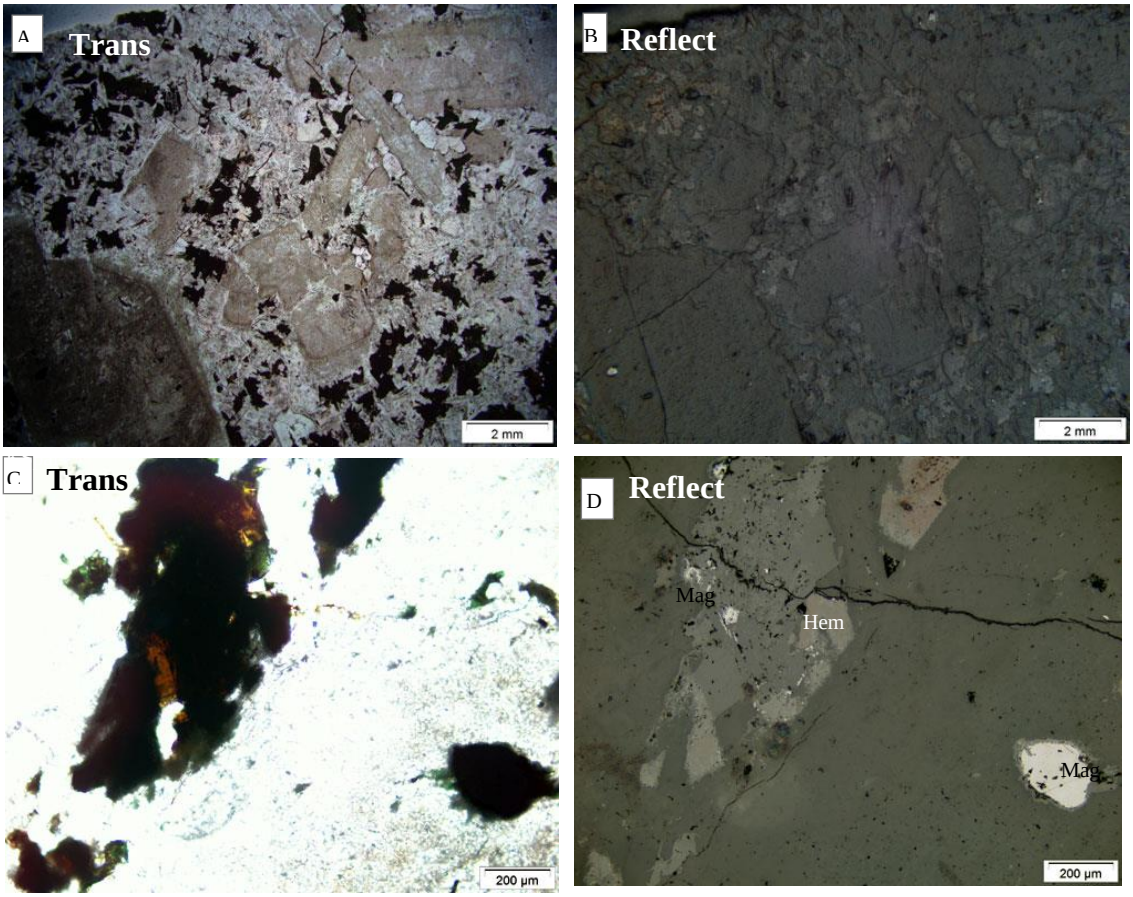

Figure 3.9 A broad view of the opaque minerals in A) and B) with smaller white magnetite grains scattered through image B). C) and D) indicate a close up view of a different area of the thin section with a fracture through the biotite and aegirine grains and white magnetite grains in D with 150 µm sized pinkish brown hematite grains.

Site 5 – grey syenite dyke

Site 5 is two kilometres north of site 1 and 2 along the grey dyke. The outcrop at site 5 is considerably weathered compared to the other sites. Sample 5.5 has relatively large opaque minerals (Figure 3.10) and alteration seen as the brown matrix in PPL (Figure 3.10 A).

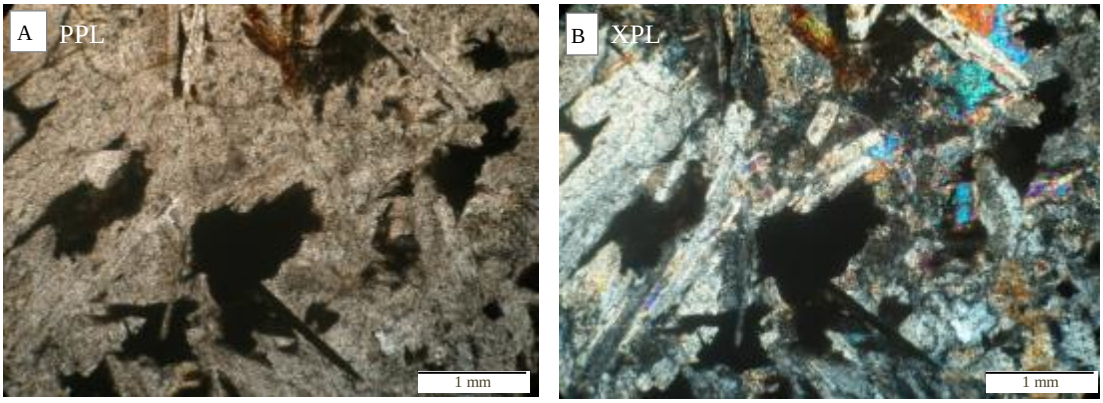

Figure 3.10 Sample 5.5 of the grey syenite dyke with large K-feldspar grains, amphibole needles and some alteration overprinting as well as large opaque minerals in transmitted light seen in A). In B) there are high birefringence blue coloured areas seen in cross-polarised light (XPL) which correlate with the clinopyroxene grains.

Sample 5 under reflected light displays a grouping of magnetite that is associated with the green aegirine (Figure 3.11 A and B). The whitish grey magnetite appears to contain some hematite (pinkish white). Some of the magnetites are associated with an area of alteration, occurring alongside small fractures (Figure 3.11 B and D).

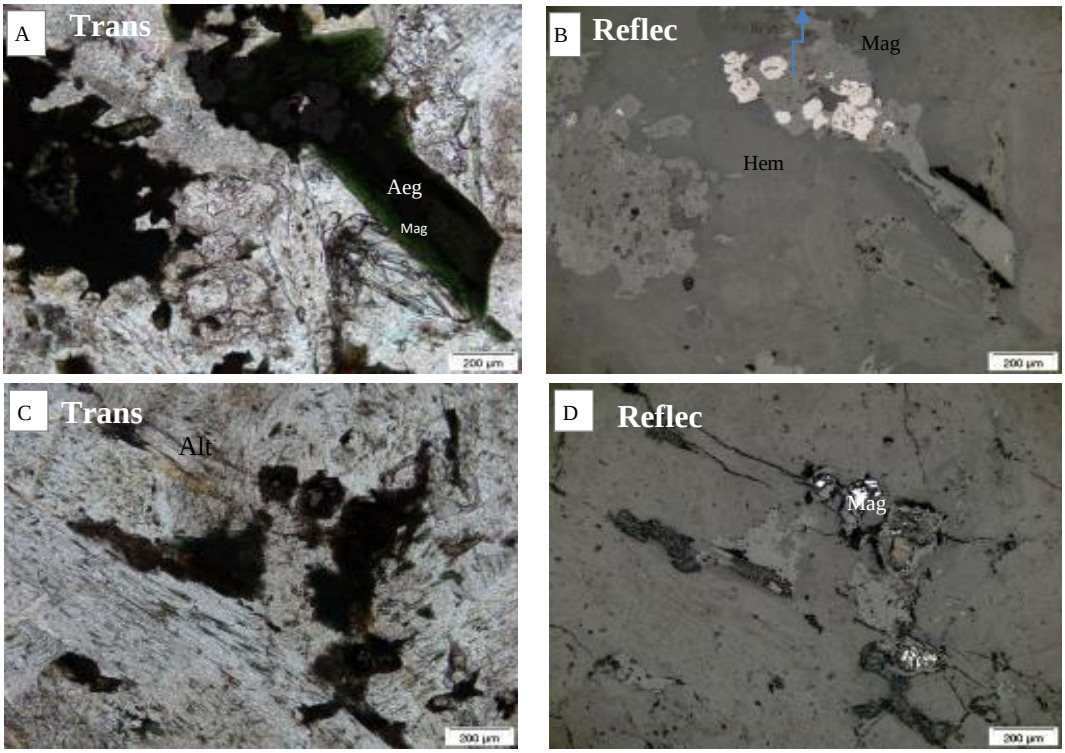

Figure 3.11 The grey syenite dyke at sample 5 has magnetite that was broken up by fractures (B and D) but the medium sized grains contain small amounts of alteration hematite. Most of the small grains contain some chalcopyrite (B).

3.1.2 Petrography of the red syenite dyke – site 3 and 4

Site 3

The mineralogy of sample 3 includes a large amount of potassium feldspar and aegirine with later crystallisation of plagioclase and sanidine. There is a large mass of aegirine in Figure 3.12 A that contains biotite and opaque minerals (in transmitted light) that is seen as magnetite (reflected light) (Figure 3.12 B). The images illustrate how the opaques occurred in the aegirine and associated with the biotite for sample 3 (Figure 3.12 A and B) but also in the matrix when associated with agerine and occasionally biotite (Figure 3.12 C and D).

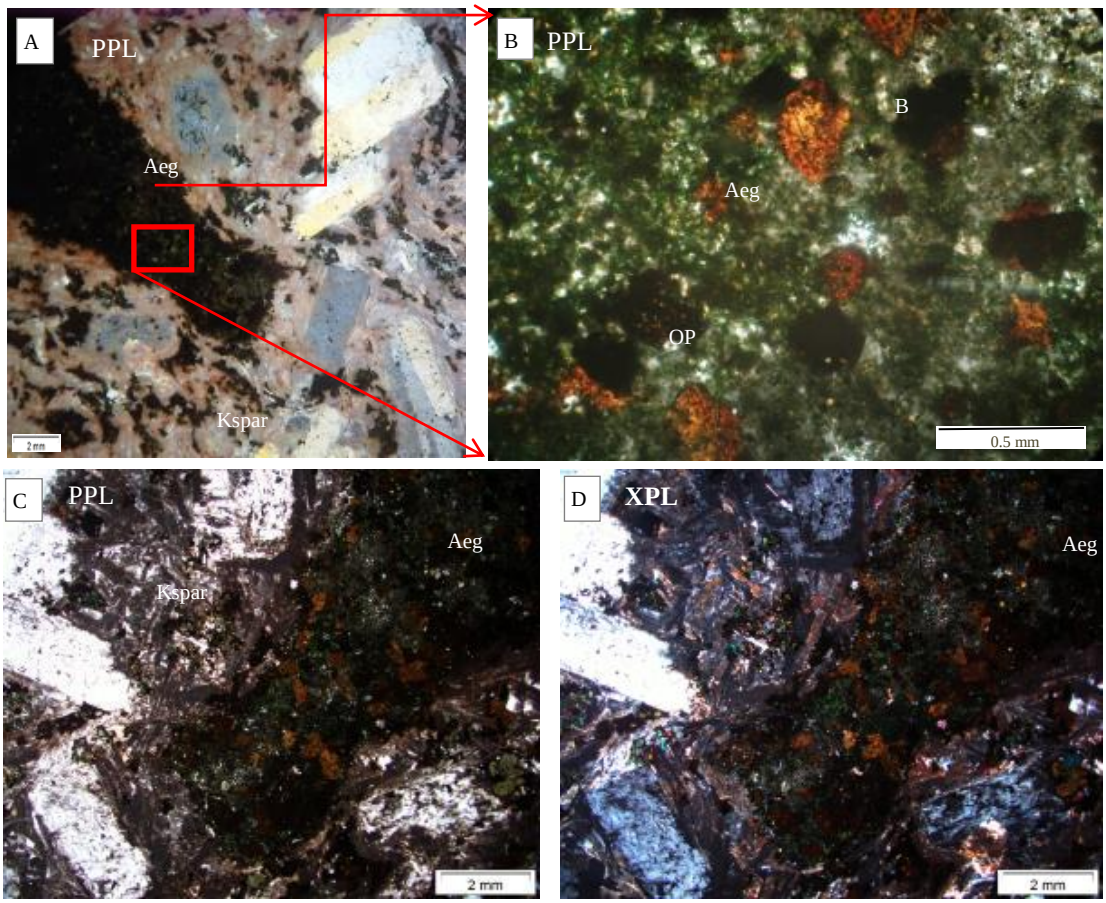

Figure 3.12 Sample 3.2 A (PPL 4x Magnification) the K-feldspar makes up the majority of the sample with a large clast of aegirine; B) the aegirine clast contains biotite and opaque minerals. C) and D) display the thin section from a different view under 1.25 magnification in PPL and XPL respectively.

The opaque mineral analysis for sample 3 from the red syenite dyke has magnetite that occurs in primary and secondary phases. The secondary phase is associated with alteration and mineralisation of the large green aegirine and smaller biotite grains (Figure 3.13).

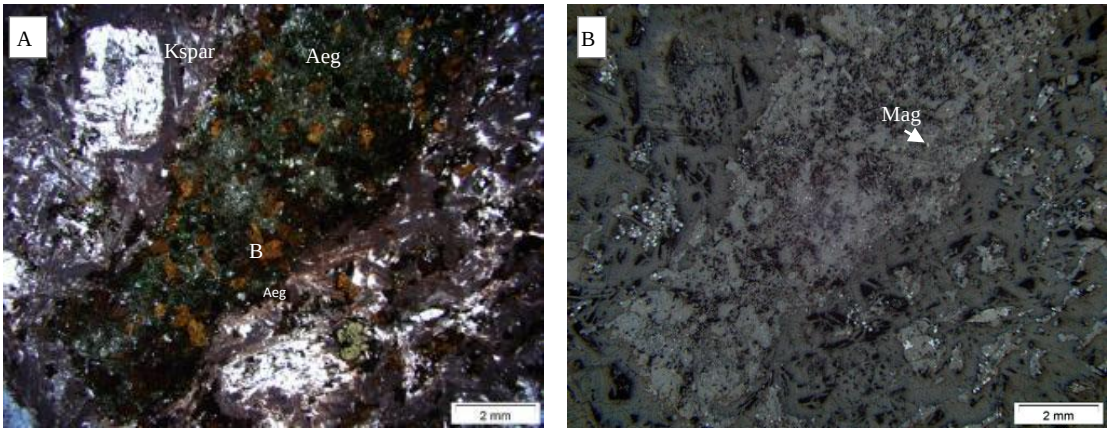

Figure 3.13 The opaque minerals in transmitted light A) are associated with the green aegirine and occasionally with the brown biotite and appear to be an alteration overprint in A), which has formed as medium sized magnetite grains (B- refl) through the aegirine clast and the matrix.

The opaque minerals are associated with the biotite lineation growth in Figure 3.14 A. In some cases; the chalcopyrite is found to be included within the magnetite (C).

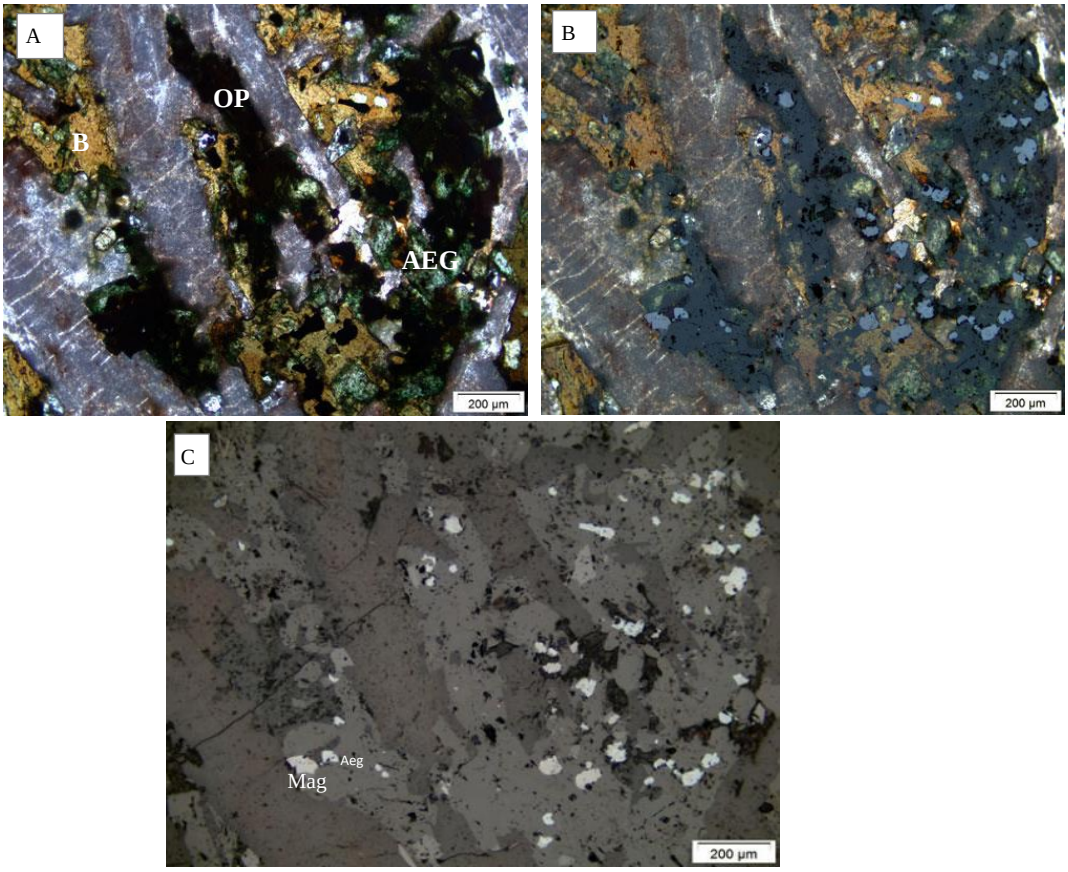

Figure 3.14 A) TRS of the linear biotite, opaque and agerine minerals in a K-feldspar matrix. B) The transition view shows the magnetite on top of the opaque of the TRS view. C) The refracted light indicates the well-formed medium size magnetite grains. Magnetite has formed in the opaque minerals that are associated with the lineated aegerine seen in A) of the red syenite dyke from sample 3

The whitish grey magnetite grains from sample 3.2 of the red syenite dyke has some sulphide minerals occurring within them. The yellow colour suggests this is most likely to be chalcopyrite. The opaque minerals in this sample are again associated with the green aegirine and altered biotite (Figure 3.15); however, in this case, they are in contact with aegirine instead of forming within the aegirine.

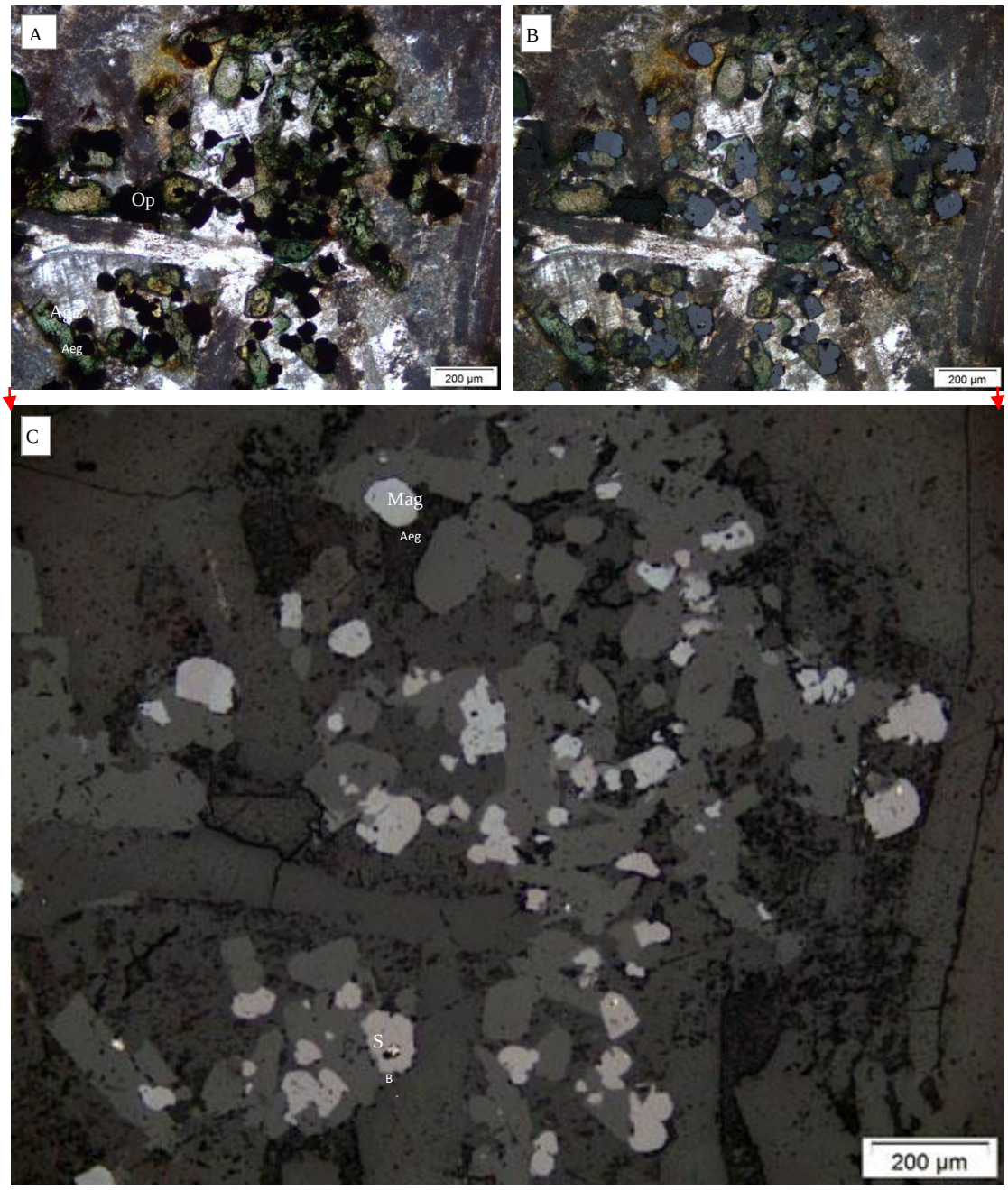

Figure 3.15 Sample 3.2 from the red syenite dyke has the black opaque minerals in association with the green aegerine in transmitted light (A). B) shows a transition view which combines both transmitted light and reflected light for comparison. C) In reflected light the opaque grains from A) are now seen as the whitish grey magnetite grains. Chalcopyrite grains (s) are found to form within the magnetite in this sample.

A close up of the thin section of the red syenite dyke sample 3.2 indicates that the magnetite grains appear to have hematite zoning rims around them and some lamellar alteration most likely attributed to hematite, which is seen as the light chocolate brown mineral associated with the magnetite at the top of the image. The transmitted plan polarized light (PPL) image indicates a considerable amount of alteration in the sample (Figure 3.16).

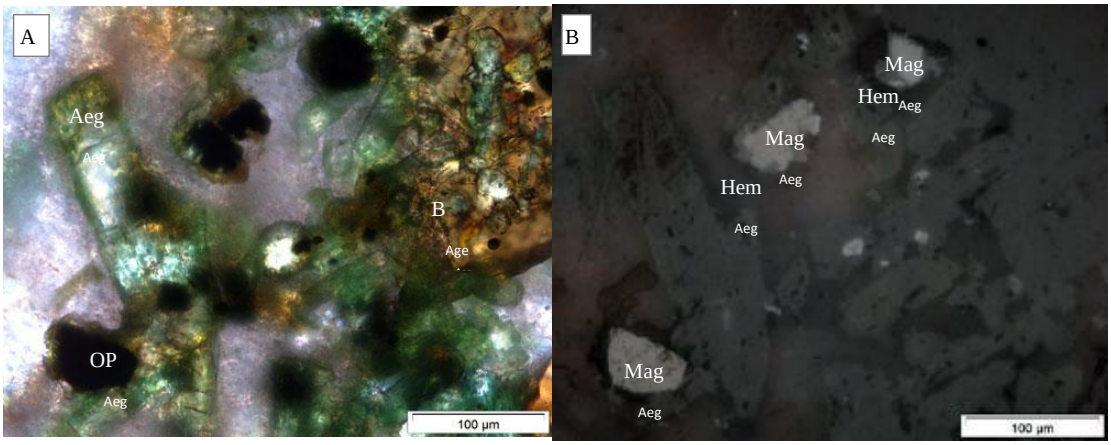

Figure 3.16 The red syenite dyke sample 3.3 is shown in transmitted PPL view in A) and reflected light view in B). This sample indicates alteration rims around the magnetite (Mag) grains. The alteration rims have been identified as hematite (Hem).

Site 4 – red syenite dyke

The mineralogy of the red syenite from site 4 is observed in a thin section overview in Figure 3.17 A, where the pink colour is from K-feldspar. The overview section also shows elongate grey sanidine phenocrysts and large phenocrysts of green aegirine. There is a large aegerine clast ~ 6 mm in Figure 3.17 C an D. Biotite and opaque minerals are found within the large clast (LC). Figure 3.17 E and F show an example of the aegirine alteration and intergrowth with the biotit grains.

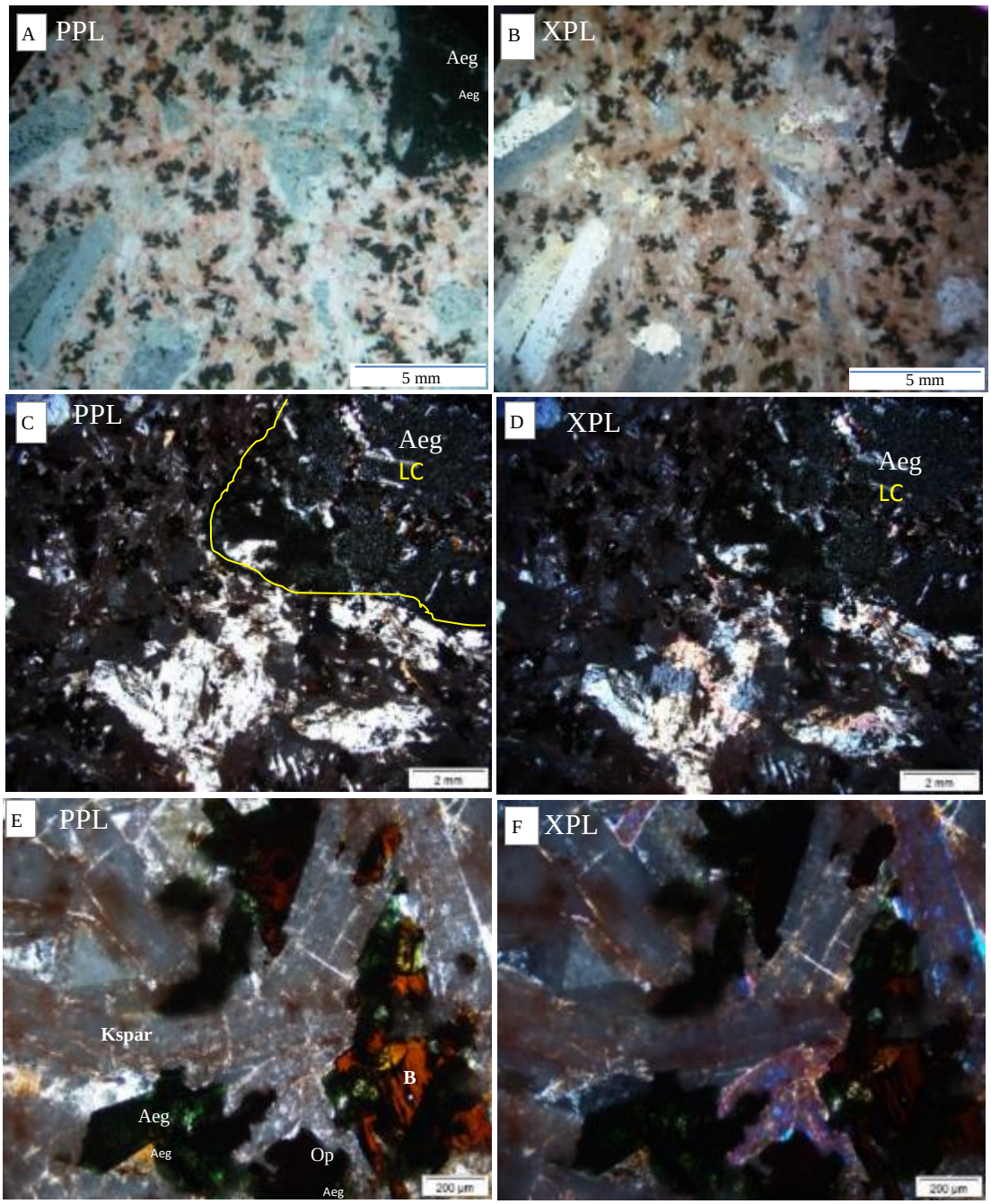

Figure 3.17 An overview of sample 4 displaying the distinct pink colour of K-feldspar in A and B as well as the large phenocrysts of green aegirine (Aeg LC). Images C to F show the intergrowth of aegirine, biotite and the opaque minerals.

The opaque analysis of the red syenite dyke from sample 4 is able to outline the greater percent of white-grey minerals in reflected light throughout the thin section (Figure 3.18). The magnetite is fine in size but consistent throughout the sample with its association with aegirine and some larger grains. The large aegirine clast (AEG LC) that makes up 40 % of the section and has smaller magnetite grains than the rest of the thin section (Figure 3.18 B).

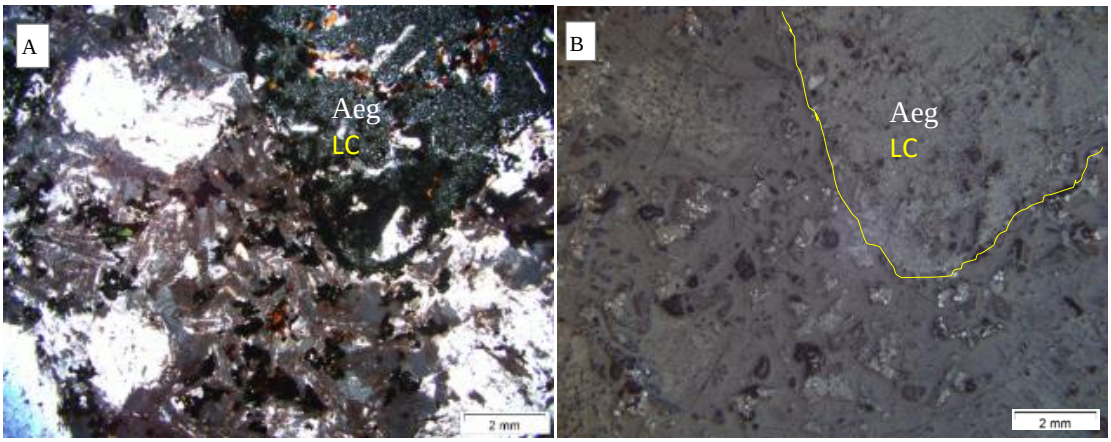

Figure 3.18 Sample 4 of the red syenite dyke viewed in plane polarised light in A) provides a comparison with the reflected light in B) to show the whitish-grey magnetite is in situ with the green aegirine. There is a varying grain size of magnetite grains that populate both the aegirine grains within the matrix, as well as finer grains magnetite grains within the larger aegirine clast.

Under higher magnification (Figure 3.19), the edge of the large green aegirine clast is examined in conjunction with the aegirine that is seen within the matrix (Figure 3.19 A). The magnetite occurring in the large clast is a smaller size (20-40 µm) than that which occurs in the matrix. In the matrix, the magnetite grains are a well-developed medium size (150 µm) that have been broken down into clusters of smaller (80-100 µm) magnetite grains (Figure 3.19 C). Along the edges of some of the magnetite grains in the matrix are small amounts of chalcopyrite (Figure 3.19 D).

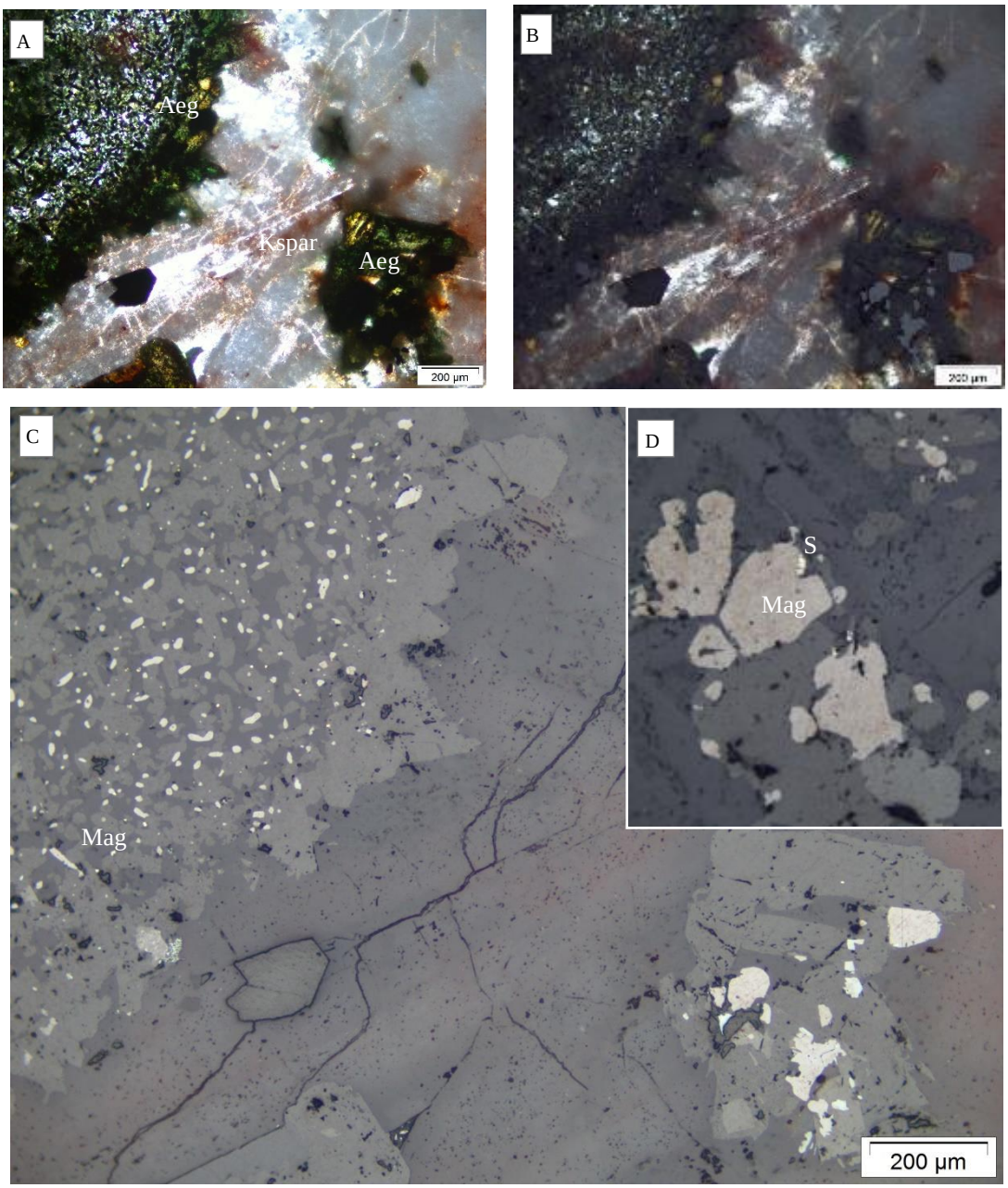

Figure 3.19 A) The large aegirine clast (Aeg) is on the left while a smaller aegirine cluster is on the right. B) is a combined view showing transmitted and reflected light where both transmitted light and reflected light characteristics are displayed. C) The magnetite grains are more frequent but smaller in size (20-40 µm) in the large aegirine clast while the magnetite is larger (80-100 µm) in the aegirine clast to the right in the matrix.

3.1.3 Petrography of the Pilanesberg Complex

White nepheline syenite – Sites 6 and 7

The mineralogy of the nepheline syenite sample as site 7 is similar to the dykes where the aegirine (Aeg), biotite (B) and opaque minerals (OP) have crystallised together (Figure 3.20). The white nepheline syenite is comprised of grains of nepheline, orthopyroxene (OPX) and clinopyroxene (CPX) (Figure 3.20). The sample also contains perthitic alteration texture.

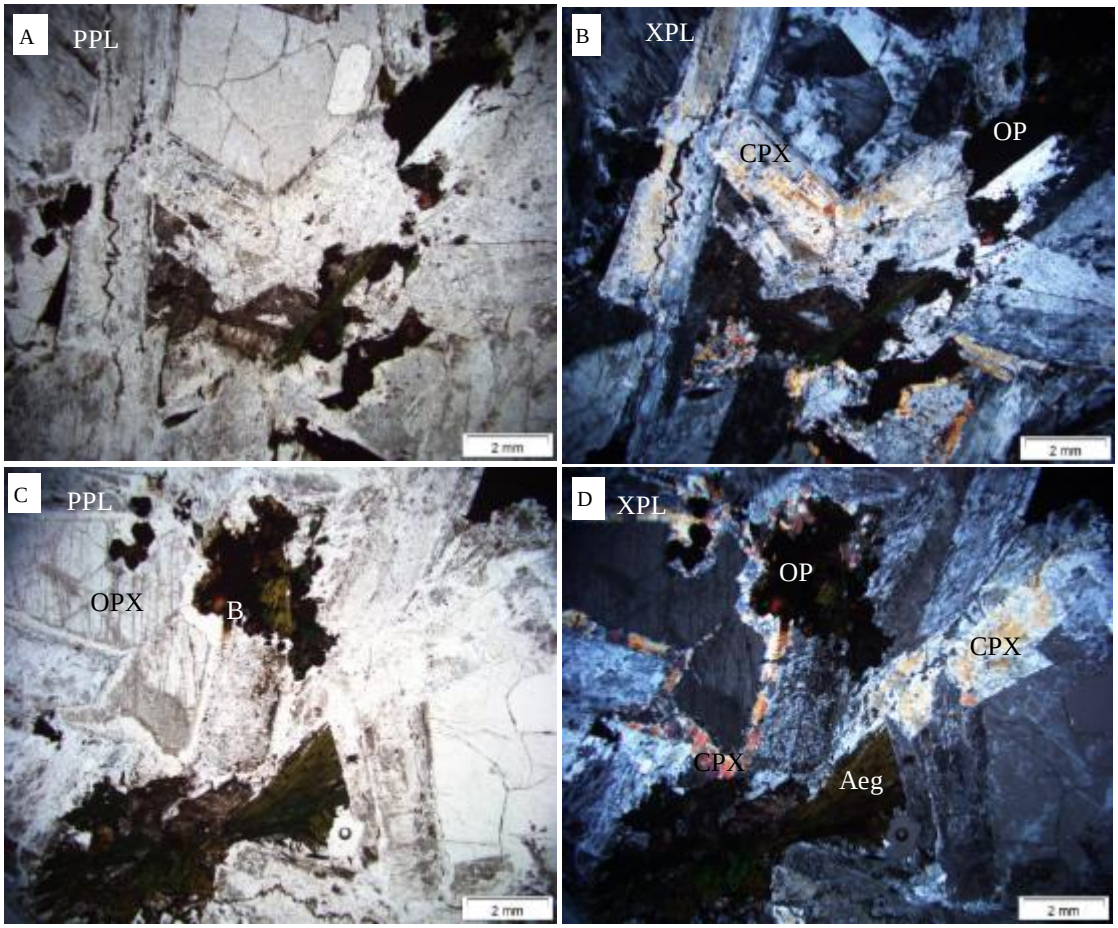

Figure 3.20 Sample 7 Pilanesberg white nepheline syenite sample has an overall white colour, which is due to nepheline, OPX and CPX grains. The opaque minerals are associated with aegirine and biotite. CPX is the orange colour that rims some of the samples in (B and D).

In comparison to the red and grey syenite dykes, the white nepheline syenite has a lot less magnetite. The magnetite occurs as relatively large grains with a very low frequency of occurrence, making up only about 2 % of the sample (Figure 3.21).

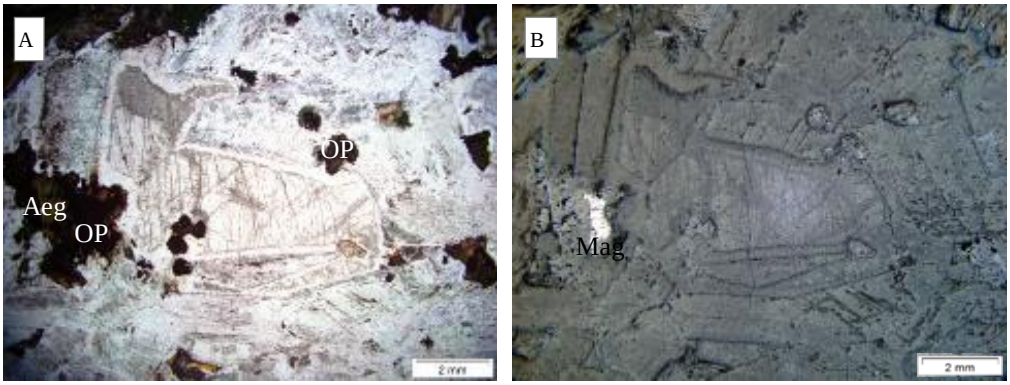

Figure 3.21 Here the white nepheline syenite indicates a 1.8 mm sized opaque mineral (OP) as well as smaller opaque minerals 0.5 mm A), where only large opaque contains any visible magnetite (Mag) in B).

Green nepheline syenite – Site 8 and 9

The green nepheline syenites are altered rocks with an alteration overgrowth occurring on some of the samples in Figure 3.22. Phenocrysts of nepheline, feldspar and clinopyroxene make up the large grains while a matrix of aegirine makes up the majority of the sample (Figure 3.22).

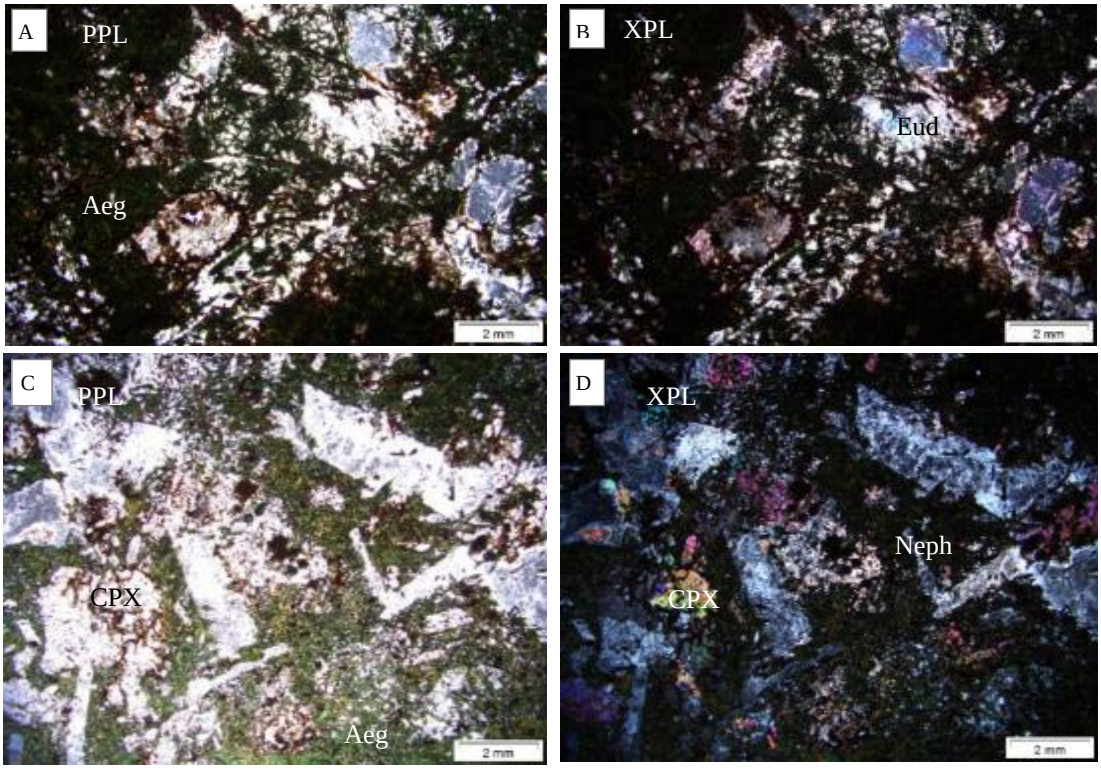

Figure 3.22 The green nepheline syenite from site 8 where A and B provide evidence of the altered state of the rock with the brown colouration forming as a secondary alteration. The nepheline phenocrysts(Neph) and CPX grain become evident under cross polarised light (XPL). The nepheline phenocrysts appear to be associated with small amounts of eudialyte(Eud) that appears on grains or as part of the alteration. In C and D, the green aegirine is in the less altered section with phenocrysts of nepheline and feldspar being a prominent and simultaneous crystallisation of CPX.

The magnetite in samples from site 8, the green nepheline syenite, occurs in both the opaque minerals associated with the aegirine as well as the opaque grains that have formed independently of the aegirine. The magnetite makes up approximately 1 % of the sample (Figure 3.23).

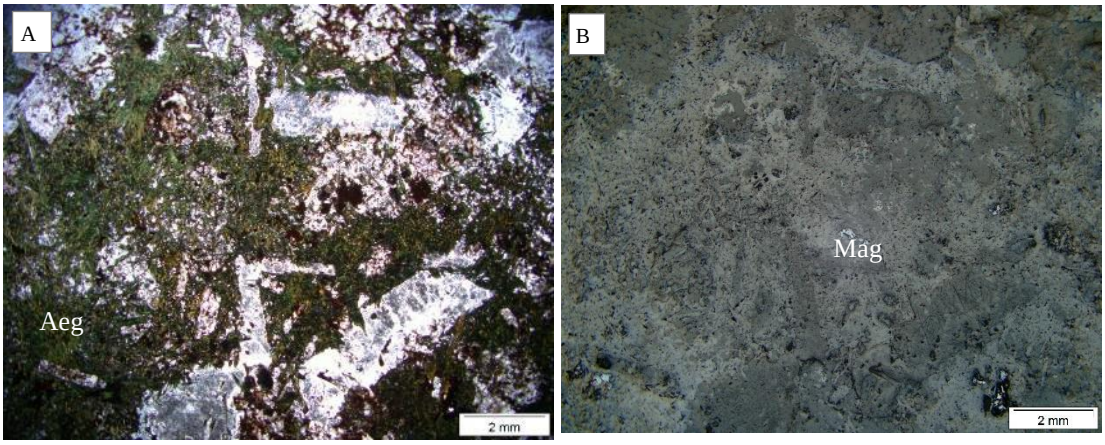

Figure 3.23 Magnetite in the green nepheline syenite occurs as 0.3 mm medium sized grains as well as groups of smaller 0.1 mm sized magnetite grains. The magnetite (Mag) is in the large independent opaque's and the smaller aegirine (Aeg) associated opaque's as well.

Site 9 – Green nepheline syenite

The green nepheline syenite whole rock sample for Site 9 was also orientated and collected from the south gate of the game reserve. Sample 9 is also part of the green nepheline syenite from the Ledig formation with a large amount of aegirine, pyroxene as well as nepheline and opaque minerals (Figure 3.24).

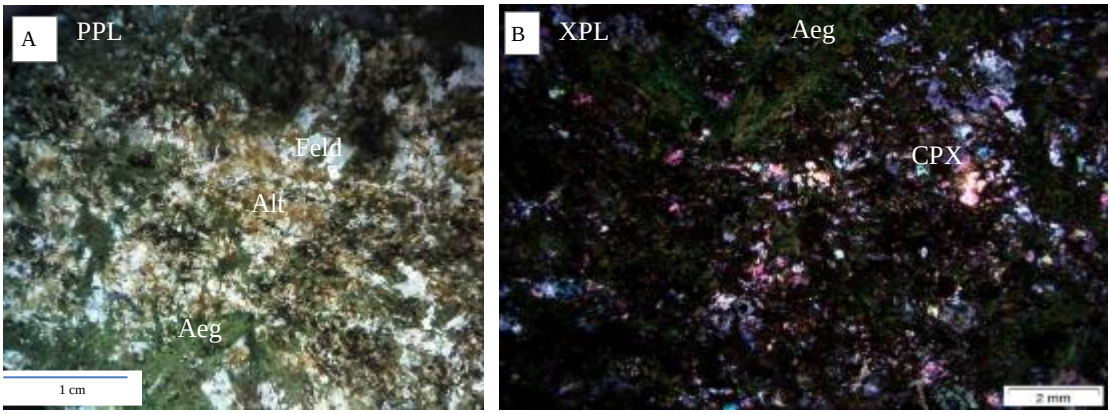

Figure 3.24 A) Provides a full slide view of green nepheline syenite. The brownish colour alteration (Alt) is in the white feldspar grains(feld) with the green colour coming from aegirine (Aeg). B) The cross-polar close up identifies a radial texture of the green aegirine. The high colourful birefringence grains are from clinopyroxenite (CPX) and feldspar grains. The black areas are the opaque minerals (Transmitted light, Plain polarised light in A).

Site 9 has an abundance of small 0.1 mm magnetite grains, which make up approximately 6% of the sample (Figure 3.25 B). This is much higher than the magnetite concentration observed for the white nepheline syenite from sample 7. In Figure 3.25 A, the presence of eudialyte is seen as a purple shadow.

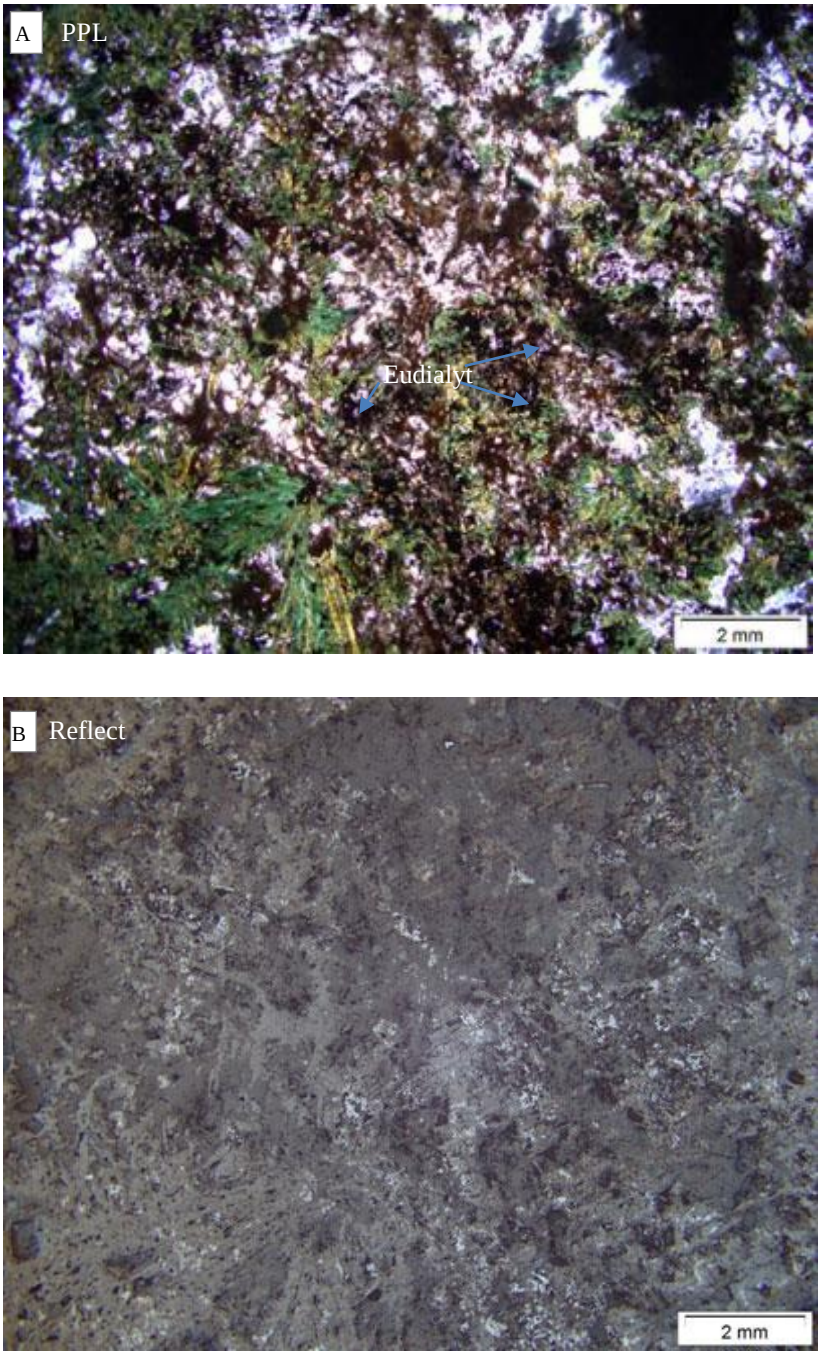

Figure 3.25 A) Green needles of aegirine have a radial texture; the sample is altered with the opaques associated with biotite. There is also a concentration of purple eudialyte. B) Fine magnetite is observed throughout the sample are seen in reflected light.

3.1.4 Opaque mineral analysis for the Pilanesberg System

A comparison of all the Pilanesberg samples in reflected light was made to estimates the different amounts and sizes of the magnetite. The analysis looks at the size of the magnetite grains; as small grains < 0.3 mm are more likely to be single domain grains. The grey syenite dyke samples 1.3, 2 and 5.5 were examined in reflected light and compared them with the corresponding transmitted light image (Figure 3.26). The grey dyke has medium sized magnetite grains that are scarce through the samples.

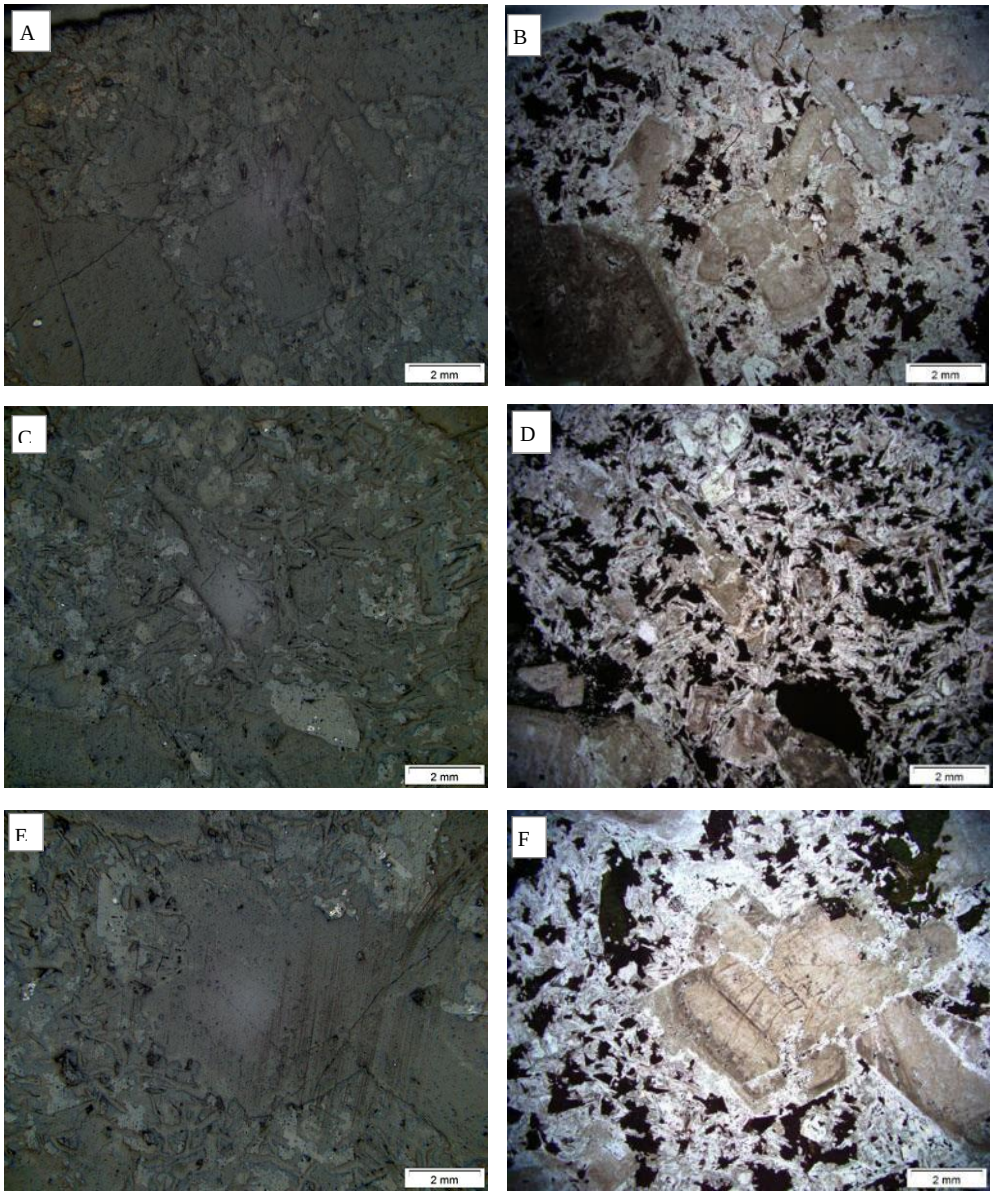

Figure 3.26 Grey syenite dyke. A and B) sample 1.3, C and D) sample 2, E and F) Sample 5.5 with reflected light and transmitted light respectively. The reflected light indicates a medium sized whitish grey magnetite grain hosted in the opaque minerals associated with the green aegirine observed in the transmitted light images.

The red syenite dyke has an abundance of magnetite and a varied grain size with 0.3 mm medium sized magnetite grains occurring in the matrix and < 0.1 mm small grains within the aegirine clast. The concentrations of magnetite in the red syenite dyke sample 3.2 and sample 4 are approximately 5% higher (Figure 3.27) than the concentrations in the grey syenite dyke (Figure 3.26).

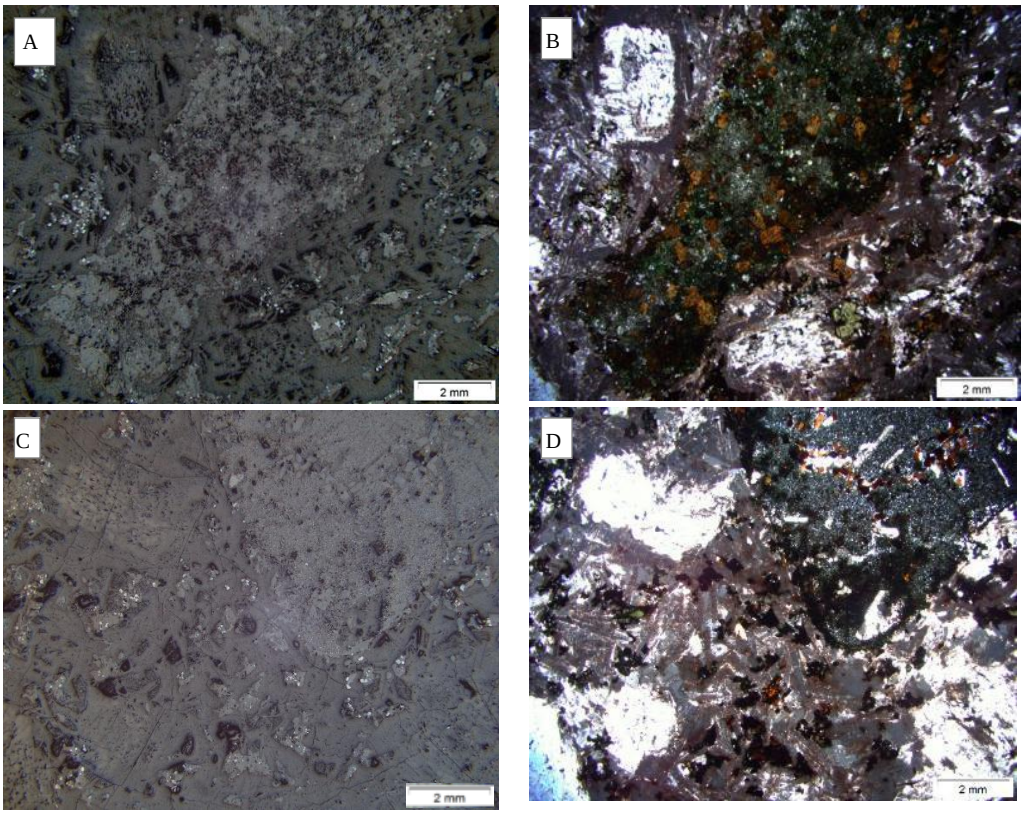

Figure 3.27 The red syenite dyke samples 3.2A (A and B) and sample 4 (C and D) display varying sizes of magnetite grains with medium sized grains seen with the aegirine needles in the matrix while the fine-grained magnetite occurs in the aegirine clast.

In the sample from site 7, there is a minimal amount of magnetite in the sample, one large 2 mm grain and a smaller 0.2 mm grains (Figure 3.28). This is problematic for paleomagnetic demagnetisation because the large grains will be MD grains that are not as stable to demagnetise as SD grains.

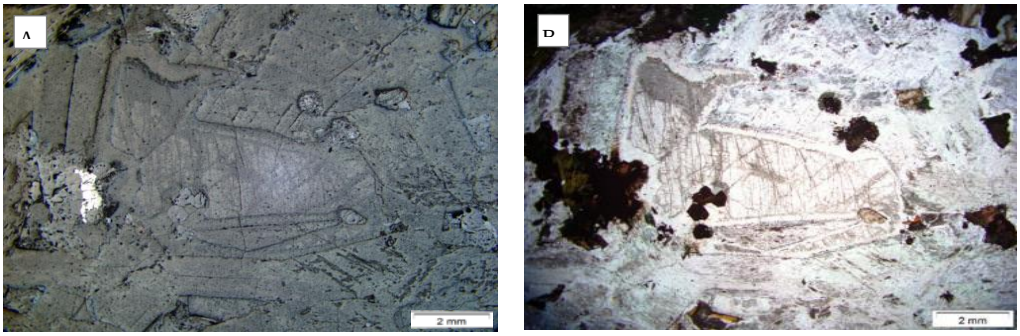

Figure 3.28 The white nepheline syenite from sample 7.2A has a small percentage of opaque minerals as seen in B); however, the magnetite concentration is minimal. When magnetite does occur, it is as large grains approximately 1.5 mm in size A).

The green nepheline syenite from sample 8.2 has 5-10 % more magnetite than the white nepheline syenite (foyaite). However, the quantity is minimal compared to the red syenite dyke. The magnetite in these samples is found in distinctive groups of small 0.1 – 0.2 mm magnetite grains that occur as clusters that approximate a medium 0.4 mm sized grain (Figure 3.29). Sample 9 seems to be rich in small magnetite grains that are well spaced through the sample associated with the green aegirine and a secondary event that occurred during alteration.

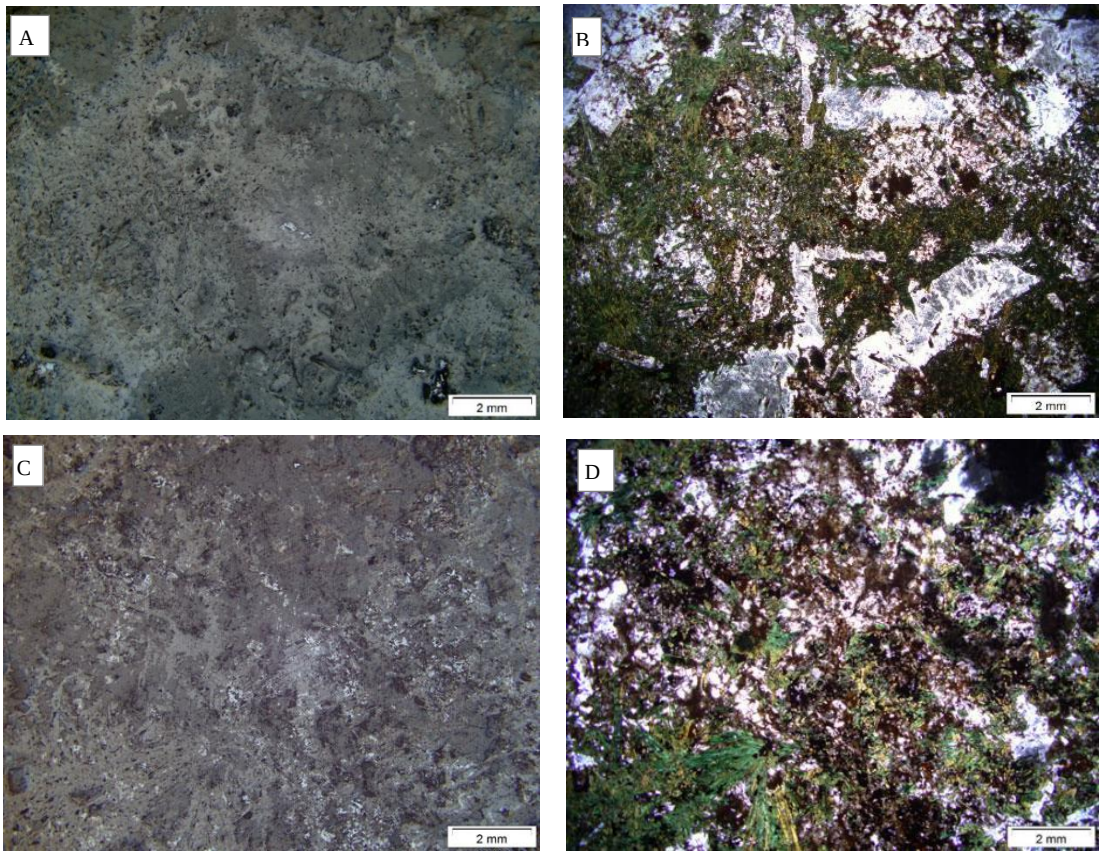

Figure 3.29 Sample 8.2 (A and B) and sample 9 (C and D) from the green nepheline syenite indicate a varying amount of magnetite with less than 5 % medium sized grains when the aegirine is fine (A and B). In images C and D, there is an abundance of medium sized magnetite has associated with large opaques and larger aegirine needles.

The rock sample and opaque mineralogy with opaque occurrence size and percentage are summarised in Table 3.2.

Table 3.2 Summary of the petrography for the Pilanesberg dykes and the Complex

Sample	Rock name	Rock minerals	Opaque minerals	Amount of opaque's	Opaque grain size
Sample 1	Grey syenite dyke	Plag (large) Aegirine (needle matrix), CPX, Biotite, Opaque	Magnetite, Pyrite	2-4 %	50-200 µm and 50-10µm
Sample 2		Kspar (perthitic) Aegirine, CPX, Biotite, Sanidine, Opaque	Magnetite, Haematite	0.5–1 %	Magnetite 50-200 µm Haematite 200 µm
Sample 5		Kspar, CPX, Opaque Aegirine, Sanidine,	Magnetite, Haematite	1-2%	50 µm
Sample 3	Red syenite dyke	Kspar, Plag, Aegirine, Sanidine, Biotite, Opaque	Magnetite, Haematite, Sulphide	Frequent 2-3%	50 – 80 µm
Sample 4		Kspar, Plag, Aegirine, Biotite, Sanidine, Opaque	Magnetite, Sulphides	Frequent 2-3%	10 - 60 µm
Sample 6 and 7	Pilanesberg Complex White Foyaite (Neph. Syenite)	Nepheline, Aegirine CPX, OPX Biotite, Opaque	Magnetite	Spars 0.5 %	1.8 mm
Sample 8 and 9	Pilanesberg Complex Green Foyaite (Neph. Syenite)	Nepheline, Plag, Aegirine CPX, OPX, Biotite, Eudialyte, Opaque	Magnetite	0.5 %	20 - 70 µm

In summary, the grey syenite dyke has a limited amount of medium-grained magnetite while the red syenite dyke has an abundance of small and very fine-grained magnetite. The Pilanesberg Complex white foyaite has large grains that are extremely scarce while the green foyaite contains varying amounts of medium-grained magnetite varying from less than 5% to between 10 and 15%. When there is inadequate energy for small grains, they will remain single-domain grains. Single-domain magnetic grains are better recorders of the paleomagnetism than multi-domain grains that have a time decay (Butler, 1992).

The abundance and size of the magnetite in each sample is essential to explaining the paleomagnetic behaviour during demagnetisation of each sample. As the size of the magnetite grains decreases, so do the number of magnetic domains. This is because the energy needed to form a domain wall is larger than the decline in magnetostatic energy from the grain dividing into domains (Butler, 1992). The grey syenite dyke can demagnetise completely with its small to medium sized grains. The red dyke has small grains that would be the most likely to demagnetise quickly, but the sample contains hematite that is a multi-domain grain that resists AF demagnetisation. In the Pilanesberg Complex white foyaite, the sample has one large 1.5 mm magnetite grain. The green foyaite is complicated because not only is the sample altered but it also has a variable amount of magnetite in its samples. This will be important for any future paleomagnetism.

3.2 GEOCHRONOLOGY INTRODUCTION

This chapter presents geochronology data from the Pilanesberg Complex as well as similar syenite dykes in the southern Pilanesberg dyke swarm and foyaites from the Pilanesberg Complex itself. The new data presented are more precise than published ages. This study shows that the Pilanesberg Complex (1602 ± 39 Ma) is substantially older than previous ages (1250 – 1400 Ma (Retief, 1963; Harmer R (unpub) from Hansen et al., 2006)), while the Pilanesberg dykes are younger than previously thought (1290 – 1330 Ma, (Van Niekerk, 1962)). Furthermore, data will be used to construct a sequence of emplacement events, and this, in turn, provides ample time for one or many magnetic reversals during the Pilanesberg event. The whole rock samples from nine locations in the Pilanesberg Complex and the southern Pilanesberg dykes were drilled numerous times in order to obtain core samples for examination.

3.2.1 Geochronology samples and methodology

Whole-rock samples collected from two dykes on the southern dyke swarm, namely

1) Grey syenite dyke (samples 1, 2 and 5)
2) Red syenite dyke (samples 3 and 4)

As well as two foyaite outcrops from the southern edge of the Pilanesberg Complex, namely

3) White foyaite (samples 6 and 7)
4) Green foyaite (samples 8 and 9).

These samples were sent to the Norwegian Geological Survey (NGU), for geochronological analysis.

The problem with dating alkaline rocks is that they nerely form datable zircons (Rollinson, 1993). The Pilanesberg Complex samples do contain zirconium, which is associated with eudialyte, meaning that zircons do not form. As such, the Pilanesberg System samples are analysed using the $^{40}Ar/^{39}Ar$ dating method.

At the Norwegian Geological Society (NGU), the samples were crushed and sieved to isolate grains of 180-250 µm. Visual inspection with a binocular microscope showed a moderate degree of alteration in most samples. The samples were washed in 5 HNO^3 for 5 minutes in an ultrasonic bath at room temperature to remove minor surface alteration and carbonate. Subsequently, the samples weres washed ultrasonically with distilled water several times.

The $^{39}K(n, p)^{39}Ar$ transformation took place during irradiation in the Institute for Energiteknikk (IFE, Kjeller, Norway) with n being the number of neutrons and p being the number of protons. Samples were calibrated against the Hb3gr hornblende standard (1080.4 ± 1.1 Ma), which is calibrated directly to the U-Pb system (Renne et al., 1998). The samples were step heated in the $^{40}Ar/^{39}Ar$ lab at NGU using a resistance furnace (Heine type). The gases extracted were swiped over SAES AP-10 Getters for 2

minutes. The getters maintain an ultra high vacuum and ensure high purity of the gas. The gas moves to a separate part of the extraction line for 9 minutes over the SAES AP-10 getters.

The method of peak hopping is used to find the peaks (at least eight cycles) on masses ^{41}Ar to ^{35}Ar on Balzers electron multiplier with an MAP 215-50 mass spectrometer. Data from unknowns were corrected for blanks before the reducing the data with the AgeMonster software package (written by M. Ganerød). This software implements McDougall and Harrison's (1999) equations by using the decay constants from Renne et al. (1998) and the trapped ^{40}Ar/ ^{36}A ratio of 298.56 ± 0.31 of Lee et al. (2006). Data reduction in AgeMonster incorporates corrections for mass discrimination, the decay of ^{37}Ar and ^{39}Ar, which are interfering isotopes produced during irradiation.

In the spectrum age diagrams, a plateau is defined according to the following requirements:

At least three consecutive steps (Figure 3.30), each within 95% confidence level, comprise at least 50% of total ^{39}Ar and mean square of weighted deviates (MSWD) less than the two-tailed student T-critical value. A weighted mean plateau age (WMPA), was calculated using the inverse of the variance as a weighting factor.

The inverse isochron results make use of a weighted York-2 for the calculation, where a valid isochron has an MSWD value less than the two-tailed F-test critical value. The inverse isochron ^{40}Ar/^{39}Ar diagrams are useful to recognise atmospheric argon and excess ^{40}Ar in the mineral lattice, which ^{40}Ar/^{39}Ar spectra cannot recognise (Kuiper, 2002). The square root expands all uncertainties (apart from the total fusion ages) (MSWD) if MSWD > 1.

3.2.2 Geochronology Argon-Argon theory

The $^{40}Ar/^{39}Ar$ method aims at finding ages for igneous and metamorphic minerals. In general, minerals record their most recent cooling event, which may not be the same as the age of intrusion. For that reason, the $^{40}Ar/^{39}Ar$ geochronology is an important igneous rock dating method as it assumes that all the ^{40}Ar remains after cooling past the closing temperature of that rock (Renne et al., 1998).

Naturally occurring isotopes of argon are ^{36}Ar, ^{38}Ar and ^{40}Ar, while the dating method creates ^{39}Ar by the fast neutron bombardment of ^{39}K in a nuclear reactor where,

$$^{39}K + n \rightarrow {}^{39}Ar + p \qquad (3.1)$$

where p stands for proton and n for neutron (Fowler, 1990). The dating process starts with irradiating the sample with neutrons, following which it is step-heated in a vacuum. The mass spectrometer is used to measure the ratio of $^{40}Ar/^{39}Ar$ at each temperature step. There is a proportional relationship between the amount of ^{39}K before irradiation to the quantity of ^{39}Ar after irradiation:

$$(^{39}Ar)_{now} = c\,(^{39}K)_{now} \qquad (3.2)$$

where c is the proportionality constant. c is a function of irradiation time and neutron energy (Fowler, 1990).

The sample contains radiogenic ^{40}Ar given by:

$$(^{40}Ar)_{now} = (^{40}K)_{now}\left(\frac{\tau_A}{\tau_A+\tau_c}\right)\left(e^{(\tau_A+\tau_c)t} - 1\right) \qquad (3.3)$$

Moreover, combining equation 3.2 and 3.3 provides the $^{40}Ar/^{39}Ar$ ratio as:

$$\frac{(^{40}Ar)_{now}}{(^{39}Ar)_{now}} = \frac{1(^{40}K)_{now}}{c(^{39}K)_{now}}\left(\frac{\tau_A}{\tau_A+\tau_c}\right)\left(e^{(\tau_A+\tau_c)t} - 1\right) = \frac{\left(e^{(\tau_A+\tau_c)t}-1\right)}{D}, \qquad (3.4)$$

where $$D^{-1} = \frac{1(^{40}K)_{now}}{c(^{39}K)_{now}}\left(\frac{\tau_A}{\tau_A+\tau_c}\right).$$

D is determined using a standard irradiated sample with known age t_s simultaneous to the study sample.

The standard (s) has a measured $^{40}Ar/^{39}Ar$ ratio is:

$$\frac{(^{40}Ar)^s_{now}}{(^{39}Ar)^s_{now}} = \frac{\left(e^{(\tau_A+\tau_c)t_s}-1\right)}{D} \qquad (3.5)$$

$$D = \left(e^{(\tau_A+\tau_c)ts} - 1\right)\frac{(^{39}Ar)^s_{now}}{(^{40}Ar)^s_{now}} \quad (3.6)$$

Introducing D back into equation 3.4 produces the age equation:

$$\frac{(^{40}Ar)_{now}}{(^{39}Ar)_{now}} = \frac{(e^{(\tau_A+\tau_c)t}-1)(^{40}Ar)^s_{now}}{(e^{(\tau_A+\tau_c)ts}-1)(^{39}Ar)^s_{now}}. \quad (3.7)$$

Equation 3.7 calculates the sample age by achieving a true age at each temperature step. A spectrum of ages was obtained when some of the minerals lost an amount of argon.

The $^{40}Ar/^{39}Ar$ method becomes problematic and will suggest old dates if an excess amount of ^{40}Ar is present in the samples. In fine-grained samples, ^{39}Ar can be lost as it recoils out of the sample from the reaction during irradiation.

3.3 GEOCHRONOLOGY DATA

The apparent ages of each Pilanesberg System sample make use of the $^{40}Ar/^{39}Ar$ furnace step heating method with analysis of feldspar and amphibole grains for a comparative analysis. The apparent spectrum age achieves a plateau equivalent to the apparent age when meeting geochronology methodology criteria. The inverse isochron diagram plots $^{36}Ar/^{40}Ar$ against $^{39}Ar/^{40}Ar$ and the age is the value of $^{39}Ar/^{40}Ar$ when $^{36}Ar/^{40}Ar$ is zero with maximum data fit. The results are presented in Figure 3.30 - Figure 3.38.

Amphiboles from the grey dyke sample 1 yield an apparent age of 1160.9 ± 9.1 Ma, using the spectrum analysis (Figure 3.30 A) and 1139.7 ± 18.3 Ma using the inverse isochron data (Figure 3.30 B). The amphibole age has a small error of ± 18.3 Ma with a spectrum data stable plateau between steps 11 and 15. The feldspar analysis is not as reliable, with the spectrum plateau steps 1-15 producing the date of 1139.7 ± 18.3 Ma. The isochron age for sample 1 was not obtainable (Figure 3.30C and D).

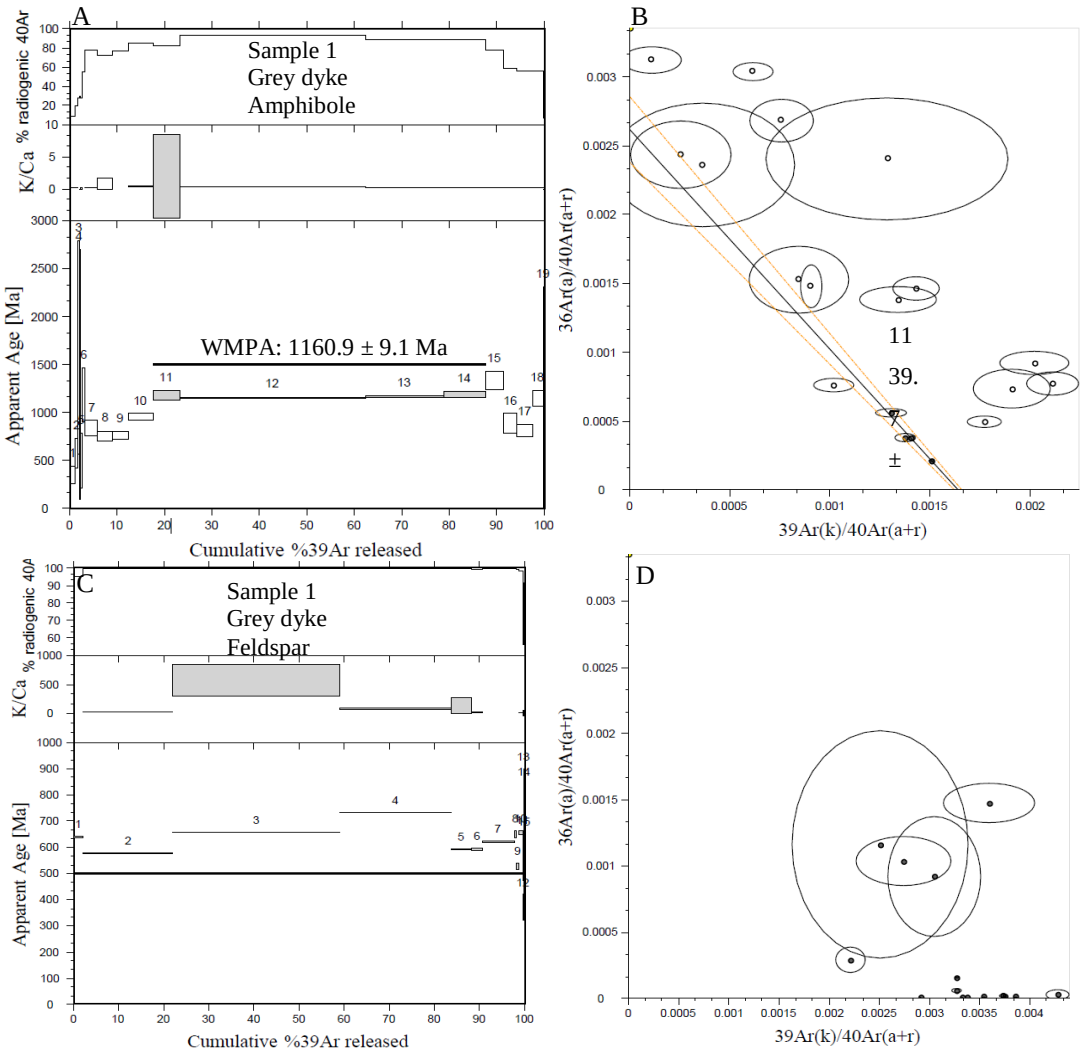

Figure 3.30 Age dating of amphiboles from sample 1 produce an apparent age of 1160.9 ± 9.1 Ma with spectrum analysis (A) and an age of 1139.7 ± 18.3 Ma with inverse isochron analysis B). Sample 1 feldspar spectrum analysis yields an age of 663.3 ± 27.7 Ma (C), and the inverse isochron analysis was not able to achieve a date (D).

The feldspar analysis on sample 2 also does not produce an age within the published ages of 1310 ± 80 Ma (Rb-Sr, Van Niekerk, 1962). Steps used for the spectrum age are from 12 to 17 (Figure 3.31 A) while the inverse isochron method did not achieve an age (Figure 3.31 B).

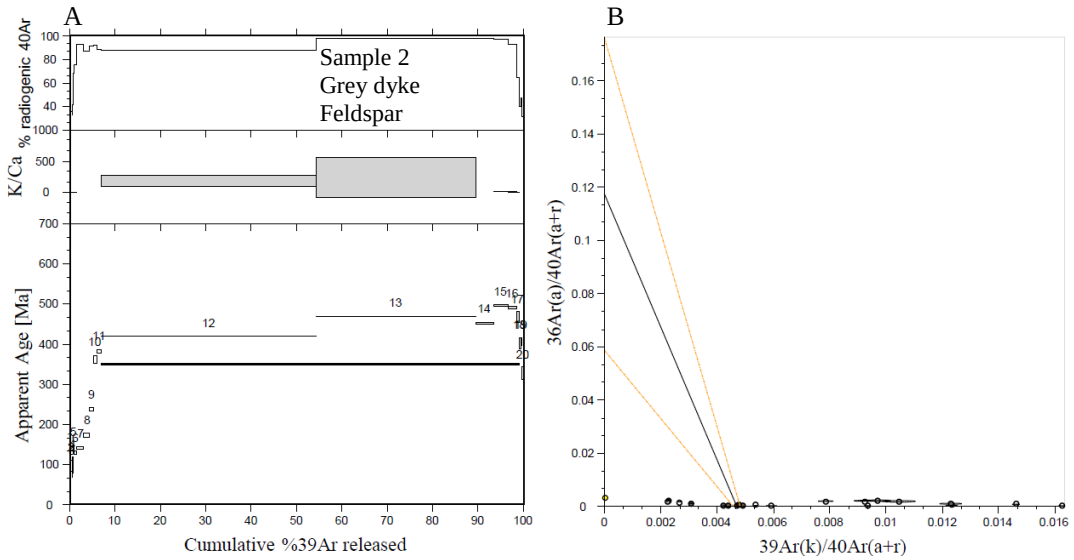

Figure 3.31 Sample 2 feldspar produced a young age of 451.6 ± 22.5 Ma with spectrum analysis while inverse isochron analysis did not achieve a date.

Similarly, the feldspar analysis of grey dyke sample 5 yields a young age of 574 ± 15 Ma (Figure 3.32), which is also much lower the Rb-Sr age of 1310 ± 80 Ma achieved by Van Niekerk (1962), suggesting that feldspar grains were unable to retain any age information for this sample.

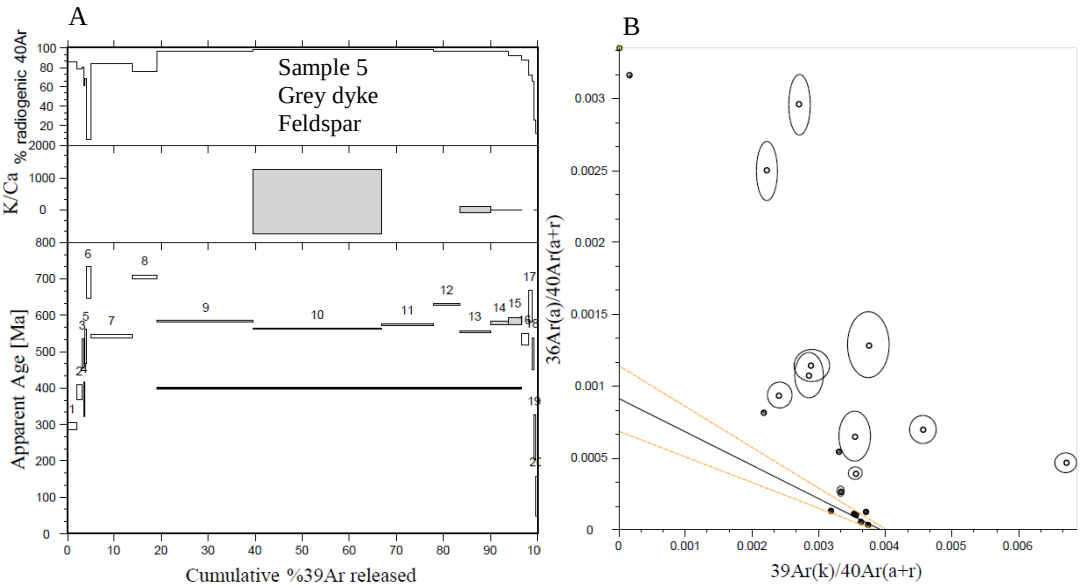

Figure 3.32 Sample 5 grey dyke; feldspar again achieved a low spectrum analysis age of 574.4 ± 15.16 (A) and 545.2 ± 20.4 Ma with the inverse isochron analysis (B).

The apparent amphibole age of 1160 ± 9 Ma is close to the error of previously published date of 1290 ± 80 Ma (Van Niekerk, 1962). However, the apparent feldspar ages are much younger between 450 and 665 Ma and do not agree with published dates.

The feldspar spectrum and isochron apparent age obtained for sample 3 from the red syenite dyke have ages of 1219 Ma with small errors of ± 7 Ma and ± 20 Ma, respectively. These are close to the published ages of 1290 ± 80 Ma (Emerman, 1991).The calculation of the spectrum age used is steps 12 to 16 (Figure 3.33).

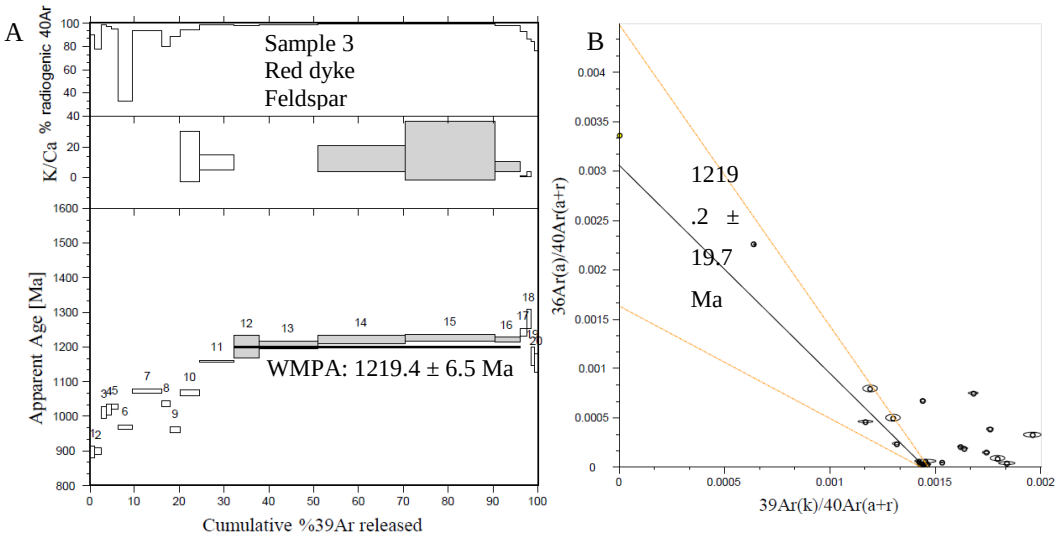

Figure 3.33 Sample 3 feldspar reliable ages are 1219.4 ± 6.5 Ma with spectrum analysis (A) and 1219.2 ± 19.7 with inverse isochron analysis (B).

The ages obtained from feldspar grains from the red syenite dyke (sample 4) are 1268 ± 10.3 Ma, with apparent age spectrum method over steps 13-15 and 1235 ± 46.8 Ma for the inverse isochron (Figure 3.34).

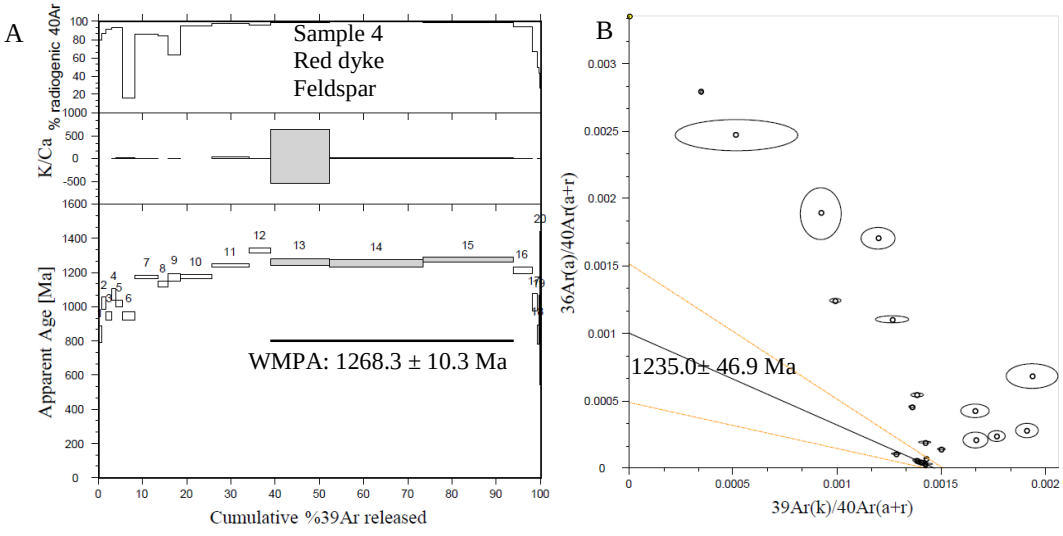

Figure 3.34 Sample 4 feldspar ages of 1268.1 ± 10.3 Ma with spectrum analysis (A) and 1235 ± 46.9 Ma with inverse isochron analysis.

Geochronology of the Pilanesberg Complex is from the outer white foyaite ring of the Complex at sites 6 and 7 and the green nepheline syenite from site 8 and 9 (Figure 3.35).

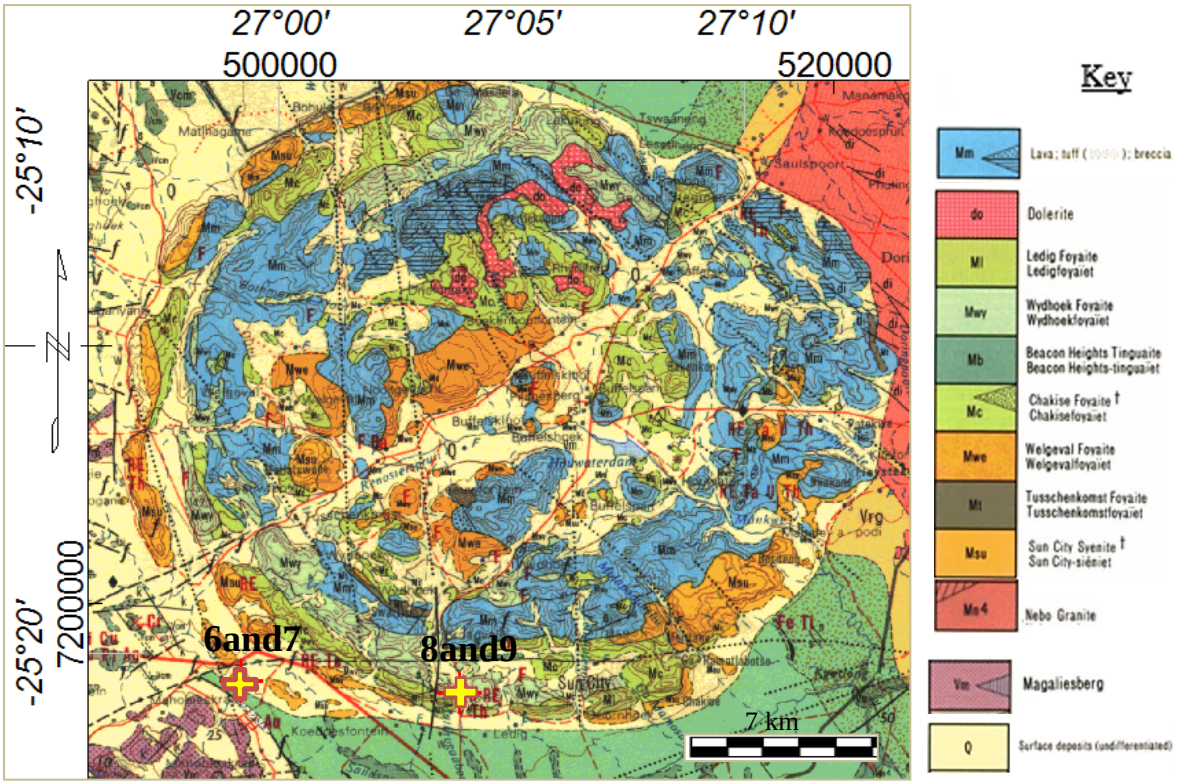

Figure 3.35 The age dating of the Pilanesberg Complex is on samples from the white foyaite at site 6 and 7 as well as the green foyaite at site 8 and 9.

Sample 6 achieves good results for the amphibole samples but young dates for the feldspar analysis (Figure 3.36). The determined ages of 1602.4 ± 38.9 Ma and 1595.4 ± 61.7 Ma are within error but older than the previous dates of ~1400 Ma. The feldspar apparent ages are 249 ± 8 Ma and 2412 ± 8 Ma. That is again too young for consideration as relevant to this Pilanesberg event with similar reasoning to that used for the grey syenite dyke feldspar data. The amphibole dates have higher uncertainties than any of the previous samples. However, the step spectrum analysis appears to be consistent with steps 14 to 17 (Figure 3.36 A).

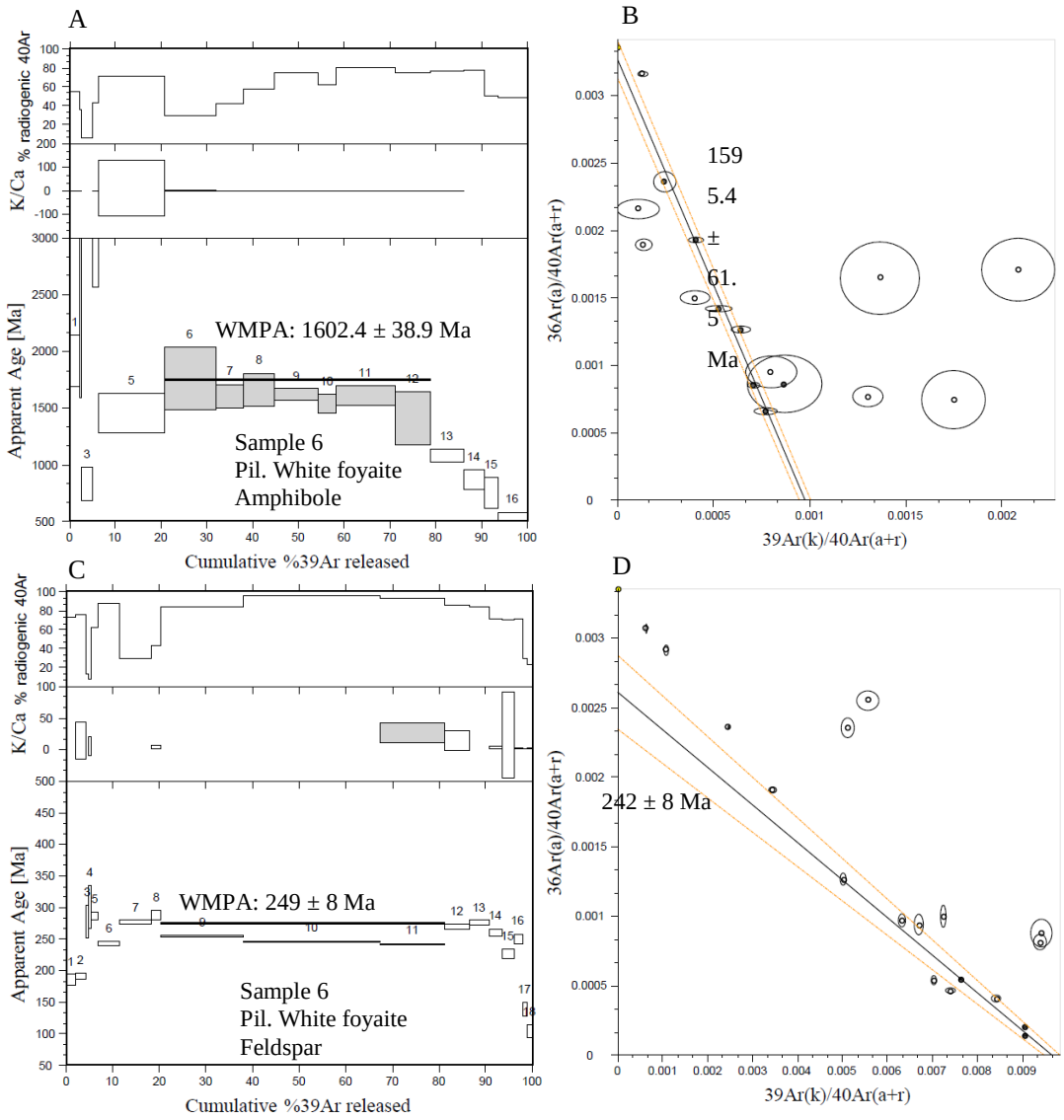

Figure 3.36 Sample 6 A-B Amphibole C-D Feldspar. The amphibole ages are closest to the expected age for the Pilanesberg Complex with a spectrum age of 1602.4 ± 38.9 Ma (A) and an inverse isochron age of 1595.4 ± 61.5 Ma (B).

The feldspar analysis of sample 7 does not provide a plausible solution. However, the amphibole analysis yields ages comparable with published dates. The spectrum analysis has the best solution with a small error, 1584 ± 10.81 Ma (Figure 3.37A). The inverse isochron analysis has a significantly larger error due to the large spread of the data points. However, the age (1613.8 ± 170.5 Ma) is similar to that of the spectrum analysis. Both ages are also comparable with the apparent ages of the amphibole sample from site 6.

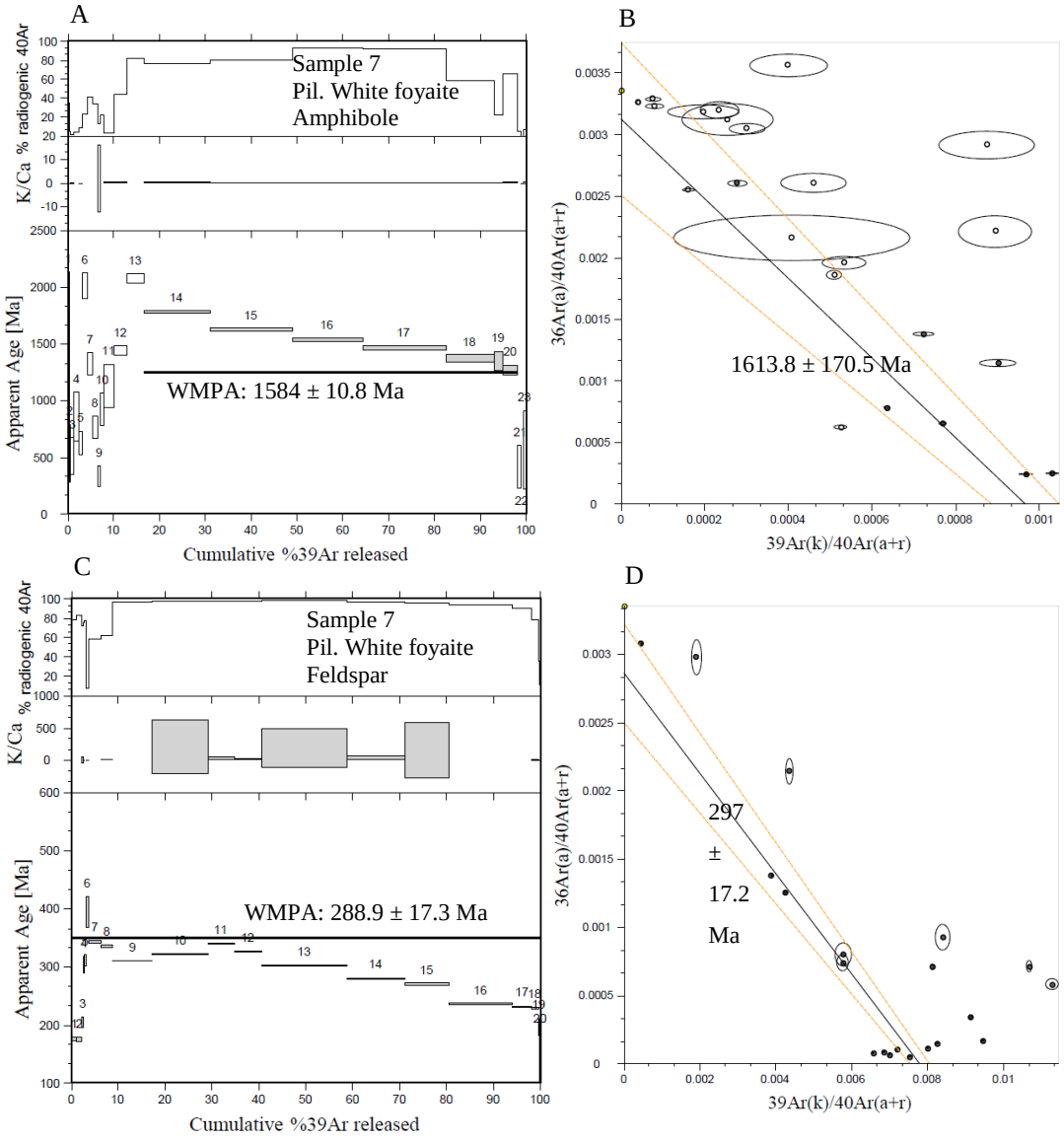

Figure 3.37 Results for sample 7 A-B amphibole and C-D feldspar for the Pilanesberg white foyaite, where A and C show spectrum analysis, B and D shows the inverse isochron analysis for the samples. Suitable ages achieved from the amphibole samples (A and B) with the spectrum analysis providing the best error analysis of ± 10.8 Ma for the sample. The apparent feldspar ages (C and D) most likely reflect a reset in the rock at that time.

The green foyaite samples from the Complex were the least reliable as they are highly altered and had a massive amount of excess argon. The only date achieved for the green foyaite was from the spectrum analysis along a two-step plateau (steps 9 and 10) for an amphibole, which yielded a date of 953.6 ± 9.5 Ma (Figure 3.38), which is younger than the published dates (~1400 Ma) and the ~ 1600 Ma age from the white foyaite. The age achieved for this sample appears to be due to alteration and chemistry to reflect an unusable date.

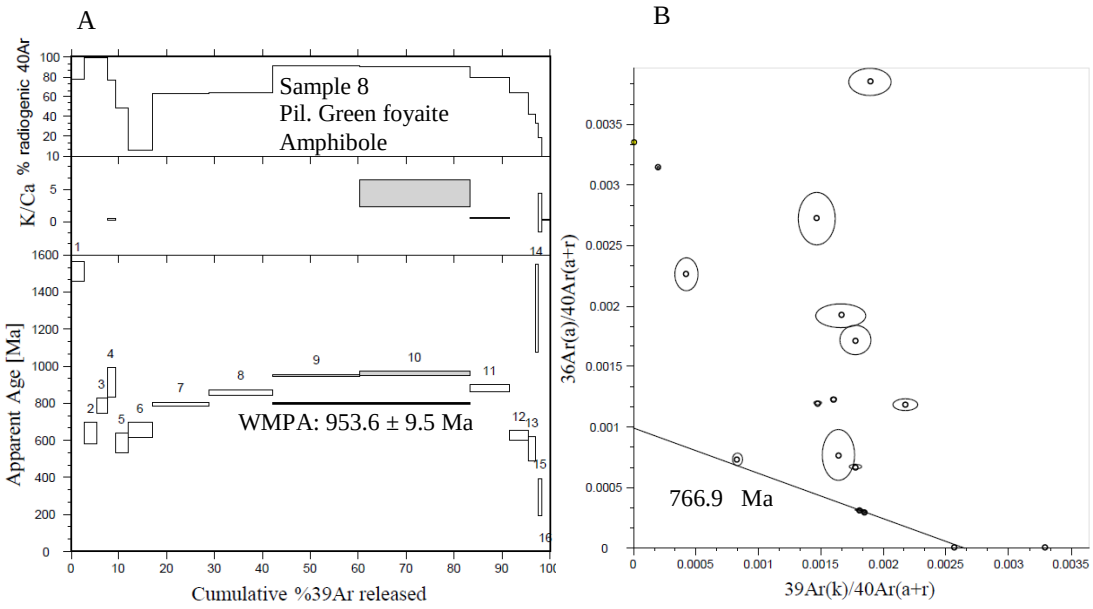

Figure 3.38 Sample 8- Amphibole analysis with an apparent age of 953.58 ± 9.51 Ma for the spectrum analysis in (A) and unreliable results in (B).

3.4 DISCUSSION OF GEOCHRONOLOGY

A summary of all the geochronology with the error analysis and respective localities is in Table 3.3. The table compares the spectrum and inverse isochron analysis for each sample. The steps (n) refers to plateaus achieved in the spectrum analysis. Both amphiboles and feldspar grains were analysed where possible. The results indicate good ages for the amphibole samples later for the feldspars. The thin sections revealed that the Pilanesberg rocks have opaque minerals identified as magnetite. The magnetite has a consistently associated with amphibole grains throughout the Pilanesberg samples. Thus, the amphibole ages are recording the age of emplacement while most of the feldspar ages are presenting a reset event.

Table 3.3 $^{40}Ar/^{39}Ar$ results for furnace step-heating experiments with the ages reported in Ma. Uncertainties are taken as analytical errors at 1.96 σ. The superscript under column sample denotes mineral used (F = feldspar, A = amphibole)

			Spectrum analysis					Inverse isochron analysis			
Sample	**Lat/long**	**Steps (n)**	**%39Ar**	**Age ± 1.96 σ**	**MSWD (P)**	**TFA ± 1.96 σ**	**K/Ca ± 1.96 σ**	**Age ± 1.96 σ**	**MSWD (P)**	**Intercept ± 1.96 σ**	**Spread %**
1^F	-25.911/27.452	1-15 (15)	100	663.26 ± 27.69	3533.685 (0)	652.25 ± 0.56	0.24 ± 0.08	-	-	-	-
1^A	-25.911/27.452	11-15 (4)	69.91	**1160.93 ± 9.10**	2.233 (0.082)	1098.27 ± 9.85	0.071 ± 0.003	**1139.71 ± 18.30**	0.547 (0.0)	381.71 ± 68.30	13
2^F	-25.911/27.452	12-17 (6)	92.05	451.63 ± 22.46	3277.42 (0)	429.17 ± 0.43	1.73 ± 1.08	-	-	-	-
3^F	-25.896/27.457	12-16 (5)	63.62	**1219.48 ± 6.51**	2.341 (0.053)	1167.14 ± 3.9	8.1 ± 6.2	**1219.18 ± 19.69**	3.051(0.027)	326.55 ± 298.4	1.7
4^F	-25.895/27.457	13-15 (3)	54.9	**1268.13 ± 10.29**	1.136 (0.321)	1219.84 ± 6.26	6.1 ± 9.2	1235.0 ± 46.85	- (-)	996.64 ± 1001.68	2.8
5^F	-25.891/27.449	9-15 (7)	77.3	574.41 ± 15.16	267.445 (0.0)	569.95 ± 1.2	2.0 ± 1.7	545.2 ± 20.4	59.51 (0.0)	1093.29 ± 534.92	15
6^F	-25.342/26.986	9-11 (3)	60.86	248.98 ± 7.46	152.6 (0.0)	248.87 ± 0.73	26.5 ± 30.5	241.62 ± 7.88	48.58 (0.0)	382.79 ± 76.31	14.8
6^A	-25.342/26.986	7-14 (7)	58.29	**1602.42 ± 38.89**	1.335 (0.237)	1490.5 ± 47.8	0.17 ± 0.02	**1595.38 ± 61.47**	1.367 (0.233)	305.27 ± 25.17	53
7^F	-25.342/26.986	1-20 (20)	100	288.92 ± 17.30	4192.95 (0.0)	289.45 ± 0.33	0.82 ± 0.29	297.01 ± 17.19	3644.04 (0.0)	349.1 ± 86.4	135.3
7^A	-25.342/26.986	15-21 (7)	81.61	**1583.97± 10.81**	258.30 (0.0)	1512.2 ± 9.9	0.36 ± 0.032	1613.75 ± 170.52	282.02 (0.0)	319.62 ± 124.09	75.7
8^A	-25.346/27.064	9-10 (2)	41.31	953.58 ± 9.51	1.884 (0.0)	870.17 ± 6.31	4.39± 3.97	766.92 ± --	--	1005.87 ± --	1.3
9^A	Massive amount of excess argon, no isochron solution										

Feldspar ages achieved for sample 1, 2, 5, 6 and 7 are affected by alteration (seen in hand sample) and have recorded a resetting event.

The results of the spectrum and inverse isochron analysis plot in Figure 3.39 for all samples from Table 3.3. The dates fall into two distinct clustering groups each with overlapping errors. The first group includes the grey and red syenite dyke from the Pilanesberg southern dyke swarm, with ages ranging between 1139 and 1268 Ma. The dyke swarm is considerably younger than the data cluster for the Pilanesberg Complex, which plot between 1583 and 1602 Ma.

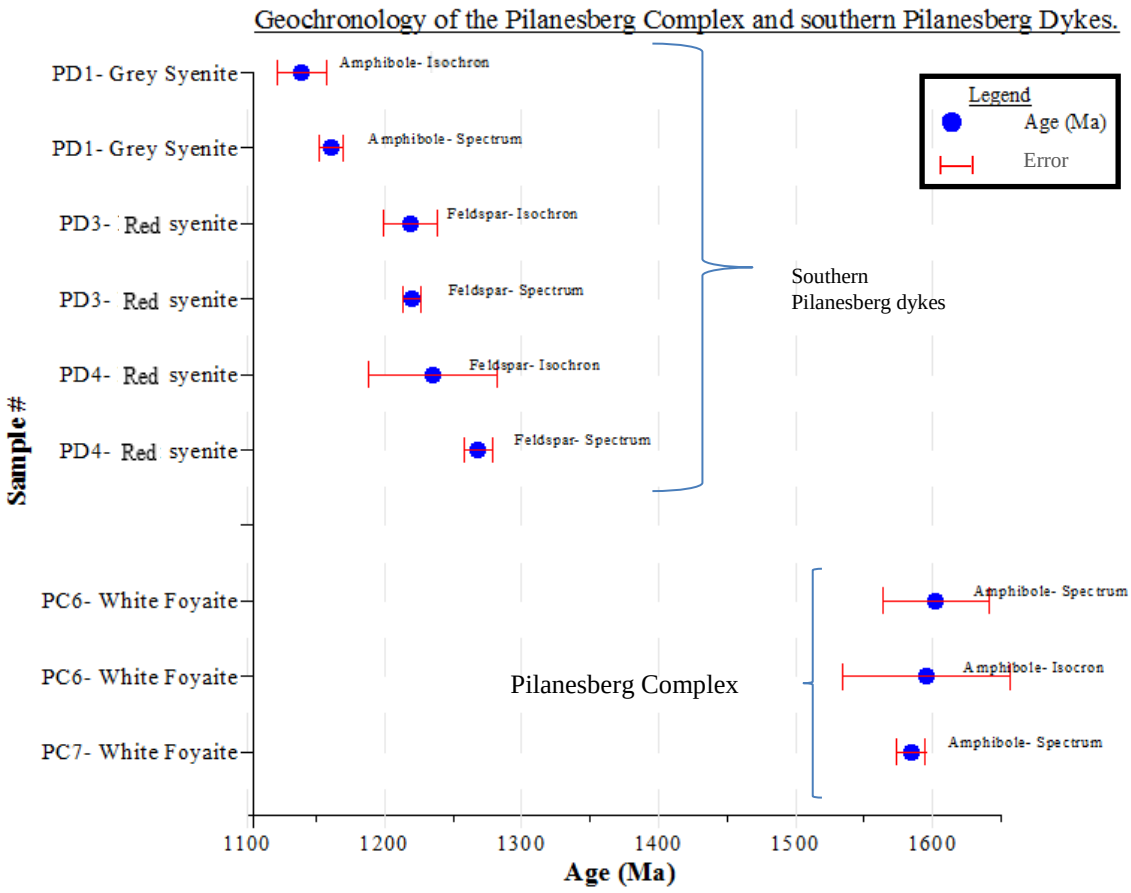

Figure 3.39 Age comparison of the Pilanesberg Complex white foyaites and the red syenite and grey syenite Pilanesberg dyke.

The new results for the Pilanesberg Complex and dyke swarm have significant implications for the age of the Pilanesberg event, identification and dating of the different episodes giving rise to the Pilanesberg System and dating of the inferred magnetic reversal between the intrusion of the Complex and the dykes. The error analysis is also considerably lower in the data than that achieved by the previously published dates. Table 3.4 presents summaries of the ages obtained in this study and the previously published dates for the Pilanesberg System.

Table 3.4 A summary of the current Pilanesberg System age dates compared with the previously published dates.

	Age ± error (Ma)	Method of Dating	Dated unit	Reference
Current age data				
Pilanesberg dykes	1161 ± 9	$^{40}Ar/^{39}Ar$ Amphibole Spectrum Analysis	Grey syenite dyke	This study
	1219 ± 7 1268 ± 10	$^{40}Ar/^{39}Ar$ Feldspar Spectrum Analysis	Red syenite dyke	This study
Pilanesberg Complex	1602 ± 39 1584 ± 10	$^{40}Ar/^{39}Ar$ Amphibole Spectrum Analysis	White foyaite (Neph. syenite)	This study
Previously published age data				
Pilanesberg dykes (Previously published)	1290 ± 80	Rb-Sr on biotite		Van Niekerk, 1962., Emerman, 1991
	1302 ± 80	Rb-Sr biotite	Dolerite	Van Niekerk (1962), Schreiner and Van Niekerk (1958) from Hansen et al. (2006)
	1310 ± 80	Rb-Sr on biotite	Robynson dyke,	Van Niekerk, 1962., Emerman, 1991
	1330 ± 80	Rb-Sr on biotite	Gemspost, Venterspost Mine	Van Niekerk, 1962., Emerman, 1991
Pilanesberg Complex (Previously published)	1193 ± 98	Rb-Sr regressed isochron		Harmer (1992)
	1250 ± 50	K-Ar		Retief (1963) from Olivo and William-Jones (1999)
	1290 ± 180	Rb-Sr Stable Isotope dilution		Schreiner and Van Niekerk (1958)
	1330 ± 80	Rb-Sr Stable Isotope dilution		Van Niekerk (1962)
	1397 ± 47	SHRIMP U-Pb titanite	White nepheline syenite	Harmer R., Armstron R. (unpub.) from Hansen et al. (2006)

The first event appears to be the intrusion of the white foyaite of the Pilanesberg Complex at 1602 ± 39 Ma. The new age (1602 Ma) is better constrained and much older than published ages. The published age data (Table 3.4) for the Pilanesberg Complex is between 1260 ± 50 Ma (K-Ar, Olivo and Williams-Jones, 1999) and 1397 ± 47 Ma (U-Pb on titanate, Hansen et al., 2006). Those dates agree that the Pilanesberg Complex was the first intrusion event of the Alkaline Province, which was followed by the Leeuwfontein Complex and Spitskop Complex (1341 ± 37 Ma, Cawthorn *et al.*, 2012). While the sequence of events is consistent with the published order, the actual age achieved for the Pilanesberg Complex is considerably older than the published dates, suggest that it was the first event in the Pilanesberg Alkaline Province. The significant time gap before the next event in the Alkaline Province may suggest that the Pilanesberg Complex is from a primary magma sequence.

The next intrusion is the red syenite dyke dated at 1219 ± 7 Ma and 1268 ± 10 Ma and followed by the grey syenite dyke at 1140 ± 18 Ma and 1160 ± 10 Ma. The Pilanesberg dykes are substantially younger than they were previously thought to be. This is seen to be especially wtruehen the dyke ages are compared to the previously published ages of 1290 ± 80 Ma, 1302 ± 80 Ma, 1310 ± 80 Ma (Robynson dyke) to 1330 ± 80 Ma (Gemspost, Venterspost Mine) (All from Rb-Sr on biotite, Van Niekerk, 1962., Emerman, 1991).

The age dating has made it possible to distinguish between different episodes of dyke intrusions, namely the older red syenite dyke and the younger grey syenite dyke. The grey dyke may have intruded later than the rest of the southern dyke swarm. Emerman (1991) described a multistage dyke intrusion in the northern dyke swarm where cooling dolerite dykes were intruded by a syenite dykes to form a composite dyke. Hansen et al. (2006) reported the multistage composite dykes extending down to the gold reef in the southern dyke swarm, indicating that this dyke swarm is also a multistage intrusion event. While the dykes sampled in the southern dyke swarm are not composite in nature, they do represent different intrusion episodes. The dykes retain their overall positive magnetisation with a north-south dyke orientation along a weakness zone from the Mesoproterozoic intraplate extension event (Michell and Liferovich, 2006; Retief, 1963).

The $^{40}Ar/^{39}Ar$ method is useful as it identifies when crystals form and when they experience different cooling events. In general, the feldspar analysis resulted in ages that are between 240 and 680 Ma, which is much younger than any published age. The feldspar analysis did not work in all the cases, or it has recorded a younger event, although, the amphibole analysis was successful. The opaque minerals in transmitted light had a consistent aegirine association. In reflected light, the opaque minerals were identified as magnetite. The magnetite association with amphibole is the reason the analyses of the amphibole grains were better able to produces reliable and relevant dates compared to the feldspar grains, which had no significant association with magnetite.

The Pilanesberg Complex white foyaite was dated at 1602 ± 39 Ma (Figure 3.36) and 1583± 11 Ma (Figure 3.37) on amphibole grains using $^{40}Ar/^{39}Ar$ spectrum analysis. The southern Pilanesberg dykes were dated at 1219.48 ± 6.51 Ma on feldspar grains (Figure 3.33) for the red syenite dyke and 1160 ± 9 Ma on the grey syenite dyke with amphibole analysis using $^{40}Ar/^{39}Ar$ spectrum analysis (Figure 3.30).

The white foyaite from the Pilanesberg Complex is ~ 200 Ma older than previously published age dates for the Complex (Figure 3.36 and Table 3.3). The dates determined on the dykes are younger than the previously published dates (Table 3.3). The red dyke is ~ 80 Ma younger and the grey dyke is ~ 160 Ma younger than the average published dates for the dykes (Table 3.3)

Gose et al., (2013) conducted a study on the Pilanesberg Complex (PC), Spitskop (S) and the Pienaars River Complexes (PR) and compared the results with other poles from the Kaapvaal Craton (Figure 3.40). These positions will be used to compare where the theoretical poles for the Pilanesberg Complex and Pilanesberg dykes would plot soley based on where the $^{40}Ar/^{39}Ar$ ages would fit in along the polar wander path.

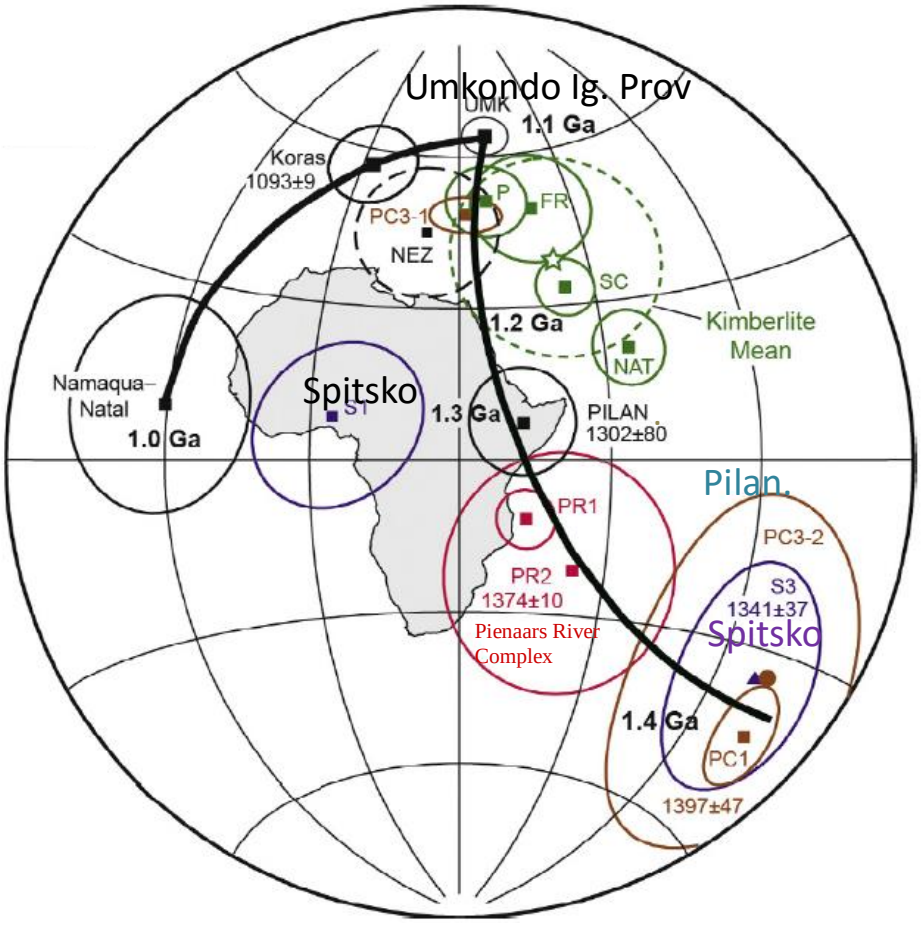

Figure 3.40 The published poles include the Pilanesberg Complex (PC), Spitskop (S) and the Pienaars River Complexes (PR) (Gose et al., 2013). The Pilanesberg dykes (PILAN, Gough, 1956), Premier kimberlite cluster (kimberlite mean, Jones, 1968; Doppelhammer and Hargraves, 1994), Umkondo Igneous Province (UMK, Gose et al., 2006), Koras Group (Briden et al., 1979) and the Namaqua–Natal belt (Gose et al., 2004, 2006). (Modified from Gose et al., 2013)

In summary, the Pilanesberg Complex is shown to be considerably older than originally believed, while the Pilanesberg dykes are substantially younger with two stages clearly determined. The magnetic map and the opposite magnetic signature between the Complex and the dykes hint that at least one magnetic reversal could have occurred between the emplacements of these alkaline bodies to achieve the opposite magnetic signature if they were from the same magma chamber. A full paleomagnetic study would be required to prove this hypothesis.

The large time gap between the emplacements does mean that numerous reversals could have taken place. However, as the intrusions of the Pilanesberg Complex and the Pilanesberg dykes are in close proximity geographically, this would suggest that the intrusions occurred in a medium period of time for both the close geographic proximity and a magnetic reversal to be possible.

The ages achieved of 1602 ± 39 Ma for the Pilanesberg Complex would plot outside of Gose et al. (2013) polar wonder path (Figure 3.40) while the Pilanesberg dykes aged at 1219.48 ± 6.51 Ma would plot much further along the polar wander path.

This proposes a conundrum where the dykes are in close proximity to the Pilanesberg Complex while having formed at a much later stage which would have meant the Kaapvaal craton would have moved and would not be above the same chamber. This however, can be explained as the dykes being part of a transition phase. This would mean that the Kaapvaal craton was stationary during the intrusion of the circular Pilanesberg Complex. At approximately the age of the dykes intrusion – the Kaapvaal craton would have started moving in accordance with Gose et al. (2013) polar wander path. This could have reactivated the magma chamber which resulted in the complex and in the process formed the well spread out Pilanesberg Dykes that spans from the Johannesburg dome through to Botswana.

CHAPTER 4: DATA IMAGE PROCESSING AND INTERPRETATION

4.1 POTENTIAL FIELD GRID MAP DATA

Airborne magnetic data over South Africa, from the Council for Geoscience, indicate that the Pilanesberg Complex carries a high induced 325 nT magnetisation (with respect to the 150 m flight height) above the background magnetic signature of the country rock. The compositionally associated remanently magnetised Pilanesberg dykes have a negative magnetic anomaly of 315 nT, (with respect to the flight survey height of 150 m) (Figure 4.1). The Pilanesberg Complex does not indicate a well-defined dipole, suggesting that it carries some remnant magnetisation, unless the Pilanesberg Complex dipole low is interfering with the intense low of the western Bushveld Complex.

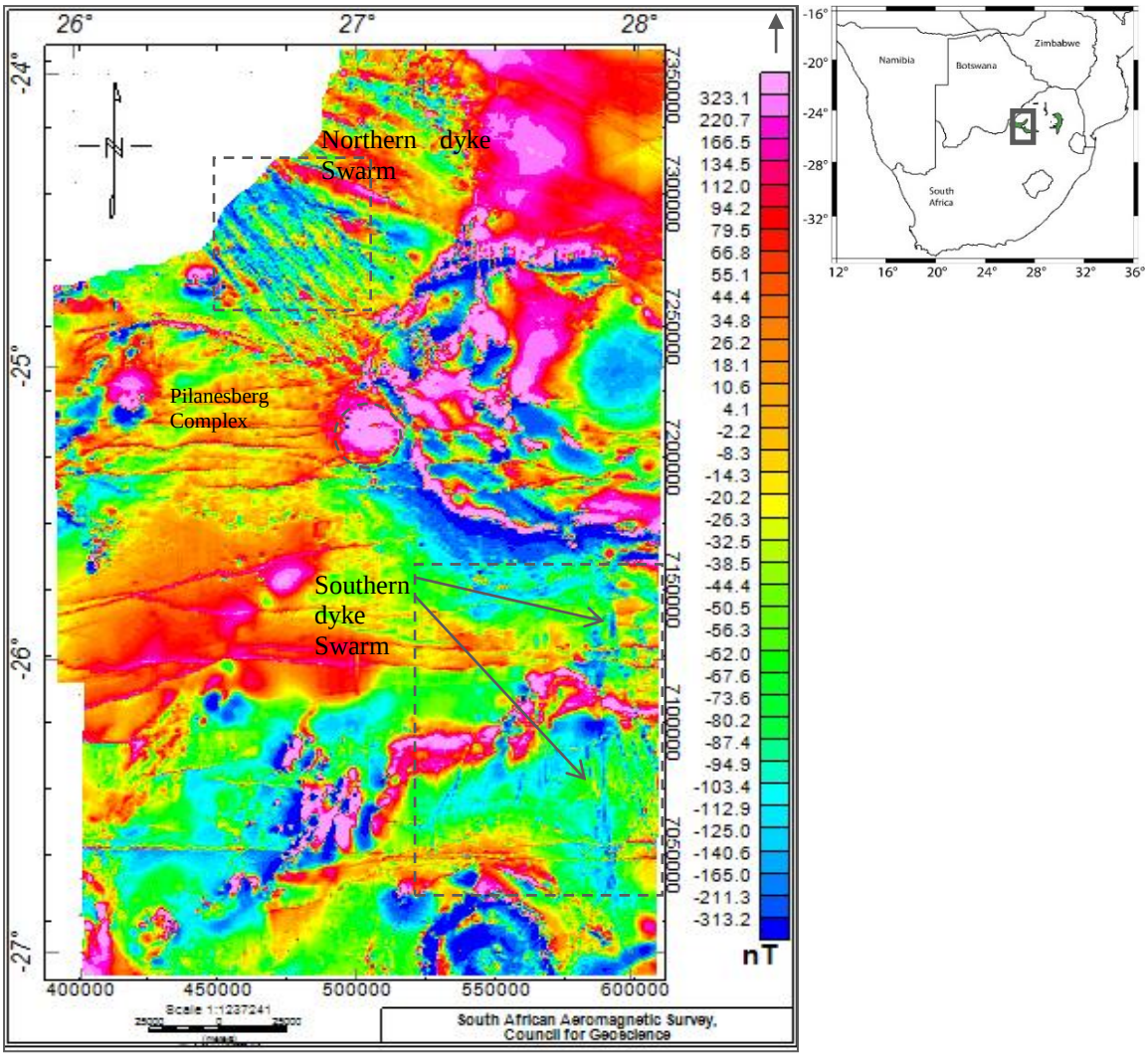

Figure 4.1 Total magnetic intensity (TMI), IGRF removed data indicating the region around the Pilanesberg Complex. The Pilanesberg Complex has a positive 325 nT signature and the Pilanesberg dykes have a negative 315 nT signature. 1:50 000 magnetic maps of South Africa 2426, 2526, 2626 (Council for Geoscience, CGS).

The Council for Geoscience national gravity grid has a negative density contrast between the Pilanesberg Complex and the Bushveld Complex granite (Figure 4.2). The density difference between the intrusions makes it possible for gravity modelling to test the shape of the Complex below the surface relationships. There is also a change in the gravity signal within the Pilanesberg Complex's ring structure that suggests there is adequate density contrast between the rings that would allow for modelling of the Complex's internal structure to be possible.

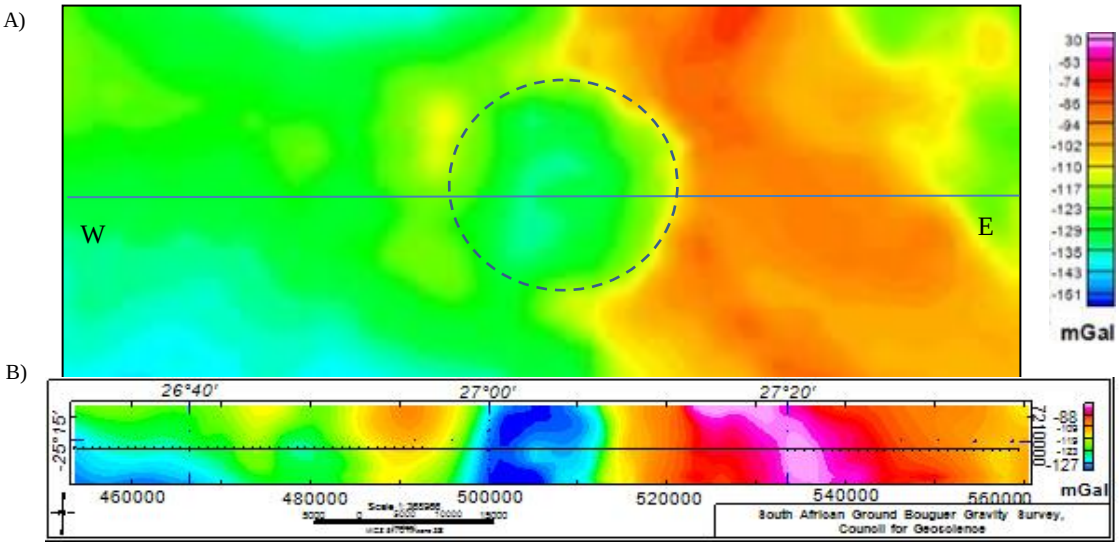

Figure 4.2 West-east Profile over a section of the Bouguer gravity map of the Pilanesberg Complex A) and the profile examined on a colour shaded gravity map where the Pilanesberg Complex (Blue) and the Bushveld Complex (Red) are well defined B).

4.2 DATA ENHANCEMENT FOR INTERPRETATION

Image processing uses geophysical filters to extract information from the data signal to assist with the interpretation process. The Fourier transform converts the data to the frequency domain where the relevant filter operation is used before the dataset is converted back to the spatial domain (Blakely, 1995). Transforming to and from the frequency domain uses the Fourier transform pair f (x, y) ⇔ F (u, v), where the 2D Fourier transform and inverse transform are:

$$F(u,v) = \int_{-\infty}^{\infty}\int_{-\infty}^{\infty} f(x,y)e^{-i2\pi(ux+vy)}dxdy, \qquad (4.1)$$

$$f(x,y) = \frac{1}{4\pi^2}\int_{-\infty}^{\infty}\int_{-\infty}^{\infty} F(u,v)e^{i2\pi(ux+vy)}dudv. \qquad (4.2)$$

Comparing the standard magnetic map (Figure 4.3 A) with the colour shaded magnetic map (Figure 4.3 B), indicates the enhanced visual 3D effect that the colour shaded map has on both the northern and

southern dyke swarms on the 2D map. The advantages of this technique are better interpretation and quality control of the data. In this case, the Pilanesberg Complex internal structure is enhanced by the image processing as the rings become clearer (Figure 4.3). A separate and younger crosscutting east-west dyke swarm appears to interact with Pilanesberg Complex as seen on the magnetic map. However, once the map has undergone processing, it is clear that the east-west dykes are crosscutting the Pilanesberg Complex (Figure 4.3 B).

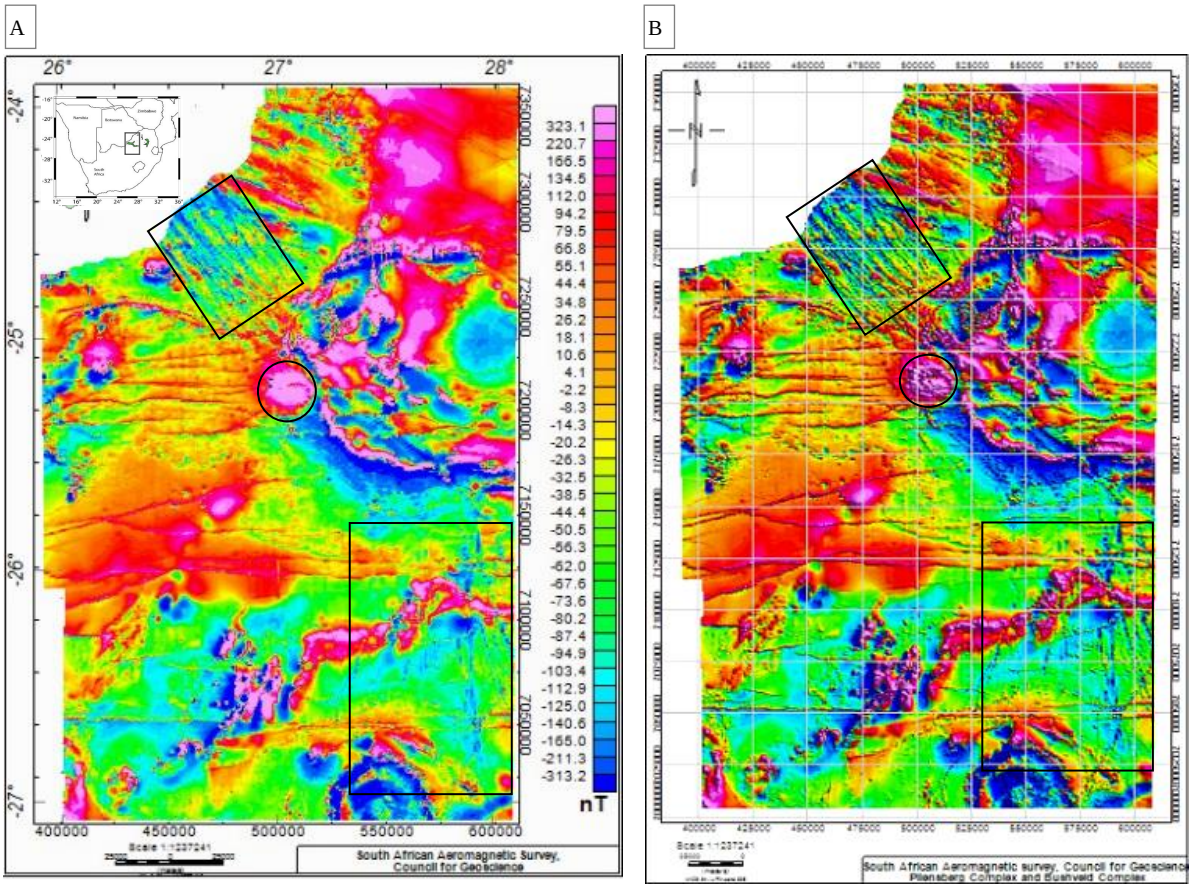

Figure 4.3 A) The TMI IGRF removed magnetic map of the Pilanesberg area (circled 323 nT anomaly) (CGS data) B) Enhanced features using normal histogram equalisation colour shading with an inclination and illumination of 45 degrees.

The further examination of the magnetic and gravity data uses the subsequent image-processing techniques in order to identify any possible internal structural features within the Pilanesberg Complex, and how the Pilanesberg Complex interacts with the host rocks and other geological features.

4.2.1 Magnetic data

4.2.1.1 Horizontal gradient of the magnetic data

The horizontal derivative is a technique used to highlight directional features along a horizontal surface. The horizontal derivative of a scalar quantity $\phi(x, y)$ along a surface is estimated from the finite difference method and scalar samples of the along the interval Δx and Δy (Blakely, 1995). If the sample measurements are ϕ_{ij}, where i = 1, 2,…, and j = 1, 2,… then at point i, j the horizontal derivative of $\phi(x, y)$ is

$$\frac{d\phi(x,y)}{dx} \approx \frac{\phi_{i+1,j}-\phi_{i-1,j}}{2\Delta x}, \quad (4.3)$$

$$\frac{d\phi(x,y)}{dy} \approx \frac{\phi_{i,j+1}-\phi_{i,j-1}}{2\Delta y}. \quad (4.4)$$

Calculating the horizontal gradient of the magnetic data (Figure 4.4) uses a 45^{o} angle along the map to amplify the north-west –south-east features. The noise in the output grid may mean the overall signal is harder to interpret than the analytic signal grid. However, the ring structure in the southern part of the Pilanesberg Complex becomes more evident with the amplified north-west- south-east features.

It is interesting to note how this method has a histogram equalisation effect on the remnant magnetisation signal where it smoothes the remnant magnetisation of a feature such that direction can no longer be obtained. It does give a good idea of whether an anomaly carries remnant magnetisation or not, and how strong the signature is (Blakely, 1995). Comparing the Bushveld Complex and the Pilanesberg Complex, which both carry strong remnant magnetisation, indicates a blue negative signal either side of the anomaly, indicating remnant magnetisation. This signal is also be seen on the northern Pilanesberg dyke swarm, which has a small amount of remnant magnetisation. In contrast, the east-west dyke swarm carries no remnant magnetisation, observed in the minimal/absence of the negative blue colouring. The horizontal gradient has positively identified the southern edge of the Pilanesberg Complex, which was not indicated very well on the TMI magnetic data.

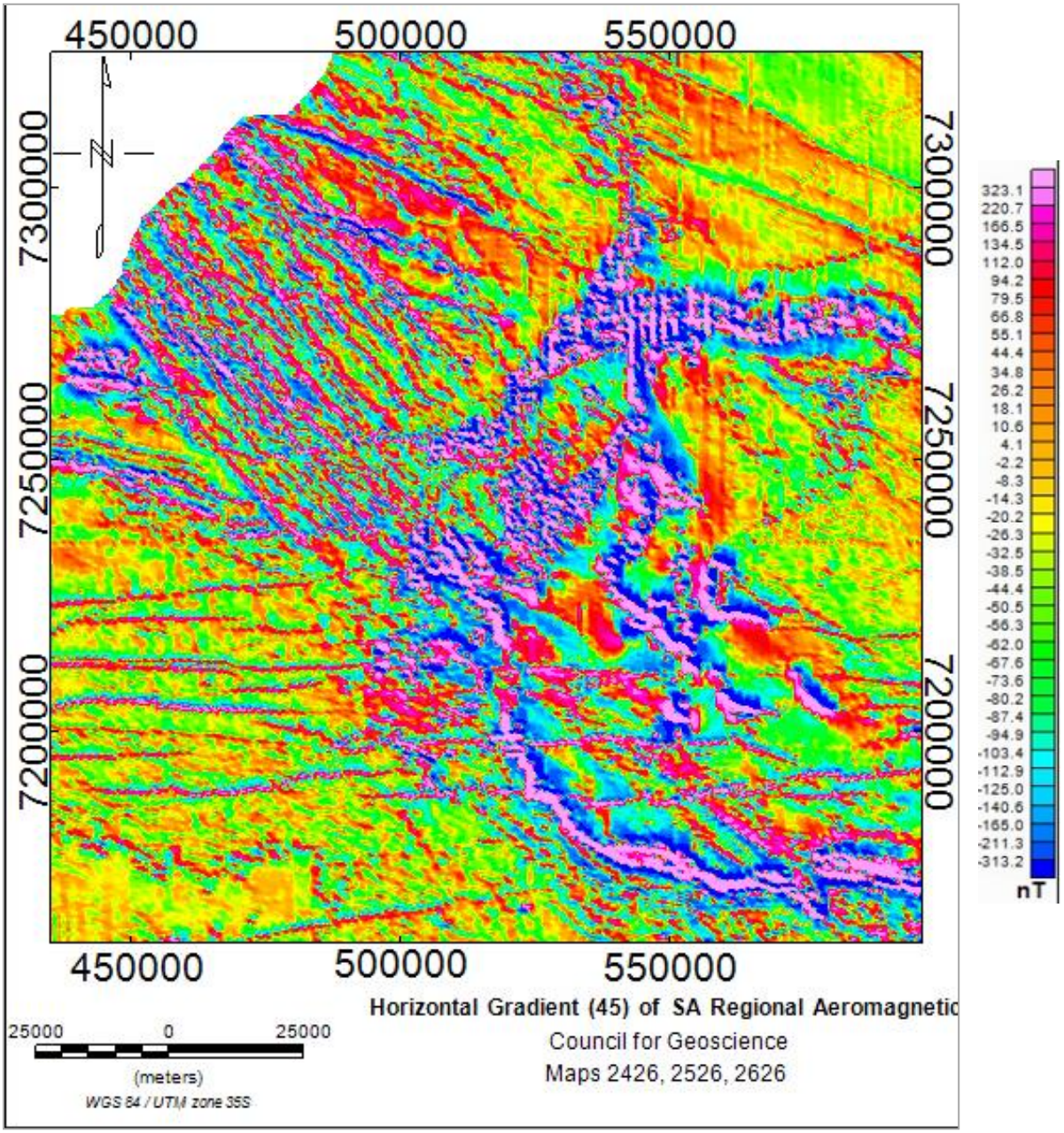

Figure 4.4 Horizontal gradient of the aeromagnetic map, amplifying NW-SE features. Features that carry remnant magnetisation have a blue negative while non-remnant features display a positive red peak only.

4.2.1.2 Vertical derivative

The vertical derivative is a data rotation of the horizontal derivative with an unchanged frequency content using a Hilbert transform applied in the frequency domain (Blakely, 1996).

The vertical derivative (Figure 4.5) indicates the outline of the Pilanesberg Complex and highlights the far southern edge of the Complex, which the horizontal derivative does not define. This is also the first processing method that has indicated the centre of the Complex with a strong signal. As the south of the Pilanesberg Complex appears to have a weaker signal compared to the north, it implies that the bedrock in the north is closer to the surface. This may assist in determining the overall dip of the Complex, as it may have intruded at an angle instead of vertically.

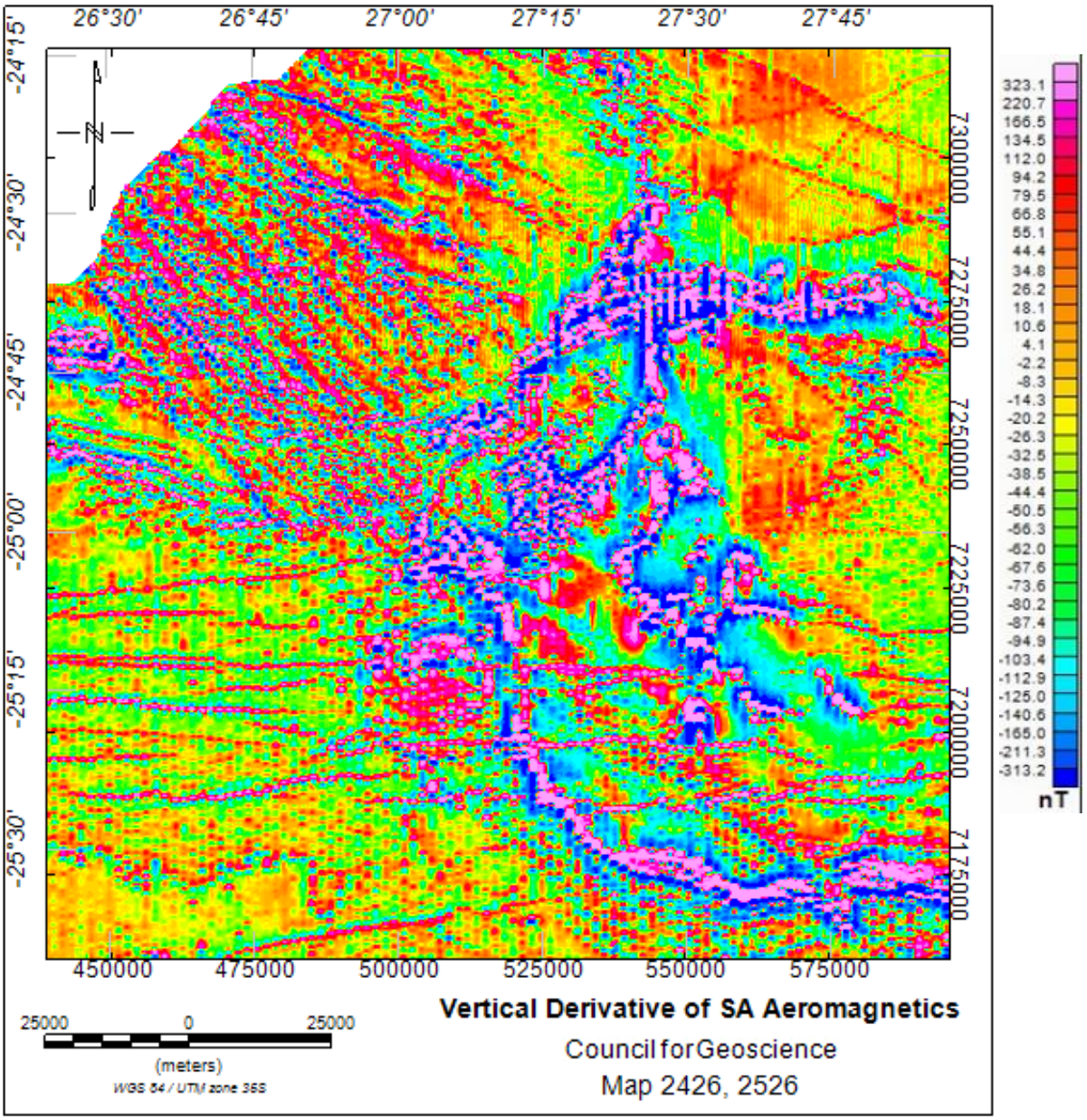

Figure 4.5 The image processed vertical derivative of the aeromagnetic map.

4.2.1.3 Analytic signal method

Analytic signal is a tool to estimate a sources depth and position. It is dependent on a bodies position but not the magnetisation direction. The analytic signal is achieved by merging a magnetic anomalies vertical and horizontal gradient (Blakely, 1995).

Additional image processing on the magnetic data is used to identify primary features, and the internal ring structure, which facilitates testing of the forward and inverse modelling. The analytic signal of the magnetic dataset combines the calculation of the horizontal and the vertical gradients of the magnetic signal (Blakely, 1995) to create the map in Figure 4.6. Identifying a bodies location becomes possible with analytic signal processing as the remnant magnetisation effect is removed as the phase shifts by $\pi/2$ to produce a positive signal with the same amplitude as the original data over the body of interest.

The analytic signal processing method amplifies the noise as seen in Figure 4.6, where the north-south flight lines become evident as 'strings of pearls' on the west-east dykes. However, the edges of the Bushveld Complex are well delineated, as are the west-east dykes that cut through the south of the western Bushveld limb. This could be significant for mining in those areas as the dykes constitute a loss of minable ground. The analytic signal can delineate some of the Pilanesberg Complex ring structures within the magnetic signature. There is a strong outer ring to the north of the Complex as well as internal rings that appear to be cross cut by the 'pearl strings looking' east-west dykes.

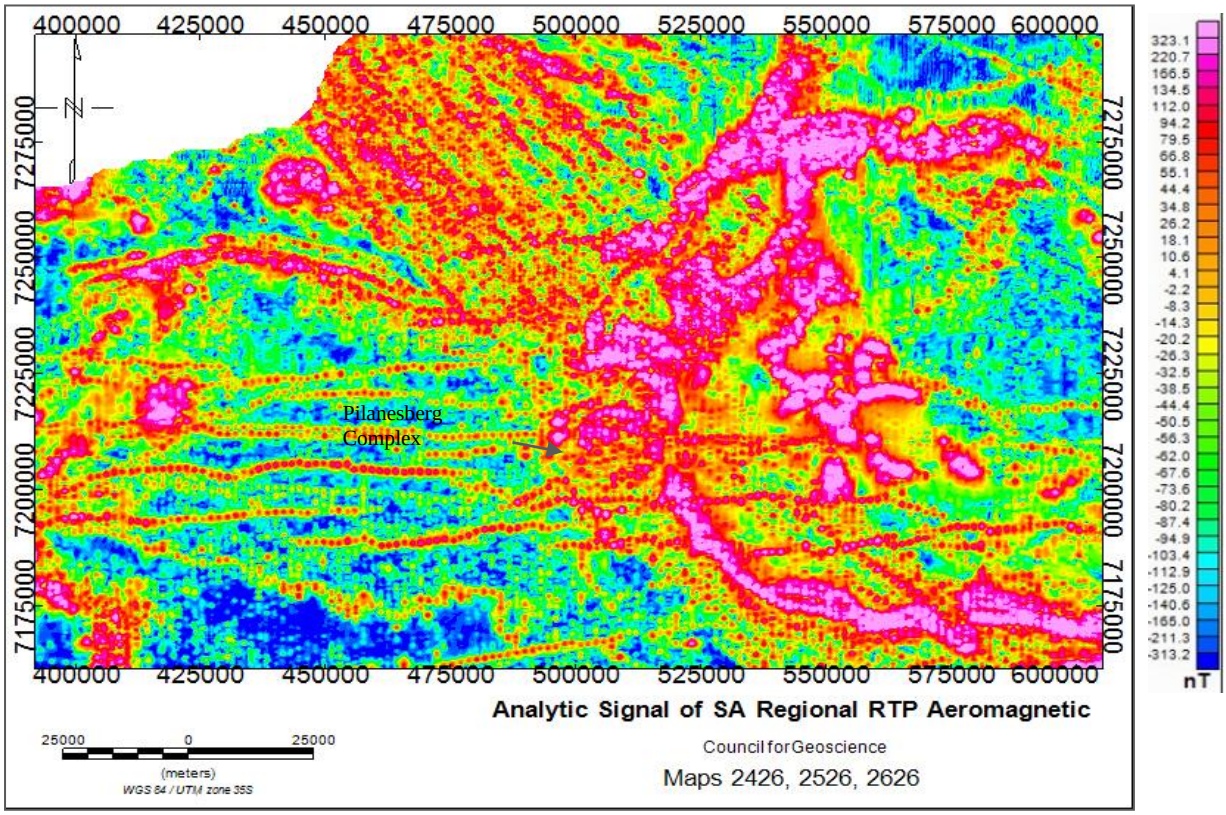

Figure 4.6 The analytic signal image processed data of the 'reduced to pole' magnetic data displays all the data with a positive signal. This method indicates the internal structure of the Complex as well as crosscutting dykes. The Bushveld Complex displays a strong positive signal, over the Bushveld Complex Upper Zone.

4.2.1.4 Sun-Shading

To suppress or enhance lineaments, a method called 'sun-shading' is applied to the data. A data map has 2D features referring to the positive and negative amplitudes. The sun is set at a certain height and azimuth will result in a reflectance R, which highlights the edges of the perpendicular features, and suppressed the parallel features (Pelton, 1987). When the sun has an inclination θ from the vertical, and azimuth φ, then the reflectance at each point is:

$$R = \frac{1+P.P_0+QQ_0}{\sqrt{1+P^2+Q^2}+\sqrt{1+P_0{}^2+Q_0{}^2}}, \qquad (4.5)$$

where P and Q are the horizontal gradients and P_o = -cosφtanθ and Q_o= -sinφtanθ.

The sun-shaded relief map for the Pilanesberg Complex (Figure 4.8) amplifies the north-west, south-east features. There appears to be a faint signature of a dyke extending through the middle of the Pilanesberg Complex that resembles the signature of the dykes of the northern dyke swarm. The crosscutting relationship confirms that the dyke swarms are younger than the Complex. One dyke, in particular, appears to be continuous through the Complex, which would mean that the dyke intruded after the Vlakfontein fault that cuts through the Complex. Humphrey (1914) stated that the dykes did not cut through the Pilanesberg Complex while Shand (1928) suggested that the dykes merely cut the outer red syenite ring. While this may be plausible with most of the dykes, the sun-shaded map indicates that at least two dykes did cut through the centre of the Complex.

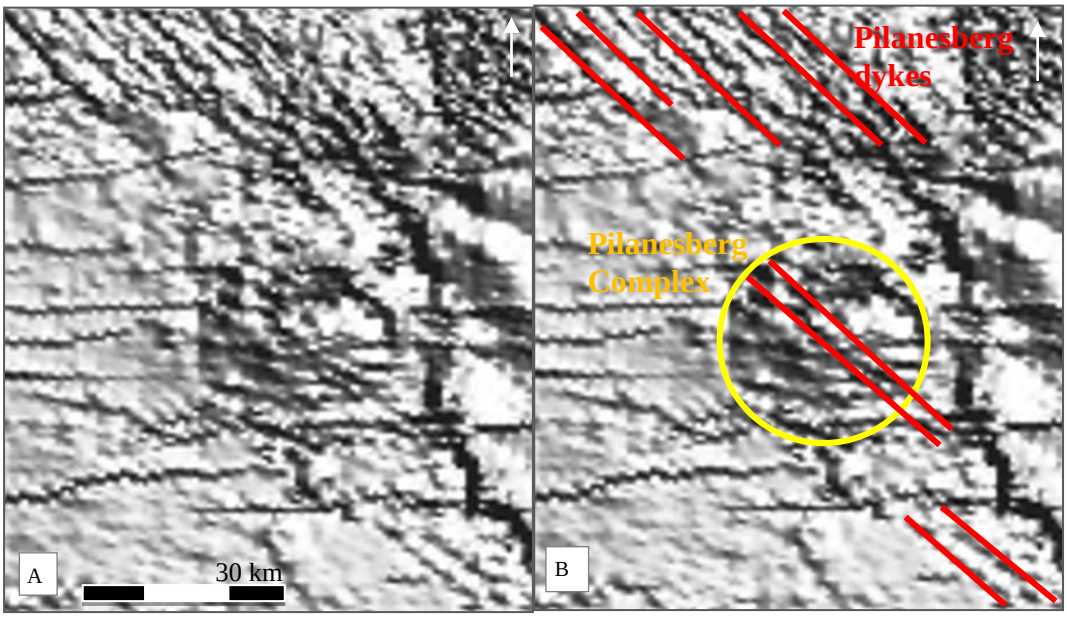

Figure 4.7 A) Shaded relief of the Pilanesberg Complex indicating a north-west, south-east linear trend. B) The interpreted sun shaded map with the Pilanesberg dyke cutting the Complex. C) Shown below- includes the entire Pilanesberg Complex area for an overview of the sun shading.

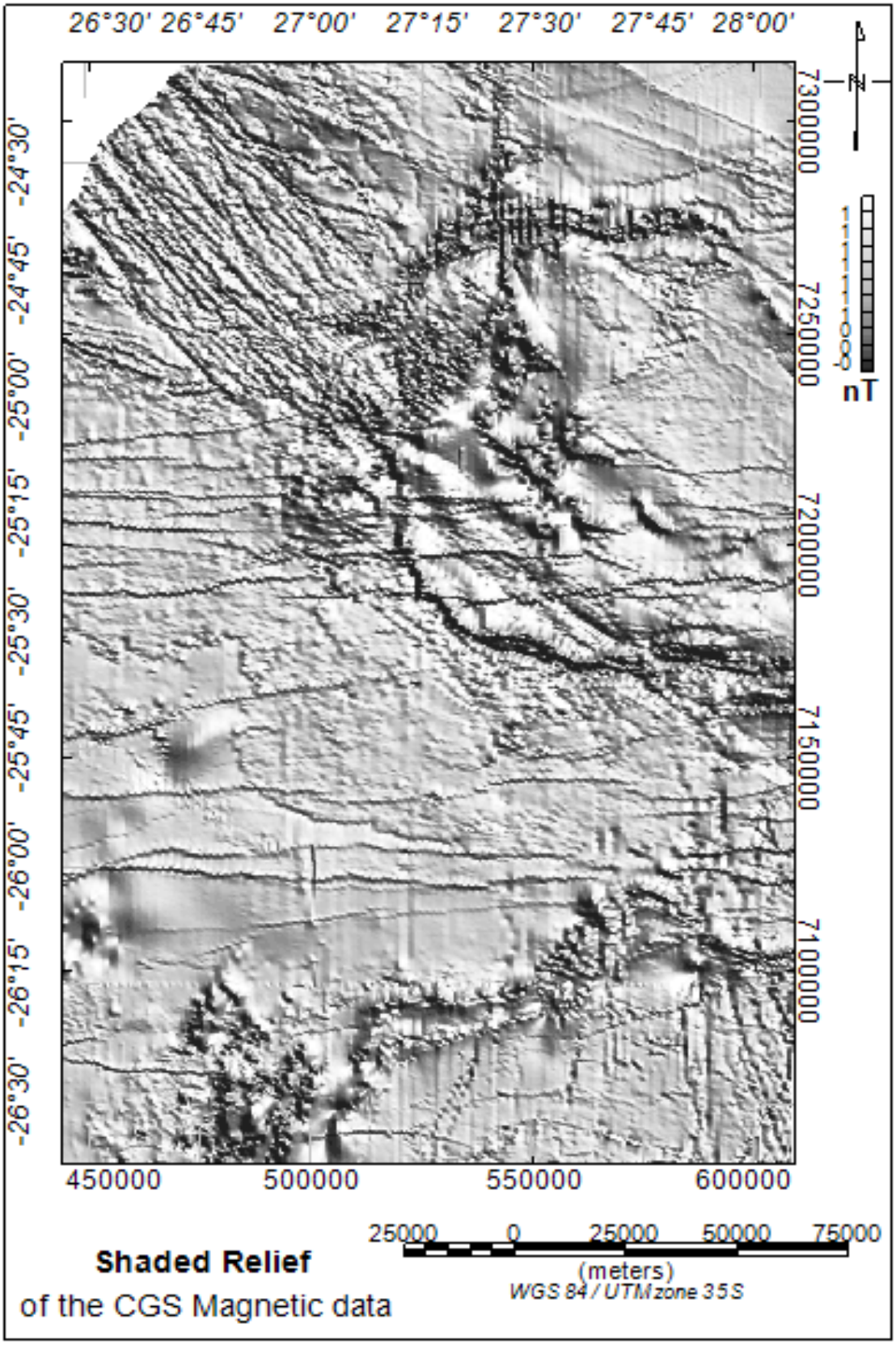

Figure 4.8 C) Shaded Relief of the CGS Aeromagnetic data.

4.2.1.5 Magnetic data Euler deconvolution

Euler deconvolution technique estimates depth and location information of magnetic and gravity datasets (Cooper, 2004). The Euler deconvolution will use the physical property contrast to constrain the 2D profile models across the Pilanesberg Complex in this thesis. The general Euler deconvolution is

$$\frac{\partial f}{\partial x}(x - x_0) + \frac{\partial f}{\partial z}(z - z_0) = -SI.f \ , \qquad (4.6)$$

Where the homogenous field anomaly f has a source depth and location (x0, z0) while it is measure at (x, z) (Thomson, 1982).

The application is useful along long profiles, as it calculates simple sources associated with gravity and magnetic anomalies. A single estimate of source location can be determined for a simple body over a windowed profile. The windowed density or magnetisation contrasts tend to cluster at geological intersections (Blakely, 1996).

A north-south profile of the Pilanesberg Complex (Figure 4.9) compares the Reduction to the Pole (RTP), and magnetic susceptibility data with results from the distance to contact (discussed in the next section). The distance to the contact overlain by the Euler deconvolution solution indicates a positive correlation. Some of the areas, which do not correlate, are due to the complexity of the Pilanesberg Complex's geometry and the quality of the data.

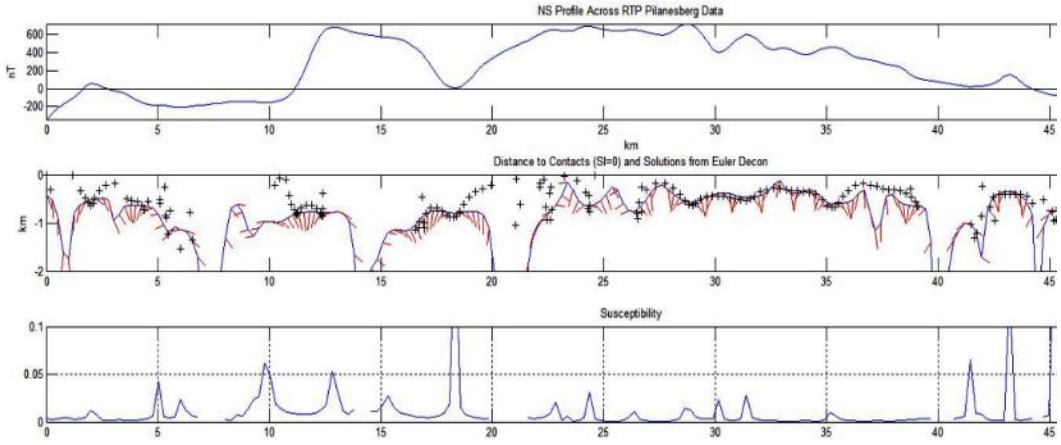

Figure 4.9 NS Pilanesberg Complex profile that compares the distance to the contact with the Euler Deconvolution and the RTP and Susceptibility data.

In the EW profile through the Complex, the Euler solution correlates even better than that achieved in the NS profile Figure 4.10. The near-zero susceptibility data correlates with large dips in the distance to the contacts, which is where the Euler solution should be used in correlation with the RTP data.

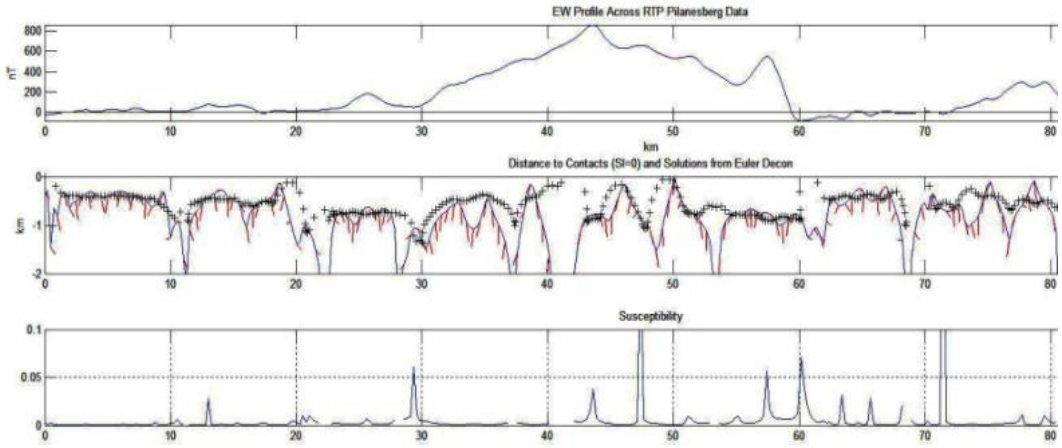

Figure 4.10 EW profile comparing Copper (2013) distance to contact depth with the Euler deconvolution, RTP, and susceptibility data.

4.2.2 Gravity Data

4.2.2.1 Automatic gain control

The automatic gain control is a noisy method of analysing the gravity data. However, it provides a simplified schematic view of the geology. The Pilanesberg Complex internal ring signal shows two rings (Figure 4.11). The Bushveld Complex mineralisation localities become evident along the mineralisation ridge of the high positive value of 77 mGal.

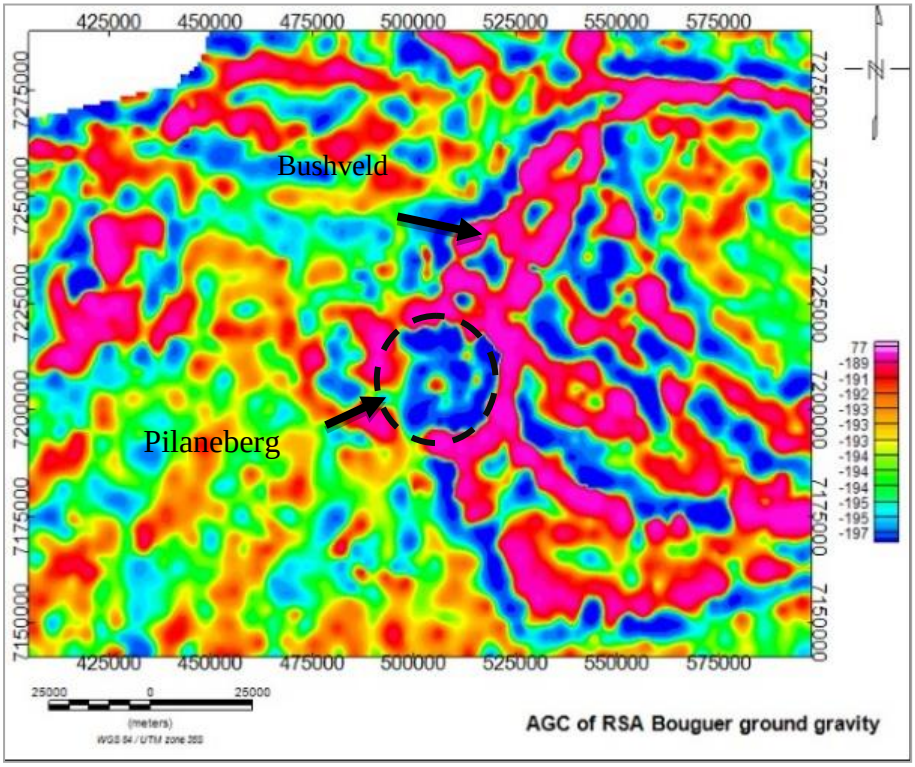

Figure 4.11 The automatic gain control of CGS Bouguer gravity data with amplified noise levels over the map. When examining the Pilanesberg Complex, this method indicates two prominent ring structures within the Complex seen as an inner ring around a central plug and an outer ring. The two rings are identifiable density changes within the Pilanesberg Complex.

4.2.2.2 *Contact depth imaging*

The Cooper (2014) contact depth dip method (Figure 4.13), determines the depth, location, and dip of contacts from the gravity data by using the ratio of the vertical to the horizontal gradient of the data. The estimated dip of the contact is comparable to the tilt depth calculation, without the distance between the contour lines. The parameters of the contacts are calculated with the noise sensitive second and third-order magnetic field derivatives. In comparison, the contact depth method (Figure 4.12) is less susceptible to interference of anomalies from nearby sources, as it uses second and third order derivatives as opposed to the Tilt-depth, which uses the first derivative.

The comparison of the contact depth dip method (Figure 4.13) with the contact depth method (Figure 4.12) and the RTP Tilt angle contours (Figure 4.14), confirms that the results are in agreement and that the contact depth dip is a suitable method to identify contact depths and dips. Equations for this method can be found in Cooper (2014).

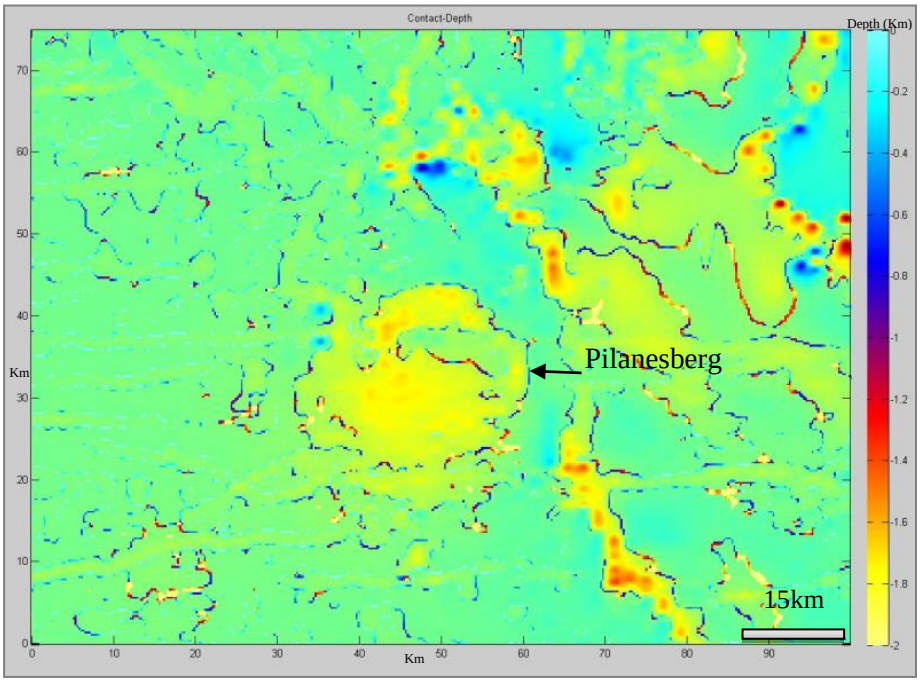

Figure 4.12 Contact depth over the Pilanesberg Complex. A shallower depth is identifiable in the north while the depth deepens in the south.

Coopers (2014) contact depth dip method displays a depth of between 90-100 in the north and becoming deeper in the south changing to range between 100 and 130. The southern edge of the Pilanesberg Complex indicates some of the shallow overburden as the signal is between 40 and 70 (Figure 4.13).

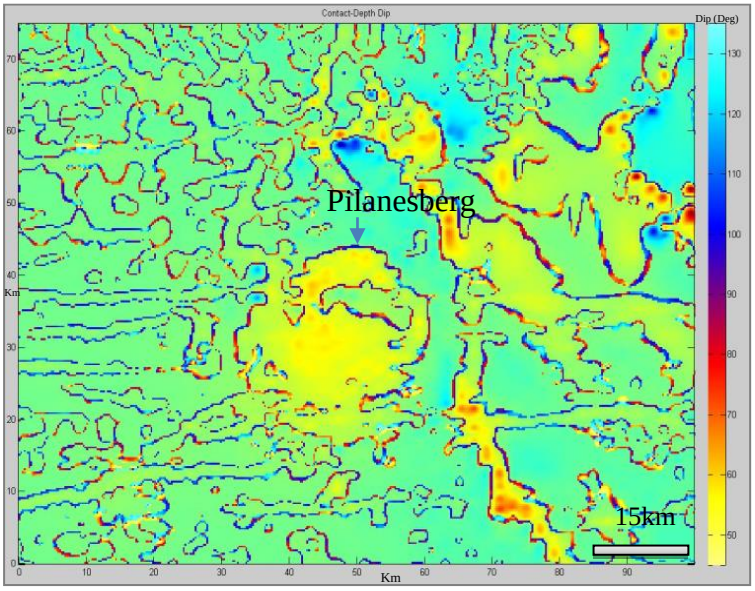

Figure 4.13 Coopers (2014) contact depth dip method can identify that the south of the Pilanesberg Complex is deeper than that seen in the north.

In Figure 4.14, the tilt angle contours are closer together in the north, indicating a shallow contact. The arrows between the contours in the south indicate that there are significant gaps between the contours, indicative of a deeper contact. These results correlate with the Coopers (2014) contact depth method in Figure 4.14, which indicates shallow depths in the north by a blue and purple colour, while deep contacts are seen as red and yellow, at the southern contact of the Pilanesberg Complex.

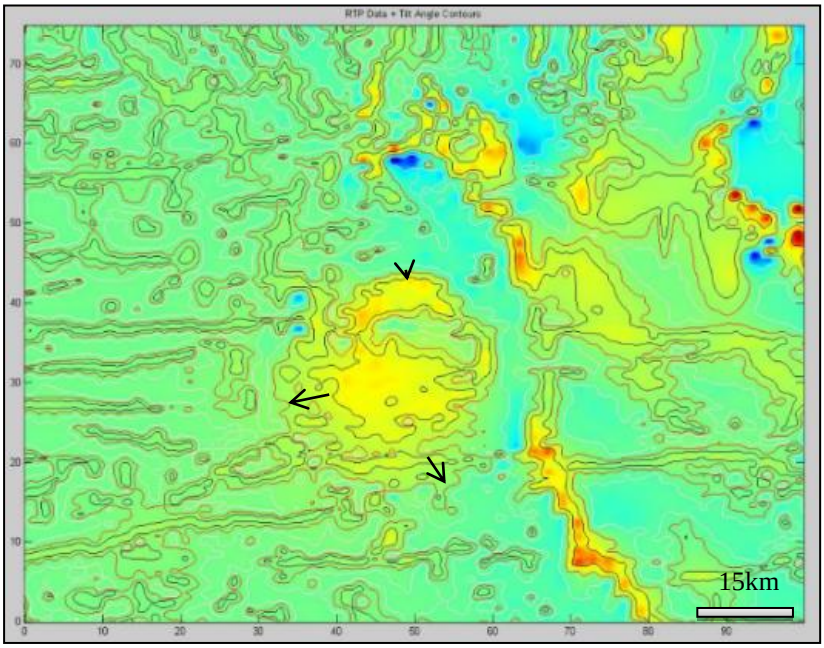

Figure 4.14 The tilt angle contours are able to confirm that the north of the Complex is shallower with contours closer together and further apart in the deeper south of the Complex.

4.2.2.3 Euler deconvolution

Five west-east and north-south profiles are extracted from the Pilanesberg Complex gravity and magnetic grids in Figure 4.15 and will be modelled in the next chapter. Euler deconvolution is a useful pre-modelling technique to gain depth and dip estimates from the physical property contrasts.

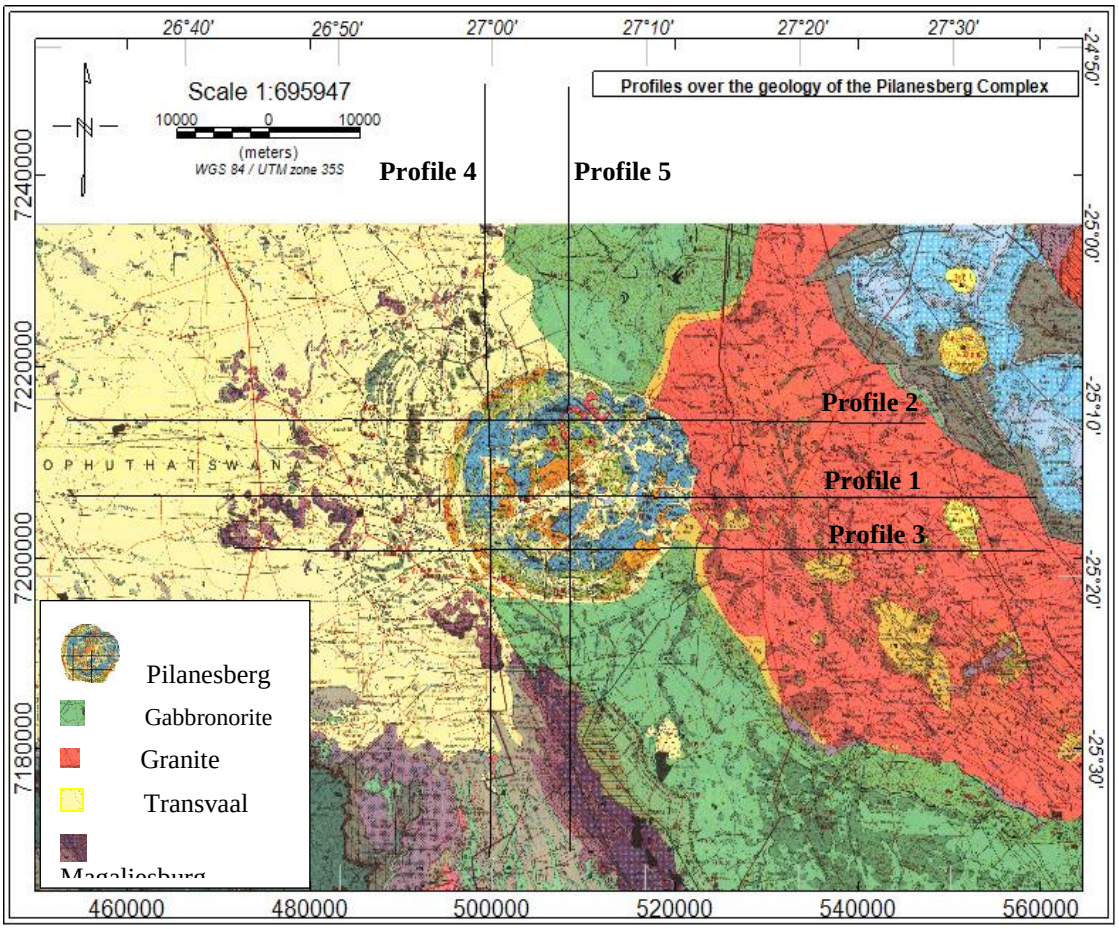

Figure 4.15 WE profile 1-3 and NS profiles 4 and 5 across the Pilanesberg Complex geology used for 2D modelling. Lithologies include Transvaal Supergroup (yellow), Pilanesberg Complex (Blue), Bushveld Gabbro (Green) and granite (red) as well as Magaliesburg quartzite (purple).

Profile 1, oriented west-east, uses the gravity data over the Pilanesberg Complex to calculate the horizontal and vertical gradients so that the windowed Euler Deconvolution points are ascertained (Figure 4.16). The estimated physical contrast points correlate well with the geology map, as the profile moves east from the Transvaal Supergroup, containing displaced Magaliesberg and Bushveld material, then through the Pilanesberg Complex gravity low and on to the gravity high associated with the Bushveld gabbro and finally through the Bushveld granite. The Euler solutions for each profile display a large variation of results dependant on the different structural indices. This is perticularly usefull for identifying the depth of a contact.

The different points per contact represent the range of structural indices used for that contact. A range structural indices are used from 1 to 3 increasing in 0.5 intervals with a window size of 11.

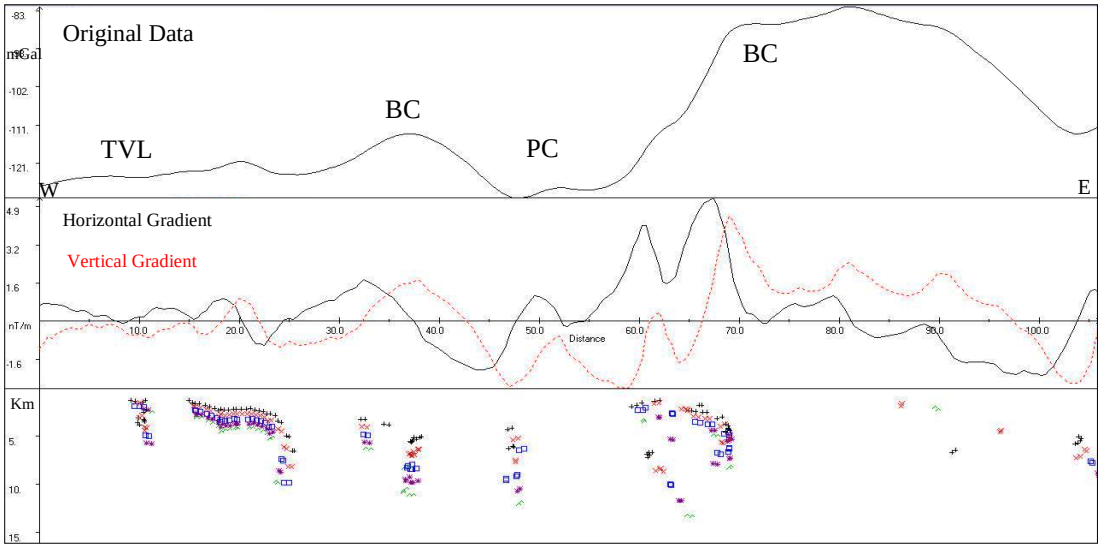

Figure 4.16 The Euler deconvolution solutions are in the bottom diagram with the Bouguer gravity west-east orientated profile 1 in the top diagram.

Profile 2 (Figure 4.17) is situated to the north of profile 1. The profile indicates an inward dipping structure associated with the gravity low of the Pilanesberg Complex. This profile also indicates a horizontal feature across the Pilanesberg Complex at approximately 5km depth. With a lack of seismic data in the area, it is hard to clarify the source of the horizontal Euler solutions within the Pilanesberg Complex. Possible explanations may be that the Pilanesberg Complex has Bushveld or Transvaal material beneath it or, more probably, it is an internal density change, which is indicative of the Pilanesberg Complex internal structure.

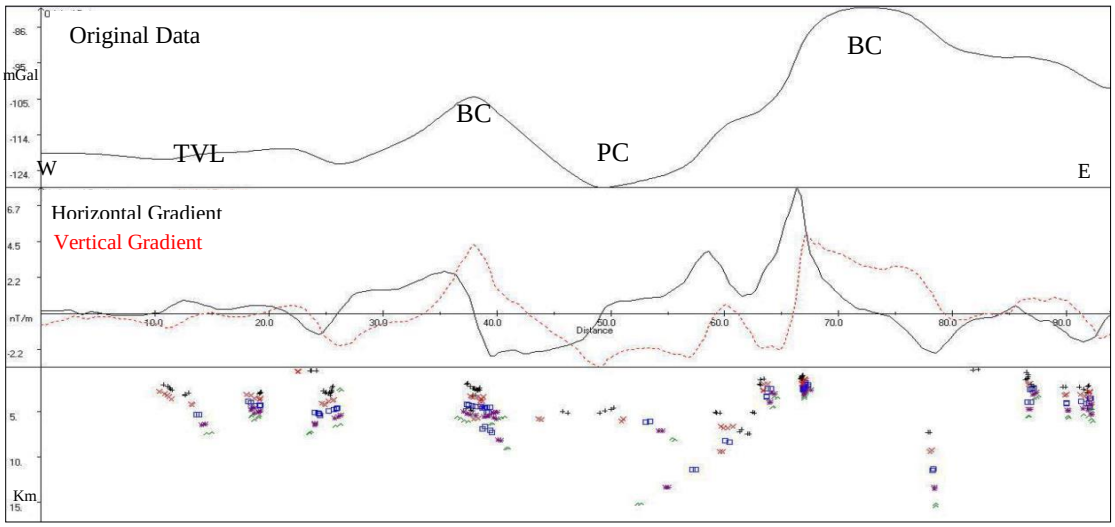

Figure 4.17 Euler deconvolution of the Bouguer gravity west-east orientated profile 2. The Pilanesberg Complex area indicates an inward dipping cone with the internal structure at ~ 5km and a maximum depth point calculated between 10 and 15 km.

Profile 3 (Figure 4.18) is the southern most profile and indicates an eastward dipping contact with the Bushveld gabbro on the east side of the Pilanesberg Complex, which is also dipping to the east.

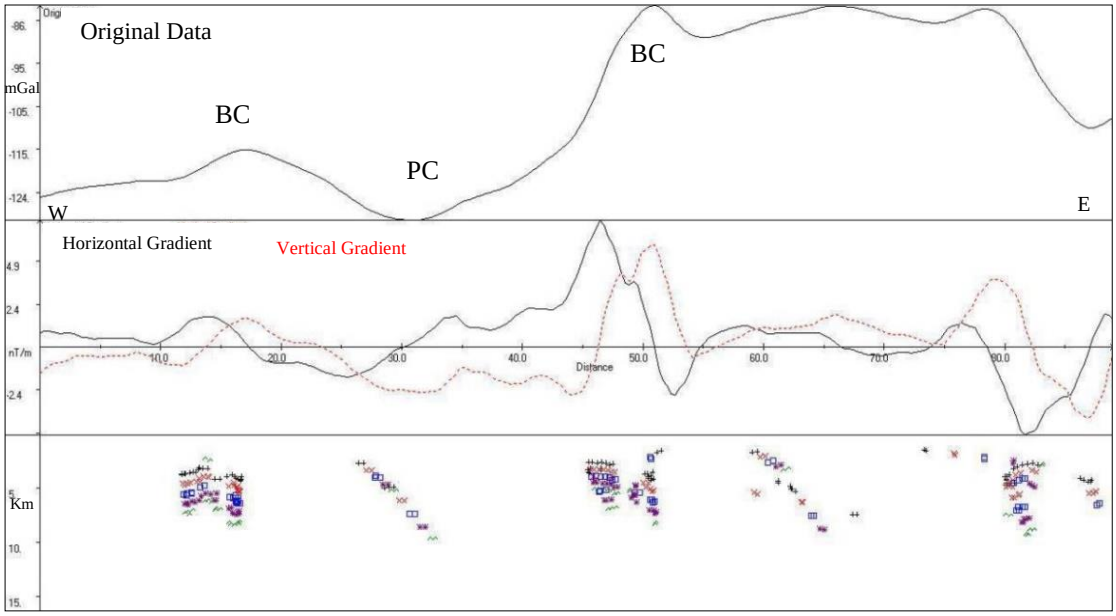

Figure 4.18 Euler deconvolution of the Bouguer gravity west-east orientated profile 3

The physical property contrast for the north-south profiles is not as defined as those seen in the previous west-east profiles. The north-south profiles have complicated solutions and display the complexity of faulting within the Pilanesberg Complex. Profile 4 (Figure 4.19) suggests that the Pilanesberg Complex is a vertical cylinder close to the surface, and begins to dip slightly outward below 5 km depth.

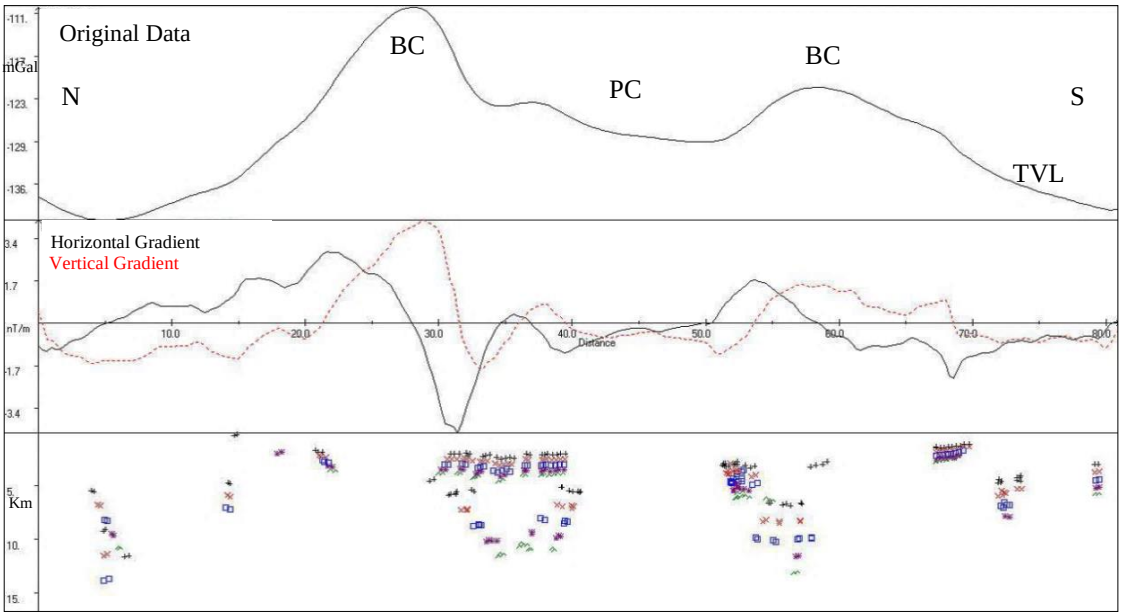

Figure 4.19 Euler deconvolution of the Bouguer gravity north-south orientated profile 4

The second north-south profile (Figure 4.20), profile 5, implies that the Pilanesberg Complex is dipping to the north. However, the profile also indicates complex solutions are making it difficult to determine true dips and contact dip directions. The north-south profiles are difficult to conceptualise for modelling the 2D models, as these profiles are parallel to the Bushveld Complex strike direction, and as such, the profiles are examining 3D structures. Thus, Euler solutions for the north-south profiles are at best a preliminary indication of the contrast density contacts and structural complexity.

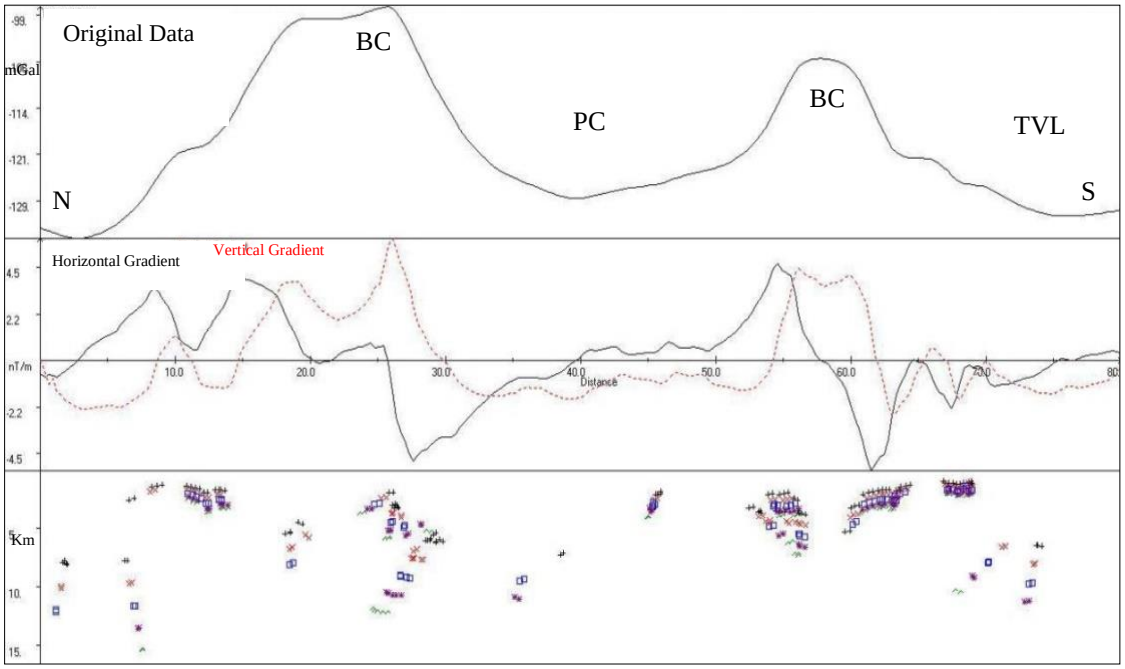

Figure 4.20 Euler deconvolution of the Bouguer gravity north-south orientated profile 5.

The Euler deconvolution profiles have hinted at the dip orientation of the Pilanesberg Complex at depth and correlated the existence of Magaliesburg and Bushveld material in the Transvaal sedimentary succession to the west of the Pilanesberg Complex, which was displaced during the Pilanesberg Complex emplacement. It is also clear that the Bushveld gabbro forms part of the Pilanesberg Complex eastern border as a buried unit below the Bushveld granite, seen on the geology map in Figure 4.15.

4.3 IMAGE PROCESSING INTERPRETATATION

A comparison of all the processed images looks at all the comparable features within and around the Pilanesberg Complex (Figure 4.21). The west-east dykes cut through the north and south of the Complex in all the images (Figure 4.21 A-F) while the sun-shaded image (B) indicates dyke like features cutting across the Pilanesberg Complex from north-west to south-east. The analytic signal and the ternary map (Figure 4.21 E and F) indicate that there are at least two internal rings within the Complex with the outer ring is clearly defined and the internal ring is close to the central ring structure.

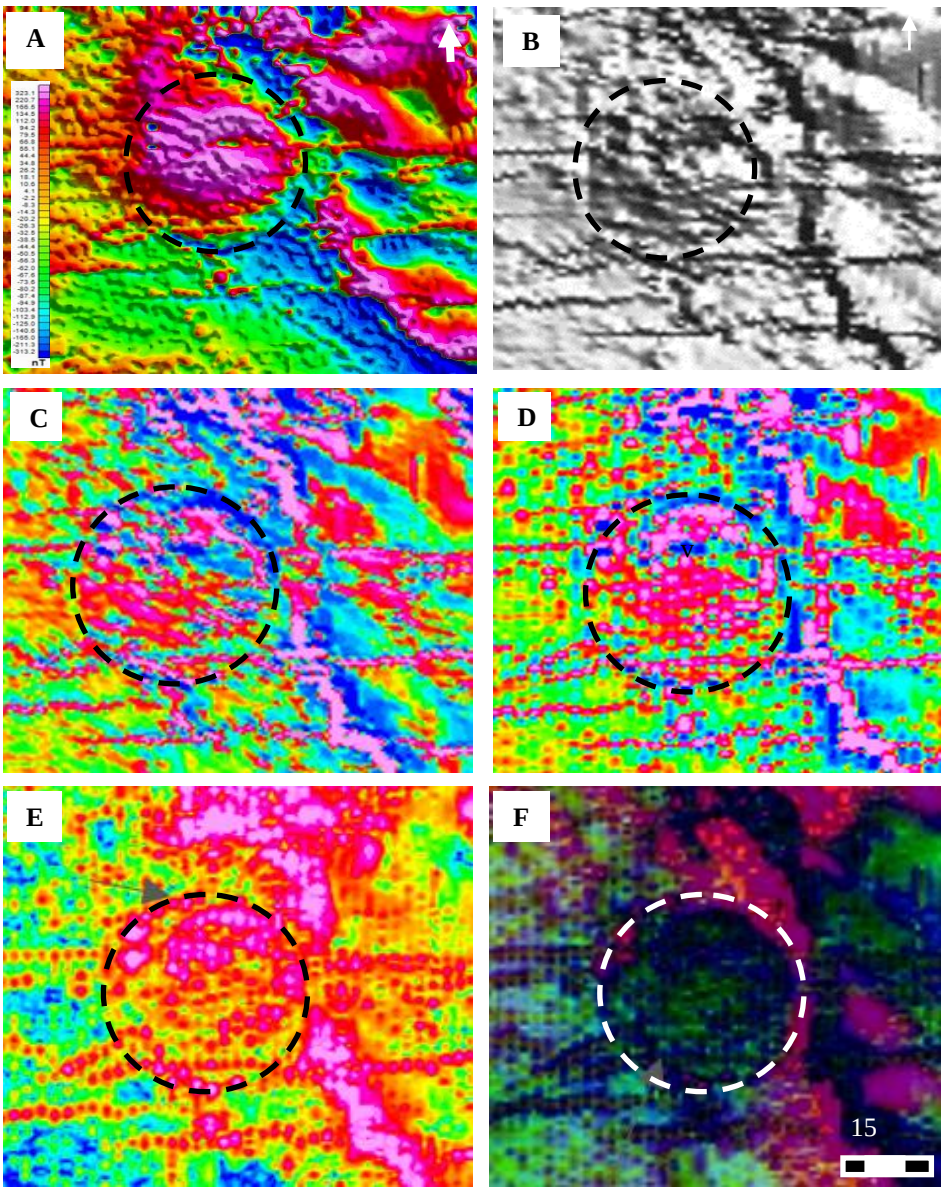

Figure 4.21 Image processed Pilanesberg Complex compared with A) Colour enhanced B) Sun-shaded C) Vertical derivative, D) horizontal derivative, E) analytical signal and F) is a ternary diagram which combines the 1st vertical derivative, analytic signal and tilt map.

The Shuttle Radar Topography Mission, SRTM, elevation data uses C-band Space borne Imaging Radar and the X-Band Synthetic Aperture Radar that NASA flew in 1994 which were sampled at 3 arc-seconds applying a resampling technique using the nearest neighbour method (Rodriguez et al., 2005). The elevation data (Figure 4.22) provides information on the surface shape of the Complex, which correlate with the gravity, magnetic and geology maps to confine the surface structures in the modelling of the Pilanesberg Complex. The elevation data indicates the split between the northern block and the southern block that are separated by the Vlakfontein fault.

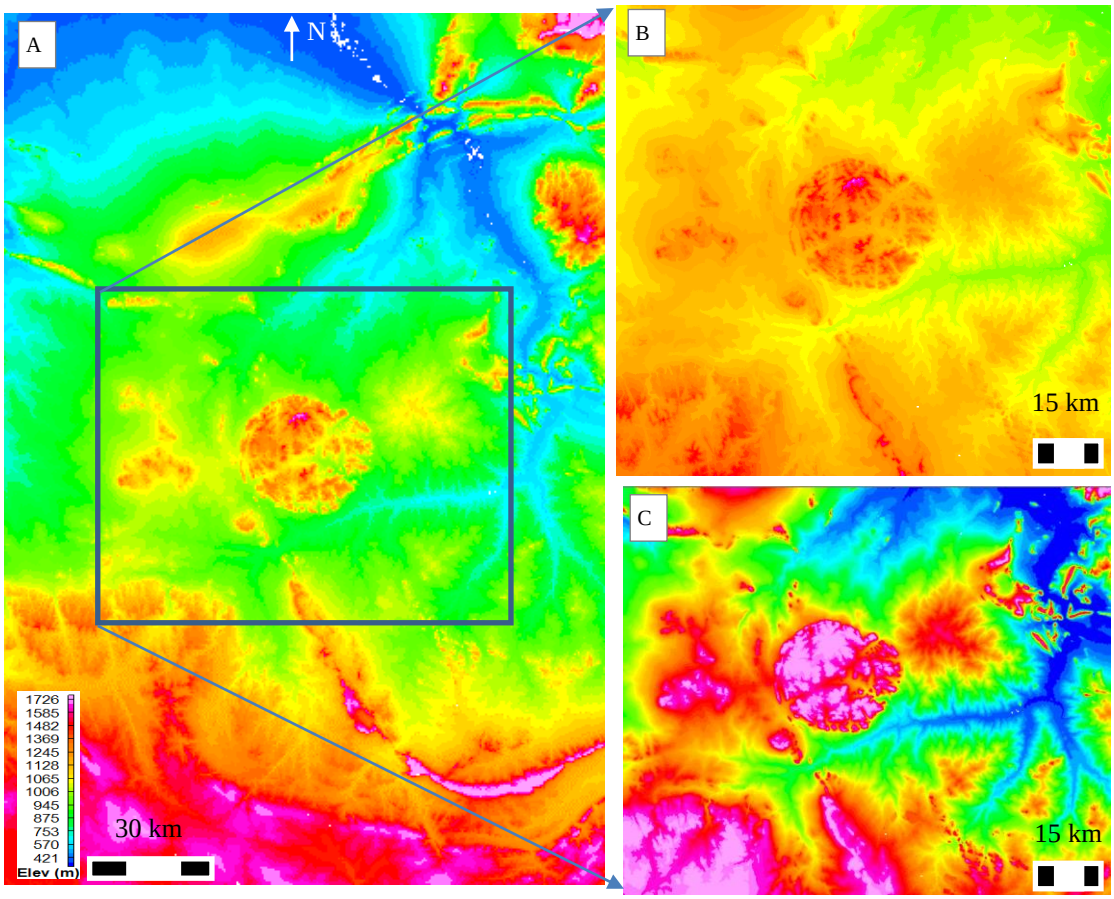

Figure 4.22 SRTM terrain map over the Pilanesberg area, B) close up of the Pilanesberg Complex. C) The grid has undergone auto recolour enhancement which recolours a viewed area of a grid with the entire colour palette to provide an even colour scale across the map to indicate the internal structure of the Complex related to the elevation.

The Landsat 7 and 8 combined USGS image highlights the structure of the Pilanesberg Complex so that ring structure can be seen in conjunction with the elevated rocks. The Landsat 7 This image highlights the faults and displacements, which indicates that the once circular intrusion has undergone block movement. The potential blocks are emphasised on the image between the schematically drawn fault lines (Figure 4.23).

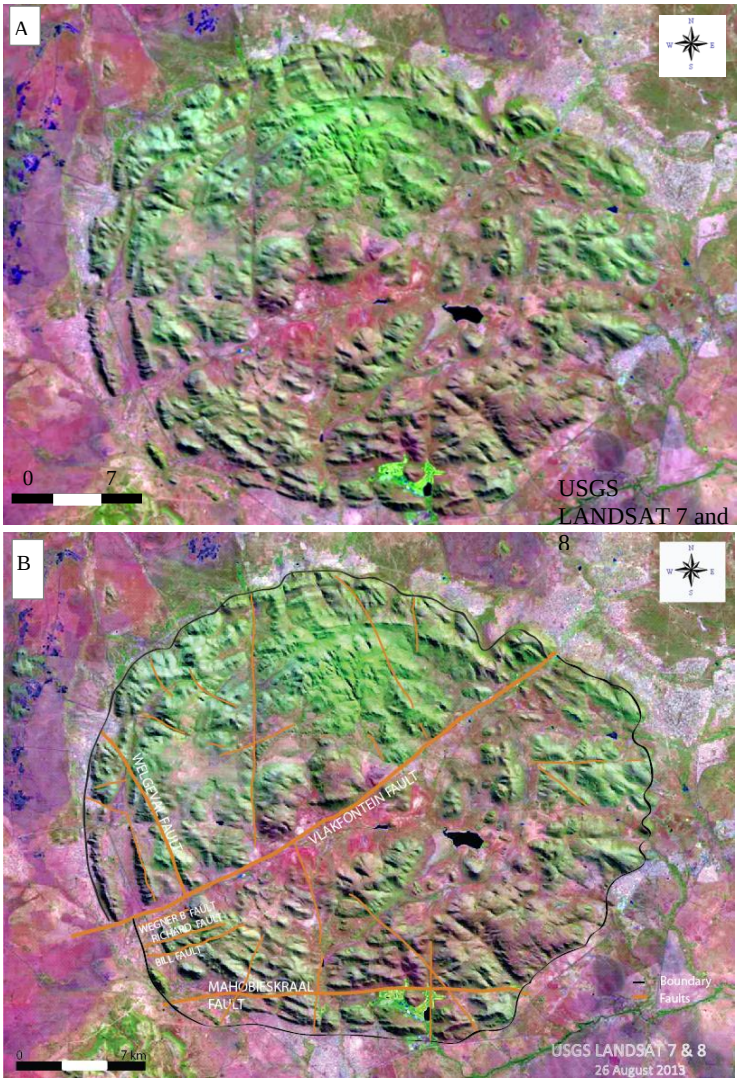

C

	L7	L8
Scenes/Day	~450	~650
SSR Size	378 Gbits, block-based	3.14 Terabit, file-based
Sensor Type	ETM+, Whisk-Broom	Pushbroom (both OLI and TIRS)
Compression	No	~2:1 Variable Rice Compression
Image D/L	X-Band GXA×3	X-Band Earth Coverage
Data Rate	150 Mbits/sec × 3 Channels/Frequencies	384 Mbits/sec, CCSDS Virtual Channels
Encoding	not fully CCSDS compliant	CCSDS, LDPC FEC
Ranging	S-Band 2-Way Doppler	GPS
Orbit	705 Km Sun-Sync 98.2° inclination (WRS2)	705 Km Sun-Sync 98.2° inclination (WRS2)
Crossing Time	~ 10:00 AM	~ 10:11 AM

Landsat-7 ETM+ Bands (µm)			Landsat-8 OLI and *TIRS* Bands (µm)		
			30 m Coastal/Aerosol	0.435 - 0.451	Band 1
Band 1	30 m Blue	0.441 - 0.514	30 m Blue	0.452 - 0.512	Band 2
Band 2	30 m Green	0.519 - 0.601	30 m Green	0.533 - 0.590	Band 3
Band 3	30 m Red	0.631 - 0.692	30 m Red	0.636 - 0.673	Band 4
Band 4	30 m NIR	0.772 - 0.898	30 m NIR	0.851 - 0.879	Band 5
Band 5	30 m SWIR-1	1.547 - 1.749	30 m SWIR-1	1.566 - 1.651	Band 6
Band 6	60 m TIR	10.31 - 12.36	*100 m TIR-1*	*10.60 – 11.19*	Band 10
			100 m TIR-2	*11.50 – 12.51*	Band 11
Band 7	30 m SWIR-2	2.064 - 2.345	30 m SWIR-2	2.107 - 2.294	Band 7
Band 8	15 m Pan	0.515 - 0.896	15 m Pan	0.503 - 0.676	Band 8
			30 m Cirrus	1.363 - 1.384	Band 9

Figure 4.23 A) Combined Landsat image 7 and 8 of the Pilanesberg Complex. B) Faults are schematically overlain on the Pilanesberg Complex Landsat image to indicate possible structural blocks. C) Include a comparative satellite overview for Landsat 7 & 8 in the left-hand table, while the right hand table includes all the band information.

An area of the gravity map around the Pilanesberg Complex including the Western Bushveld and the Transvaal sedimentary succession compares the different image-processed images of the gravity data in Figure 4.24. The colour-shaded image increases the edges of the Pilanesberg and the Bushveld Complex

(Figure 4.24 B). The analytic signal and automatic gain control of the gravity show that there is a clear central plug. The analytic signal also identified 2-3 ring that appears as a 'swirl' on the processed images (Figure 4.24C and D-F).

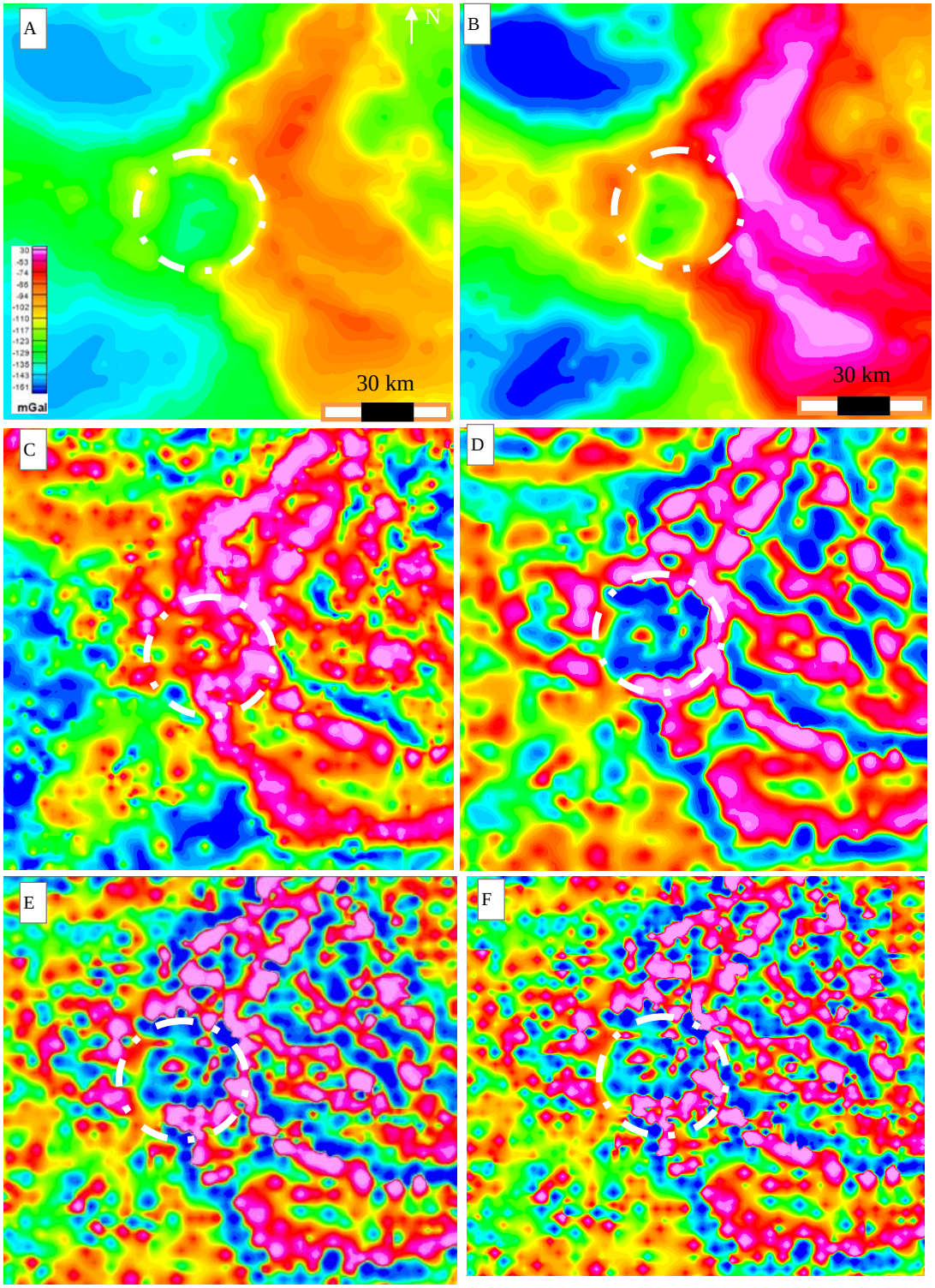

Figure 4.24 A) Bouguer gravity map of the Pilanesberg Complex area from the National gravity map (CGS). B) Bouguer gravity Colour enhanced- Auto recolour grid (recolours a viewed area of a grid with the entire colour palette). C) Gravity analytic signal – with FFT z-derivative method. D) Full amplitude max gain AGC cell size 10, E) AGC cell size 5. F) AGC cell size 3.

Aspects such as structurally controlled faults and the Pilanesberg dyke system, which were highlighted by the image processing techniques, have been used to recreate a map of the Pilanesberg Province that also includes some of the smaller alkaline and carbonatite Complex's (Figure 4.25). Maps used for comparison include those in the work of Letts (2007), Lurie (1986) and Shand (1928) as well as the image processed magnetic, gravity and geology map previously discussed.

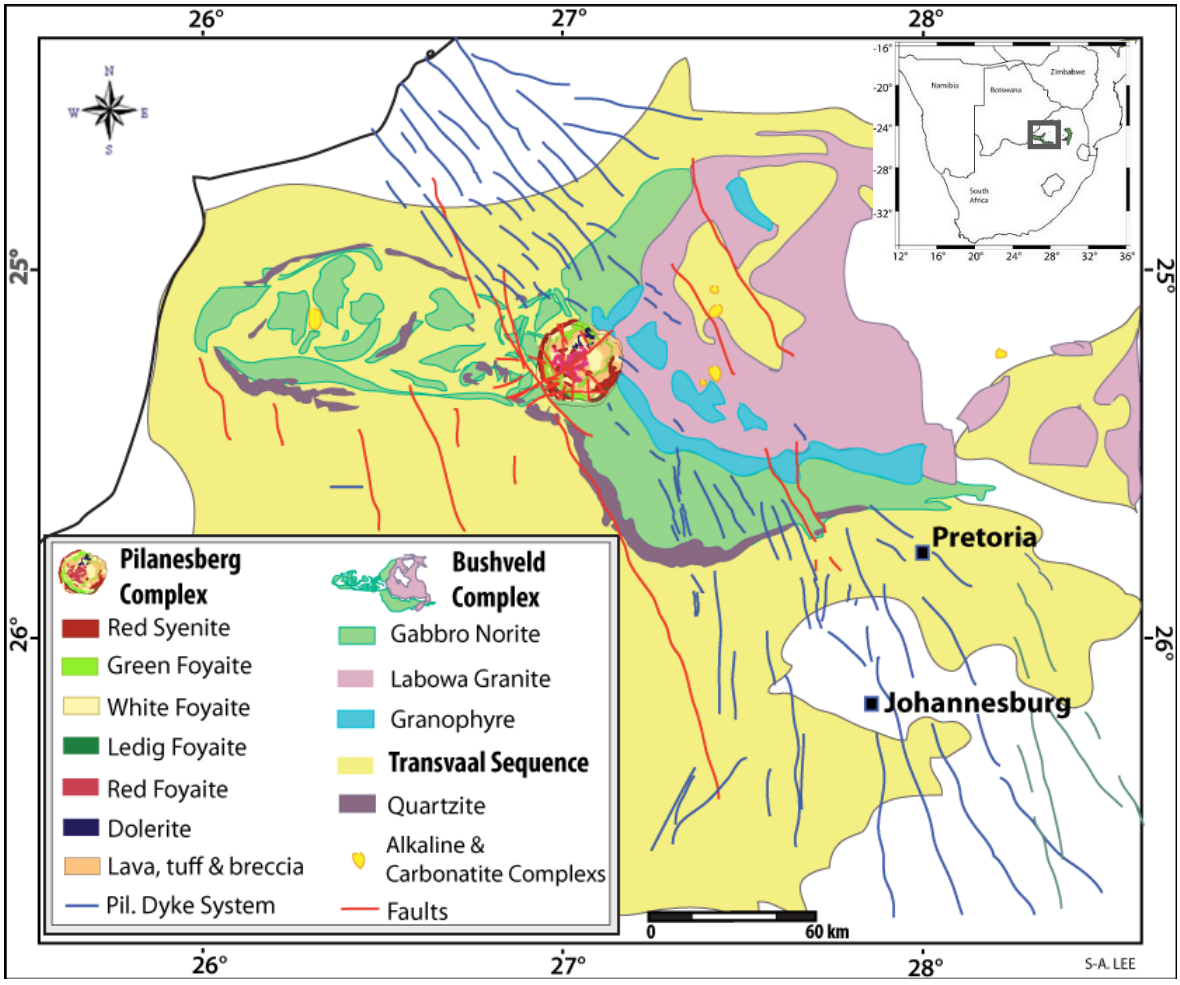

Figure 4.25 The geology of the Pilanesberg Province includes the Pilanesberg Complex, the Pilanesberg dyke System and the associated alkaline and carbonatite Complexes.

The faults identified with the image processing and map comparison will assist in explaining the 3D geometry and emplacement history of the Pilanesberg Complex.

4.4 SUMMARY

Data enhancement and image processing techniques of the magnetic and gravity maps assist in resolving geological features not identified on the geological map by changing parameters and directions on the enhanced maps. The aim of the Pilanesberg Complex internal geometry investigation is to determine the internal ring structure of the Complex and define how the gravity, magnetic and enhanced data sets represented the ring structure.

The gravity data was collected with stations approximately every 3 km over the 28 km Pilanesberg Complex. As such, some of the image processing techniques indicated significant noise levels, which made identifying any features very difficult. However, identifying characteristics in the gravity data was successful with the following techniques: automatic gain control, contact depth imaging and Euler deconvolution.

The automatic gain control of the gravity data indicates a simplistic ring structure with a positive outer ring aided by the contact with the Bushveld Complex as well as two central rings. The middle ring displays a break in the northeast of the ring structure that corresponds to the location of the Vlakfontein fault. This slight high appears to continue in the centre of the Complex as well, with the central ring indicating an oval shape to the south-west along the projection of the fault.

The contact depth imaging and the tilt angle contour on the gravity data were able to identify the outer edge of the Complex as well as some of the middle ring. The depth estimates indicate that the contact is closer to surface in the north and that the Pilanesberg Complex contact is deeper in the south. A structural event such as the Pilanesberg Complex tilting or caldera events could explain those findings.

The horizontal gradient, vertical derivative, analytical signal, ternary map, sun-shading and Euler deconvolution are the techniques used to process and enhance the magnetic data.

The horizontal gradient indicates that both the Pilanesberg Complex and the northern Pilanesberg dyke swarm carry prominent remnant magnetisation. The vertical derivative was able to define the southern edge of the Complex, which is not clear on the magnetic map. This method also identified the central plug, which occurs south of the Vlakfontein fault with this technique.

The analytic signal of the magnetic data identifies two rings within the internal structure of the Complex. Interesting observation is how the analytic signal picks up detail on the northern block but almost nothing on the southern block: this coincidence appears to run along the Vlakfontein fault, which could suggest different block movement.

Euler deconvolution of the Pilanesberg Complex indicates a complex geometry. The west-east profiles largely indicate an inward dipping structure. The most northern west–east Profile 1 has an inward dip of ~ 60° on the western edge and eastern edge is vertical before it picks up the dip of the Bushveld Complex. The average depth on this profile is 12 km. The central west–east profile 2 displays an inward dipping structure with an angle of ~ 70° degrees to a depth of 10 km on the western edge. The eastern edge of the Pilanesberg Complex is vertical up to a depth of 5 km after which the contact dips inward at ~ 50° to ~ 15 km depth. The southern profile 3 has a dip of 45° to the west and a vertical contact on the east to a maximum depth of 10 km. The north-south profiles both indicate an outward dipping edge in the north of ~ 52 ° on profile 4 (westward) and ~ 60° on Profile 5 (central profile). The northern edge of the Pilanesberg Complex extends out to a depth of ~ 11-12 km. The southern edge starts as a vertical to outward dipping contact bounded by the Bushveld to a depth of ~ 6 km after which the Pilanesberg Complex contact dips inward between 6 - 10 km at ~ 65°.

The ternary map combines the first vertical derivative, an analytical signal map and the tilt data. The result is a defined internal structure with the outside contact, two internal rings in close proximity and a central plug. The Vlakfontein fault forms a discontinuity in the elevated rocks to the south-western edge of the Complex.

The ternary map, analytic signal and vertical derivative amplify the west-east dykes, the positive Bushveld gabbronorite anomaly as well as the signal from the northern syenite Pilanesberg dykes, which crosscut through the Pilanesberg Complex and dissipates just south of the Bushveld Complex. The ternary map displays how the younger west-east dykes cut through the Transvaal Supergroup, Pilanesberg Complex and the Bushveld Complex. However, only the sun-shading can define that the west-east dykes crosscut the Vlakfontein fault.

The image processing observations are used to help constrain some of the 2D and 3D models and to explain the resulting behaviour of the gravity and magnetic data in the next Chapter.

CHAPTER 5: QUANTITATIVE METHODS: MODELLING OF MAGNETIC AND GRAVITY DATA

5.1 FORWARD AND INVERSE MODELLING

Forward modelling calculates a data response to a geological bodies signal by using estimates of a sources size, depth and magnetic susceptibility or density contrast to build a theoretical model. Inverse modelling uses the observed anomaly to provide information on the geology and physical properties that would otherwise be unknown. The inverse computation of such models works iteratively to decrease the difference between the calculated model and the observed anomaly, with known geological constraints used to aid the model (Blakely, 1995; Coomber, 2008).

2D, 2.5D and 3D forward modelling of the Pilanesberg Complex data investigates the geometry of the Pilanesberg Complex contacts and the internal structure. 2D models use a profile view with an infinite strike length on either side while 2.5D uses a defined strike length. The 3D modelling obtains the model's 3D geometry using algorithms and the application to both forward and inverse modelling. The 2.5D profiles use Talwani and Ewing's (1960) algorithm to calculate the forward model's responses (Cooper, 2011) while the 3D forward models and inverse models use the Blakely algorithm (1995).

5.1.1 Calculating Gravity Anomalies

The gravitational attraction (g) and gravitational potential (U) at the point P which is due to a volume of mass V and a density ρ is:

$$U(P) = G \int_V \frac{\rho(Q)}{r} dv \qquad (5.1)$$

$$\vec{g}(P) = \nabla U = -G \int_V \rho(Q) \frac{\hat{r}}{r^3} dv \qquad (5.2)$$

where r is the distance from P to an element of the body Q and G is the gravitational constant (Figure 4.1) (Blakely, 1995).

With a positive down z-axis and right-hand Cartesian coordinate system then the vertical attraction of gravity g is:

$$g(x,y,z) = \frac{\partial U}{\partial z} = -G \int_{z'} \int_{y'} \int_{x'} \rho(x',y',z') \frac{(z-z')}{r^3} dx'dy'dz', \quad (5.3)$$

where $r = \sqrt{(x-x')^2 + (y-y')^2 + (z-z')^2}$.

The general form is:

$$g(x,y,z) = \int_{z'} \int_{y'} \int_{x'} \rho(x',y',z') \varphi(x-x', y-y', z-z') dx'dy'dz', \quad (5.4)$$

where Green's function φ(x, y.z) = $-G\frac{z}{(x^2+y^2+z^2)^{3/2}}$ is the gravitational attraction at (x, y, and z) of a point mass at (x', y', z') in Figure 5.1:

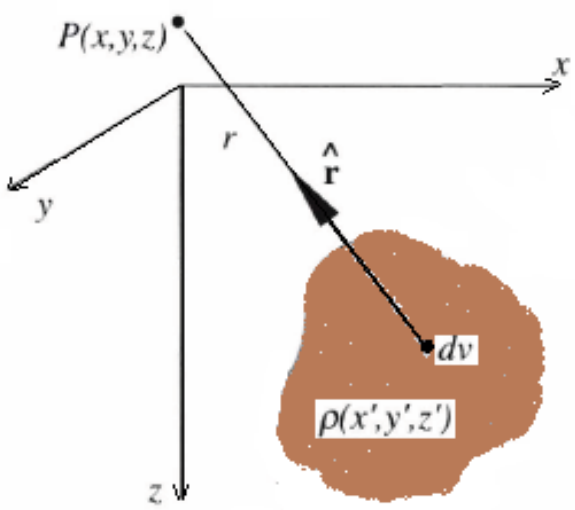

Figure 5.1 The calculation point P(x, y, z) from an element of the mass P that has a density ρ(x',y',z') separated by the unit vector $\hat{r}$. Modified from Blakely (1995).

The model calculation is able to subdivide and calculate a response for each of the N simple geological bodies. This is then summed for the overall response. Fast Fourier Transforms, rectangular prisms and stacked lamina are used to find the gravity output for a layer constrained by two surfaces (Blakely, 1995; Coomber, 2008) such that:

$$g_m = \sum_{n=1}^{N} \rho_n \varphi_{mn} \quad (5.5)$$

with g_m is the vertical attraction at the mth observation point ρ_n, the density of part n and the gravitational attraction φ_{mn} at point m due to part n with unit density.

5.1.2 The Rectangular Prism

A group of rectangular prisms (Figure 5.2) sub-divides a geological model and approximates a volume of mass, provided the prisms are small enough to assume a constant density within each prism. Summing the effect of all the prisms provides the gravitational anomaly of the body at the observation point. The time it takes to compute the model is related to the number of input and outputs, N, with smaller prisms allowing for a greater number of prisms which would requiring more time compared to larger prisms which would have a lower number of prisms to calculate for a body the same size. Using larger prisms would thus offer a quicker calculation with a less accurate approximation of the body.

Calculating the gravitation attraction of a single prism uses the integration of equation 5.3 over limits of a single rectangular prism. The vertical gravitation attraction at the origin g of a prism with dimensional limits x1< x <x2, y1< y <y2, z1< z <z2 and constant density ρ is:

$$g = G\rho \int_{z1}^{z2} \int_{y1}^{y2} \int_{x1}^{x2} \frac{z'}{(x'^2+y'^2+z'^2)^{3/2}} \, dx' \, dy' \, dz' . \qquad (5.6)$$

The gravitational attraction of the entire approximated body in Figure 5.2 is the result of summing the calculated gravitation attraction of each prism.

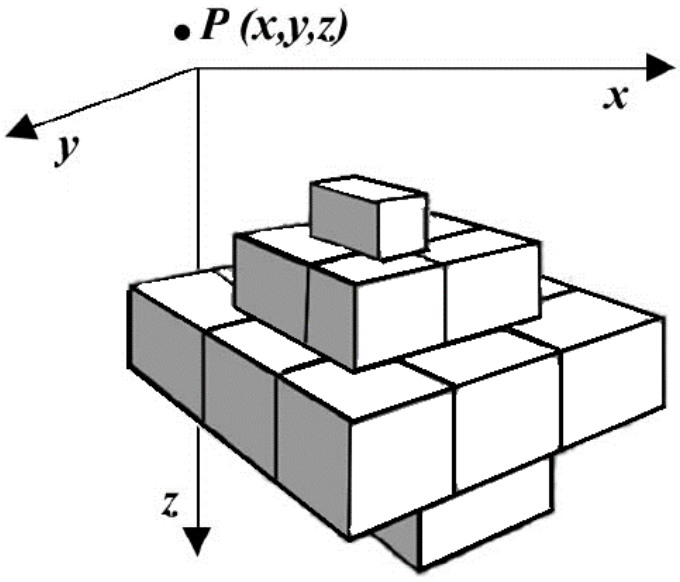

Figure 5.2 The schematic diagram displays a collection of rectangular prisms that approximate a 3Dimensional body. Modified from Blakely (1995).

In reality, this approach is difficult to use as prisms are poor approximations for geological bodies and this method is unable to do one calculation for adjacent prisms with the same density making it highly computational.

5.2 2.5 DIMENSIONAL PROFILE MODELLING OF THE PILANESBERG COMPLEX

2D profiles across the Pilanesberg Complex and surrounding area are extracted from the Bouguer Map of South Africa obtained from the Council for Geoscience. Cooper's (2011) Grav2Dc forward modelling programme was used to model a geological representation that would match the geophysical data across the profile. This uses the Talwani and Ewing (1960) algorithm for the computation. The programme allows for 2.5D modelling as it accounts for the strike of a body.

Accurate modelling of the data uses combined input data from different sources. The inputs include; a seismic line looking at the dip of the Bushveld close to the Pilanesberg Complex, constrained geological maps and physical property measurements from Pilanesberg Complex samples as well as the CGS physical property database. Coomber (2008) examined a seismic line of the Bushveld Complex, which confirmed that the Complex dips steeply at the edges with an average dip of 18° and shallows out at between three and five km depth until it flattens out considerably at approximately 8-10 km below the surface (Figure 5.3).

2D gravity and 2D magnetic profiles are modelled across the Pilanesberg Complex to test the possible geometry of the Complex and the physical properties that define the different components within the Complex. The 2D profile models are produced from the information pertaining to the measures density and magnetic susceptibility values, which will help to constrain the modelled bodies in the 2D profile models. Simple models will define the dip orientation and shape of the Complex by matching a model to the data of the profile. The profiles are obtained from the grid data of the Bouguer map in Figure 2.4 and the magnetic map in Figure 2.3.

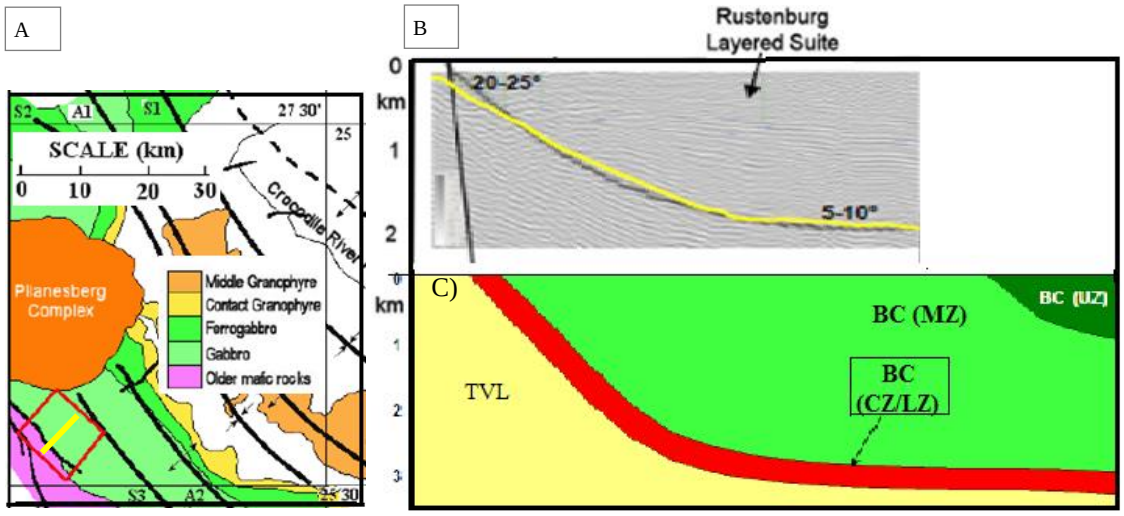

Figure 5.3 A) Coomber (2008) investigated the area in red, south of the Pilanesberg Complex and studied the Bushveld Complex reefs dip angle on the Seismic line (B), which has been interpreted by Coomber in the illustration in C). Modified from Coomber (2008).

The west-east profile modelling is correlated with the surface geological from the map in Figure 5.4. The contacts on surface form hard constraints for the bodies that are modelled to depth. Using the geological map also helped to identify the sections of the Bushveld Complex that shifted to the west when the Pilanesberg Complex was emplaced. Evidence of this is seen in the profile data as a gravity peak to the west of the Pilanesberg Complex (Figure 5.4).

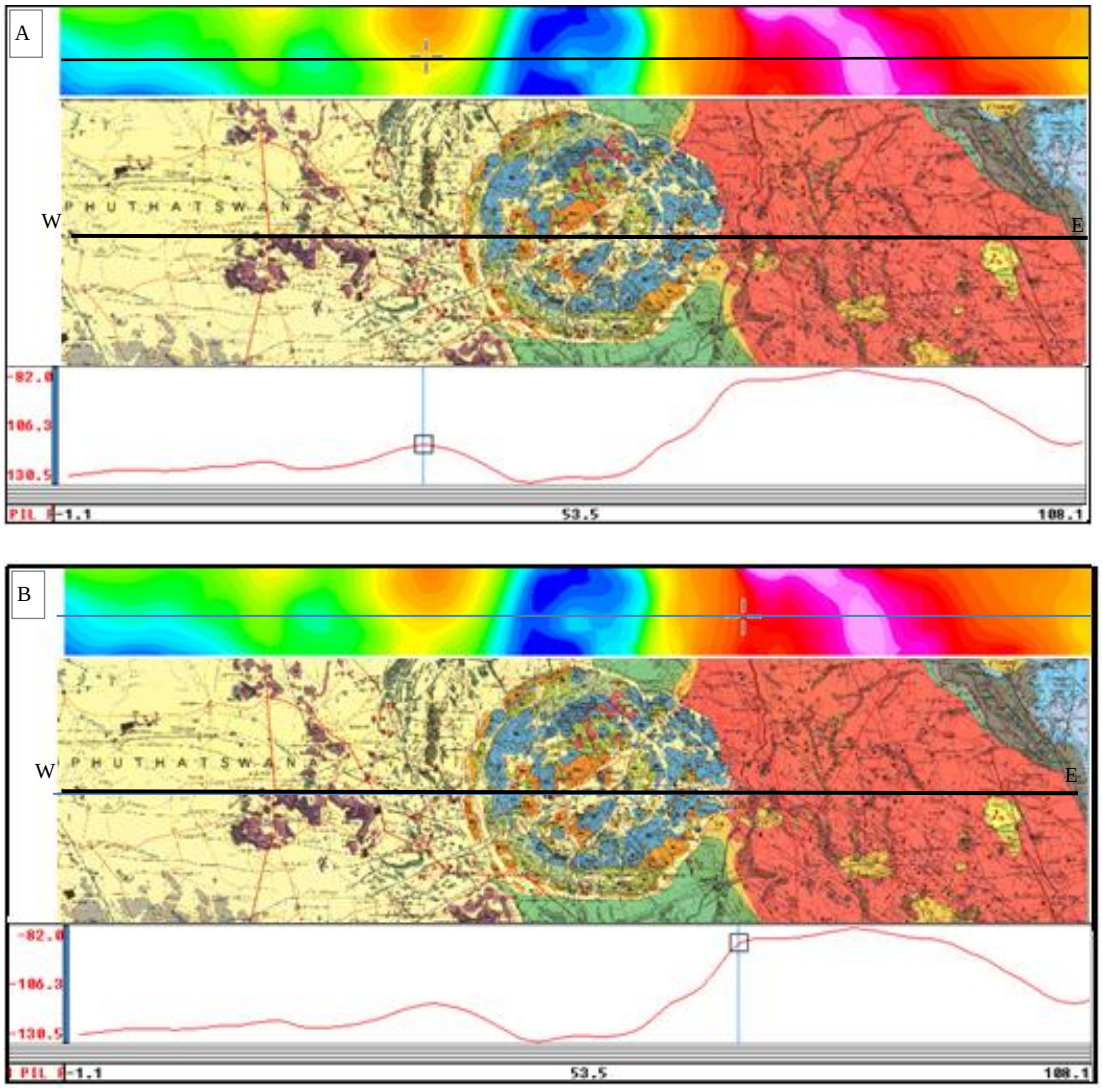

Figure 5.4 Comparison of the Bouguer gravity data with the geology map, along the west-east Bouguer profile to confine the geological contacts on the surface. Geology sections modified from the 2526 Rustenburg map 1:250 000 geological series, (Department of mineral and energy affairs). The blue vertical line on the profile data indicates the position of the cross that corresponds on the gravity and geological maps. A) indicates the alignment of the profile with the gravity and geological map to the west of the Pilanesberg Complex while B) displays the alignment of the profile with the gravity and geological map on the eastern edge of the Pilanesberg Complex.

The depth extent is constrained by Webb et al. (2004), and continental crust ranges (Figure 5.5).

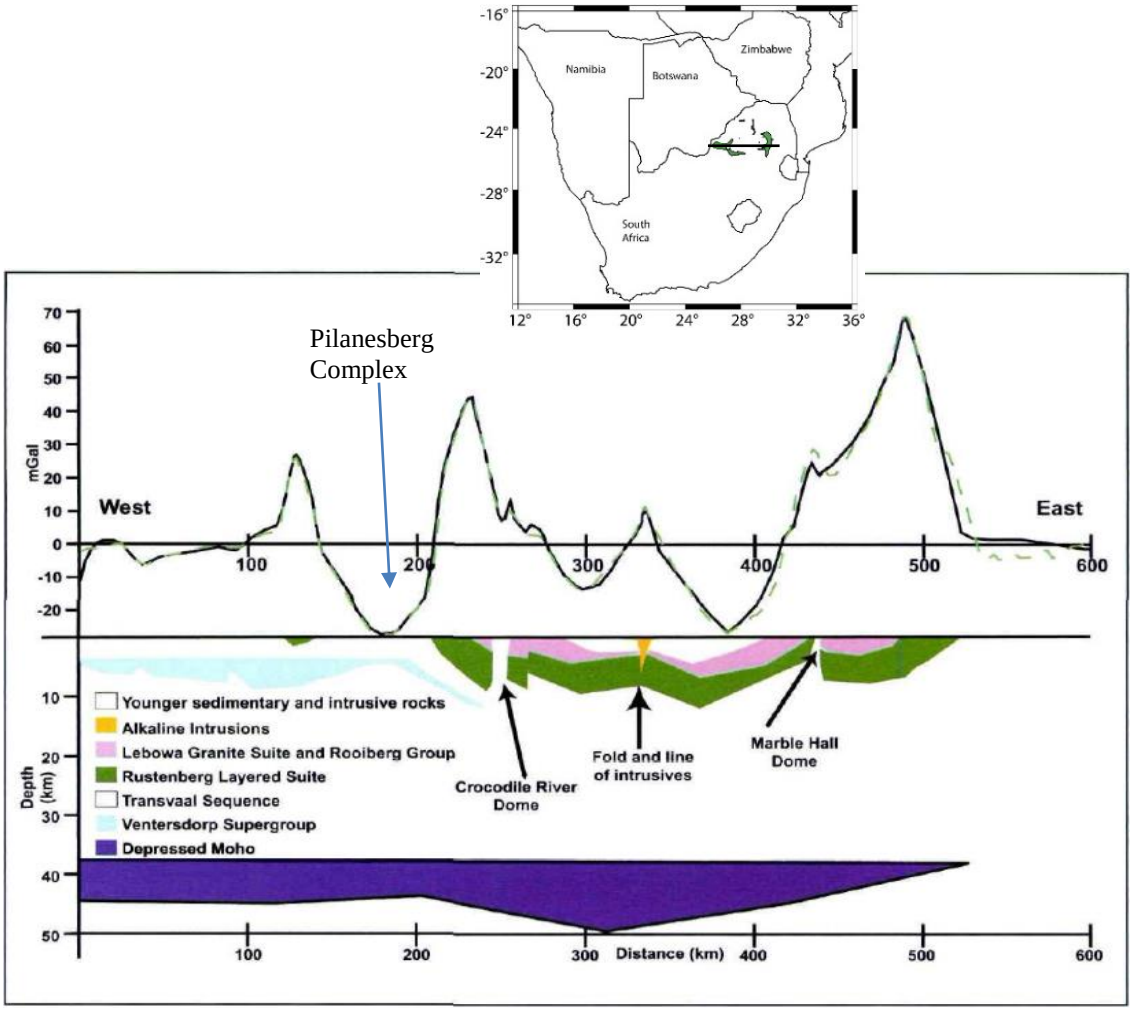

Figure 5.5 Gravity model by Webb et al. (2004) presents the depths expected of the Bushveld Complex. This model also shows the small amount of the western Bushveld Complex that displaced westward by the intrusion of the Pilanesberg Complex. Modified from Webb et al. (2004).

The internal structure of the Pilanesberg Complex has dip directions indicating an overall inward dip within the Complex. Lurie's (1986) geological model (Figure 1.10) is one of the surface constraints with dip information used to assist with matching a model with the Bouguer gravity data. This information tests if the external boundary of the Pilanesberg Complex is an outward dipping ring dyke or an inward dipping cone sheet. 2D profiles test the possible external geometry using the geological modelling below surface either to agree with the data or to disprove the geometry through anti-correlation of the data.

The first profile is a west-east profile extracted from the Bouguer gravity map (Figure 5.6). An overview of the constraints used in the 2D models includes the surface outcrops, mapped geology and lithology boundaries, dip directions, seismic lines and Bushveld boreholes.

The unknown shape of the Pilanesberg Complex below the measured surface relationship is tested using gravity data over the area. From Lurie 1986, the internal structure dips inward which is conceptualised using the west-east profiles through the middle of the Pilanesberg Complex.

The profiles extracted from the Bouguer gravity (Figure 5.6) for 2D modelling have been compared with the magnetic grid and other maps. The three west-east profiles pass from the Transvaal Supergroup in the west through the green circle of the Pilanesberg Complex and over the pink gravity high of the Bushveld Complex's gabbronorite. Additionally, the Pilanesberg Complex geometry analysis continues with the modelling of two north-south profiles.

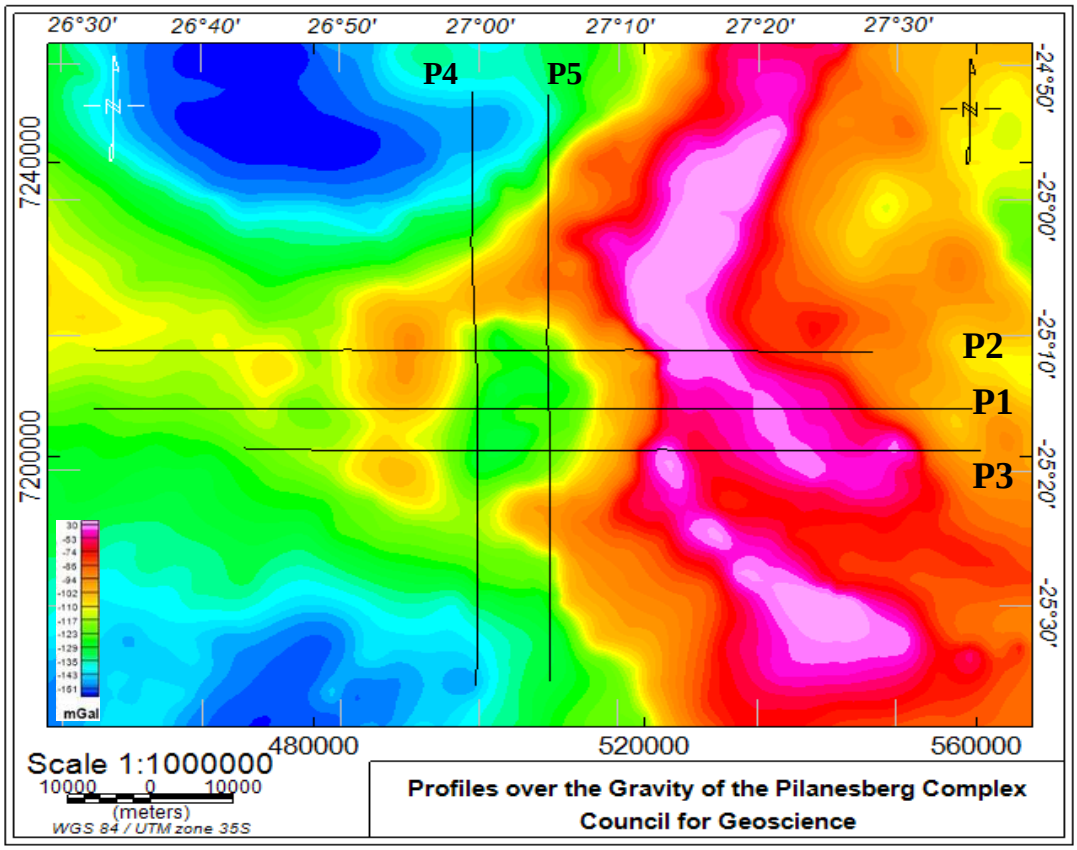

Figure 5.6 Profiles extracted from the Bouguer gravity grid over the Pilanesberg Complex.

The geological map with the profiles overlain compares the data with the magnetic and gravity grids and the data profiles in order to constrain individual signatures with different geological units. Using the geological map (Figure 5.7) during 2D modelling allows the bodies to be constrained at the surface of the model such that the dip, depth and physical contrast can be modelled off the constrained surface geology and structures.

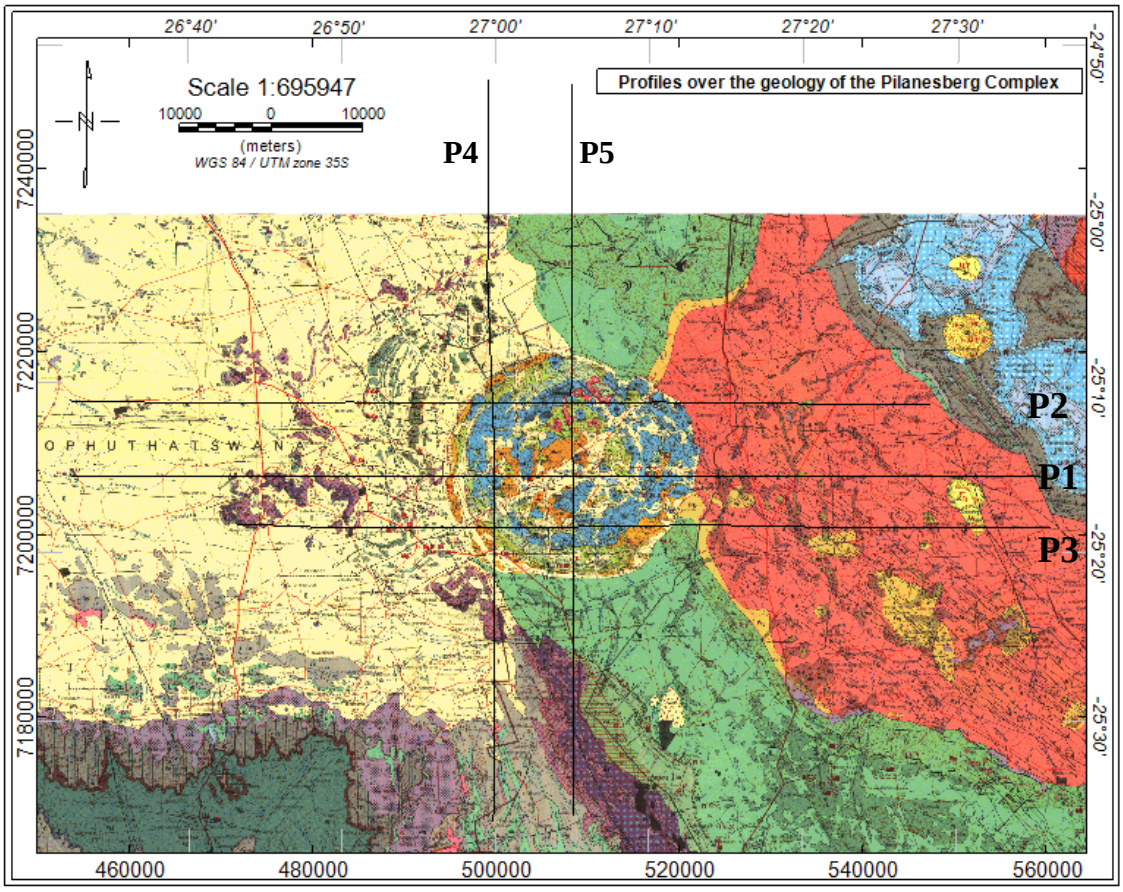

Figure 5.7 Profile overlay on the Pilanesberg Complex geology for comparison with the magnetic and gravity data

The 2D profile 1 model (Figure 5.8) investigates how the shape of the Complex relates to the calculated field (from Figure 5.6). The shape of the Complex is uncertain below the surface field relationships. Thus, the shape of the Complex was tested with different geometries that include an inward dipping model (Figure 5.8) and outward dipping (Figure 5.9A) and a cylindrical model (Figure 5.9 B). All the models have been constrained by the geological map (Figure 5.7) as well as known dip information for the Bushveld Complex and Transvaal Supergroup. The inward dipping model was tested with various depths. The model displayed in Figure 5.8 indicates that the Complex came up from the Moho. The model achieves an accurate fit with the gravitational data based on the inward dipping edges. The specific depth of the bottom contact becomes insignificant in this model, as the fit does not change with changing depth as the model fit is based on the dipping edges.

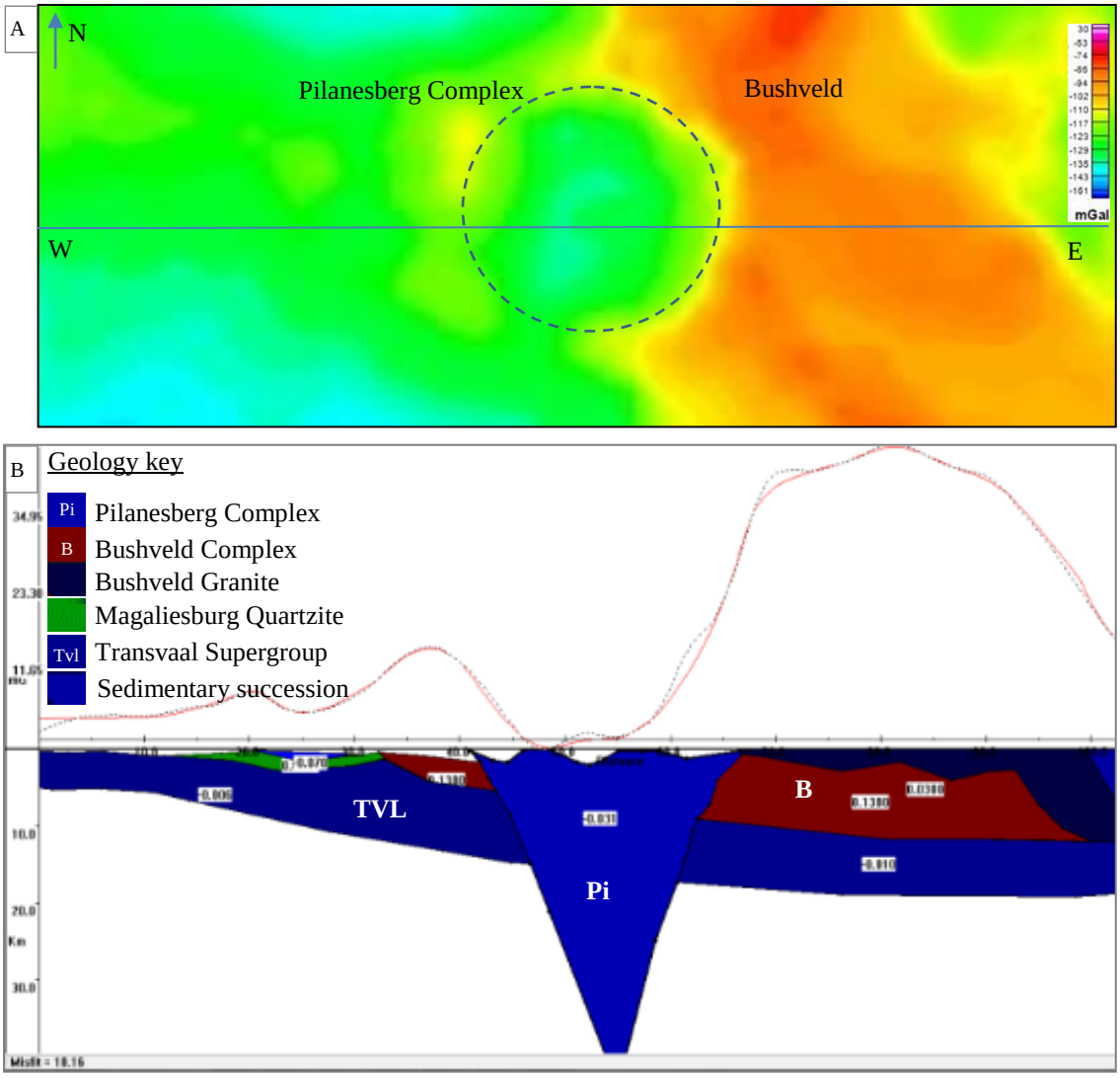

Figure 5.8 2D profile 1 of the Bouguer gravity (black dots) and the modelled geological response (red line) over the inward dipping Pilanesberg Complex and Transvaal Supergroup under the Bushveld Complex gabbronorite and granite layers. Profile extends from west to east of the Complex. Produced using Grav2Dc.

The Pilanesberg Complex is often referred to as a ring dyke and for clarity; this refers to the manner in which the Pilanesberg Complex formed, where the rings of the Complex were emplaced from the outer ring to the inner ring. This is not a reference to the Complex's overall geometry. In Figure 5.8 the inward dipping cone sheet fits the Bouguer gravity acceptably with a misfit error of 10.16 %. The same west-east profile is tested with other possible geometries including an outward dipping ring dyke (Figure 5.9 A). This is unable to match the Bouguer gravity signal achieving a large misfit of 58.46 %. The straight cylinder (Figure 5.9 B) has a slightly better fit but still has a great misfit of 31. 57 %. Both models tested for different depth and similar to Figure 5.8 the depth became insignificant on the amplitude of the signal. The signal was changed by an angle of the edges close to the surface.

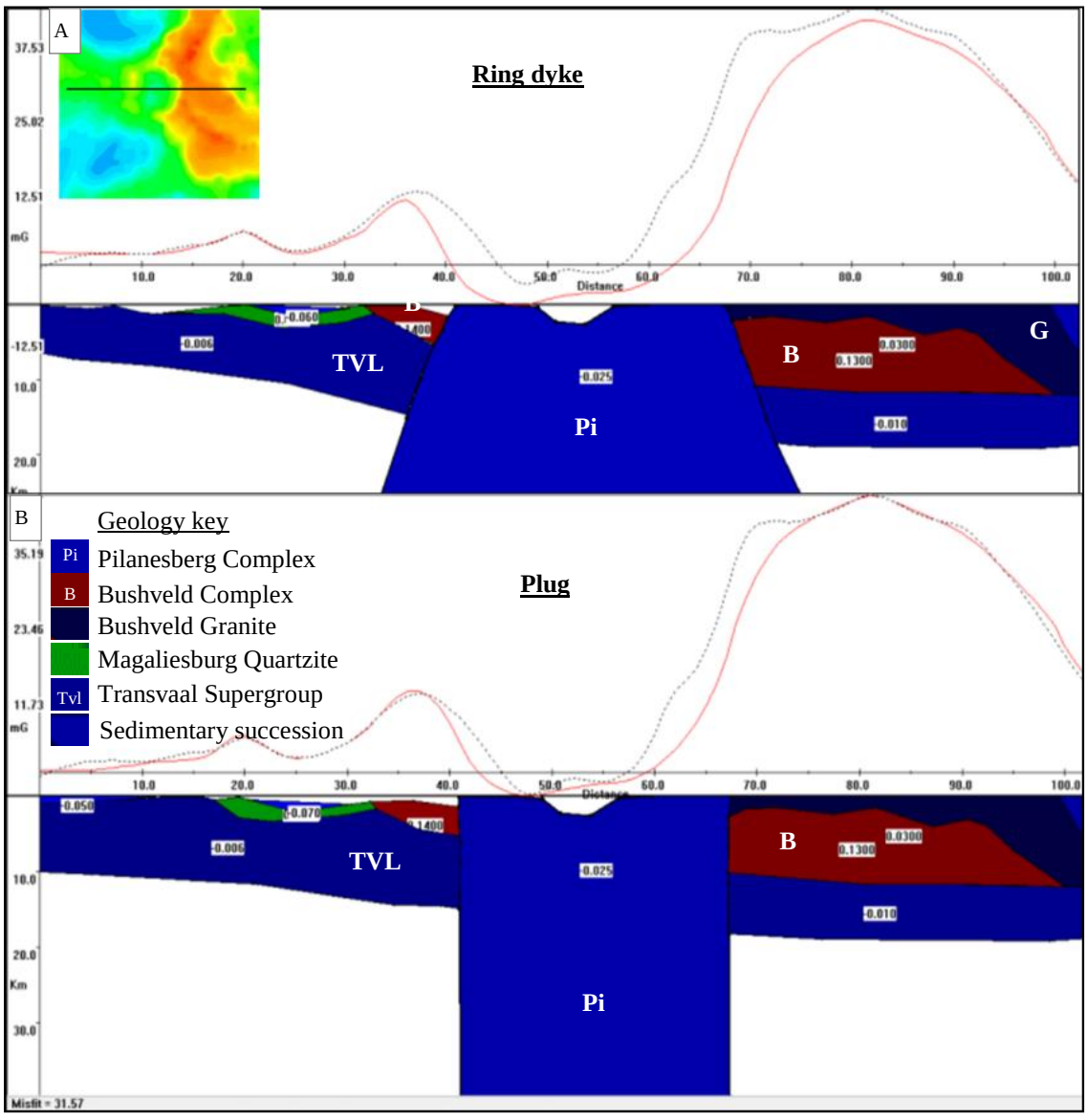

Figure 5.9 Preliminary modelling of the 2D west-east Pilanesberg Complex (Pi) profile 1. The geometry of the outward dipping ring dyke (A) and the straight cylinder (plug) (B) models are test examples that are unable to fit the Bouguer gravity (black line). TVL-Transvaal, Magaliesburg quartzite (green), B-Western Bushveld Complex, G-granite.

The west-east Bouguer gravity of profile 1 tests different shaped models over the Pilanesberg Complex. The test models indicate that a body with vertical or outward-dipping contacts do not match the gravitational data over the area. However, a body with inward-dipping contacts provides a superior fit with the potential field data along a west-east profile.

5.2.1 2D Profile Comparison with Euler Deconvolution

Determination of the depth estimates, using Euler deconvolution solutions from section 3.2.7, are overlain on the 2D gravity forward models for depth and contact comparison. The Euler solutions along the Magaliesburg quartzite, which is the green body in Figure 5.10, agree with the geology within 10% of the known overlap. The Euler deconvolution solutions identify the denser material of the Bushveld Complex by identifying a point source associated with the disturbed material on the west of the Pilanesberg Complex and the gabbronorite layer on the east of the Pilanesberg Complex. The Euler solution on the western contact of the Pilanesberg Complex has a similar pick up a contact that is further within the Pilanesberg than the 2D modelled contact. There is approximately a 20% difference between the Euler solution and the modelled contact as the modelled contact has been constrained by the geology of the surface. The eastern Pilanesberg Complex contact signal is overpowered by the Bushveld signal and is identifying the Bushveld gabbronorite layer dipping towards the east.

The Euler solutions are plotted separately in Chapter 4 Figure 4.16 to Figure 4.20. The purpose of the images in Figure 5.10, Figure 5.12 and Figure 5.14 is to compare the modelled profiles with the Euler solutions to see the accuracy of both the 2D profile models as well as the data processing.

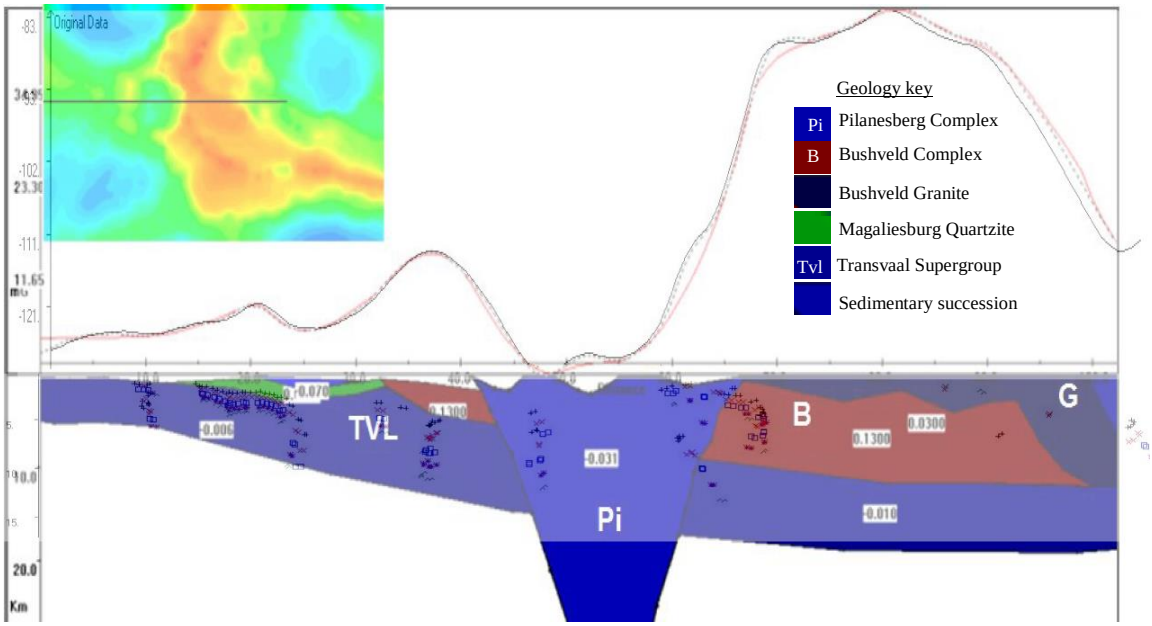

Figure 5.10 The Euler deconvolution solutions overlain on the WE profile 1, overlain for comparison over the 2.5D geological model. The bottom contact of the Pilanesberg Complex is not defined indicating that the intrusion came up from the Moho.

Profile 2 (Figure 5.11) is ~ 8km north of profile 1 from west to east and has the same geological characteristics including the dipping Bushveld Complex over the Transvaal sedimentary succession with some Magaliesburg material to the west. The main difference is that the Pilanesberg Complex has less outcrop on the surface and requires more Bushveld matter underneath it to reach the acceptable model misfit of 10.71 percent. The Pilanesberg Complex requires positive areas along the surface which are not consistent with the geology map. This could be explained by a higher density of one or more of the Pilanesberg Complex rings or that the dykes which were seen to cut through the Complex in chapter 3, have a positive density contrast with the Pilanesberg Complex.

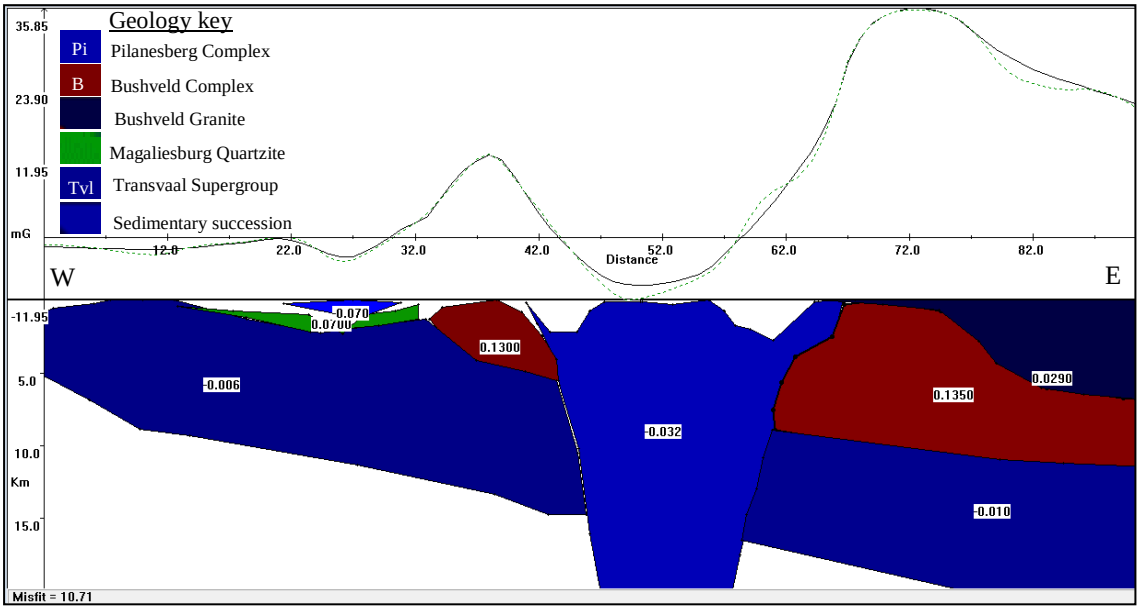

Figure 5.11 Profile 2- Northern most west-east Bouguer gravity profile over the Complex

The overlain Euler solutions on profile 2 positively identify the Bushveld mass. The Pilanesberg Complex solutions are identifying a positive density bodies in the internal structure that could be a deeper contact with a fresh rock at 5 km depth or a dyke that is cutting through the Complex. The Euler solutions plots further in towards the centre of the Pilanesberg in comparison to the 2D modelled profile which would require a steeper inward dipping eastern contact to fit the Euler solution point (Figure 5.12).

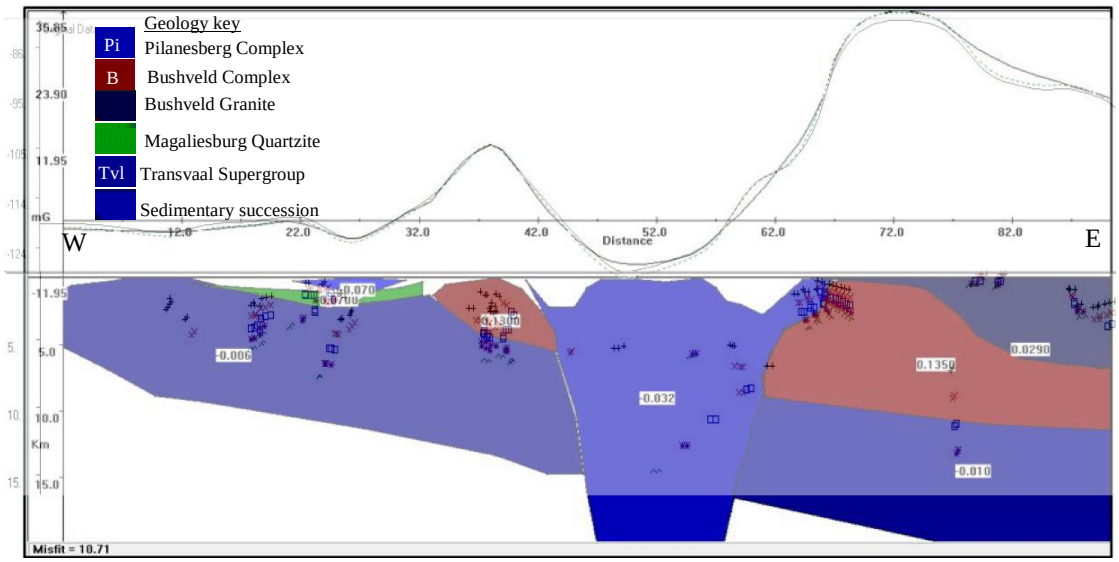

Figure 5.12 Euler deconvolution over the Bouguer Gravity 2.5D model of the WE Profile 2. The white gaps between the Pilanesberg Complex and Magaliesburg samples represent areas of sedimentary material.

Profile 3 (Figure 5.13) is located ~ 7 km south of profile 1. The Pilanesberg area has a broader anomaly with less detail in the signal suggesting that the body is deeper than in the other profiles. This is seen on Google Earth as the profile is over an area that has more sedimentary cover than profile 1 and 2. This also accounts for less surface contact in the model where the positive bodies (white) are due to sedimentary cover. The model indicates that a larger amount of Bushveld Complex Main zones is required closer to the surface to represent the gravitational signal associated with the geology.

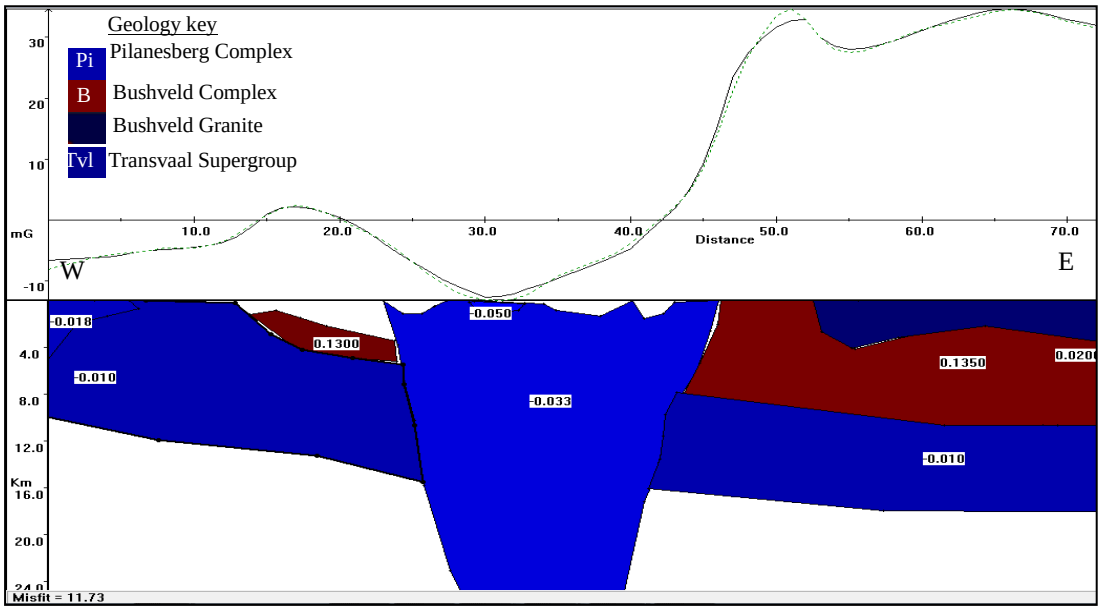

Figure 5.13 Profile 3- Southernmost WE Bouguer gravity profile over the Pilanesberg Complex. The white gaps between the Pilanesberg and Bushveld samples represent areas of sedimentary material.

The Euler solution over profile 3 picks up two point along the western edge that excludes the different structural indices fall off and a basic extrapolation between the two points suggests an eastward dipping model with the contact dipping at ~ 50º (Figure 5.14). The surface of the model is constrained by the geology. This agrees with Euler solutions; however, while the Bushveld contacts appear to fit the solutions, the Euler angles for the Complex are much steeper than the 2D model predicted.

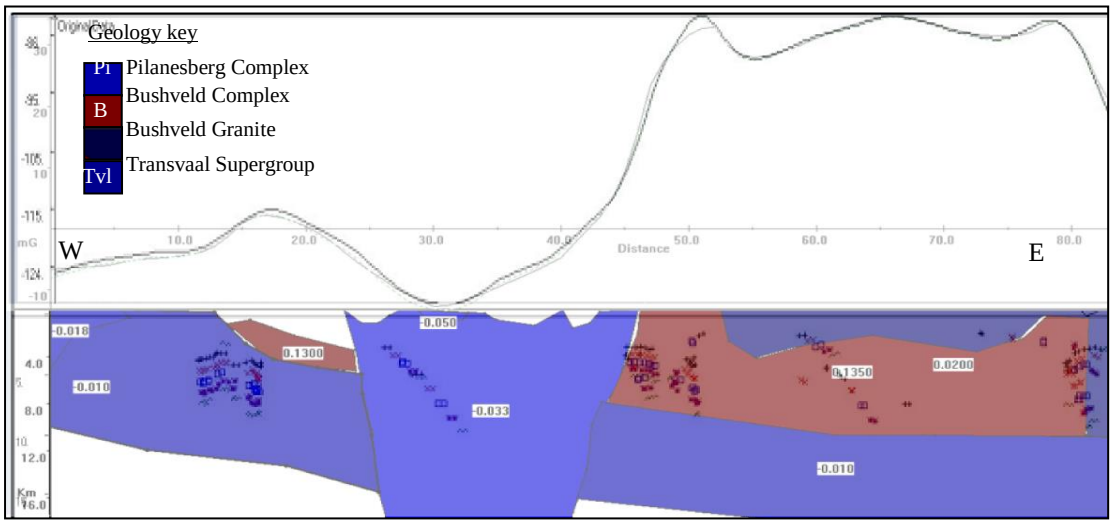

Figure 5.14 West-east Bouguer gravity profile 3 with the Euler Solutions overlain to indicate a comparison of the 2D forward modelled data with the theoretical calculation.

The north-south Bouguer gravity sections through Pilanesberg Complex are simpler than the west-east profiles. The 2D model is able to fit the data in profile 4 with a small misfit error of 2.87 %. The northern Pilanesberg Complex requires a slightly higher density material than the rest of the Pilanesberg Complex indicating that the profile cuts through more Bushveld Complex material in that area (Figure 5. 15).

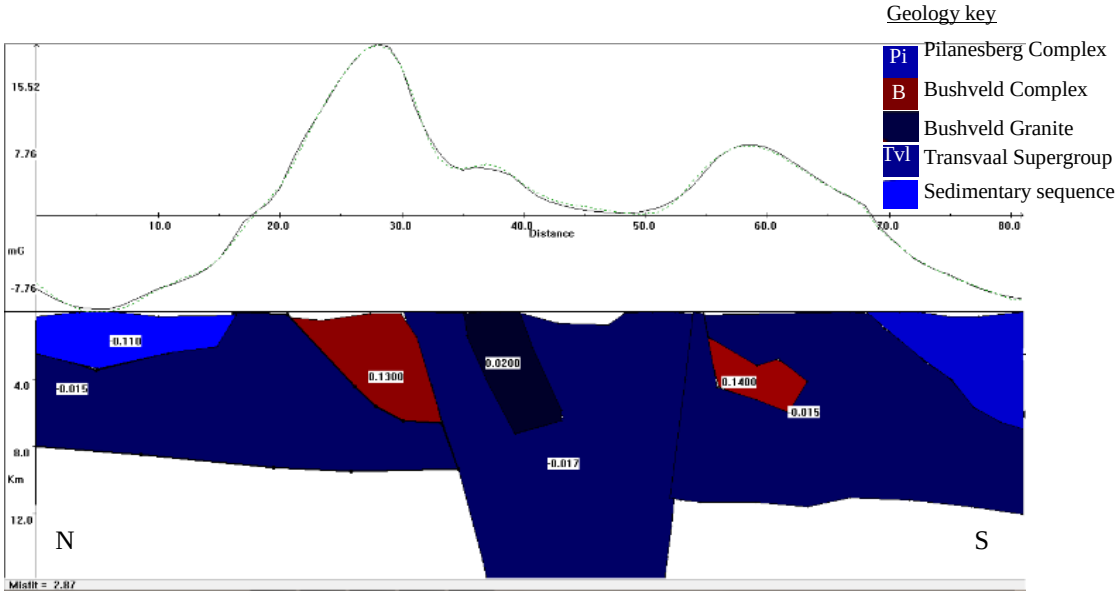

Figure 5. 15 The western north-south Profile 4 over the Pilanesberg Complex and surrounding.

The 2D model for profile 5 is similar to profile 4. However, this profile was selected east of profile 4 and is in contact with more Bushveld material in the north, and the material south of the Complex is closer to the surface (Figure 5.16).

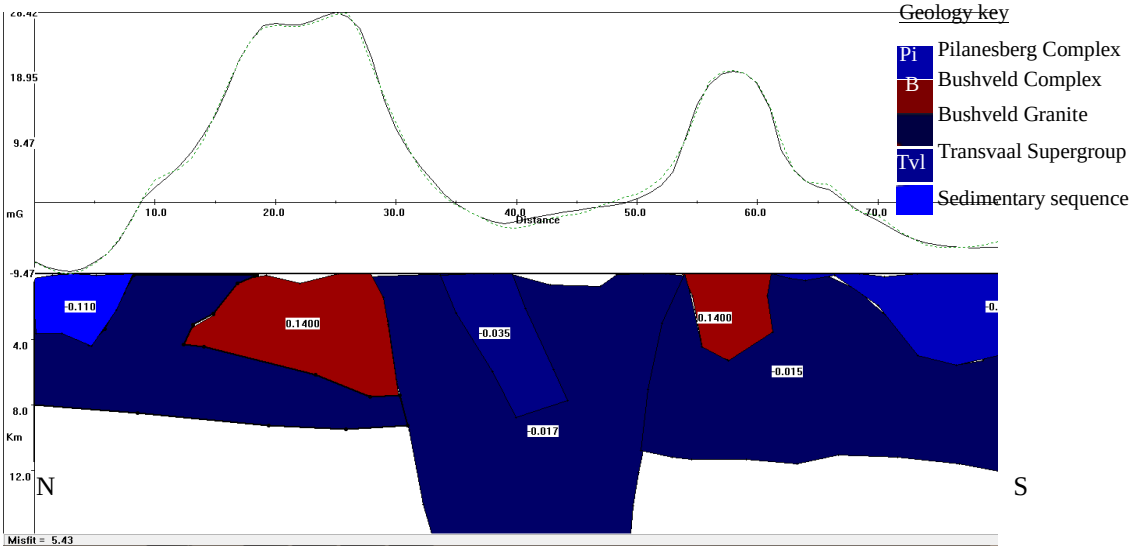

Figure 5.16 The Eastern north-south Profile 5 over the Transvaal Supergroup, Bushveld Complex and Pilanesberg Complex.

5.2.2 Magnetic profiles extracted for modelling

Five aeromagnetic profiles were extracted from the national dataset. These profiles are in the same location as the Bouguer gravity profiles. The geological contacts dip information was extracted from the geological map to correlate the magnetic signature along the profiles with the respective lithologies (Figure 5.17).

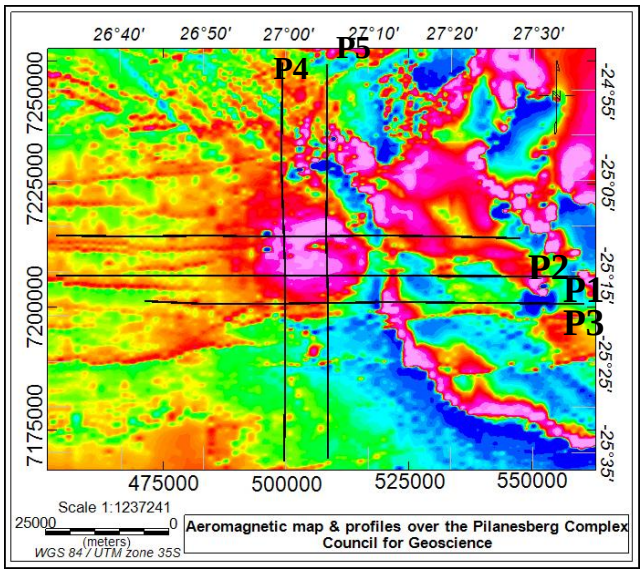

Figure 5.17 The location of profiles extracted from the magnetic grid over the Pilanesberg Complex.

The Magaliesburg quartzite has a rutted appearance within the flat Transvaal sedimentary succession. An observation from within the Pilanesberg Complex is that the overlying lava produces magnetic lows as it covers the normally magnetic rocks of the Complex (Figure 5.18 A). The magnetic peaks within the Pilanesberg Complex correspond to the syenite and red foyaite in the centre of the Complex (Figure 5.18 B) and with the white foyaite and green foyaite from the northern profile 2 (Figure 5.19).

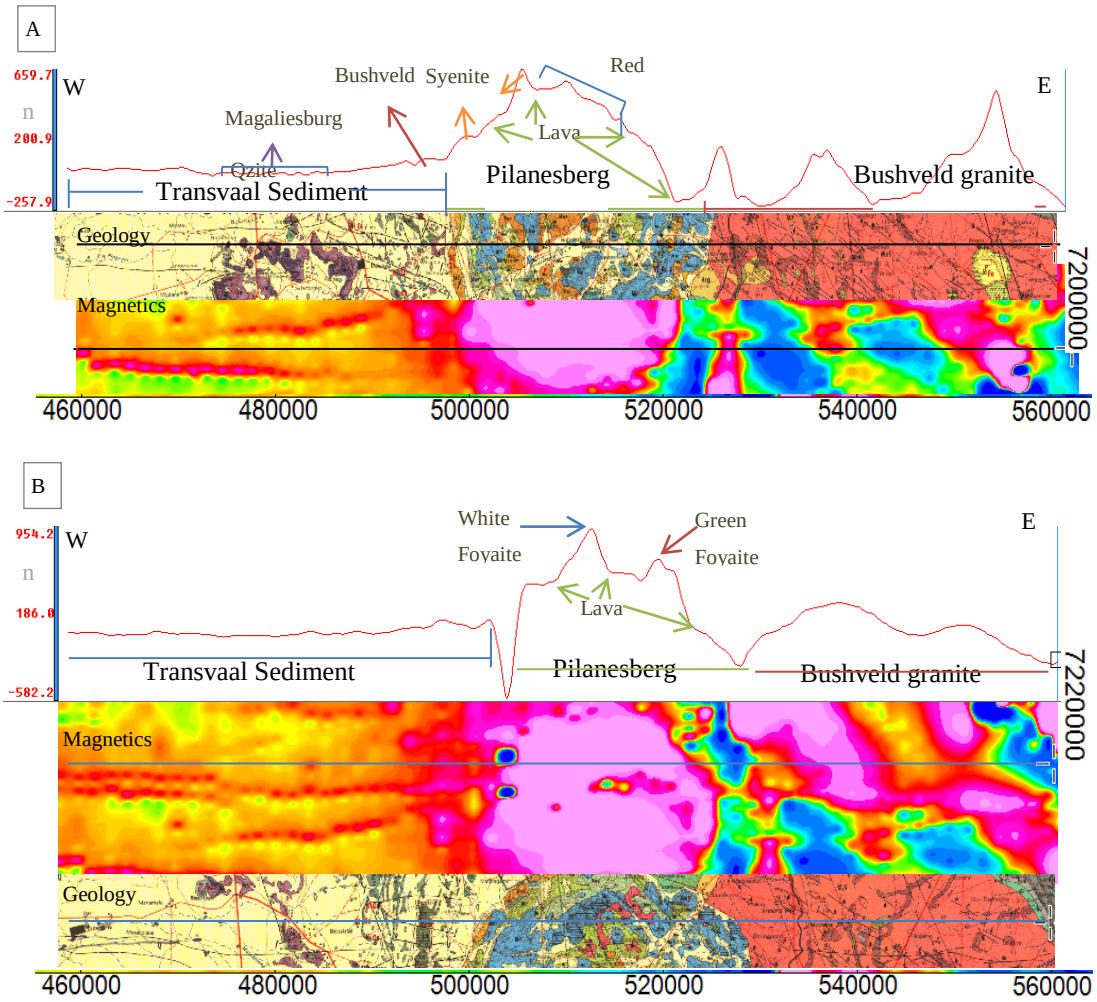

Figure 5.18 A) The extracted west-east magnetic profile 1 compared with the geological data and magnetic map along the profile 1. B) West-east magnetic profile 2 compared with the magnetic and geological data.

The north-south profile (Figure 5.19) indicates less difference between the different lithologies compared to the west-east profiles, as the flight acquisition lines are orientated north-south. The positive magnetic signature of the Pilanesberg Complex has a longer wavelength feature for the white foyaite and red foyaite (Figure 5.19). High amplitude signature of the Bushveld Complex is associated with the Pilanesberg Complex with a dipolar negative to the north in Figure 5.19 as well as to the east of the Pilanesberg Complex in Figure 5.18.

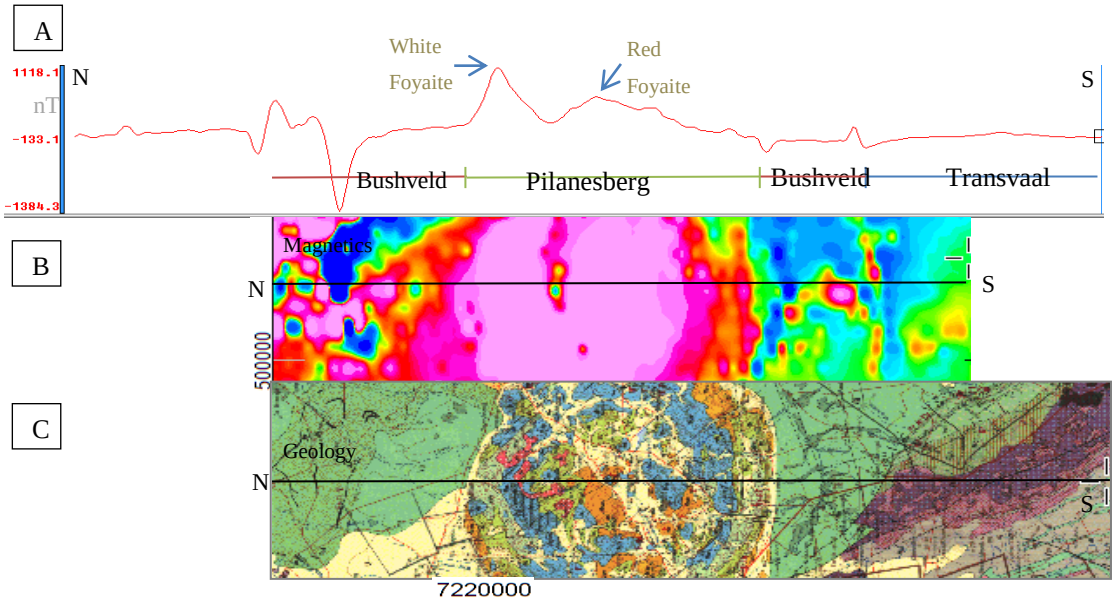

Figure 5.19 A north-south profile through the western Bushveld Complex and the Pilanesberg Complex. The profile compares the extracted magnetic profile in A) with the magnetic grid in B) and the geology map in C).

5.3 3D FORWARD MODEL

3D forward models are used in a similar way to 2D forward models, where geometries and theoretical lithologies can be tested to determine the field potential responses to be expected. The next step would be to input real data and build a plausible geological model to fit the data. The Pilanesberg Complex data will be used in this manner to turn the 2D profile models into 3D geological models.

5.3.1 1PyGMI and Python

PyGMI or Python Geophysical Modelling and Interpretation is a freeware programme coded in Python by Patrick Cole of The Council for Geoscience. PyGMI is a 3D forward modelling package that is simple and quickly allows the modelling of 2D profiles in a 3D setting. This aids in better accuracy of the bodies shape location and size as it is computing in a 3D sense and sums information from adjacent profiles to achieve a regional response.

PyGMI uses 3D modelling in a voxel environment, which allows quick computation forward modelling. The advantage of this modelling platform over the 2.5D profile models joined in 3D sections and 3D polygon models are that the forward model is a true 3D representation that can be altered easily. The calculation uses Blakley's algorithms (1995) by assuming a potential field cube for each voxel and sums the solutions over the entire voxel volume (Cole, 2012).

The rectangular prism magnetisation M is orientated parallel to x, y and z-axis where

$$\mathbf{M} = M\,(\hat{\mathbf{i}}\,\acute{M}_x + \hat{\mathbf{j}}\,\acute{M}_y + \acute{\mathbf{k}}\,\acute{M}_z), \qquad (5.7)$$

with dimensions $x_1 \leq x \leq x_2$, $y_1 \leq y \leq y_2$ and $z_1 \leq z \leq \infty$. The prism anomaly parallel to the regional field $\hat{\boldsymbol{F}} = (\hat{F}x, \hat{F}y, \hat{F}z)$ will have a total-field anomaly at the origin given by:

$$\Delta \boldsymbol{T} = C_m M \left[\frac{\alpha_{23}}{2}\log\left(\frac{r-x'}{r+x'}\right) + \frac{\alpha_{13}}{2}\log\left(\frac{r-y'}{r+y'}\right) - \alpha_{12}\log(r-z1) - \hat{M}x, \hat{F}x \tan^{-1}\left(\frac{x'y'}{x'^2+rz_1+{z_1}^2}\right) - \hat{M}y, \hat{F}y \tan^{-1}\left(\frac{x'y'}{r^2+rz_1-x'^2}\right) + \hat{M}z, \hat{F}z \tan^{-1}\left(\frac{x'y'}{rz_1}\right)\right] \Bigg|_{x'=x1}^{x'=x2} \Bigg|_{y'=y1}^{y'=y2}$$

, (5.8)

where $\alpha_{12} = \hat{M}x, \hat{F}y + \hat{M}y, \hat{F}x$, $\alpha_{13} = \hat{M}x, \hat{F}z + \hat{M}z, \hat{F}x$, $\alpha_{23} = \hat{M}y, \hat{F}z + \hat{M}z, \hat{F}y$, $r^2 = x'^2 + y'^2 + {z_1}^2$.

Similarly, the gravitational attraction of each rectangular prism can be calculated with the use of equation 5.4 and 5.5. With constant density ρ and limits of $x_1 \leq x \leq x_2$, $y_1 \leq y \leq y_2$ and $z_1 \leq z \leq z_2$ the vertical attraction at the origin is

$$g(x,y,z) = \gamma\rho \int_{x1}^{x2} \int_{y1}^{y2} \int_{z1}^{z2} \frac{z'}{(x'^2+y'^2+z'^2)^{\frac{3}{2}}} dx'dy'dz'. \quad (5.9)$$

This lithology-based design assigns a geophysical property to each lithology instead of each cube making computation considerably faster. Editing is also fast as the programme is comparable with the drawing programme paint. As the volume is drawn, the voxels become active or de-active as you work on different layers of the model from the side 'profile' view or top 'map' view.

Data constraints such as lithological contacts, SRTM terrain data, density contrasts and susceptibility measurements are imported into the programme as constraints and modelling aids. The geology map of the area is converted into a colour map that can be used to draw on (Figure 5.20). Being able to draw the surface layer on the geology map makes the surfaces contacts substantially more accurate.

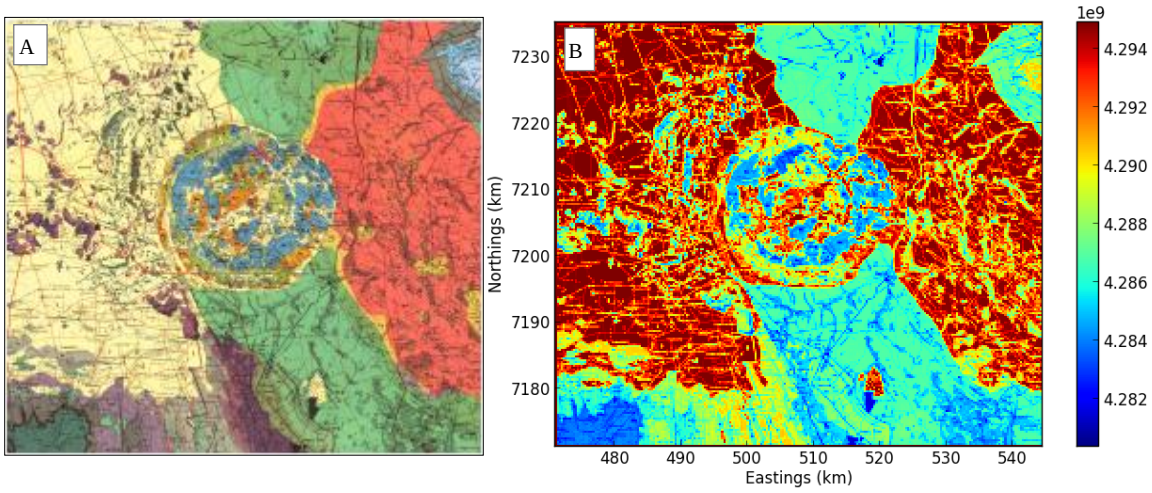

Figure 5.20 A) The input geology map converted to a PyGMI colour map (B) that can be used for surface geology references. The program converts the complicated colours of the geology map into a simple RGB colour range map. The colour bar legend (B) refers to the colour mapping of the geological lithologies from A) simply referring to whether they have been converted to a red tone or a blue tone. This is very simplistic but allows for the maps to be drawn on easily while switching between different data sets that are all colour converted.

The magnetic and gravity maps are drawn on to provide an accurate signal match on the surface. Figure 5.21 indicates the PyGMI converted Bouguer gravity map with a profile going across it. Each profile can have the susceptibility and density bodies drawn on them, in an x-direction, y-direction and map view on the surface down to the specified depth. The modeller is able to draw a body with both density and susceptibility specified and the 3D forward model will recalculate the fit to the data as it is drawn (Figure 5.21).

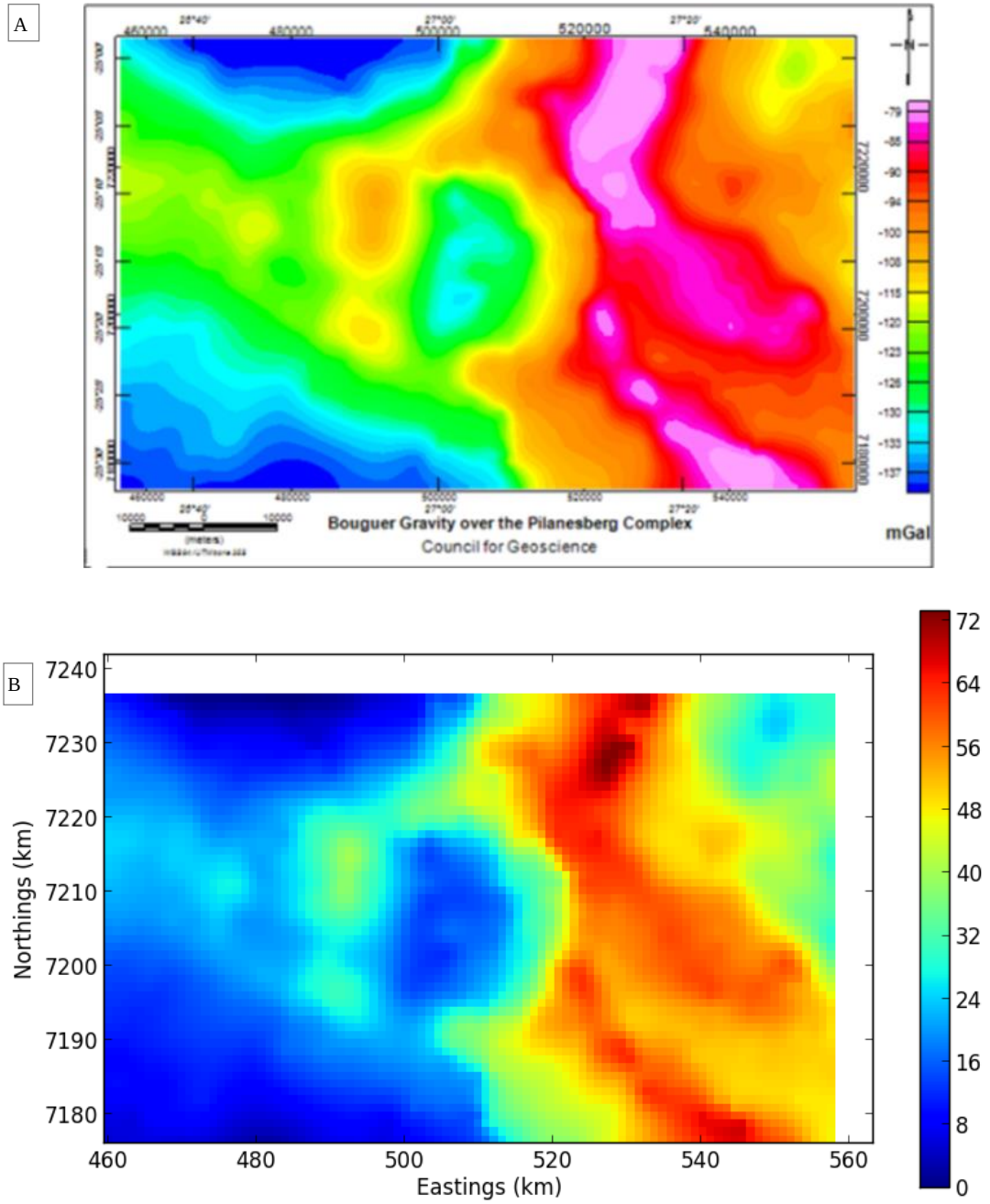

Figure 5.21 A) Original gravity map, B) PyGMI converted Bouguer gravity grid over the Pilanesberg and Bushveld Complex into a pixilated colour map where a high gravity value is represented by a red pixel and a low gravity value represents a blue pixel.

5.3.1.1 PyGMI west-east model

The profile cross sections (Figure 5.22) progress through the PyGMI forward model to indicate how the geometry and host rock accommodation changes as the west-east profiles progress northward. The jagged edges display the 3D modelling aspect of the geometry along NS, WE profiles and depth layers. The model indicates an estimate geometry that is providing a possible solution to the gravity data. The PyGMI model is a forward model however it is important to note that the model presented is a fully 3D model.

The profiles presented (Figure 5.22 and Figure 5.23) represented slices through the 3D model (Figure 5.24) that indicate the change in geometry. Densities use are 2.68 g.cm^{-3} for the Pilanesberg Complex, Bushveld Gabbronorite 2.99 g.cm^{-3}, Granite 2.62 g.cm^{-3} and the background 2.65 g.cm^{-3}.

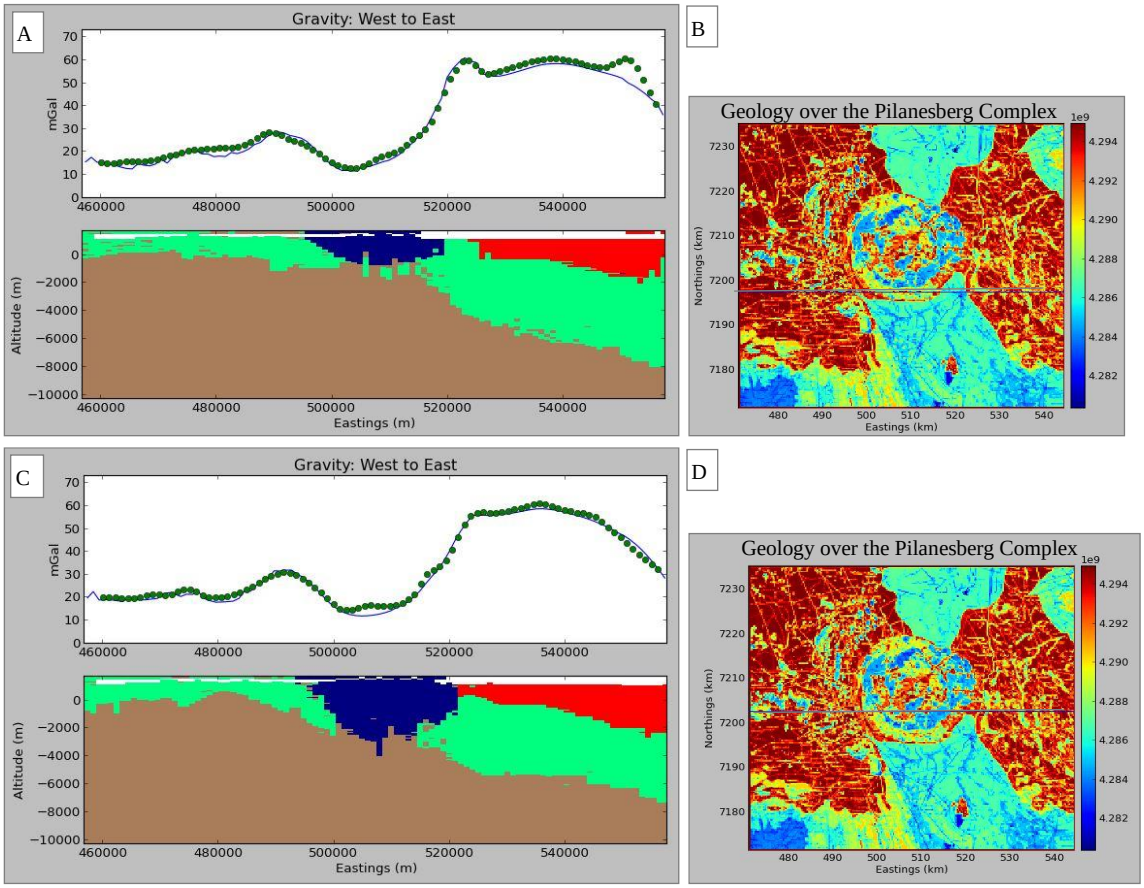

Figure 5.22 A and C) PyGMI profile views of the 3D forward model with the blue line representing the gravity data and the green dots are the calculated response to the modelled geometry. B) The first profile is a west east profile through the southern edge of the Pilanesberg Complex. A) On the southern edge of the Pilanesberg Complex, the profile cuts through a small section of the Pilanesberg Complex that would have intruded from the centre outwards hence there is Bushveld material below it. C) A profile slightly northwards (D) indicates the increasing depth of the Pilanesberg Complex as well as an inward dipping geometry along the west-east profile. Model key: Blue – Pilanesberg Complex, Green- Bushveld Gabbronorite, Red- Bushveld Granite.

As the profiles progress north towards the centre of the Pilanesberg Complex (Figure 5.23 A) and further north (Figure 5.23 D), the Pilanesberg Complex modelled with a density of 2.68 g.cm^{-3} has an average

depth extent of ~ 5 km. The PyGMI model does not indicate linear feature such as faulting. However, the shift in the Bushveld material accommodating the intruding Pilanesberg Complex gives an idea of how the rock may have faulted and shifted. This concept is observed on the west of Figure 5.23 A where two blocks seem to have formed as the Pilanesberg Complex pushed into the Bushveld Gabbro. Similarly, Figure 5.23 D the gabbro appears to be deeper on the east of the Pilanesberg as it moved down into the fractured Transvaal Supergroup to accommodate the Pilanesberg Complex.

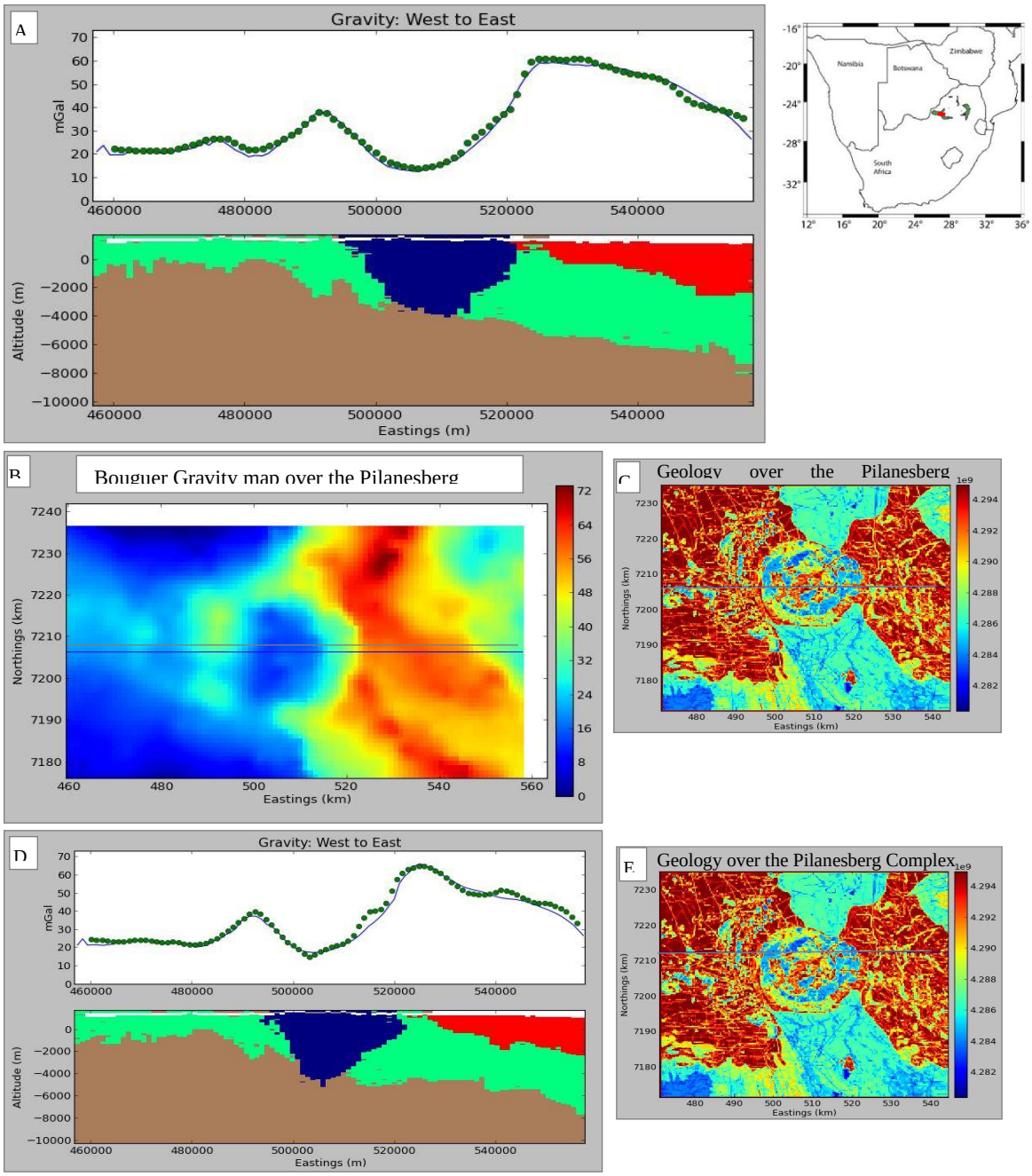

Figure 5.23 West-east profile sections through the 3D PyGMI model. A) The profile over the centre of the Pilanesberg Complex shows the Pilanesberg Complex inward dipping (in blue) into the Bushveld Complex (green) and Bushveld granite (red). These features correspond to the gravity map in B), and geological map in C). D) and E) are a profile slightly to the north of the centre showing a change in angle of the Pilanesberg Complex.

Once all the profiles in the x, y and z-direction have been drawn, in correlation with all the available data, and then the 3D forward model can be displayed. In Figure 5.24, the 3D model has the Transvaal Supergroup set as translucent so the Pilanesberg Complex (Blue) can be seen extending down to ~ 5 km and is surrounded by the Bushveld Complex gabbronorite (Green) and granite (red) to the east.

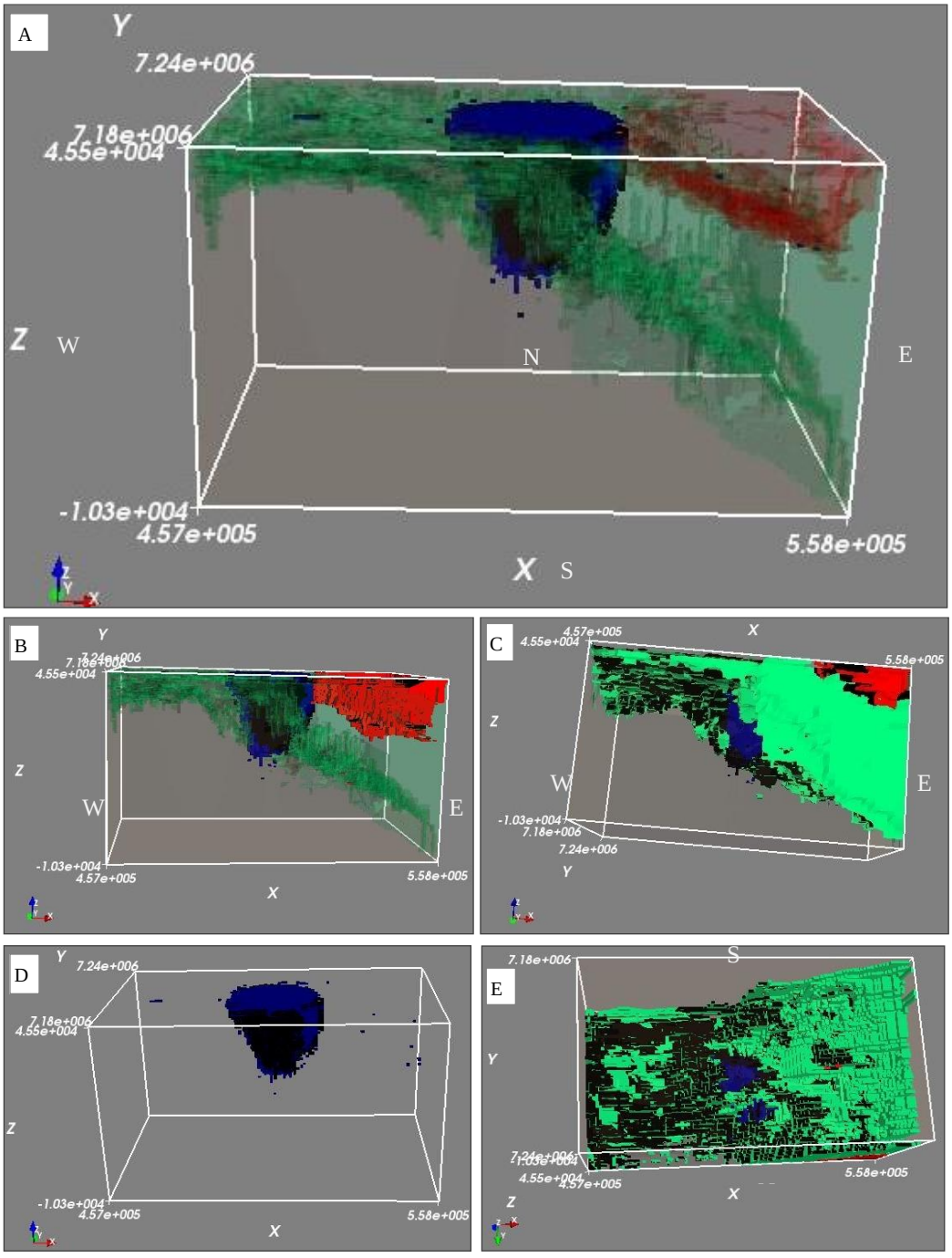

Figure 5.24 3D PyGMI forward model with the Pilanesberg Complex (blue), Bushveld Complex (green) and Bushveld granite (Red). A-D) indicates the southern edge of the model with different translucency layers. E) Rotates to a bottom view, observe gabbro below the Pilanesberg Complex.

From the west-east profiles, it is seen that the gravity and geology map are comparable with the 3D model providing a possible solution to the data. The overall geometry is of an inward dipping cylinder that has a depth extent of ~ 5km. The eastern edge in contact with the Bushveld granite is vertical before dipping inward. A bottom view of the 3D model indicates that there is Bushveld Gabbro below the Pilanesberg Complex. This could mean either that the Pilanesberg Complex pipes intruded around that material on emplacement or that the granite was shifted there during the structural events explored to explain the northward dip.

The depth of the model is based on the densities measured in Appendix D for the Pilanesberg rocks. The density constrains and the shape and dip information from the Euler deconvolution solutions and 2.5D forward models assist with modelling the 3D model to fit the gravity data. The depth of the 3D modelled Pilanesberg Complex is based on the realistic densities. The solution space of the bottom contact varies by ± 2 km with the body being slightly deeper with a lower density and slightly shallower for a higher density.

The north-south Bouguer gravity profiles are modelled with the PyGMI forward model to test Lurie's (1986) geological model of an outward dipping Complex on the northern edge. The 3D model slices through the Pilanesberg Complex at intervals in order to give an overview of the geometry of the Complex along the north-south profiles (Figure 5.25). The densities used in this model include the Pilanesberg Complex at 2.68 g.cm^{-3}, the Bushveld gabbronorite at 2.98 g.cm^{-3} and the Bushveld Granite at 2.62 g.cm^{-3}.

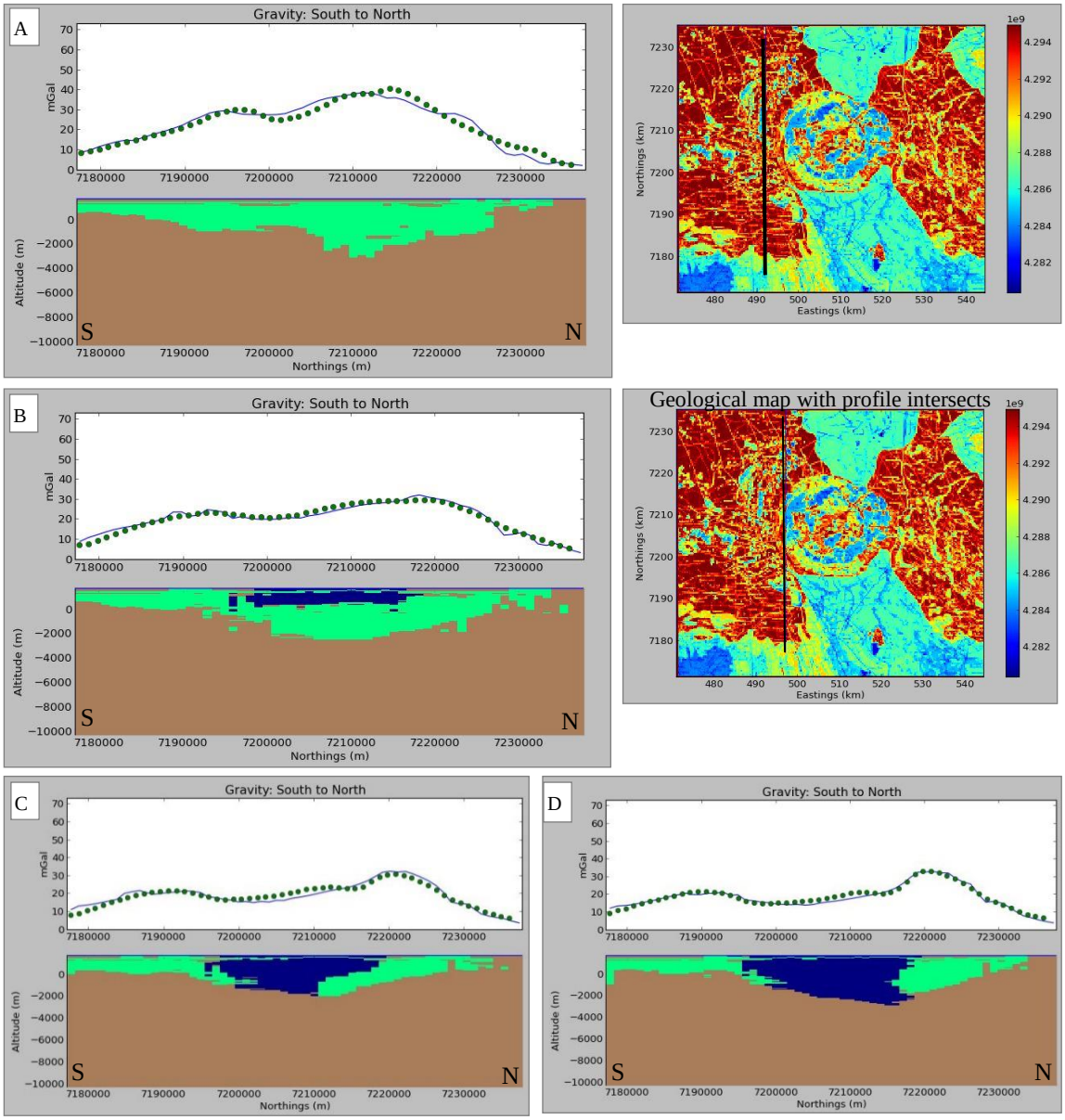

Figure 5.25 A) The profiles start cutting through the displaced gabbronorite of the Bushveld Complex. The profile moves east to intersect the Pilanesberg Complex, B) as it continues some of the northern dip is starting to indicate C) and D). Green – Bushveld Gabbronorite, Blue- Pilanesberg Complex

As the north-south profiles continue towards the Pilanesberg centre, the geometry indicates that the northern edge dips to the north while there is an inward dip from the southern edge (Figure 5.26). One observation is that the outward northern dip is not very specific as a constant edge (Figure 5.26 C) as well as a hooked edge (Figure 5.26 A) both fit the gravitational data so long as the overall dip is an outward dipping northern contact.

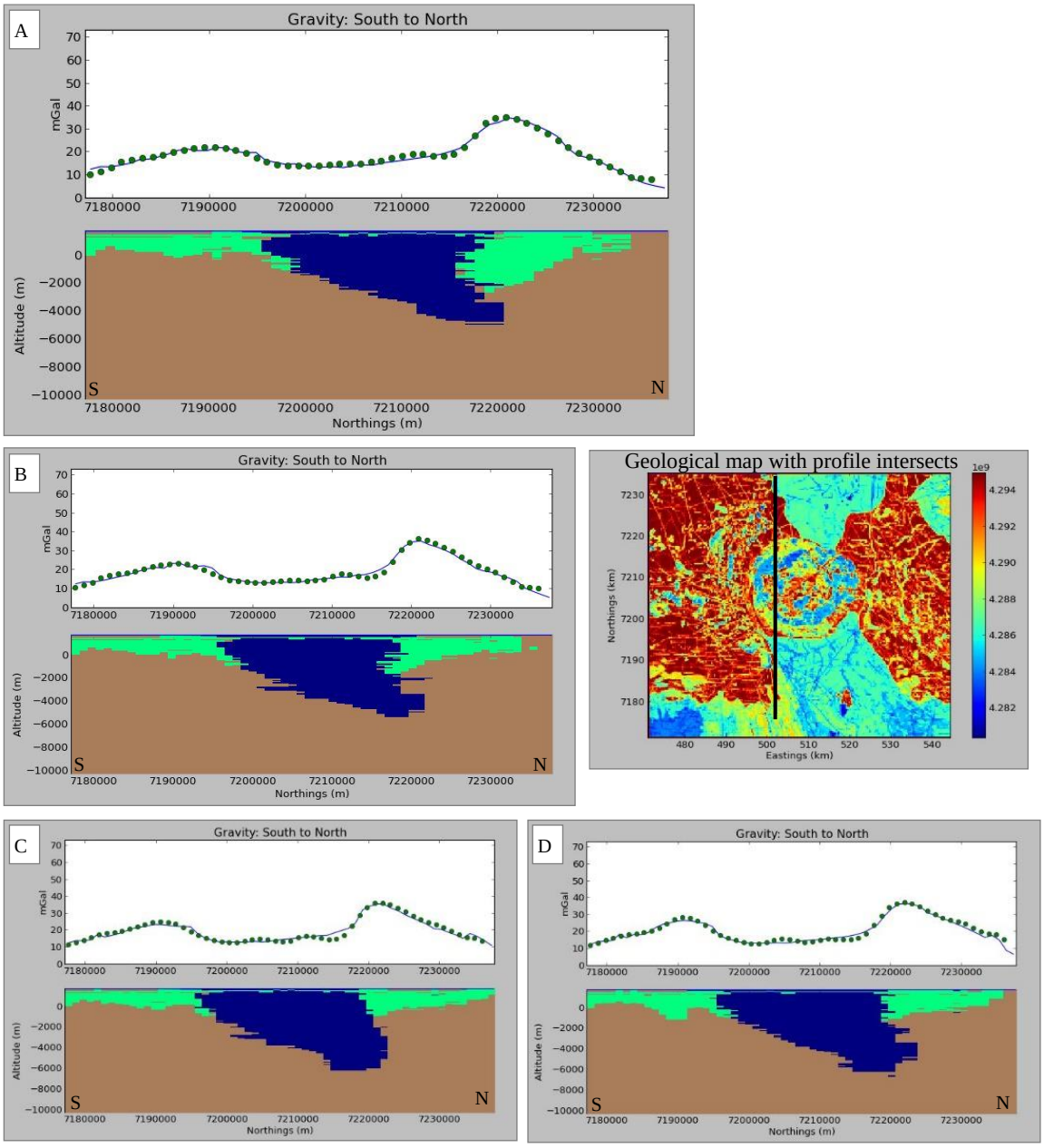

Figure 5.26 The north-south Bouguer forward model profiles cut through the Pilanesberg Complex in an easting direction. The profiles indicate how the Complex is increasing in depth and how the northern outward dip is developing as viewed in A-D). Green – Bushveld Gabbronorite, Blue- Pilanesberg Complex.

The central profile crosscuts through the Complex to indicate the modelled body reaches a maximum depth of 8 km with the majority of the mass averaging a depth of approximately 6 km (Figure 5.27).

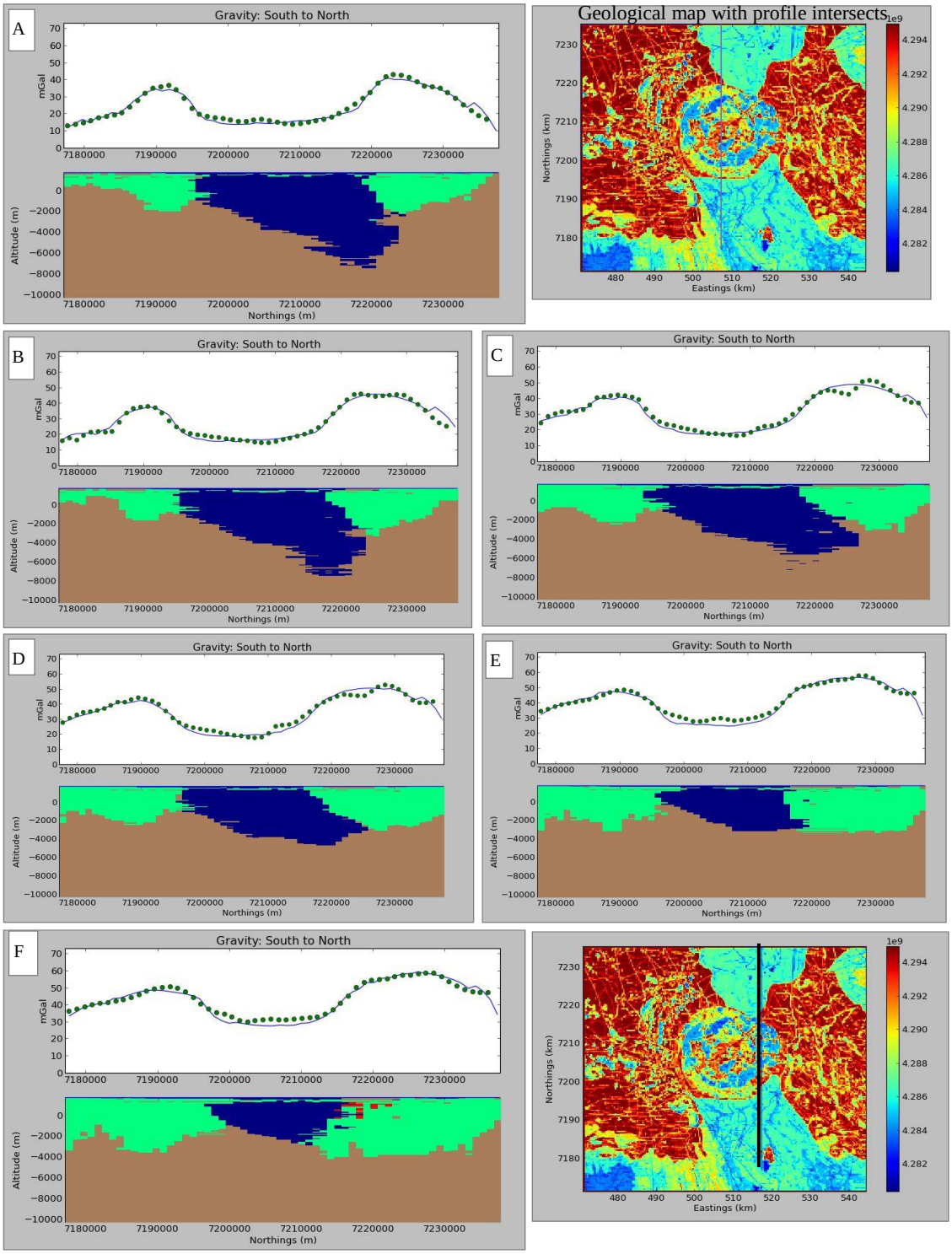

Figure 5.27 A and B) The centre of the Complex reaches a depth of ~6km. C-E) the geometry maintains the outward dip to the north as the profiles continue to move east while they decrease in depth. F) Finally, the eastern edge of the Complex intersects some of Bushveld granite. Green – Bushveld Gabbronorite, Blue- Pilanesberg Complex, Red-Granite.

The results of the modelling are compared by examining the original Bouguer gravity data (Figure 5.28 A) with the resultant calculated gravity (Figure 5.28 B) produced from the calculated response to the 2D profiles and 2D layers that make up the 3D bodies. The calculated gravity is an overall match to the Bouguer gravity data, with slight differences seen in the shape of the Pilanesberg Complex in the south as well as more Bushveld material to the west of the Pilanesberg Complex.

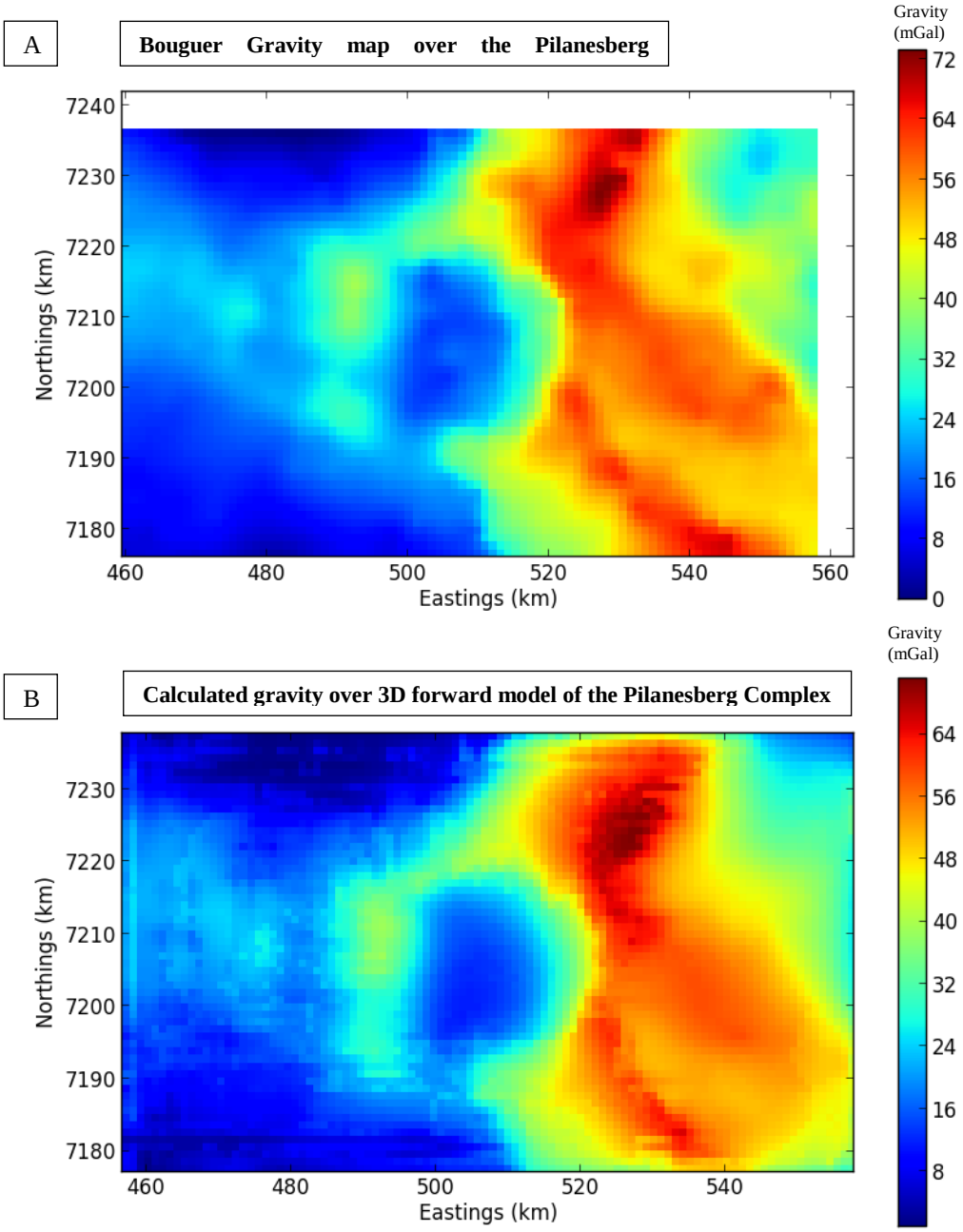

Figure 5.28 A) Bouguer gravity data map imported in to PyGMI. B) The calculated gravity response modelled in layer view, forming a 3D representation of the calculated response to the Pilanesberg geometry.

The 3D forward model (Figure 5.29) is based on the best-fit Bouguer gravity profiles displayed in Figure 5.27 to Figure 5.29. This is a single model seen in three views to illustrate the Pilanesberg Complex intruding in to the Bushveld Complex with the northern edge dipping out to the north.

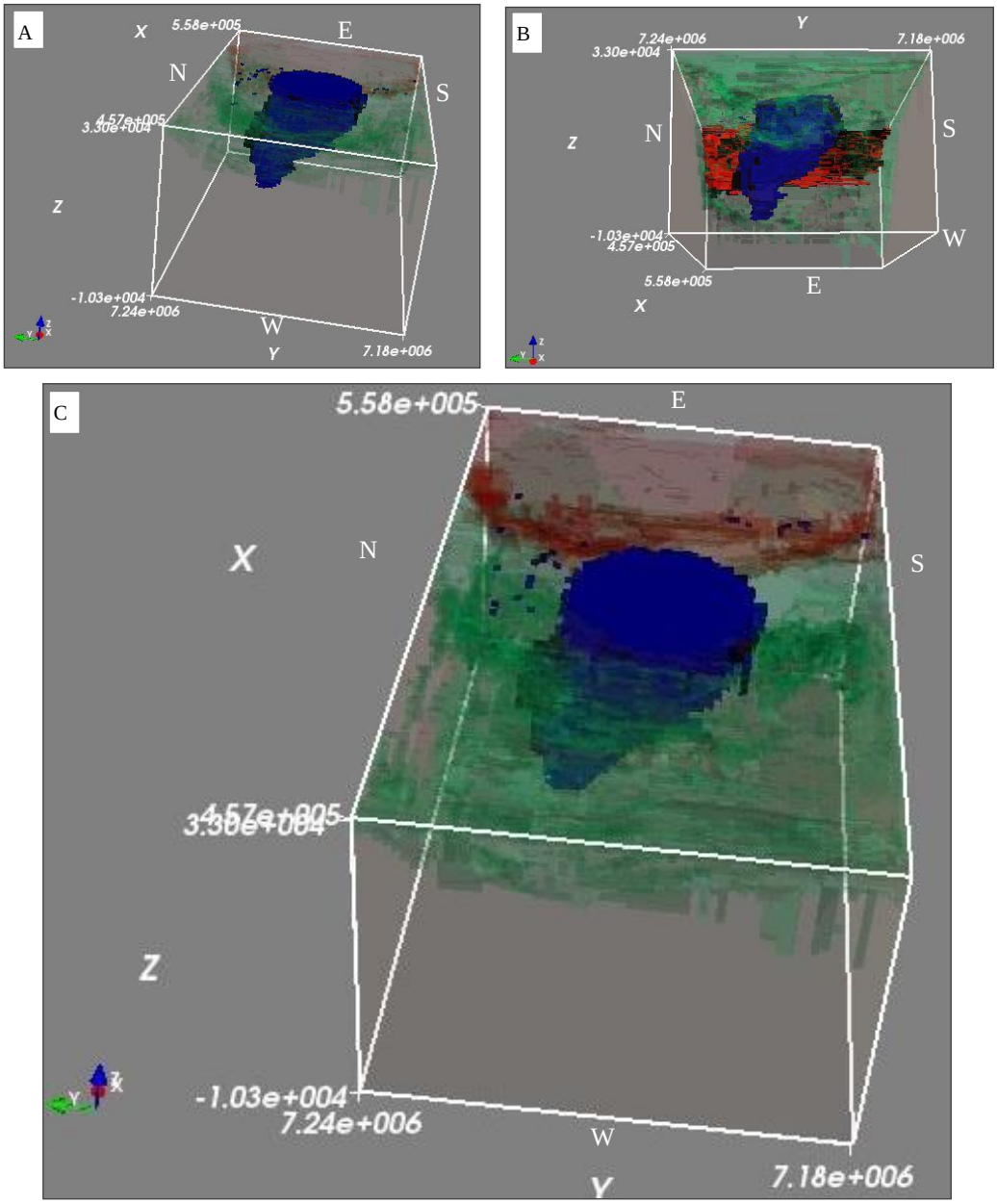

Figure 5.29 A 3D forward model produced with PyGMI from the Bouguer gravity data. A) Illustrates how the Pilanesberg Complex intruded from depth up towards the surface. B) Indicates the outward dip towards the north and C) indicates how the Pilanesberg Complex intruded into the Bushveld Complex.

The final 3D PyGMI Bouguer gravity forward model indicates that the Pilanesberg Complex dips out to the north while dipping inward from the east, south and west. The depth estimate is approximately 5 km on the west-east forward model while the depth is estimated to a maximum of 6 km on the north-south forward model with an average of approximately 5 km.

5.4 3D INVERSION METHOD

The use of 3D modelling and inversion techniques extends the 2D investigation into an understanding of the bodies' 3D geometry, internal structures, depth extent and an idea of how the body came to be. Using the magnetic data over the Pilanesberg Complex, a 3D Voxi model inverts for the body and internal structure (**Figure 1.6**). The Voxi model uses a block of cells in which each cell is a calculated density or susceptibility to make up a 3D model based on the Blakely theory (1995).

5.4.1 3D Application to the Pilanesberg Complex

Assessing the Pilanesberg Complex geology is followed by an investigation into the mode of emplacement for the Pilanesberg Complex. The 3D geometry of the Complex and its intrusion affected on the crust is investigated by 3D modelling of gravity data and inversion techniques to determine the basic shape of the Pilanesberg Complex.

The development of the 3D inversion model will use both gravity (**Figure 1.8**) and magnetic data (**Figure 2.20**) as the initial defining physical constraints for the model limits. The other constraints inputted in to the model include the upper limit of the body, the physical properties, gradients changes along the bodies shape and the approximated lower bound or bottom depth.

5.4.2 University British Columbia inversion theory

The University of British Columbia (UBC) 3D inversion based on the Bouguer gravity data was used to identify constraints on the Pilanesberg Complex geometry and the interaction with the Bushveld Complex (BC). The inversion is based on Blakely's (1995) inversion algorithm.

The national gravity grid has a low resolution due to the average 2 km station spacing. Thus, the UBC method of inversion is only able to produce a first pass model to suggest the dip directions of Pilanesberg contacts with the surrounding host rocks (Figure 5.30). While the Pilanesberg geometry has not been achieved in these inversions but the confirmation of dip directions is important for confirming any geometries proposed by the 2D test or forward models.

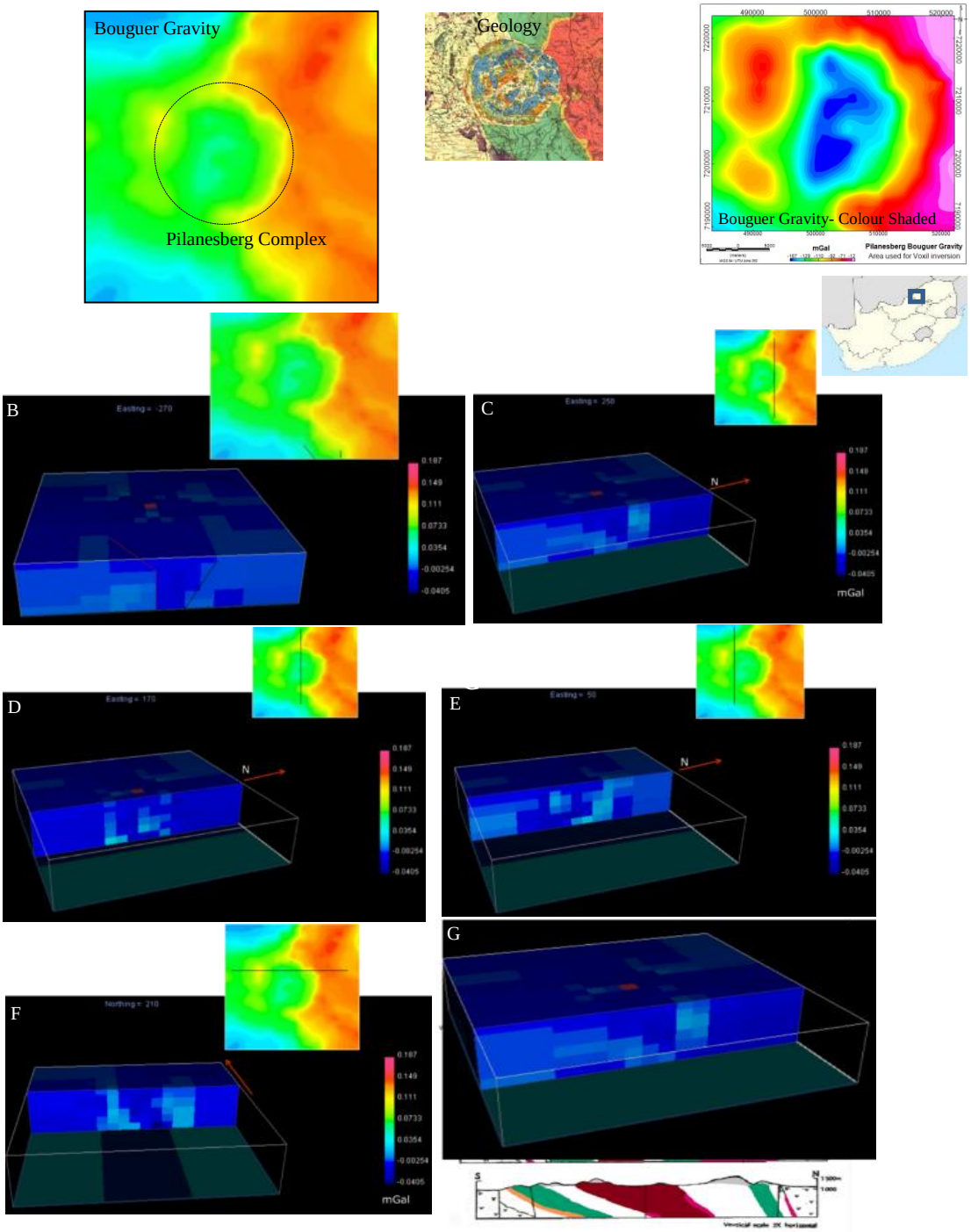

Figure 5.30 3D UBC Bouguer gravity inversion has horizontal slices indicating density contrasts between the Pilanesberg Complex and the Bushveld Complex (BC). A) Bouguer gravity map used to invert with the geology map, B) 3D UBC inversion indicates inversion edge features on the Bouguer gravity map, C) NS slice indicates the Pilanesberg Complex dipping to the north, D) central NS slice indicates a vertical body, E) Eastern NS slice indicates a dipping inward body, F) WE slice indicates a dipping side to the west and solid mass in contact with the BC. G) Comparison of the NS slice with Lurie's (1986) reprint indicates the inward dip toward the south and outward dipping structure to the north in contact with the host rock.

The results from the UBC inversion are consistent with the shapes and edges conceived in the 2.5D profile models and 3D PyGMI model. The inversion fits the density and gravity data with a limited depth extent. The UBC model, while limited in detail due to the quality of the gravitation data it inverted for, indicates that there is some interesting internal structure that could not be modelled in the forward models.

The next inversion method will concentrate on the internal structure of the Pilanesberg Complex.

5.4.3 Voxi inversion theory

A Voxi inversion model is composed of a block of 3D cells used to a calculated the density or susceptibility of individual cells to make up a 3D model based on the theory calculated with Blakely's equations (1995). The inversion of the Voxi model uses the Magnetization Vector Inversion (MVI) technique. This accounts for varying magnetisation direction in a model so that effects such as remanence, demagnetization, anisotropy and induced magnetisation are accounted for. (Burns, 2012). This represents a rock magnetisation model with measured magnetic rock properties. The equivalent gravity model uses the rocks measured densities to calculate the inversion model. The Voxi model allows densities and susceptibility clipping, so a portion of the model can become transparent to indicate the internal structure. This allows for in-depth investigation into the geometry and internal structures.

The Voxi has an x, y, z-cell wireframe below selected area. In this case, an area directly around the Pilanesberg Complex selected on the aeromagnetic map is overlain on the wireframe. The magnetic data is used as one of the constraints as susceptibility data for the computation of the model. The computation uses 'cloud' based servers hosted by Geosoft, which produces an output that can be further constrained be susceptibility, upper, and lower bounds, gradients, starting models and weighting.

The stacked 3D cells in the inversion space are computed for the grid over 50x by 50y by 50z cells in the x, y and z-direction. This cell size offers computation on small areas of only a few kilometres, so the larger area has a lower resolution as the same number of cells spread over a smaller area. The Pilanesberg Complex, which is approximately 30 km wide and the number of cells to invert for is limited, so the Complex will not have the highest resolution model but it will be able to indicate large-scale features in the magnitude of the complex internal geometry. The magnetic grid used for the inversion just encompasses the Pilanesberg Complex structure (Figure 5.31). This means that only the internal structure is examined with this method. An external geometry interpretation would require an area 3 times the size of the one selected to see the shape of the Pilanesberg Complex.

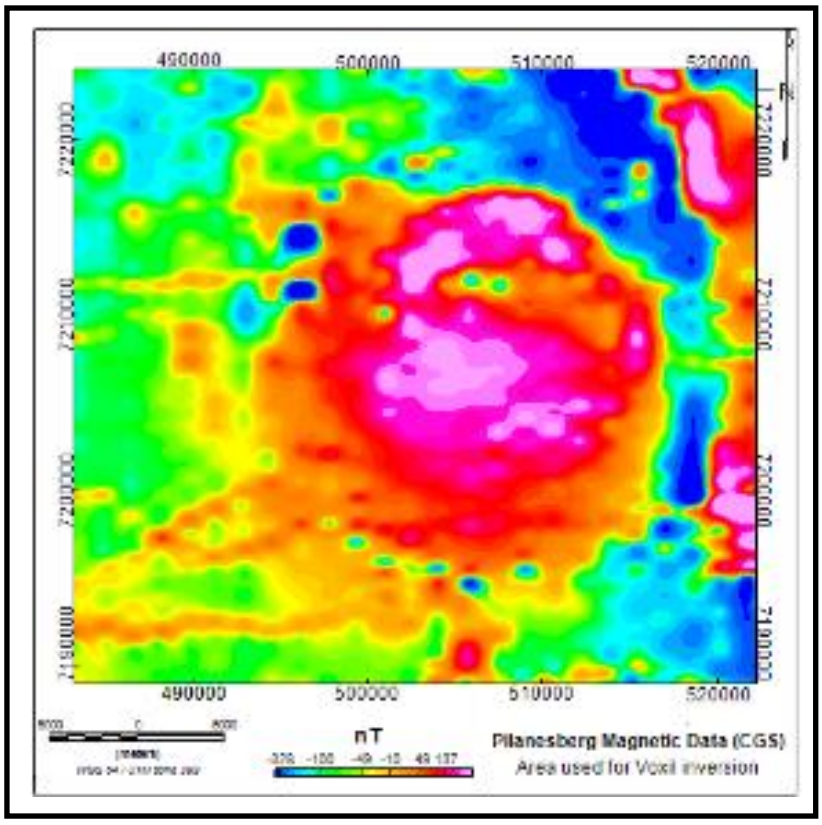

Figure 5.31 Magnetic grid exclusively over the Pilanesberg Complex with the hexagon outlining the 3D Voxel inversion space.

An idea of the internal geometry within the Pilanesberg Complex is observed when the Voxi models weaker susceptibilities are clipped away so that the stronger susceptibility layers can be interpreted from the internal structure (Figure 5.32).

This provides an inversion interpretation of the internal geometry and trends in the internal structure may provide evidence for the external geometry of the Complex. A side-by-side view indicates a northward-orientated 3D model that starts with the magnetic data over the grid and changes to the inverted model. The bottom views of the Voxi indicate the internal central structure, which also is clipped off the lower susceptibilities to indicate the internal structure (Figure 5.32).

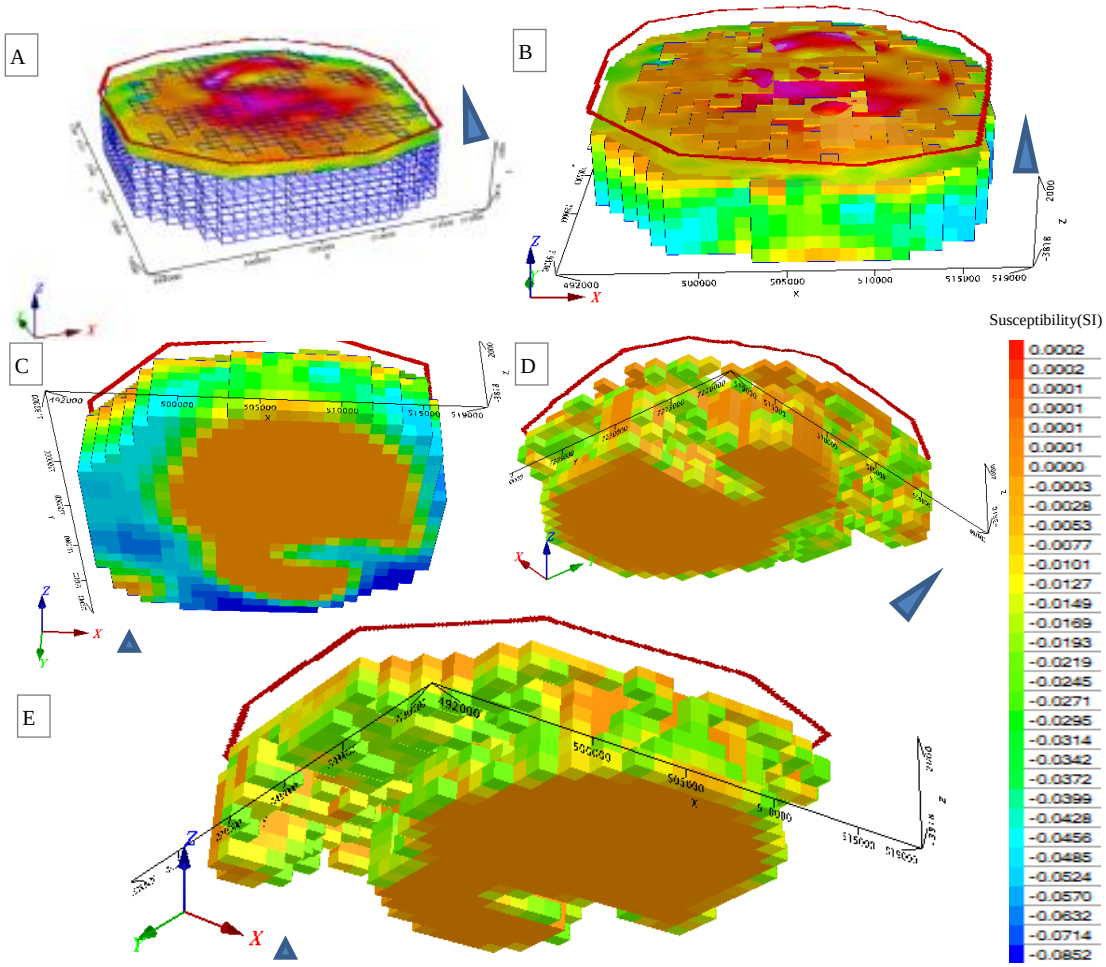

Figure 5.32 Magnetic data over the Pilanesberg Complex indicated as a (325 nT) positive anomaly. (A) 3D Voxel Inversion using the South African Aeromagnetic map indicating the mesh that is used, (B) A preliminary susceptibility inversion of the Pilanesberg magnetic data into a 3D Voxi model using a 27x27x9 cell inversion. (C) View from below, (D) View from below showing how the Complex decreases in size from the surface to depth. The model has been cut away to identify the internal structure within the Complex. (E) View from the East.

Continuing to examine the internal structure of the Pilanesberg Complex, west-east sectional views through the model from the south to the north display the internal changes within the Complex by showing how the different susceptibility layers interact with each other (Figure 5.33).

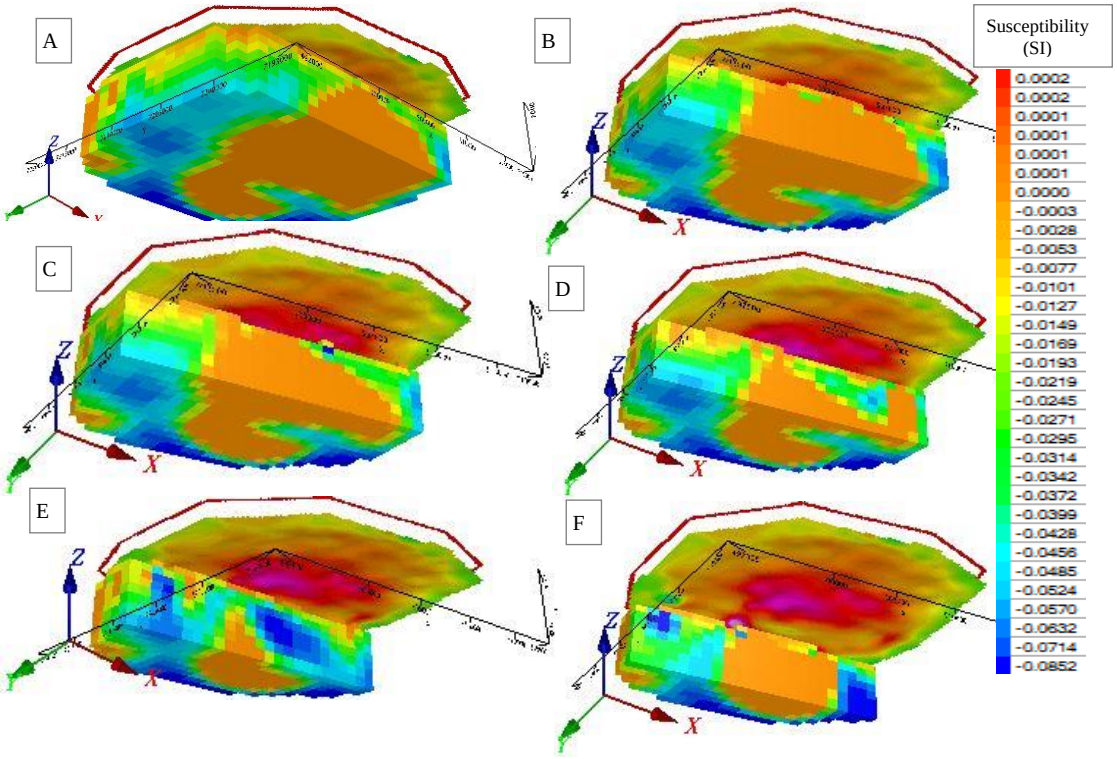

Figure 5.33 West-east sectional views through the 27x27x9 magnetic susceptibility inversion of the Pilanesberg Complex. The view is from the bottom of the Voxi with the magnetic map overlaid for reference. A 3-D displays the central magnetic anomaly, which has an outward dip to the east. E and F display a good correlation with the magnetic map, where another less dense body in the range of -0.071 SI has either intruded between the plug like susceptibility body of 0.001 SI. North is in the Y direction.

The same inversion model examines the north-south sections viewed from the west. The western view (Figure 5.34) depicts a gradational model, which has a surface susceptibility of -0.0127 nT and middle value of -0.0271 and a susceptibility at the bottom of the model of -0.0458 nT. As the sections move towards the east/middle of the inversion, the plug-like body appears to be intruding up towards the surface of susceptibility -0.0003 nT (Figure 5.34 C-F) and finally seems to cut through the lower susceptibility material (G and H) as it heads for the surface. This may be depicting two different 'Pilanesberg rings' that have a similar susceptibility and thus have been inverted as part of the same body.

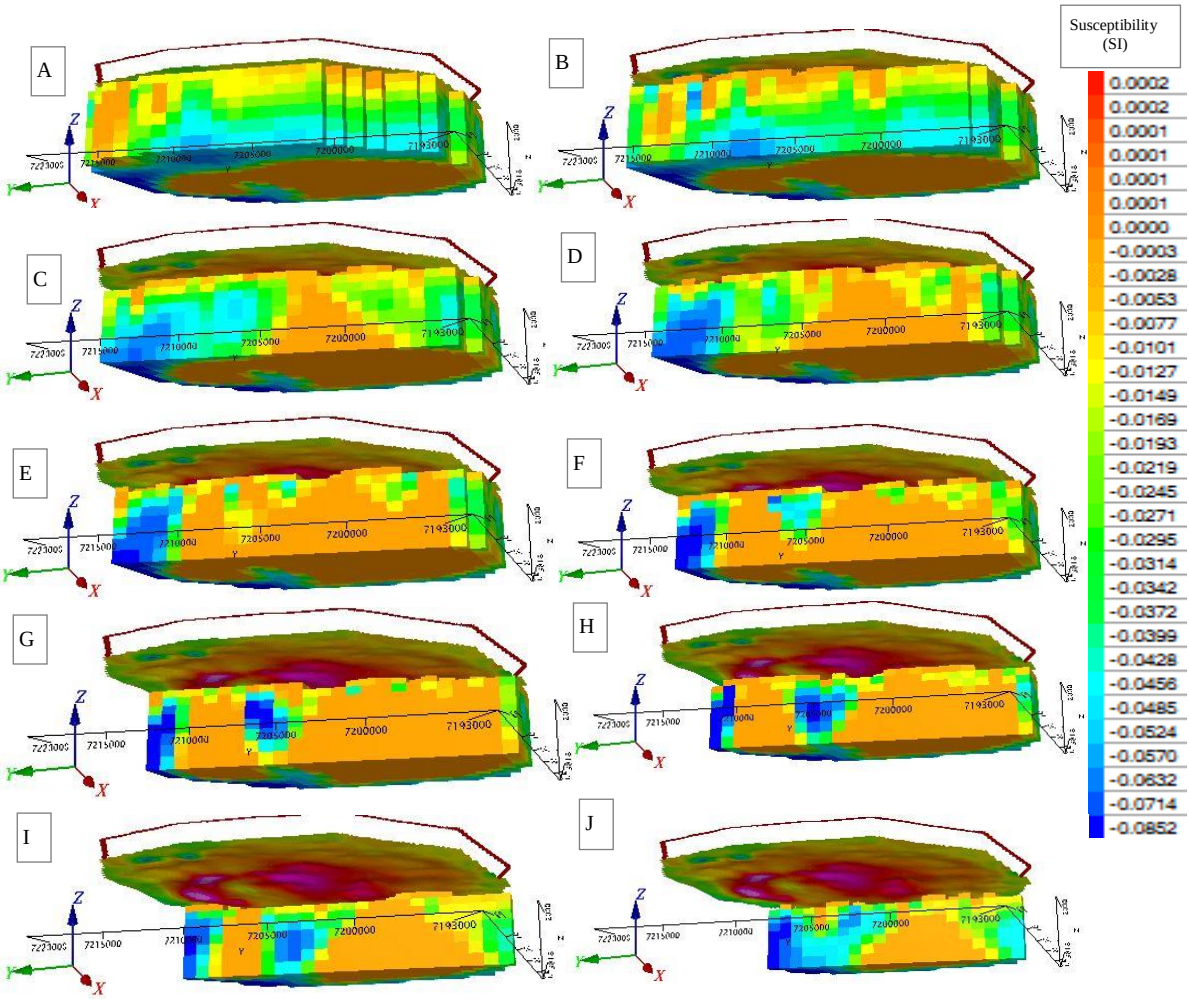

Figure 5.34 North-south sections through the Pilanesberg Voxi susceptibility inversion viewed from the west. A-B) The western side has a multilayer susceptibility. C-F indicates how the central susceptibility of -0.0003 has come up and intruded towards the surface. G-I indicates that the central body (-0.0003 SI) intruded into and cross cut the low susceptibility body (-0.0714 SI).

The Voxi method is able to compute models from both gravity data in the form of free-air, Bouguer, isostatic residual gravity as well as residual magnetics once the data has been corrected and processed for the diurnal correction, and IGRF removed from the magnetic data. In this case, the magnetic data that was collected by the Council for Geoscience in the 1970s', and is DGRF corrected.

The Magnetic Vector Inversion (MVI) still uses the same inversion theory to create a 3D model. However, this one is inverting for the vector as opposed to the susceptibility. The inversion uses 55 X cells, 58 Y cells and 15 Z cells to produce a total volume for the model of 3496.69 km^3 and a standard deviation of 0.007. Figure 5.36 indicates the MVI with more cells and a greater volume. The volume indicates a larger amount of magnetic matter in the north of the Pilanesberg Complex. The magnetically clipped layer appears to be deeper in the southern half of the Complex (Figure 5.35). The magnetic susceptibility of the voxel model has been clipped in Figure 5.35 to reveal that the material of a similar magnetisation is closer to surface in the north and extends to a greater depth of the Complex's southern block.

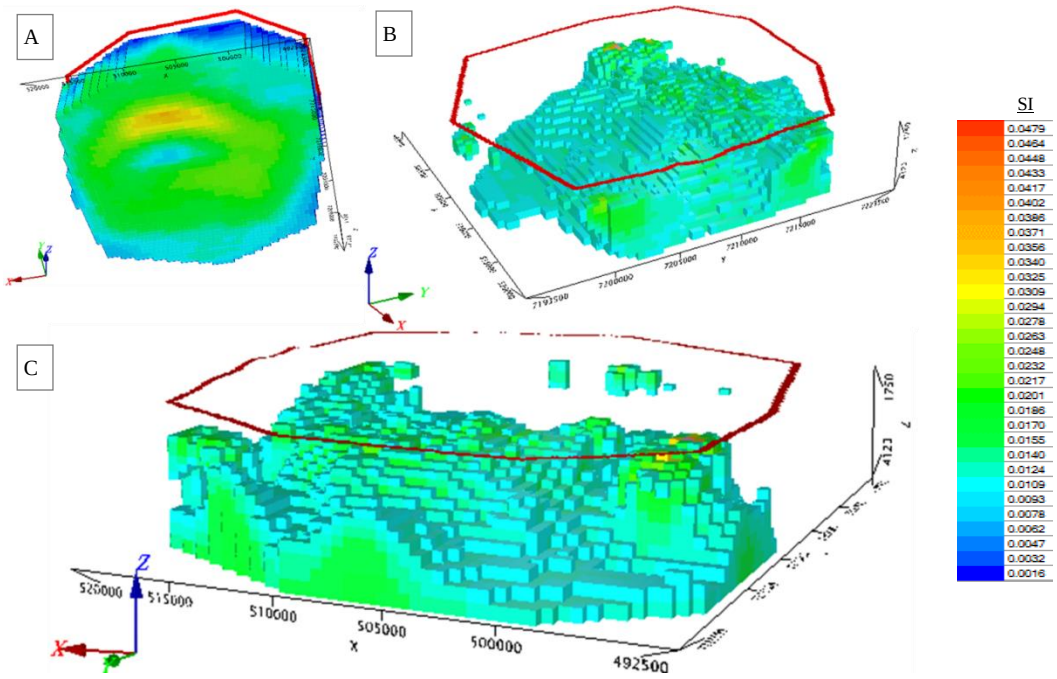

Figure 5.35 Aeromagnetic data 3D is inversion-using cell a cell mesh of dimensions (x, y and z): 55x58x15. This model indicates the internal structure of the Complex as well as identifying the dip of the structure where the northern edge is closer to the surface and becomes deeper towards the south. A) Bottom view, B) South view and C) West view.

The magnetic vector inversion picks up a difference in depth from the surface to a magnetic body, which indicates that the south has a magnetic mass that is deeper than the magnetic material in the north. This could be due to the way the body has intruded or due to faulting, tilting and weathering. Interestingly the MVI is able to pick up the geological Vlakfontein fault, which cuts through the Pilanesberg Complex from the northeast to the south-west (Figure 5.36).

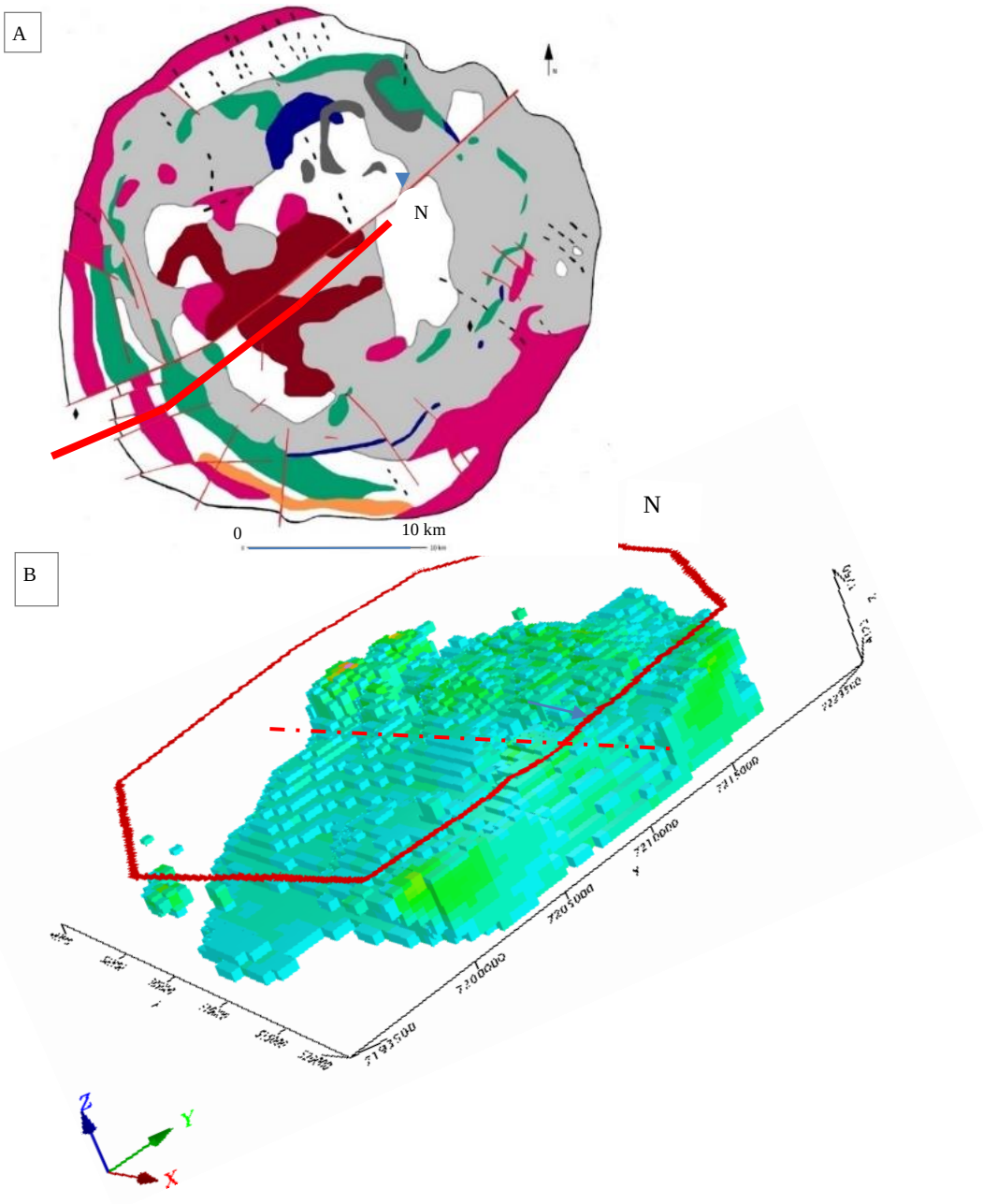

Figure 5.36 The Vlakfontein fault seen to cross cut the geology of the Complex in A) has been picked up by the magnetic vector inversion in B) which indicates the north of the Complex at the specified magnetic intensity to be closer to the surface while south of the fault is deeper.

The internal structure of the Pilanesberg Complex also examined through sectional views and depth slices. The depth slices indicate a continuous internal ring at depth (Figure 5.37 A) which progressively is disturbed by a lower density material as the depth slices move towards the surface (Figure 5.37 B-F).

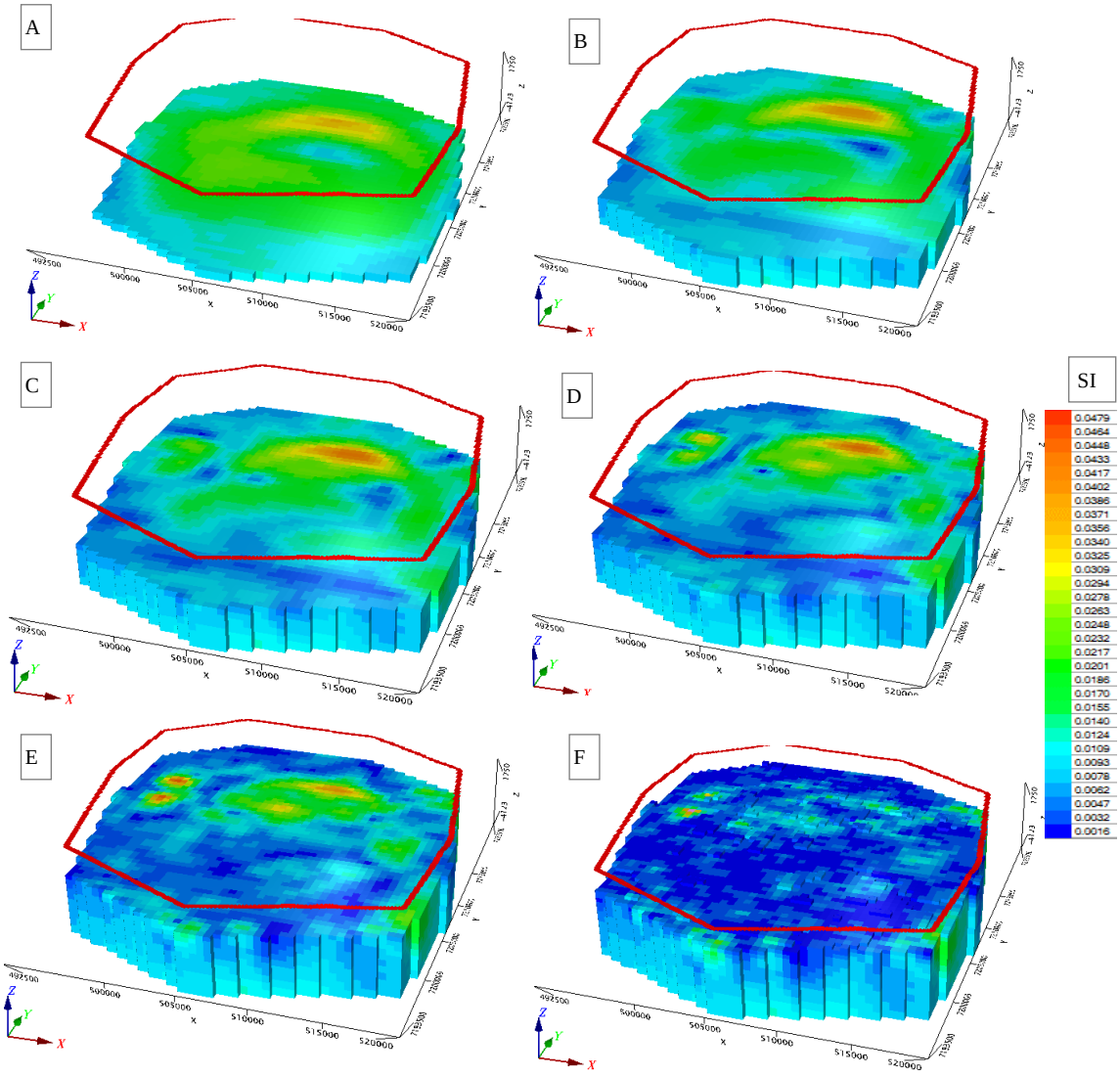

Figure 5.37 A Z-slice progression through the 55x58x15 magnetic vector voxel inversion from the bottom at A through to the surface at F.

The Voxel inversions indicate denser internal bodies to the north of the Pilanesberg Complex, and a plug can be identified further north. The complicated ring structure is also identifiable with denser layers at the bottom of the model. These give an idea of the internal structure and how it behaves in relation to the geometry of the Complex. The inversions do not provide a new theory for the Pilanesberg Complex overall geometry. The next two images provide a section view through the Pilanesberg Complex with the sections moving from south to north displaying changes in the sub-surface with depth (Figure 5.38).

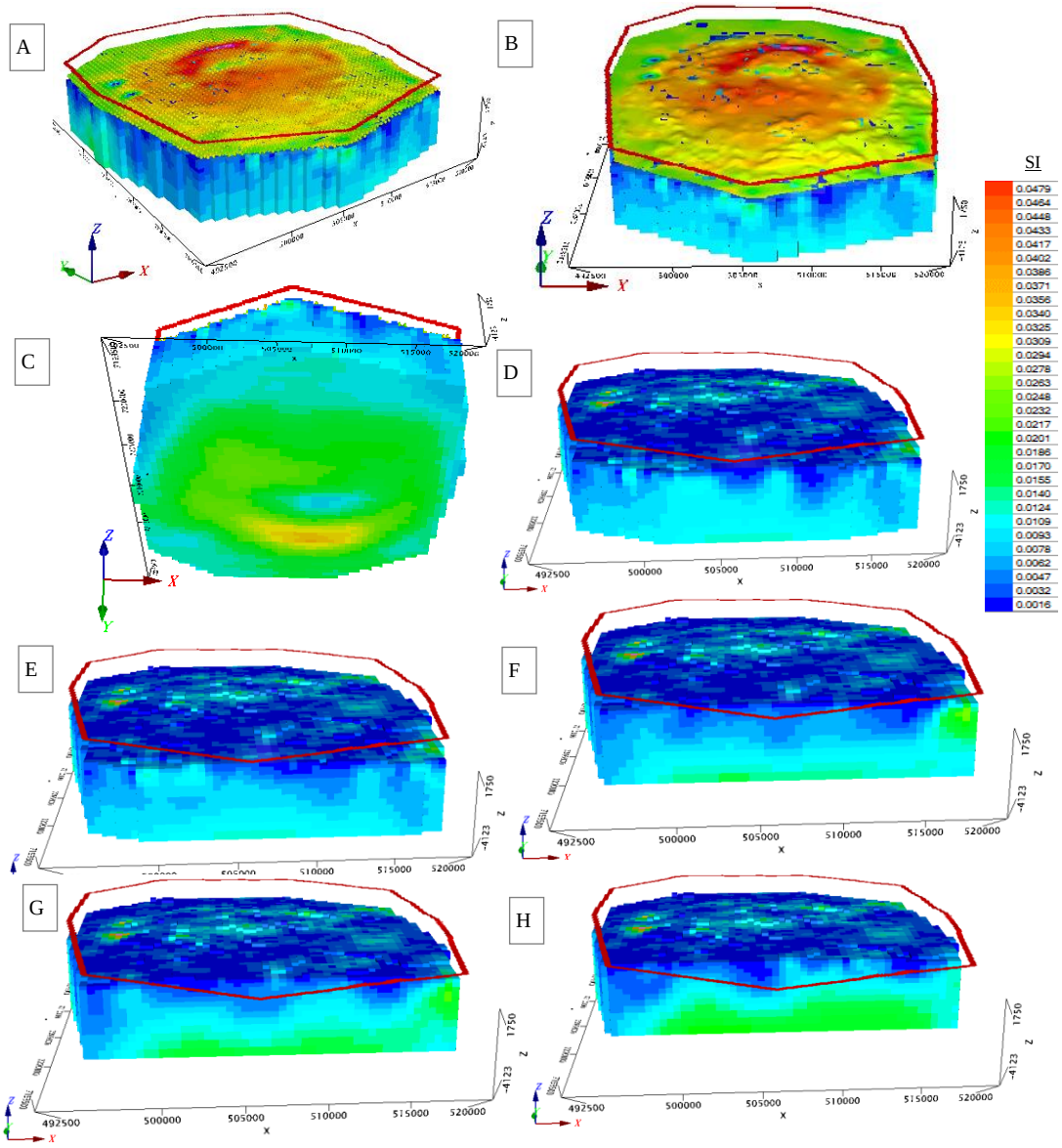

Figure 5.38 MVI Voxi inversion of the Pilanesberg Complex of the magnetics (A and B), A bottom view in C and sectional views moving from the south in D, north towards the centre of the Complex in H.

Moving along the MVI model in a northern direction, the density observed within each profile increases and throughout the model, there are stages of intrusions that would relate to the different lithologies or rings of the Pilanesberg Complex (Figure 5.39).

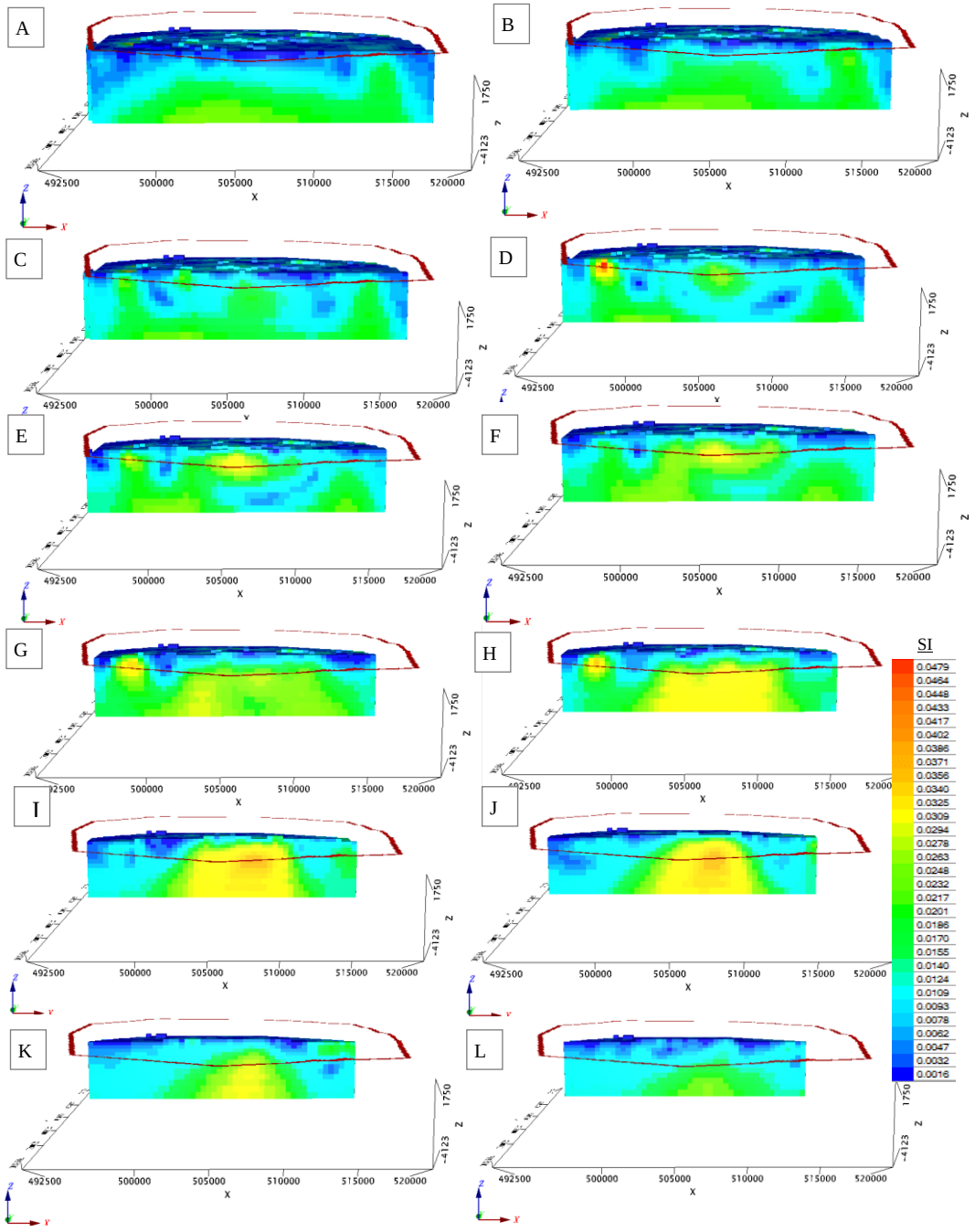

Figure 5.39 East-west sections are moving northward from A to L of the Pilanesberg Voxi MVI inversion. In A and B, the three-layer susceptibility is evident. In the centre (C-F) the -0.0217 SI body is introducing in different places through the model. Towards the north of the model (H-K), a higher susceptibility layer (-0.0309 SI) of the body is closer to the surface.

The north-south sections viewed from the west for the 55x58x15 cell mesh Magnetic Vector Inversion (MVI) indicates how the magnetic material is closer to surface in the north and slopes deeper to the south (Figure 5.40). Often, there is a gap between the -0.0217 susceptibility body that has a correlation with the location to the Vlakfontein fault. The sectional view continues in Figure 5.41.

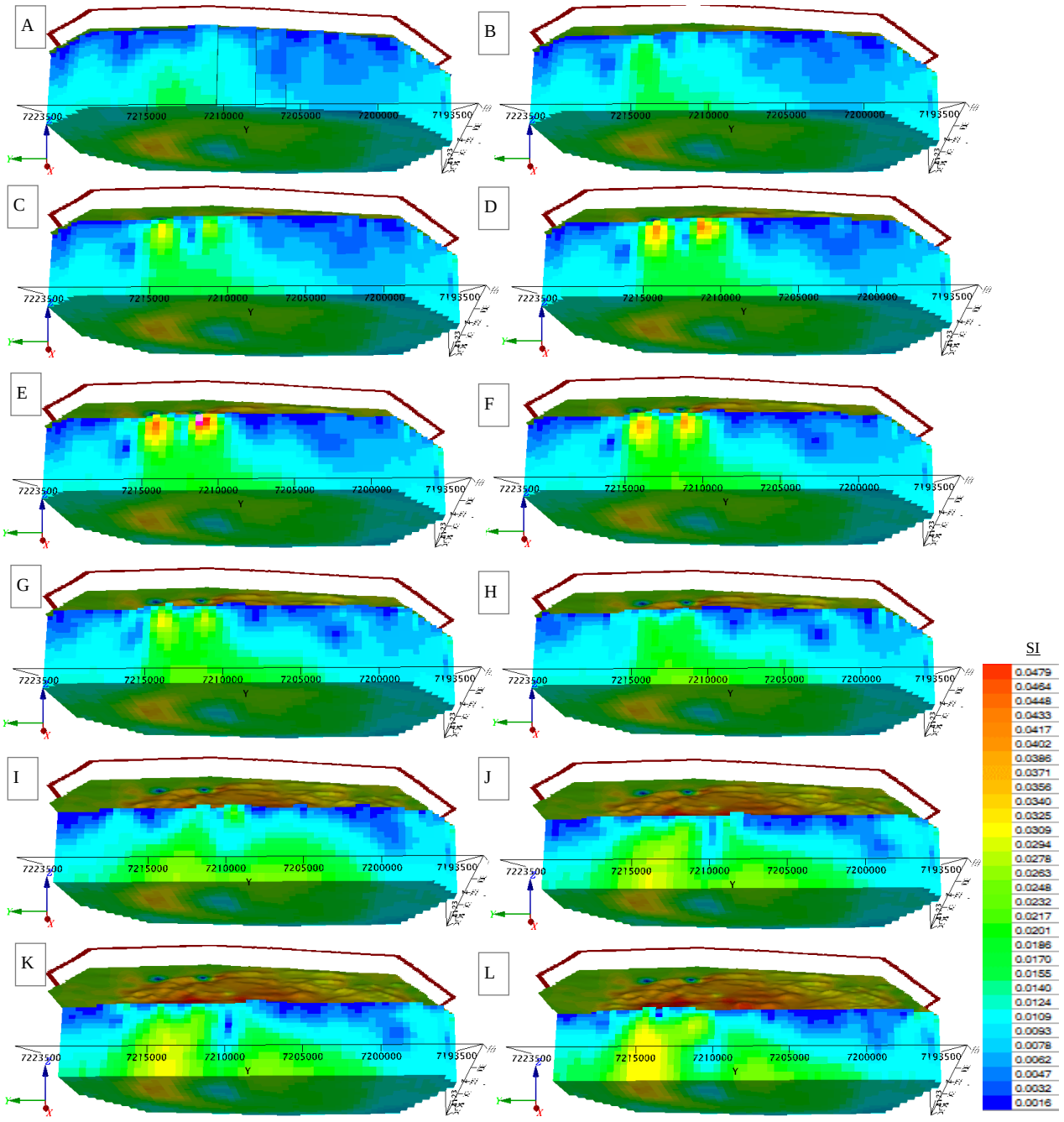

Figure 5.40 A bottom and north-south section of the MVI 55x58x15 cell inversion viewed from the west with the magnetic map above the model. The models

Similarly, as the sections continue in an eastward direction through the MVI inversion, the higher susceptibility material becomes more prominent towards the centre of the model before fading slightly towards the eastern edge. There is a gap in the centre which could either be a body coming out up to surface in two parts, like 'rings', or the disturbance is due to the Vlakfontein fault that bisects the north and south of the Pilanesberg Complex (Figure 5.41).

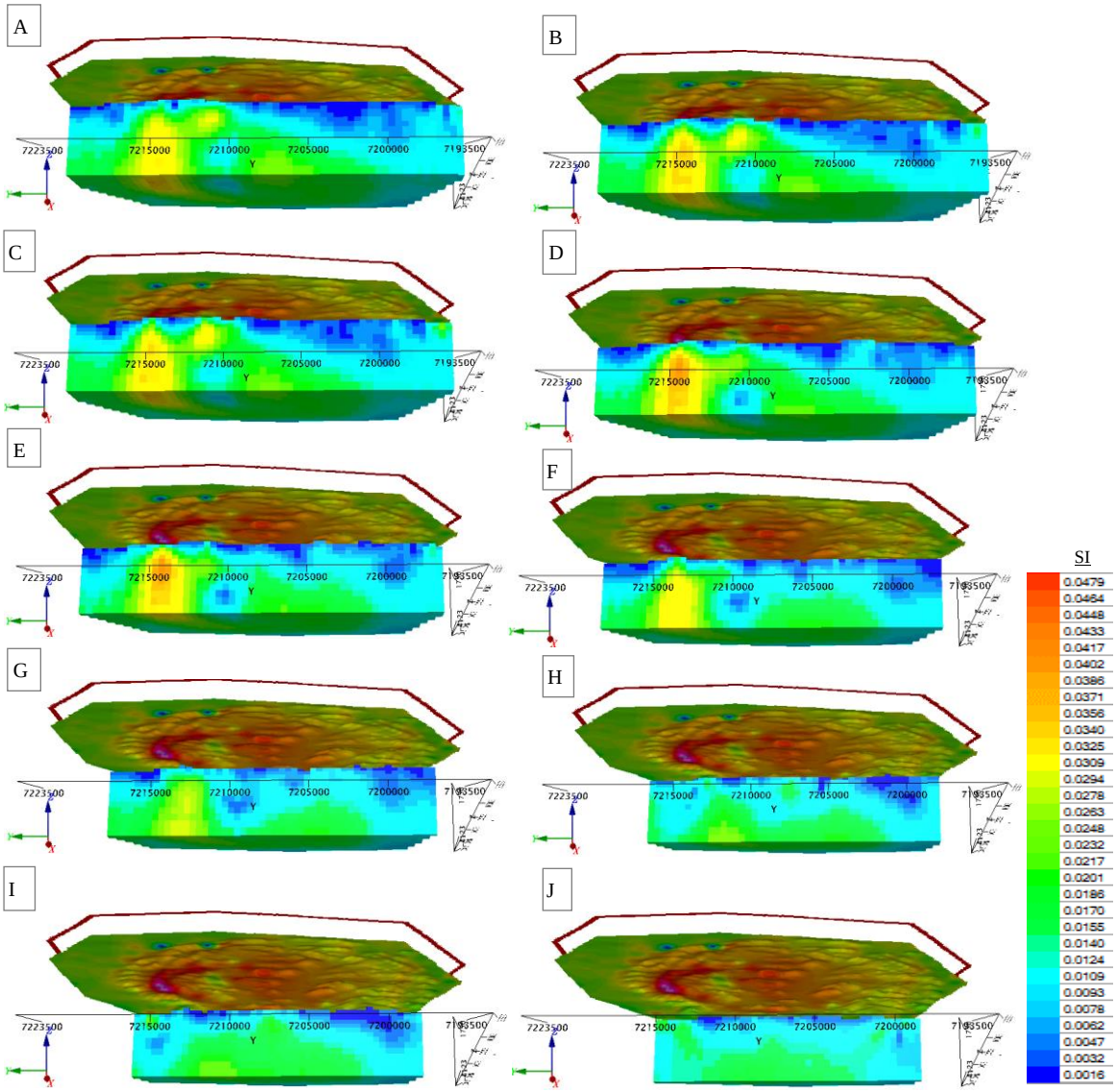

Figure 5.41 Continuation of the north-south sections, moving in an eastward direction along the 55x58x15 cell MVI Voxi Pilanesberg Complex model. A higher magnetic susceptibility area is again seen to the north of the model, which slopes deeper towards the south.

5.5 SUMMARY

The aim of modelling the Pilanesberg Complex was to produce a model that confines the geometry of the Complex in relation to the Bushveld Complex and surrounding rocks and to investigate the internal structure of the Pilanesberg ring structure.

Various models were created and calculated to test the field potential responses. To start, the 2D forward modelling produced with Grav2Dc tested the shape of the Pilanesberg Complex in relation to the surrounding rocks with the gravity data and surface geology constraining the models. The test models indicated that an inward dipping model best fits the gravity data while the cylindrical and outward dipping models were unable to satisfy the gravity data over the Pilanesberg Complex.

PyGMI, the 3D forward modelling package, allows simple drawing of a representative geology model along 2D profiles in both an NS and WE orientation. The geological bodies drawn on depth sections increase the accuracy of the vertical sections, and together these form the 3D perspective of the forward model. The calculation for the forward model indicates the disparity between the measured data and the drawn model after the computation of the 3D forward model. The advantages of this model are that it accounts for a 3D calculation for the bodies making it more realistic than the 2.5D profile models. However, the bodies are subject to an amount of artistic licence with the bodies drawn along vertical and horizontal sections. The error in this type of forward model is substantial due to the amount of artistic licence involved. Unlike most other forward modelling packages. However, this kind of forward model is advantageous because of the quick 3D output model. The models can be used to test for multiple solutions, to provide an essential idea for a simple geological model that has a rough match to the data. The results indicate that the west-east model has an inward dipping geometry that reches a depth of ~ 5km. The north-south model indicates that an outward dipping edge on the north is able to fit the Bouguer gravity data. This model achieves a maximum depth of 6 km with an average depth of ~ 5km.

The inversion of the Pilanesberg Complex was achieved with various programmes to compare the results.

The University of British Columbia (UBC) inversion uses the gravity data to create a 3D geometry. The model is course due to the 3 km station spacing of the gravity data, but the inversion model can indicate the contact geometry of the Pilanesberg Complex with the host rocks. The 3D inversion indicates that the Pilanesberg Complex has an inward dipping geometry in the south and outward dipping to the north. The

western edge is also inward dipping while the eastern edge appears to be vertical in contact with the Bushveld Complex.

The gravity data was used with the PyGMI 3D forward model and the UBC inversion. The results for both methods are very consistent showing the largely inward dipping geometry with an outward dipping northern edge.

The magnetic data was used with the 3D Voxel inversion by Geosoft, which has a minimum number of cells available for inversion due to the computation of the algorithm. As such the inversion area, in this case, has been constrained to the edge of the Pilanesberg Complex. The resulting inversion model concentrates on the internal structure and physical property differences as opposed to the geometry relationship with the surrounding rocks. A course model with a cell size of 27x27x9 investigates a susceptibility inversion. This model indicates a central plug that forms a 'C' like shape with the majority of the rock mass in the south. The plug may exhibit this shape due to the disturbance in the geology from the Vlakfontein fault, which causes a 'C' like shape in the central plugs instead of the expected concentric plug. The central plug appears to intrude towards the surface from depth as it indicates a dip towards the east along some of the cross-sectional views.

The finer cell model inverts for a 55x58x15 cell volume using a Magnetic Vector Inversion. The west-east sections through the voxel model detect the central plug as a prominent feature. This model indicates greater detail indicating a delineated physical property difference between the ring structure. The model also indicates that the different rings are extending towards the surface.

5.6 INTEGRATION AND GEOLOGICAL INTERPRETATION

In this Section, the information gathered from the gravity and magnetic inversion models and the 2D and 3D forward gravity models will be used to develop a final geological model that both confirms and refutes certain models from previously published models of the Pilanesberg Complex. The paragraphs that follow present literature key concepts that explain the features seen on the forward and inversion modelling as well as geological processes required to define the geological model.

In this case, the fractionation of large magmas occurred in the crust at depths greater than 10 km (Ferguson, 1973). Shand (1928) suggested that even though the Pilanesberg Complex was the focus of the unsaturated alkaline magma chamber, the extent of the Pilanesberg dykes indicates a widely developed magma chamber beneath the Bushveld Complex in the Western Transvaal. This magma migrates upward in large pipes.

The Pilanesberg magmas were able to move towards the surface through a broken-up network of fault blocks associated with the Bushveld Complex syncline axis and an intersection of two weakness zones that are now associated with the Pilanesberg dyke System (Shand, 1928). Most of the ideas about the Pilanesberg intrusion suggest that the magmas came up in conducts, which would have expanded closer to the surface. The first noteworthy event is the magma exploding on the surface to form tuffs. The tuff forms a layer that caps the Pilanesberg ring structure (Ferguson, 1973).

Two of the intrusion process ideas propose that the Pilanesberg Complex is a laccolith or large horizontal body. The ring structure in the buoyant migration of a laccolith occurs from caldera processes, where the central magma cools and sinks, allowing fresh magma to well up around it (Shand, 1928). Alternatively, Cawthorn (2015) suggested that the Pilanesberg Complex intruded as a large horizontal body with feeder pipes forming the different horizontal layer lithologies that are then eroded away with an angular erosion surface that resulted in the ring structure seen on the surface (Figure 1.12). However, those ideas do not correlate with the inward dipping layers mapped by Lurie (1986) (Figure 1.10).

Lurie's (1986) models indicate that the northern edge of the Complex dips to the north (Figure 1.10) and that makes it difficult to model a laccolith that would fit the concept. Here, the gravity and magnetic forward and inversion models (Figure 5.8, 5.10, 5.24-5.31, 5.36-.5.44) are used to produce a schematic representation of how the Complex intruded. The interpretation examines the Pilanesberg Complex from both west-east as well as north-south orientations to indicate the magma sequences, but also the structural process.

The 2.5 D gravity profiles over the Pilanesberg Complex tested an in inward dipping geometry, a cylinder and an outward dipping cone with the confirmation that the inward dipping model was the best-fit geological representation for the gravity data. The Euler deconvolution solutions provide depth estimates considered for the geology model. The Euler solutions along the west-east gravity profile (Profile 1, Figure 4.16) indicated there was a straight contact on the western edge to a depth of ~ 12 km while the eastern contact is vertical to 7 km. In contrast, Profile 2, which is the west-east profile to the north, shows the overall inward dipping structure where the western edge of the Pilanesberg Complex dips inward to ~ 8 km while the eastern edge also has an inward dip to ~ 15 km below the surface. Figure 4.18 shows the southern west-east profile, which has an inward dipping Euler solution to 10 km on the west and an 8 km vertical contact on the east.

The UBC inversion was able to identify edges and correlate the inward dip in the west and south of the Complex as well as the vertical edge to the east. The northern contact appears to be vertical in this inversion but the image shows only a basic outline Figure 5.30.

The 3D forward PyGMI gravity modelling (Figure 5.29) agrees with an overall inward dipping structure to a minimum depth of 5 km. The depth estimate of 5 km with this model is less than the average 10 km depth estimated with the Euler profiles discussed above. The Euler solution profiles estimated the Pilanesberg/Bushveld contacts so the 10 km could refer to the edge defined by the Bushveld and not the Pilanesberg Complex. The produced geological model uses the PyGMI 5 km as a minimum depth estimate for the geological model.

The Euler deconvolution solutions indicate that the northern contact does dip to the north to a depth of 12 km (profile 4, Figure 3.19). The 45° outward dipping northern contact is modelled with a positive data solution using the 3D forward PyGMI gravity model (Figure 4.26 – 4.30).

The first vertical derivative image processing of the magnetic data (Figure 3.5) has identified the outer ring as a positive magnetic ring with a remnant blue edge, a less magnetic second ring and a final highly central magnetic plug. The magnetic rings are associated with the density change between the outer red syenite, the white foyaite and the inner red foyaite.

The magnetic voxel inversion (Figure 4.30) further analyses the Complex's internal structure. The model indicates a defined magnetic anomaly in the heart of the Complex representing the plug. The west-east sections through the Voxi inversion indicate the central plug intruded toward the surface. This disproves any horizontal layer emplacements such as the model described by Cawthorn (2015) (Figure 1.12). The north-south profiles, however, indicate a break in the central plug, which is in the location of the

Vlakfontein fault on the surface (Figure 4.34). The possibility of block vertical movement is seen in Figure 4.39 and 4.40, which indicate that the block to the south has vertically displacement and is deeper in comparison to the northern block.

The geological model for the intrusion of the Pilanesberg Complex uses key concepts from published literature as well as features identified in the geophysical models to schematically describe how the Pilanesberg Complex formed.

The schematic sequence of events (Figure 5.42) indicates the magma is moving up through a fault network from a depth greater than 10km and into the edge of the western Bushveld as seen on the west-east profiles (Figure 5.42 A). The magma forms surface explosions to produce a layer of breccia and tuff (Figure 5.42 A and B). The initial magma (red) represents the red syenite. The continued rising magma and surface explosions result in a lateral widening of the magma toward the surface. The magma forms the ring structures by multiple stages of injection that widen the intrusion from the centre. This is made possible by the block faulting and fractures in the Bushveld Complex where the intrusion of the Pilanesberg Complex with the assistance of regional extension events was able to shift some of the Bushveld material to the west of the Pilanesberg Complex (Figure 5.44). The central red foyaite (orange) is the next layer to intrude into the centre. Vents and pipes take advantage of the fractured host rock to allow the emplacement of the white foyaite (Figure 5.42 C). The white foyaite intrudes around the central red foyaite through a process of caking or magma settling, which is equivalent to caldera settling, where the central red foyaite body sinks slightly, and the white foyaite wells up around it (Figure 5.42 D). The final ring to form is the green foyaite (Figure 5.42 E), which follows a similar process to the white foyaite. As the internal rings moved through the process of their formation and the Pilanesberg continued to expand, the Bushveld material to the east was fractured and faulted so it was able to move down to accommodate the new body. This is a very simplistic overview. It is expected that the fractures and block movement are substantially more complicated with accommodating factors such as uplift, extensional environment and erosion making up for aspects required for the simple illustration to be possible (Figure 5.42)

The intrusion events are envisaged in Figure 5.42 with a West-East profile schematic sequence, and Figure5.44, which indicates the corresponding North-South profiles. Sequences A-F in these diagrams represents equivalent time slots. Faulting and tilting episodes after the intrusion of the Complex are shown in the North-South profiles in Figure 5.47. The present-day West-East and North-South situations are shown in Figure 5.43 and Figure 5.48, respectively.

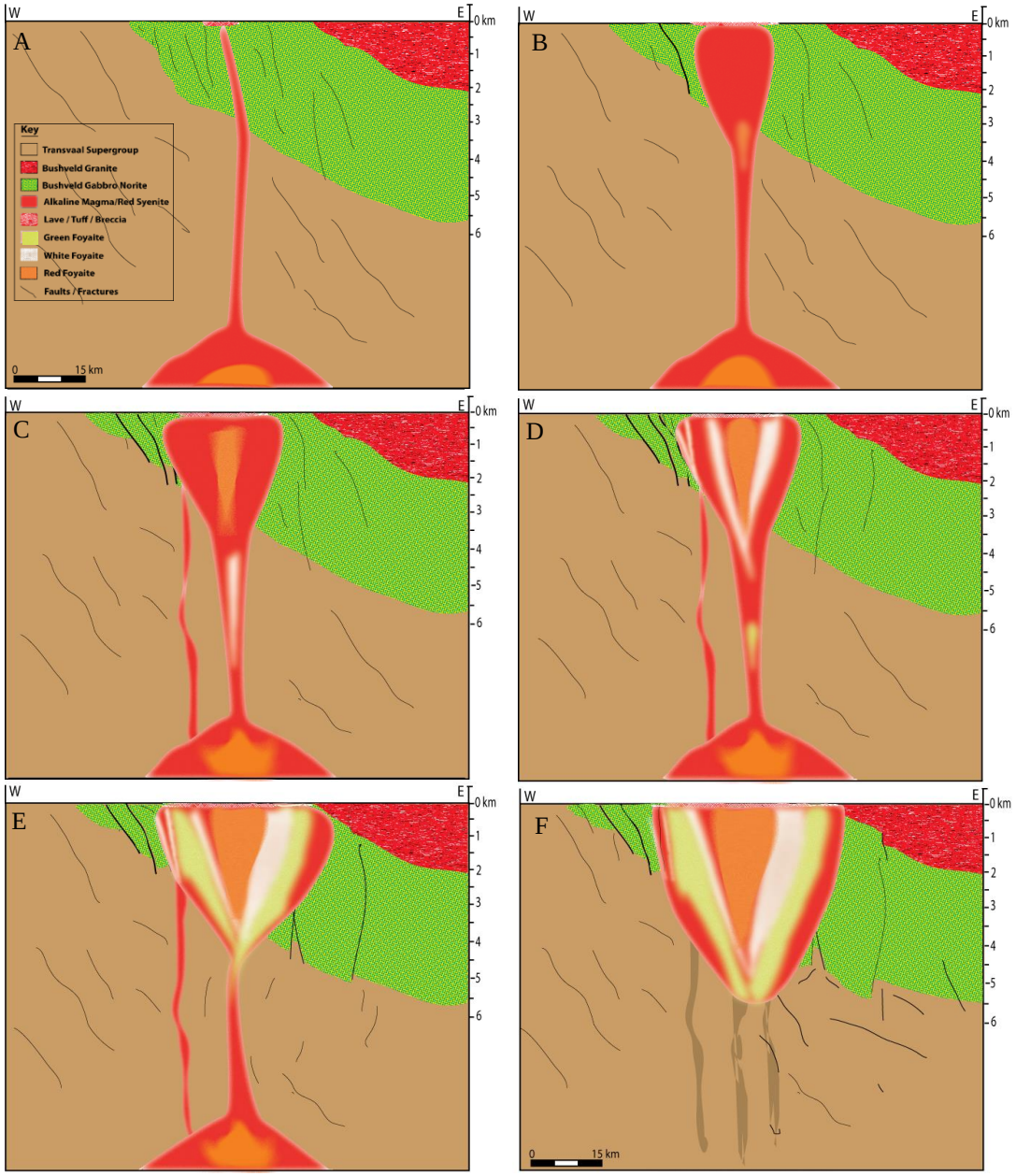

Figure 5.42 A schematic representation of the Pilanesberg magma intruding into the Bushveld Complex along west-east profiles. A) An under saturated alkaline magma moves upward through cracks and fractures associated with a weakness point. Surface explosions form a layer of breccia and tuff. B) Continued explosions cause the magma rising to widen toward the surface. The initial magma (red) represents the red syenite. C) The central red foyaite (orange) is the next layer to intrude into the centre. Vents and pipes use the fractured host rock to allow the emplacement of the white foyaite D). The white foyaite intrudes around the central red foyaite, where the central red foyaite body sinks slightly and the white foyaite wells up around it. E) Similarly, the green foyaite wells up around the white foyaite and finally, the magma process is complete F). The Bushveld accommodates the intrusion by moving fault blocks to the east while the west involves block compression and slight vertical movement of some faulted blocks.

The final model for the west-east profile schematic interpretation indicates the Pilanesberg Complex intruded into the Bushveld Complex (Figure 5.43). Some of the Bushveld gabbronorite has been displaced to the west as blocks. The Pilanesberg Complex layers have intruded into each other against a

tuff layer with rings formed from subsequent magma flowing up the centre and from caldera settling and magma introduced from pipes. The image depicts the current terrain and erosional surface, as well as the large central bisecting Vlakfontein fault in the centre and other faults from the graben subsidence (Figure 5.43).

A

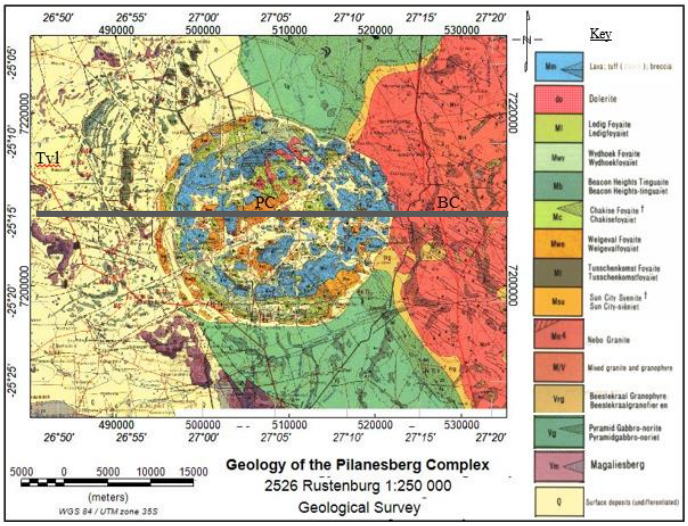

B

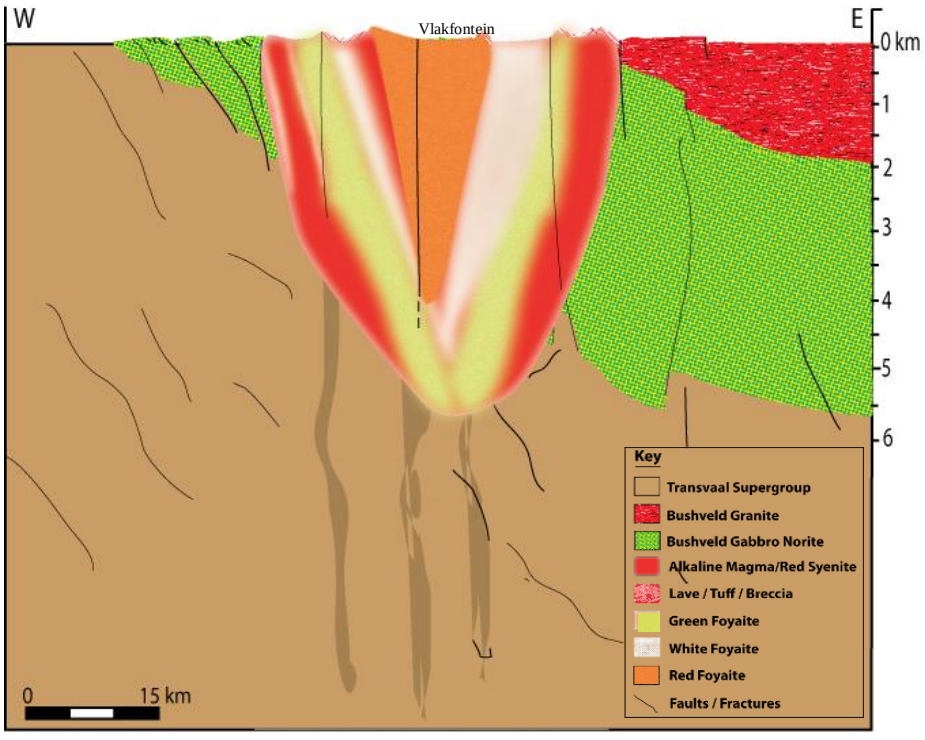

Figure 5.43 A final west-east depiction of the Pilanesberg Complex geometry in the Bushveld Complex and surrounding Transvaal Sequence. A) The profile corresponding to the geology map is a west east profile through the centre of the Pilanesberg Complex. B) The model indicates the displaced Bushveld gabbronorite to the west and the complex ring structure associated with the different magma events of the Pilanesberg Complex.

The north-south profile cuts the strike direction of the Bushveld gabbronorite. The magma intrusion for the north-south profiles (Figure 5.44) follows the same sequence already shown for the west-east profiles.

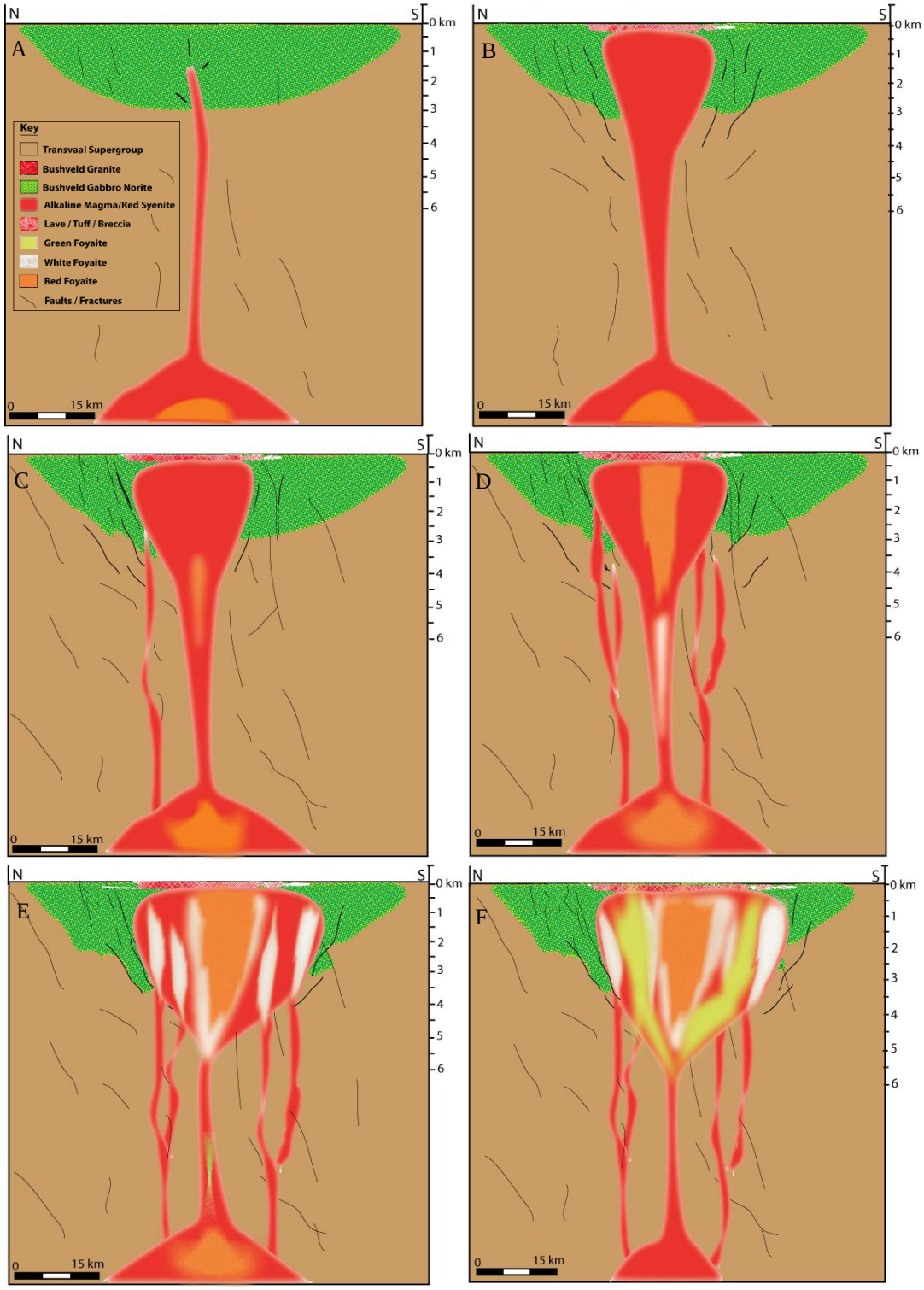

Figure 5.44 The intrusion sequence of the Pilanesberg alkaline magma into the edge of the western Bushveld Complex examined along north-south profiles from the initial magma and tuff layer to pipes and the different foyaite rings forming. The sequence A-F is the same as for Figure 5.42.

Once formed, the intrusion experienced a complicated central subsidence where a northern-hinged trap door graben caused the Complex to dip to the north (Figure 5.47, Figure 5.48, Figure 5.49). The rotation to the north is aided by a bisecting fault (the Vlakfontein fault, Figure 4.23) that allows the northern

block to move above the current erosional surface at the northern edge dips outward from the Complex (Figure 5.45).

Trap door graben settling is difficult to conceptualize for such a large intrusion, which requires a hingeing northern edge. Thus, the schematic in Figure 5.45 provides another possible structural explanation for how the Complex acquired its outward (northern) dip. The suggested structural model requires north-south extension and block movement along faults to cause the necessary rotation.

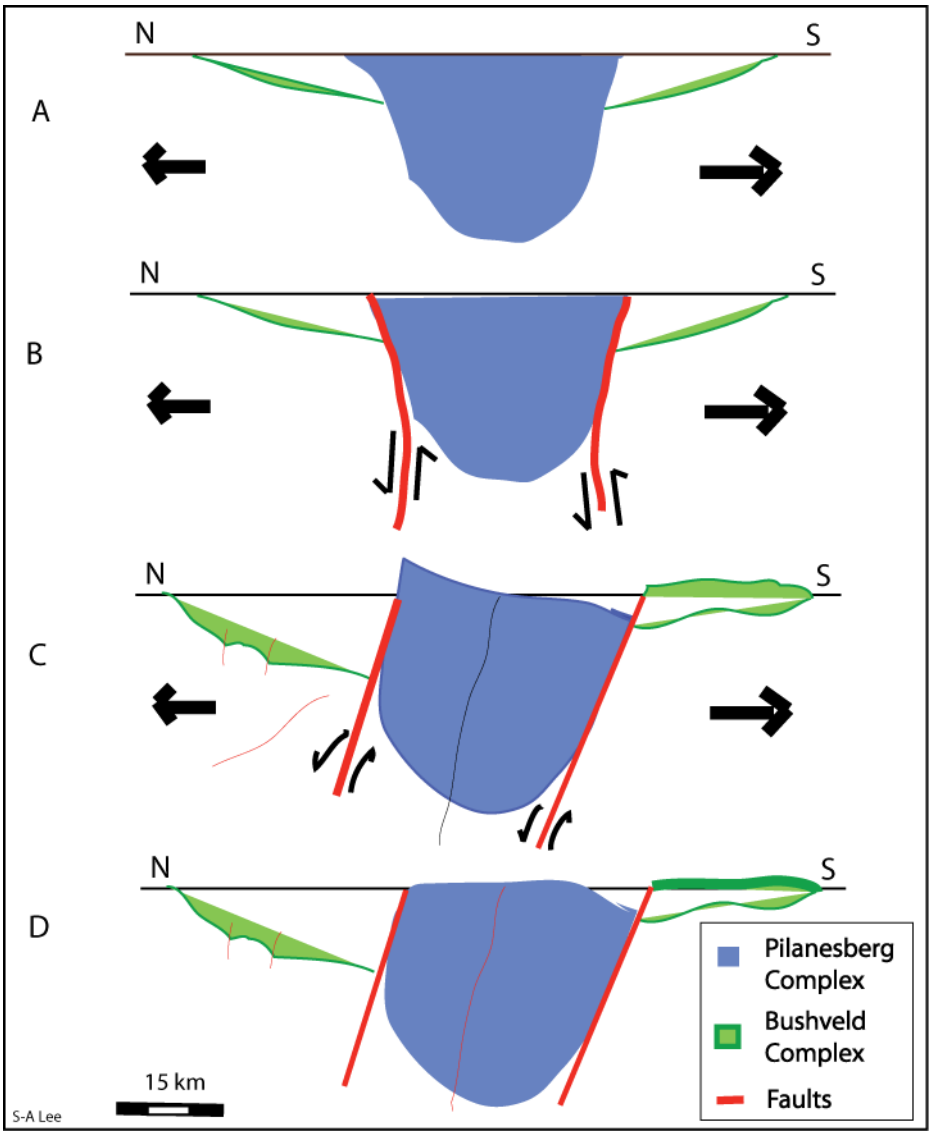

Figure 5.45 The Pilanesberg Complex is in an extensional environment A). B) As a result faults form. The modelling indicated C) block movement along the faults under the influence of the extension results in the outward dip on the north edge of the Pilanesberg and the Bushveld Complex.

The three-compartment block movement does explain all the observations seen throughout the modelling in this chapter. However, the block movement schematic requires a fault on the northern edge, which does not exist according to the geological maps. Figure 5.46 indicates the direction of the extension as

well as the Mahobieskraal fault that indicate the block movement on the southern edge suggested by the schematic in Figure 5.45, Figure 5.47and Figure 5.48.

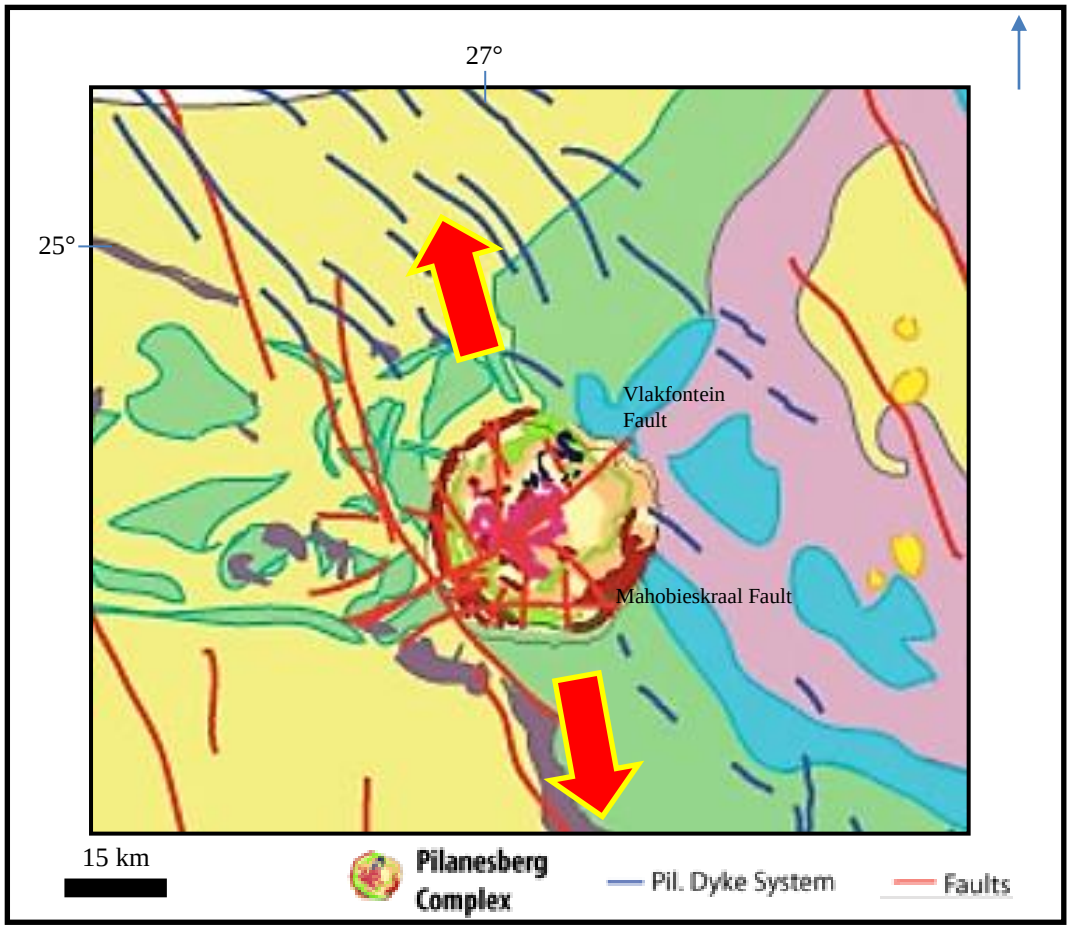

Figure 5.46 A set of west-east faults around the Pilanesberg Complex result from a north-south extension. The existence of the Mahobieskraal fault is a possible block movement point for the tilting of the Pilanesberg Complex.

The north-south profiles depict the structural changes to the Complex after the magma intrusion and ring formations. This starts with a subsidence and a graben trap door, which hinges on the northern edge and subsides in the east. This process is aided by the bisecting Vlakfontain fault so that the north and southern blocks can move semi-independently. The northern block experiences uplift while the southern block rotates with the northern block to become deeper in the south. The erosion forms the final step (Figure 5.47).

The southern block moves down with the trap door graben but the fault also causes some vertical displacement that was first identified by the different depth of the two blocks on the magnetic inversion models.

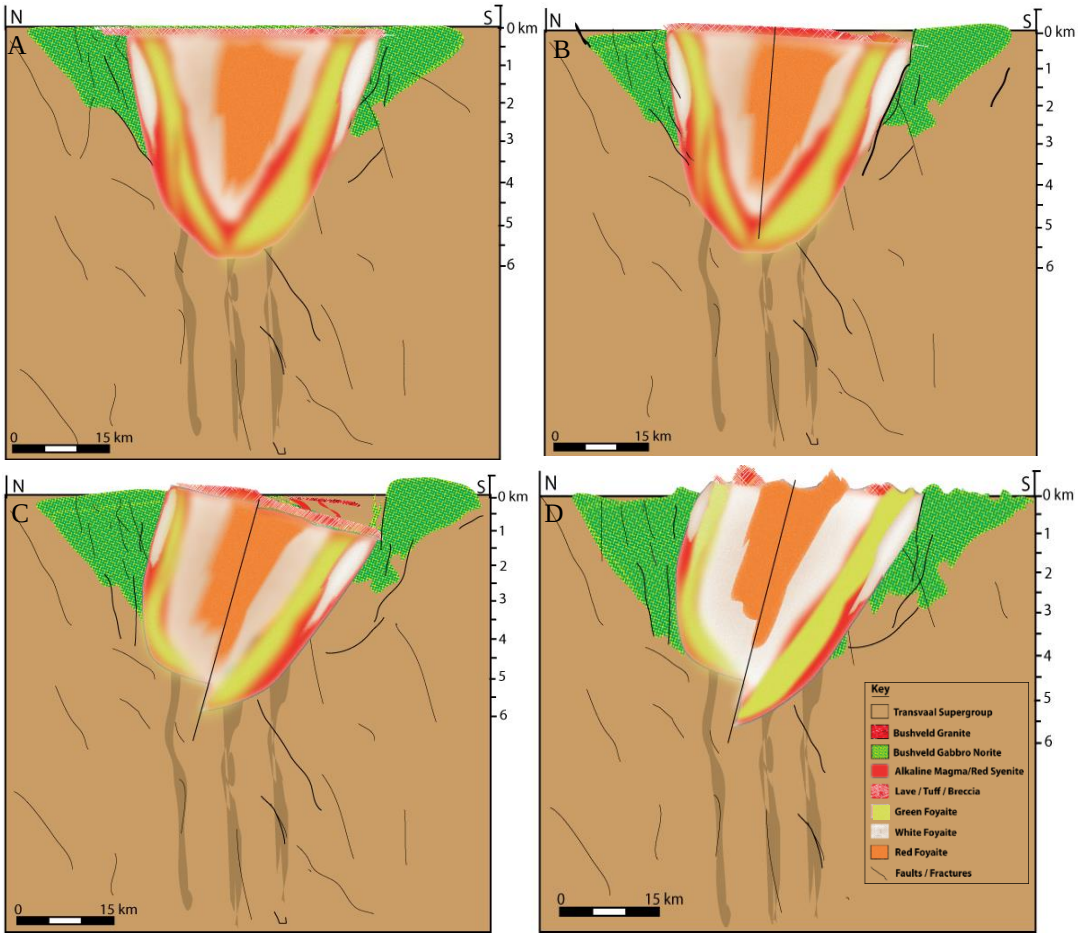

Figure 5.47 The schematic representation of the Pilanesberg Complex intrusion along a north-south profile showing the transition from the intruding pipe to a northward dipping tilting structure with faults and a trap-door graben structural event. A) The intruded magma and ring structure shortly after emplacement. B) The Complex begins to tilt as due to the extensional environment and graben setting along with fault and block movement. C) Further movement and accommodation by the host rock. D) A schematic representation of the Pilanesberg Complex after an erosion period with a basic topography indicated and an indication of how the host rock has responded to the intrusion.

The final model for the Pilanesberg Complex is explained with a combination of both concepts. The northern edge is the hinge of a trap door with a normal fault on the southern edge that allows the Pilanesberg Complex to slip down, tilt and achieve and outward dipping northern edge (Figure 5.48). A final stage of erosion leaves the intrusion at the current situation.

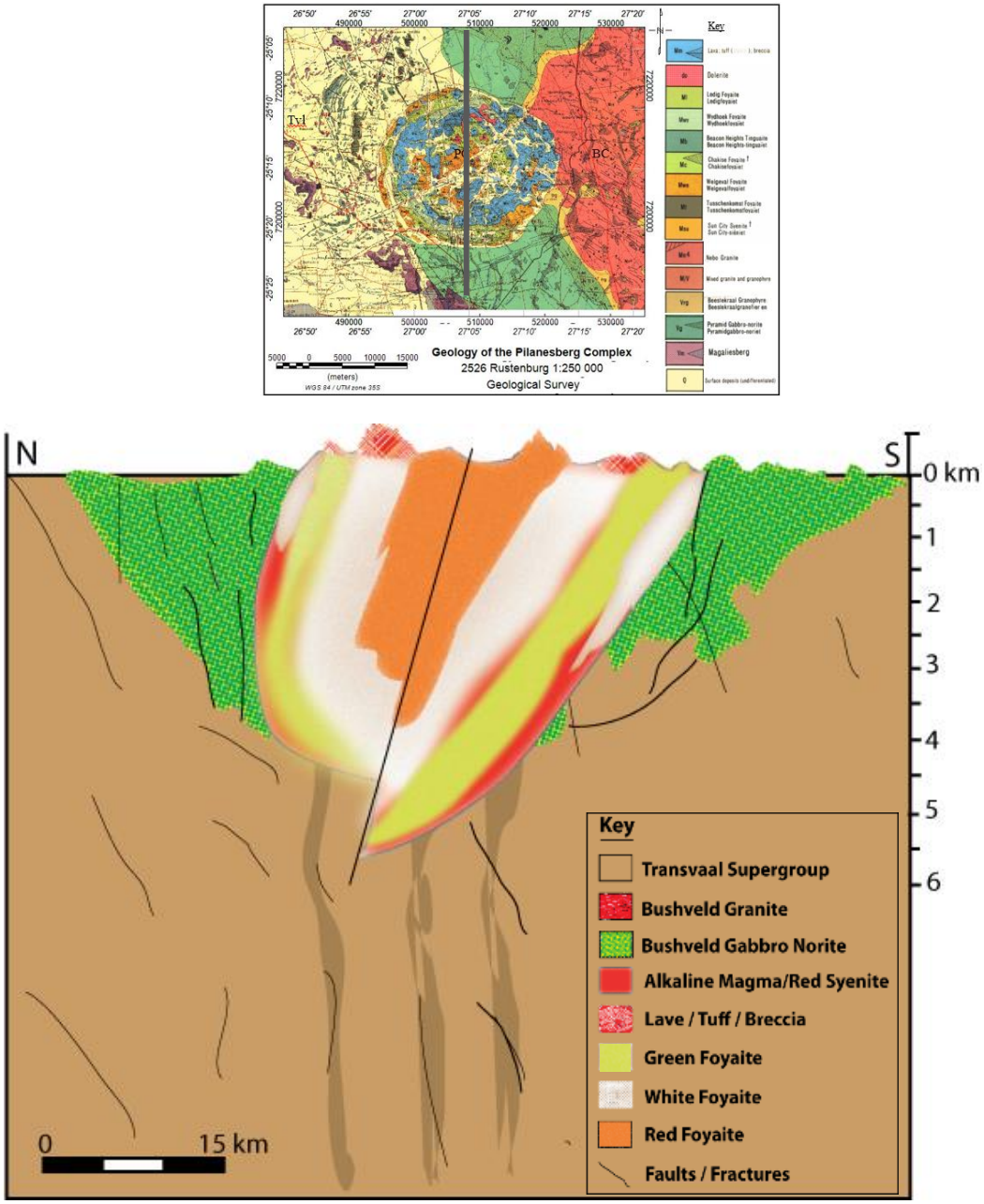

Figure 5.48 A final north-south schematic interpretation of the Pilanesberg Geometry and ring structure below the surface in relation to the country rocks.

In conclusion, the Pilanesberg Complex intruded through pipes and vents in an extensional zone weakness point with a fault network along the edge of the Bushveld western limb. A tuff layer capped the magma that intruded in vertical layers producing the dipping ring structure, which expanded the Complex horizontally. The Complex dips to the north due to a trap door graben subsidence that included rotation and block movement with the help of the internal Vlakfontein fault and a fault on the southern edge. Complicated faulting and movement of the Bushveld Complex have accommodated the ~30 km Pilanesberg Complex in the Bushveld western limb.

CHAPTER 6: SUMMARY AND CONCLUSION

6.1 SUMMARY and DISCUSSION

6.1.1 Model Interpretation

The Pilanesberg Complex was analysed to determine the internal structure and the Complex's overall geometry with the country rock. To achieve this, the modelling of the Pilanesberg Complex includes 2.5D forward models, 3D forward models and 3D inversion gravity and magnetic models. Concepts proposed in published literature will be discussed first. Modelling results and their interpretation will follow the discussion.

Image processing of government gravity and magnetic data revealed distinct circular features within the Pilanesberg Complex (Figure 3.21 and Figure 3.24). These circular features correlate with the lithological rings on the Pilanesberg Complex surface map published by Lurie (1986) (Figure 7.1). The cental region of the Pilaneberg has a low density area that is related to the internal ring structure of the Pilanesberg Complex where the density changes from the syenite to the foyaite ring. The gravity data indicates the low-density anomalies along the 2D gravity profiles requiring a less dense body that may be due to erosion/weathering or due to distinct variation in density associated with the different lithologies. The Voxel inversions identify the distinct density change within the Pilanesberg Complex as a large plug like structure (Figure 4.30) surrounded by a ring of less dense material. The small central peak in the Bouguer gravity also correlates with a magnetic high and could relate to the large 'plug' intrusion in the heart of the Pilanesberg Complex (Figure 4.30). The first vertical derivative of the magnetic data (Figure 3.5) indicates a positively magnetized 160 nT outer ring with a blue edge, a -30 nT magnetic second ring and a final 300 nT magnetic central plug. The magnetic rings correlate spatially with the density variation between the outer red syenite, the white foyaite and the inner red foyaite. Theses observation correspond with Lurie's (1986) describtion of the Complex being an inward dipping ring structure around a central plug, with large faulted blocks resulting from a collapsed caldera formation with approximate angles of 35° in the south, to 45° to the west, and 30° in the east. The rocks in the north, however, dip northward at a 70° angle towards the north (Figure 6.1). The 2D, 3D forward and inversion gravity models tested Lurie (1986) surface dip measurements.

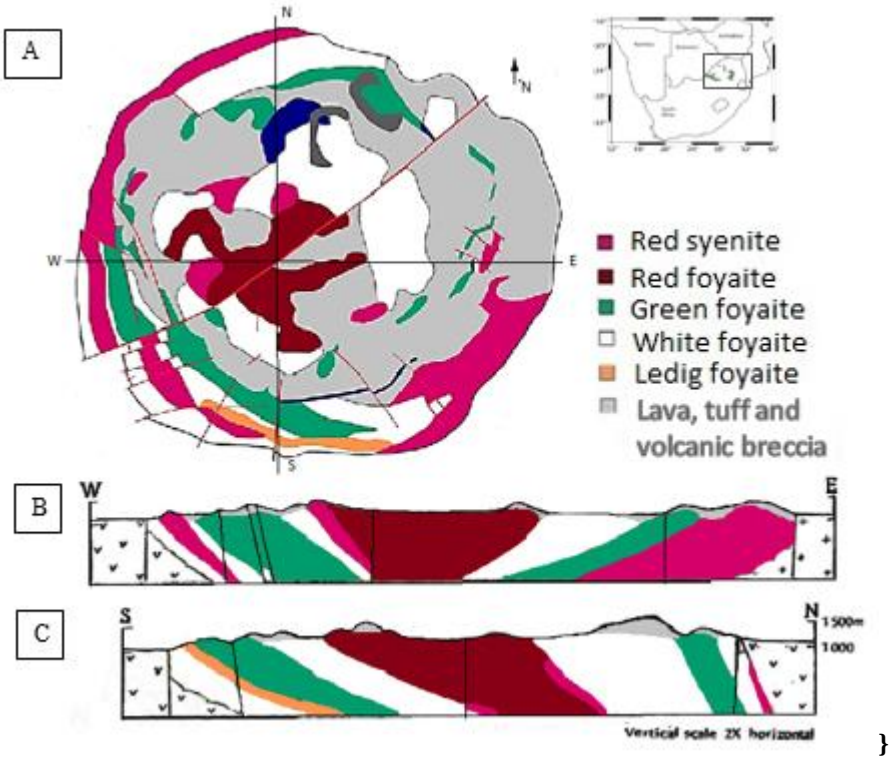

Figure 6.1 Geological overview of the Pilanesberg Complex in A) as well as a WE profile in B) and a NS profile through the Pilanesberg Complex in C), Modified from Lurie (1986), Cawthorn (1988).

Cawthorn (2009) considered a modified model in which the Complex emplaced as horizontal sheets that proceeded centripetal subsidence. Cawthorn (2015) argues that the Complex is too large and coarse-grained to be either a ring dyke or a cone sheet, which are fine-grained intrusions (Cawthorn, 2015). Moreover, those intrusions could not account for the removal of the country rock into which it intruded. Cawthorn (2015) suggests that the Pilanesberg Complex is an inward-dipping sheet that had late stage

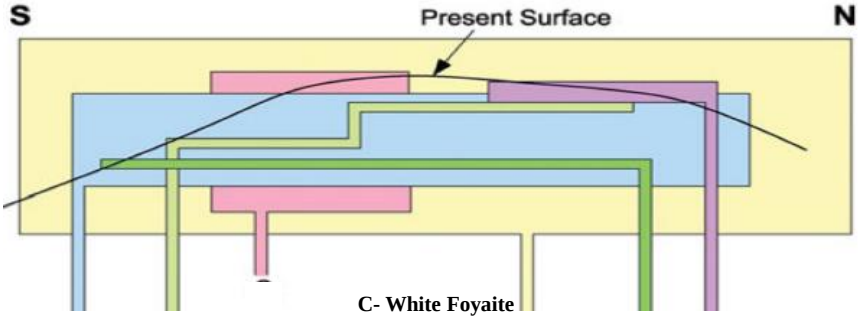

mber (Figure 6.2). This particular model

s not extend to depth (no depth scale was

C- White Foyaite

A- Red Syenite

B- Red Foyaite

D- Green Foyaite

E - Tinguait

F- Ledig Foyaite

Figure 6.2 Cawthorn (2015) proposed the Pilanesberg Complex forms as an inward-dipping sheet with magma injections. The order of intrusion is as follows: A- Red Syenite, B- Red Foyaite, C- White Foyaite, D- Green Foyaite, E- Tinguaite and F- Ledig Foyaite.

Cawthorn (2015) discussed that the Bushveld Complex was not displaced by the intrusion of the Pilanesberg Complex, which appears as a requirement in Lurie's (1986) funnel model. However, Cawthorn (2015) only refers to the non-displacement of the Bushveld Complex to the north and south of the Pilanesberg Complex along his north-south preliminary gravity profile. Analysis of the surrounding Pilanesberg Complex rocks indicates that some of the Bushveld Complex Main Zone rockswere shifted to the west of the Pilanesberg Complex, which is consistent with the Bouguer gravity forward models and suggests that horizontal deformation occurred, shifting rocks to the west by a few kilometres.

Cawthorn (2015) proposed model contribute aspects toward a possible geological emplacement model. The erosion surface along Cawthorn (2015) model suggests there is more of the white foyaite to the north of the model dipping beneath the Bushveld Complex. The 3D susceptibility model developed from magnetic data and the MVI Voxi inversion models support this interpretation. Both models suggest there is a large magnetic mass that would be equivalent to the white foyaite in Figure 7.4.

Some of the other Complex intrusion theories include those of Ferguson (1973) and Shand (1928). Ferguson (1973) considered that the Pilanesberg Province (including the Pilanesberg Complex, Pilanesberg dyke system and other intrusions) originated from fractionation of 'large magmas' in the crust at a depth greater than 10km. These magmas then buoyantly migrated upward using the passive stopping process. Shand (1928) insinuated that the isolated occurrence of the magma intrusion is due to a point of weakness caused by numerous structural factors. The Pilanesberg Complex is on the axis of the Bushveld syncline and it lies in a zone of weakness where the dykes trend N.N.W-S.S. E such that the intrusion would take place at this critical intersection point and distribute itself symmetrically about the axis of the zones intersection (Shand 1928). The deep processes assist in explaining how the shifting Bushveld Complex material was accommodated while the intrusion sequence of the Pilanesberg Complex addresses the surface processes.

The cylinder orignates from a broken up network of faulted blocks that the magma can well up through in channels that are thin at depth and expand to wards surface due to the recurring explosions from the magma rising (Shand, 1928). Tuff would eventually cover the surface, after which tuff cones would grow above the fissures. The fissures discharge would flow together in a laccolithic magma body between the fractured host rock and the tuff. The red foyaite and syenite at the top of the intrusion become semi solid stagnant grains, after which this solid crown would sink (caking) into the fluid interior causing later magma to well up around the edges thus forming the distinct Pilanesberg Complex rings. This process would occur again to form the green foyaite and Tinguaite. Shand (1928) stated central subsidence followed the intrusion.

Testing possible geometries of the Pilanesberg Complex with 2.5 D Bouguer gravity models demonstrated that an entirely outward dipping model was not able to fit the gravity data (Figure 4.9), even when constrained by surface geology and depth estimate for the Transvaal, Bushveld and Magaliesburg rocks. The cylindrical pipe or vertical sided model has a better fit to the data with only a 10.16 % misfit (Figure 4.8). The depth extent of the Pilanesberg Complex does not significantly affect the fit of the data in the 2.5 D model, which means that the gravity cannot constrain the depth perameter while the gravity response depends on the dip and dip direction of the Pilanesbergs edges.

The 2D Bouguer gravity profiles indicate the signal increases by ~ 15 mGal on the west and 40 mGal on the east of the Pilanesberg Complex. The significant increase in the bouguer signal on either side of the Pilanesberg Complex is due to the proximity of the dense Bushveld Complex (Figure 4.8) on the east as well as the displaced Bushveld matterial to the west of the Pilanesberg Complex.

The University of British Columbia (UBC) inversion model identified outer edges of the Complex that correlate with the inward dip on the western and southern edge of the Complex as well as the vertical edge to the east of the Complex. The northern contact appears to be initially vertical in this inversion and changes to a northward dipping contact below 5 km depth (Figure 4.39). The Euler deconvolution solutions provide depth estimates for contacts between the Pilanesberg Complex and the Bushveld Complex. These contacts extend to depths of ~ 12 km, 8 km and 10 km on the western edge of the Pilanesberg Complex and on the eastern edge the depths extend to 7 km, 15 km and 8 km on Profile 1, Profile 2 and Profile 3 respectively (Figure 3.16 -3.18). The 3D PyGMI gravity forward modelling (Figure 4.25) is consistent with an overall inward dip of between 25 and 40° to a minimum depth of 6 km. The depth estimate of 6 km with this model is less than the average 10 km depth estimated with the low sensitivity Euler profiles. The Euler solution profiles estimate the Pilanesberg/Bushveld Complex contacts; thus the 10 km depth estimate could refer to the edge defined by the Bushveld and not that of the Pilanesberg. This is plausible as the Bushveld extends to ~ 10km depth (Coomber, 2008) while the Pilanesberg Complex is estimated to be between 5 – 8 km depth (Figure 7.3). The produced geological model uses the PyGMI 5 km as a minimum depth estimate for the geological model. The Euler deconvolution solutions indicate that the northern contact does dip out to the north to a depth of 12 km (profile 4, Figure 3.19). The 45° outward dipping northern contact of the Euler solutions is consistent with the 3D PyGMI forward gravity model, which has a true dip of between 40 and 50° (Figure 4.26 – 4.30).

The 3D PyGMI forward modelling confirms that the Pilanesberg Complex has an overall inward dipping structure (Figure 7.3); however, it has less depth extent than the 2.5 D models suggest. The Euler solutions confine the depth of the Complex to a range of 8 to 12 km depth along the gravity profiles. The estimated depth of the Pilanesberg has a minimum depth estimate of 5 km according to the 3D PyGMI forward modelling Figure 7.3). The depth of the ~28 km diameter Pilanesberg structure is proportional to

the Bushveld Complex, which extends over an area of ~ 500 km and has an estimated depth extent of ~10 km, calculated from mining and seismic interpretations (Coomber, 2008).

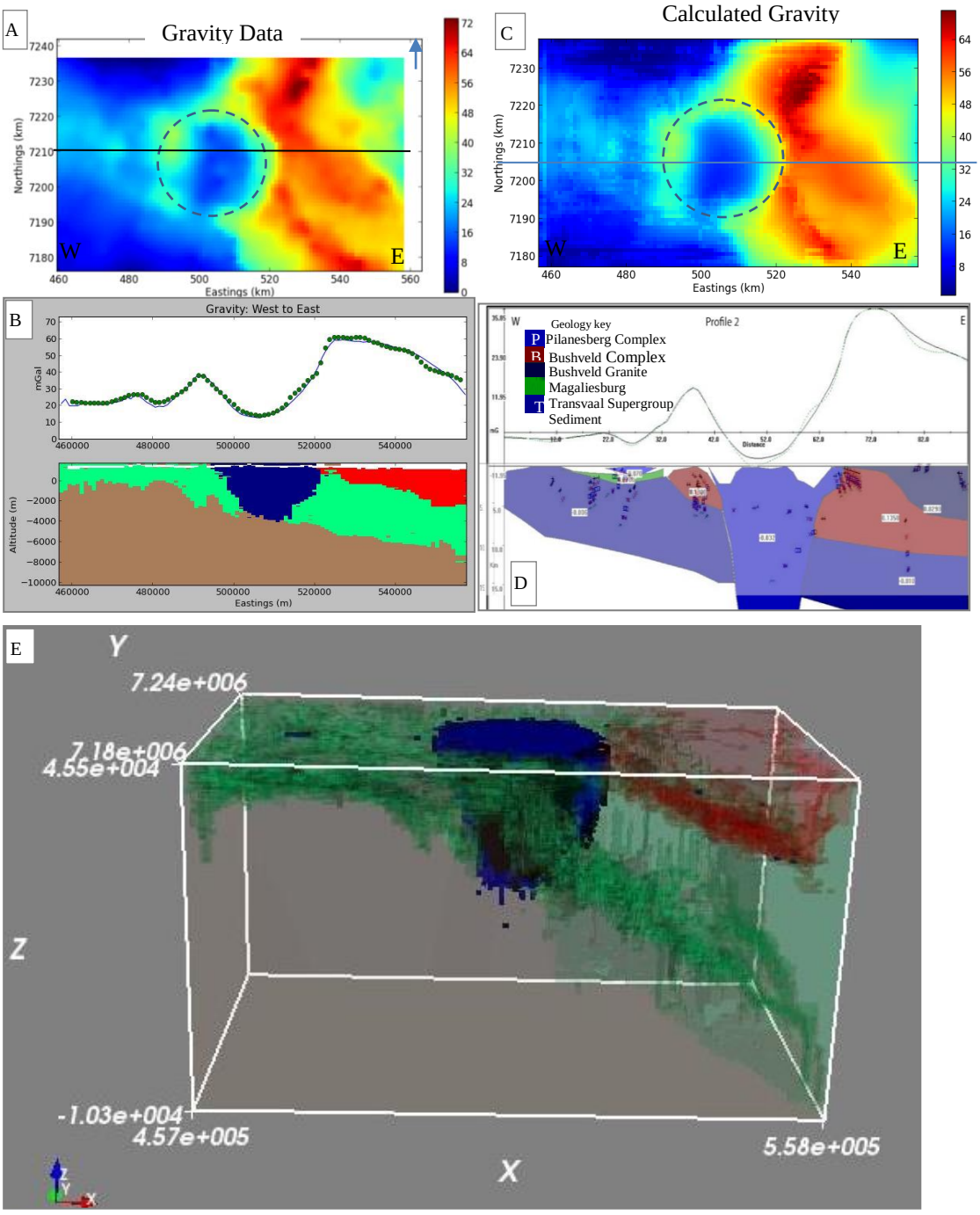

Figure 6.3 A) West-east profile through the Pilanesberg Complex. A) The gravity map and B) the corresponding 3D forward model profile from PyGMI indicating a realistic depth extent of approximately 5 km. C) the calculated gravity map and D) 2.5D gravity profile displaying in inward dipping Complex with the Euler solutions overlain. E) Finally the 3D gravity forward model showing the inward dipping Pilanesberg Complex in the dipping Bushveld Complex Gabbronorite and next to the Bushveld Gabbro.

The 2.5D gravity test models below 10 km suggesting that the Complex intruded from depth. The Pilanesberg Complex most likely made use of a weakness point discussed by Shand (1928) that allowed the symmetrical Complex to intrude the Bushveld Complex. Ferguson (1973) insinuated that the Pilanesberg's origin was from mafic magmas in the crust at a depth greater than 10 km. The Euler deconvolution solutions support this by delineating the Pilanesberg Complex edges to an average depth of 10 km.

Shand (1928) disagreed with a batholith intrusion, as the emplacement of the Pilanesberg Complex did not dissolve the host rock. The PyGMI 3D gravity forward model suggests that there was a shift of the Bushveld material to the west (Figure 6.3). The PyGMI forward models display simple continuous bodies that do not show direct structural features such as faults. However, the bottom edge of the Bushveld Complex has changes in gradient around the Pilanesberg Complex, suggesting that the area was faulted, and the fault blocks moved up and down vertically to accommodate the westward shift of material as the Pilanesberg Complex intruded (Figure 6.3).

The final 3D PyGMI Bouguer gravity forward models suggest the Pilanesberg Complex dips to the north (Figure 6.4) at ~ 50° while dipping inward from the east, south and west between 25 and 37°. The bottom surface of the Pilanesberg Complex has a depth extent of approximately 5 km on the west-east forward model. While the estimated north-south forward model's depth extent is a maximum of ~ 6 km (Figure 6.4) with an average of approximately 5 km for this model. The PyGMI model presents an entirely 3D perspective on the Complex, even though it is a forward model, and the model agrees with the dip directions of the Euler deconvolution solutions, the UBC inversion and the geological models by Lurie (1986).

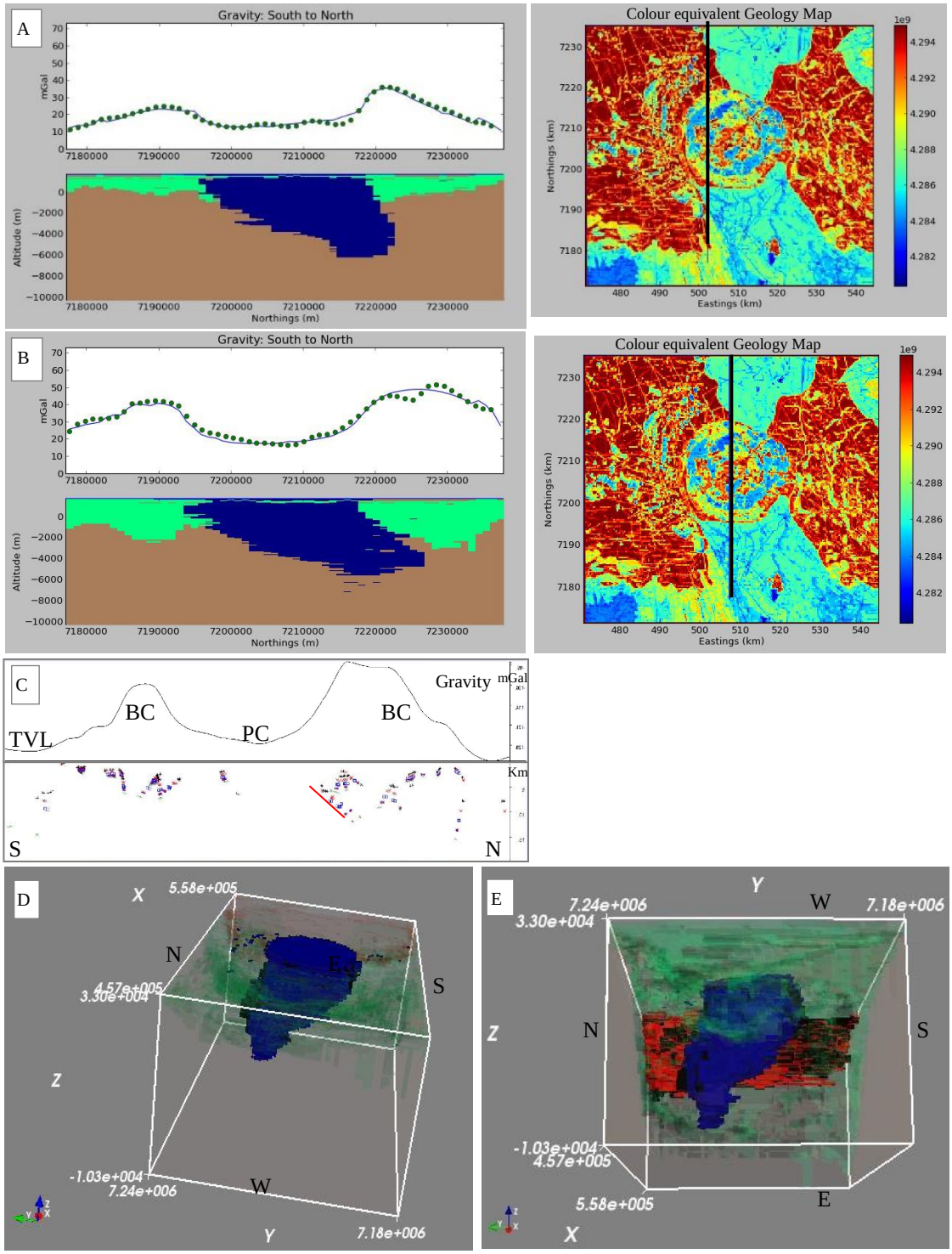

Figure 6.4 The PyGMI north-south forward model profiles indicate an inward dipping southern edge and an outward dipping northern edge for the Pilanesberg Complex A) and B). The depth extent of both profiles extends to ~ 6 km. C) Compares the dip direction on the Euler Deconvolution gravity profile of profile 2 with the PyGMI modelled results. D) Moreover, E) display the 3D forward model of all the profiles and layers that match the gravity data. D) Indicates the dipping Pilanesberg Complex, while E) highlights the granite to the east of the Pilanesberg Complex.

Changing from the forward models to the inversion models now, the 3D Voxel inversions of the magnetic data of the Pilanesberg Complex revealed internal geometries that help explain the emplacement of the Pilanesberg Complex. Two Voxel models are analysed. The first Voxel is a coarse susceptibility model, which inverts the magnetic map on a 3D solution space, which has 27 cells in the X direction, 27 in the Y direction and 9 cells in the Z direction (The 27x27x9 3D Voxi inversion of the Pilanesberg Complex. The internal geometry indicates a 'C' shape in A) that appears to be the intrusion towards surface B), which acts as a 'plug' for the intrusion.

The second model has twice as many cells to invert with 55 in the X direction, 58 in the Y direction and 15 cells in the Z direction to form the 3D solution space (Figure 6.5). The second model inverts for magnetic vectors. Both models are strictly examining the internal geometry and do not extend beyond the edge of the Pilanesberg Complex. The interpretation of these models is that there is three-layer gradational susceptibility model, which decreases in susceptibility towards the surface. The coarse model clearly indicates a central 'C' shaped 'plug' that intruded towards the surface in places, occasionally cutting through the overlying lower susceptibility material (Figure 6.5).

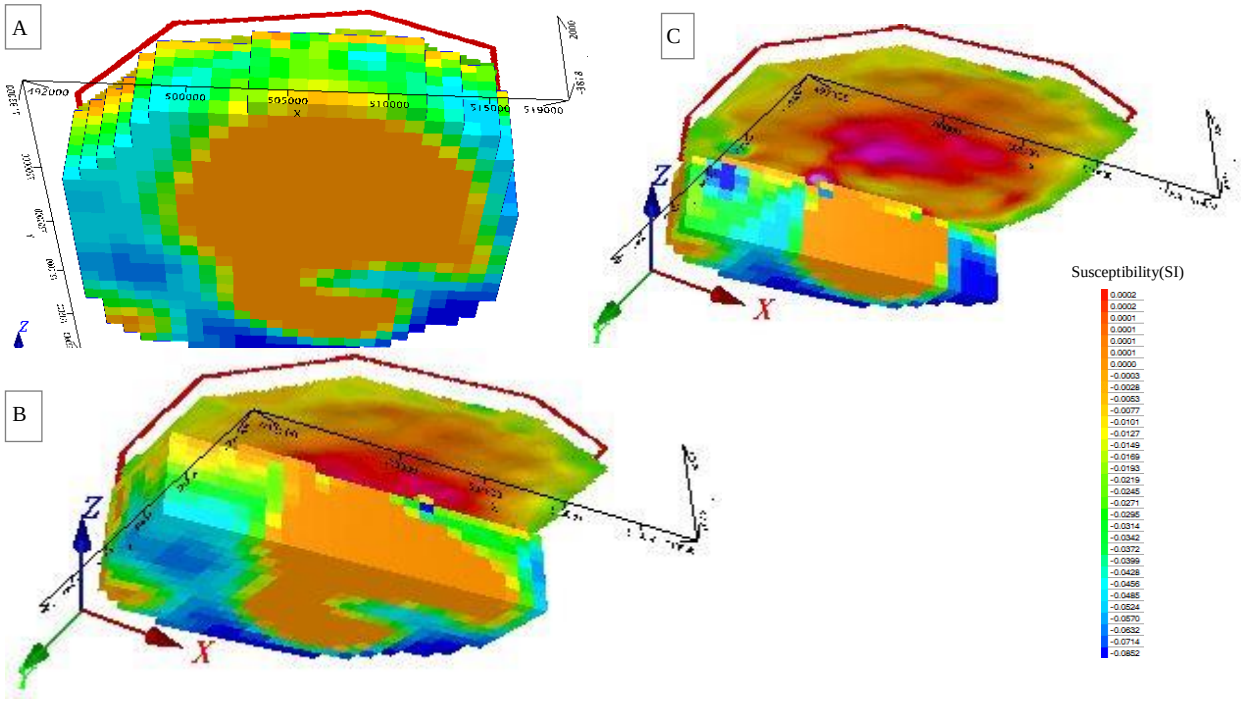

Figure 6.5 The 27x27x9 3D Voxi inversion of the Pilanesberg Complex. The internal geometry indicates a 'C' shape in A) that appears to be the intrusion towards surface B), which acts as a 'plug' for the intrusion.

The Complex's internal structure is further examined by analysing the magnetic vector inversion model (Figure 6.6). The model indicates a defined magnetic vector in the heart of the Complex representing the plug. The west-east sections through the Voxi inversion indicate the central plug that moved up toward the surface that refutes the horizontal layer emplacement model described by Cawthorn (2015) (Figure

6.2). Also, the north-south profiles indicate an offset in the central plug, which is a normal lystric fault observed as the Vlakfontein fault on surface, where the northern block has been uplifted (Figure 5.32). The displacement of the northern block by vertical movement apears in Figure 5.38 and 5.39, which identifies that the block to the south, has been downthrown.

Both models indicate that the higher susceptibility 'plug' is closer to the surface in the northern half of the model. The north-south profile consistently displays a disturbance through the high susceptibility material, which correlates with the Vlakfontein fault on the surface (Figure 6.6).

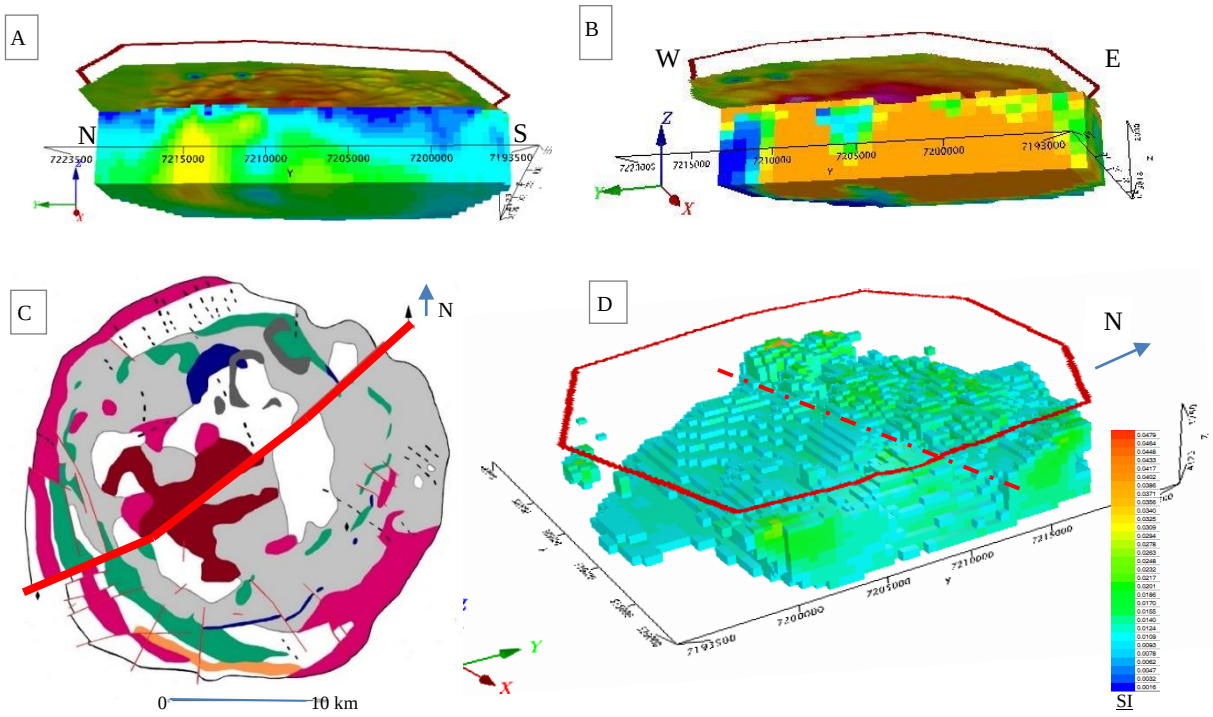

Figure 6.6 A) The fine MVI voxel model (55x58x15) bisected from north to south – indicating the mass closer to surface in the north and becoming deeper in the south. B) (Figure 5.32 F) the course susceptibility model Voxel (27x27x9) from west to east indicating the internal structure which is cut by the Vlakfontein fault in the north identified in C-D). D) The northern block has a magnetic mass that is closer to the surface than that of the southern block. The image has been susceptibility clipped from the surface down, showing the block vertical movement between the northern and the southern block.

The characteristics identified through modelling is summarised in Table 6.1. The table lists the dip angle and depth estimate from all the models showing that multiple solutions and models fit the data. However, it confirms the overall inward dip and northward dipping northern edge. The variation in depth and dip angle over the models is somewhat varied but proposes a geological possible model.

Table 6.1 Depth and dip orientation summary for all the forward and inversion models.

Model Type	Package		West	East	North	South
Published	From Lurie (1986)	Dip	45	30	70	35
Forward Models	Grav 2Dc Profiles	Depth Estimate (km)	~ 15			
		Dip (°)	74	73	61	81
	PyGMI 3D Voxel	Depth Estimate (km)	5		6	
		Dip (°)	25 - 37	25 - 37	50	39
Inversion Models	Euler Deconvolution	Depth Estimate (km)	5	10	10	6
		Dip (°)	45			
	UBC 3D Voxel	Depth Estimate (km)	Cut off at between ~ 9.33 and14 km			
		Dip (°)	45	50	50	35
	Geosoft 3D Voxel	Depth Estimate (km)	Cut off 9.33 km with 27x,27y,9z and 7.5 km with 55x,58y,15z voxel			
		Dip (°)	-	-	-	-

The 2.5D Grav2Dc forward models (Figure 4.9-4.10) and 3D UBC inversion models (Figure 4.29) confirm that the Complex emplaced as a vertical inward dipping pipe with the northern boundary contact dipping outward or to the north. The 3D geometries observed in the UBC model and the 3D forward model (Figure 4.26-4.28) fit with Lurie's (1986) inward dipping model. An aspect that is not discussed by either Cawthorn (2015) or Lurie's (1986) model is the dense magnetic body that is closer to surface in the north of the Complex and is at a greater depth on the southern side of the Pilanesberg Complex (Figures 4.33-4.40). Possibilities to explain this firstly include that the body could have intruded at an angle from a magma chamber located to the north of the Complexes location. An angled intrusion is not realistically likely and would not account for the denser central mass being deeper in the south of the Complex. The second possibility is that the Complex may have tilted after emplacement, and the third possibility is that the Complex was faulted and encountered block movement where the southern block moved down. The Vlakfontein fault is a geological feature bisecting the north and south of the Complex so the last possibility could be a plausable explination. The outward dip of the Complex's northern edge can be explained by a combination of tilting and faulting, which would fit with the northern block being closer to the surface and the southern block having a greater amount of overburden. Shand (1928) discussed the Complex undergoing caldera settling. The outward dipping northern edge was structural controlled by caldera settling during magma cooling with a trap door graben effect occurring. Thus the northern edge would act as a hinge on the surface while the southern edge slipped to depth. During the swivel action process, the Vlakfontein fault formed allowing the southern block to slip down while the northern block tilted northward to accommodate the moving southern block.

A set of schematics is used to explain the intrusion sequence, which uses a combination of the modelling results along with previously published intrusion theories. The schematics include a west-east traverse and a north-south traverse across the Pilanesberg Complex (Figure 6.7).

The intrusion events envisaged for the West-East profile schematic sequence (Figure 6.8), also apply to the North-South profiles for the corresponding time slots. Structural events including faulting and tilting episodes proceeded the intrusion of the Pilanesberg Complex. The resulting model is displayed in the

north-south profiles in Figure 6.9. The present-day outcropping conditions of the west-east and north-south profiles are shown in Figure 6.10 A and Figure 6.10 B respectively.

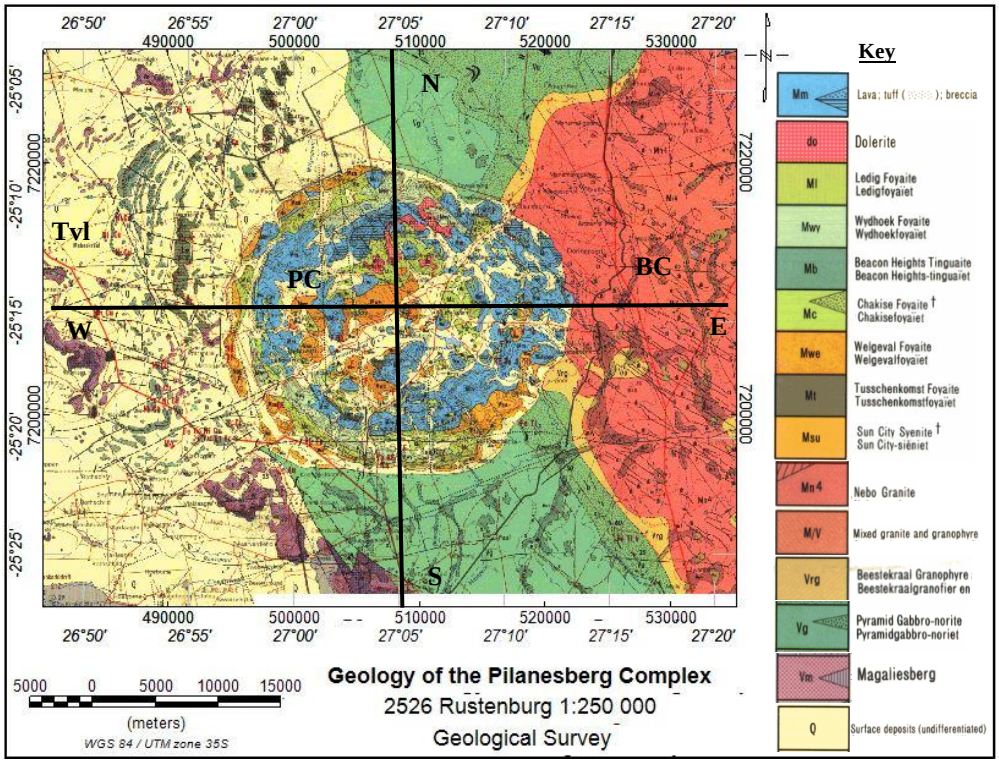

Figure 6.7 The Pilanesberg Complex locality map with the north-south and west-east profiles used for the schematic geology interpretation of how the Pilanesberg Complex intruded into the Bushveld Complex.

The schematic event sequence (Figure 6.8) shows the magma moving up from depth through a fault network and into the edge of the western Bushveld as seen on the west-east profiles (Figure 6.8 A). The surface explosions produce a layer of breccia and tuff. Plagioclase and hypersthene grains in the tuff confirm that this was an initial event where the rocks were blown to bits and ejected as tuff and breccia Shand (1928). The initial magma (red) represents the red syenite. The continued rising magma and surface explosions result in a lateral widening of the magma toward the surface (Figure 6.8 B). The ring structures form by multiple stages of magma injection that widened the intrusion from the centre outwards. Block faulting and fractures in the Bushveld Complex make it possible to accommodate the process of the widening Pilanesberg Complex intrusion with the assistance of regional extension events that shifted some of the Bushveld material to the west of the Pilanesberg Complex (Figure 6.8). The central red foyaite (orange) is the next layer to intrude into the centre. Vents and pipes take advantage of the fractured host rock to allow the emplacement of the white foyaite (Figure 6.8 C). The white foyaite intrudes around the central red foyaite through a process of caking or magma settling, where the central red foyaite body sinks slightly and the white foyaite wells up around it (Figure 6.8 D). The final ring to form is the green foyaite (Figure 6.8 E), which follows a similar process to the white foyaite. The Pilanesberg Complex expanded as the internal rings formed and simultaneously the fractured and faulted Bushveld material to the east shifted downed to accommodate the new body. This is a very simplistic

overview. The fractures and block movement are expected to be substantially more complicated whereby including processes such as uplift, extensional environment and erosion to make up for aspects required for the simple illustration to be possible (Figure 6.8)

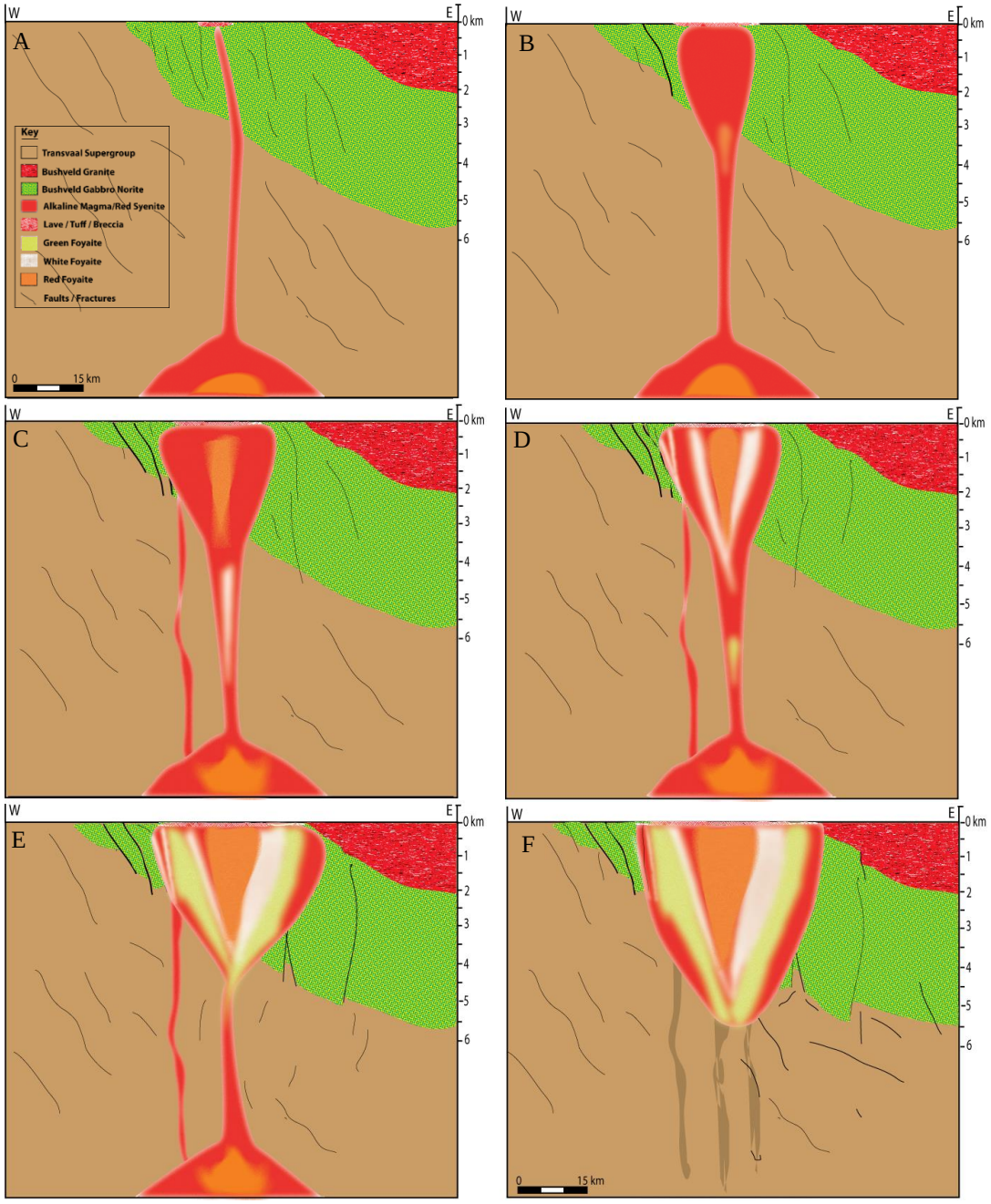

Figure 6.8 A schematic representation of the Pilanesberg Complex magma intruding into the Bushveld Complex along west-east profiles. A) An unsaturated alkaline magma moves upward through cracks and fractures associated with a weakness point. Surface explosions form a layer of breccia and tuff. B) Continued explosions cause the magma rising to widen toward the surface. The initial magma (red) represents the red syenite. C) The central red foyaite (orange) is the next layer to intrude into the centre. Vents and pipes use the fractured host rock to allow the emplacement of the white foyaite D). The white foyaite intrudes around the central red foyaite, where the central red foyaite body sinks slightly and the white foyaite wells up around it. E) Similarly, the green foyaite wells up around the white foyaite and finally, the magma process is complete F).

The north-south profiles depict the structural changes to the Complex after the magma intrusion and ring formations. The structural changes starts with a subsidence and a graben trap door, which hinges on the northern edge and subsides in the east. This process is aided by the bisecting Vlakfontain fault so that the north and southern blocks can move semi-independently. The northern block experiences uplift while the southern block rotates with the northern block to become deeper in the south. The erosion forms the final step (Figure 6.9).

The southern block moves down with the trap door graben but the fault also causes some vertical displacement that was first identified by the different depth of the two blocks in the magnetic Voxel inversion models.

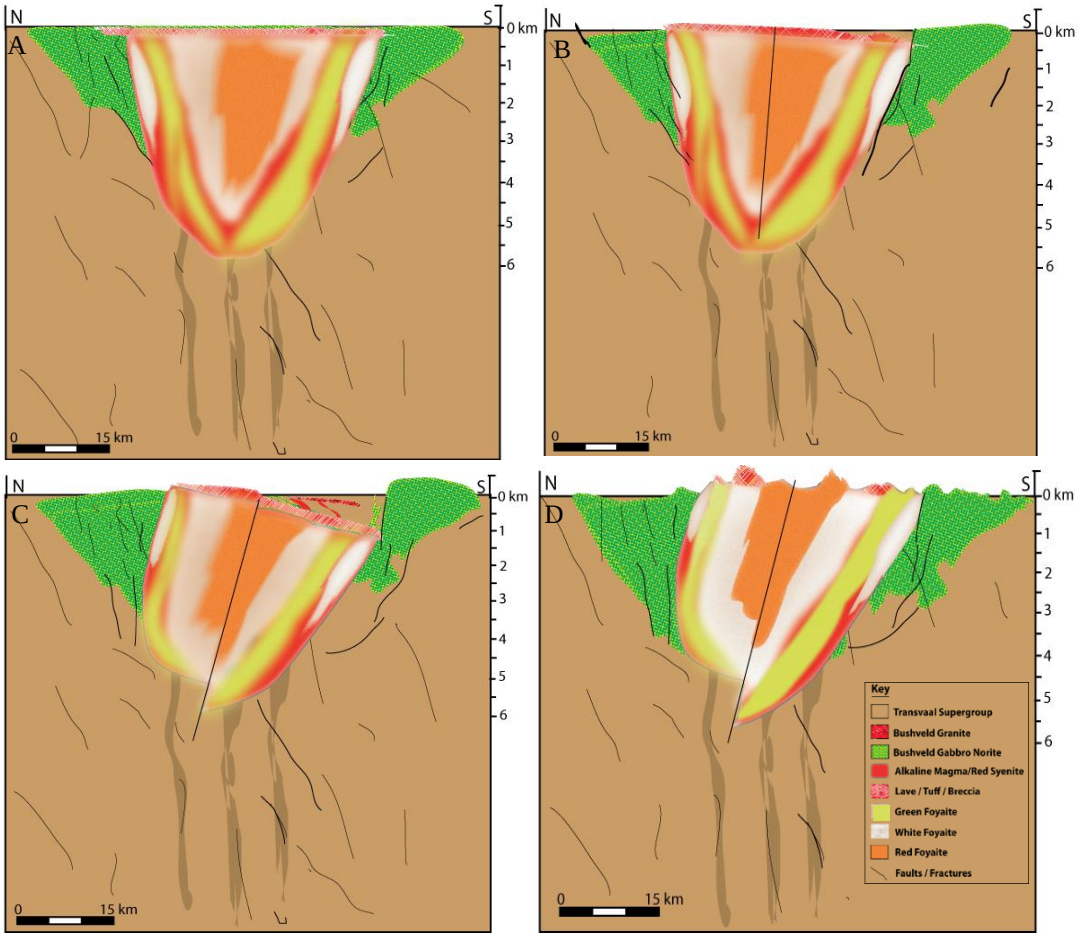

Figure 6.9 The schematic representation of the Pilanesberg Complex intrusion along a north-south profile shows the transition from the intruding pipe to a northward dipping tilted structure with faults and a trap-door graben structural event. A) The intruded magma and ring structure shortly after emplacement. B) The Complex begins to tilt as due to the extensional environment and graben setting along with fault and block movement. C) Further movement and accommodation by the host rock. D) A schematic representation of the Pilanesberg Complex after an erosion period with a basic topography indicated and an indication of how the host rock has responded to the intrusion.

The final model for the west-east profile schematic interpretation shows the Pilanesberg Complex intruded into the Bushveld Complex (Figure 6.10 A). Some of the Bushveld gabbronorite was displaced to the west as shifted blocks around the Pilanesberg Complex. The Pilanesberg Complex layers intruded into each other against a tuff layer with both rings formed from subsequent magma flowing up the centre as well as caldera settling and magma introduced from pipes. The image depicts the current terrain and erosional surface for the Pilanesberg with the large bisecting Vlakfontein fault in the centre and other faults from the graben subsidence (Figure 6.10 A).

The Pilanesberg's final model is a combination of caldera settling and graben subsidence. The northern edge is the hinge of the graben trap door with a normal fault on the southern edge allowing the Pilanesberg Complex to slip down, tilt and achieve and outward dipping northern edge (Figure 6.10 B). A final stage of erosion leaves the intrusion at the current situation.

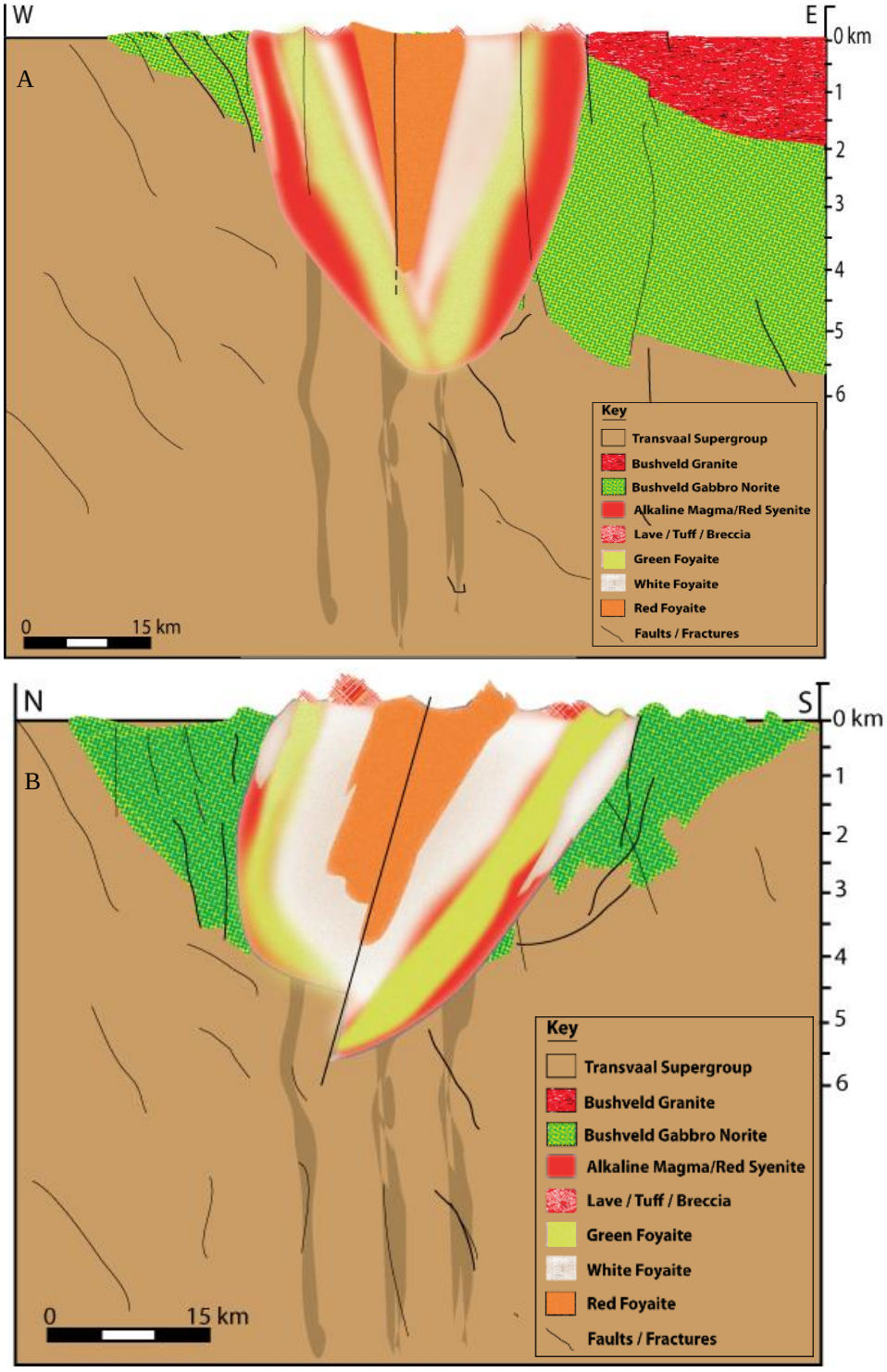

Figure 6.10 A) The final west-east depiction of the Pilanesberg Complex geometry as it is in relation to the Bushveld Complex and surrounding Transvaal Sequence. The model indicates the displaced Bushveld gabbronorite to the west and the complicated ring structure associated with the different magma events of the Pilanesberg Complex. B) A final north-south schematic interpretation of the Pilanesberg Complex geometry and ring structure below the surface in relation to the country rocks.

Once formed the intrusion experienced a complicated central subsidence where a northern-hinged trap door graben caused the Complex to dip to the north (Figure 5.47, Figure 5.48). Once the trap door motion had begun, the north to south clockwise rotation of the Complex was aided by a bisecting fault (the Vlakfontein fault, Figure 4.23) that allowed the northern block to move above the current erosional surface as the northern edge dipped outward from the Complex as part of the rotation (Figure 5.45). The trap door graben requires a hingeing northern edge and north-south extension block movement along faults to cause the necessary rotation.

In conclusion, the Pilanesberg Complex intruded through pipes and vents in an extensional zone weakness point with a fault network along the edge of the Bushveld western limb. A tuff layer capped the magma that intruded in vertical layers producing the dipping ring structure, which expanded the Complex horizontally. The Complex dips to the north due to a trap door graben subsidence that included rotation and block movement with the help of the internal Vlakfontein fault and a fault on the southern edge. Complicated faulting and movement of the Bushveld Complex have accommodated the ~ 28 km Pilanesberg Complex within the Bushveld western limb.

6.1.2 Geochronology Interpretation

Shand (1928) suggested that even though the Pilanesberg Complex was the focus of the unsaturated alkaline magma, the extent of the Pilanesberg dyke swarms indicate a wide spanning developed magma chamber beneath the Bushveld Complex in the Western Transvaal. The dykes intrude along a series of normal faults directly related to extensional tectonics and alkaline magmatism (Hansen et al., 2006). Hansen et al. (2006) reported alkaline and carbonatite Complexes intruding along Archean terrain boundaries or younger extensional faults where there is a rise of mantle-derived magma and controlled by the deep lithological zones of weakness. The Mesoproterozoic orogeny triggered the intraplate magnetism within the Namaqua-Natal-Maud Belt (Hansen et al., 2006).

Verwoerd et al. (1993) identified the northern north-west trending dykes as a Pilanesberg dyke swarm, which is part of the Pilanesberg dyke System, which also includes the southern north-south trending dyke's swarm. The chemical affinity of dyke swarms relates them to the Pilanesberg Complex. However, while the chemistry may have similarities the geochronology and reversals indicate they do not have a direct link. Both the northern and southern dyke swarms have negative anomalies in the range of -150 to -320 nT compared to the circular Pilanesberg Complex anomaly ranged between 166.5to 330 nT on the magnetic map.

The polished thin sections opaque mineralogy identification used reflected light and transmitted light to determine any associations with other minerals. The general trend in all the Pilanesberg Complex and dyke samples is that the opaque minerals have an association with green agerine seen in transmitted light. The ore minerals were identified as magnetite in reflected light. In the red syenite dyke, the magnetite appears as small, abundant phenocrysts

The intrusion relationship of the bodies in the Pilanesberg Province were examined with a $^{40}Ar/^{39}Ar$ geochronology study. Analysis of the ages achieved in a time sequence indicates that the oldest occurrence of the samples collected was the white foyaite from the Pilanesberg Complex at 1602.42 ± 38.89 Ma. The next intrusion from the examined samples is the red syenite dyke at 1219.48 ± 6.51 Ma, followed by the grey syenite dyke at 1139.71 ±18.30 Ma. Finally, the green foyaite from the Pilanesberg Complex is recorded at 953.58 ± 9.51 Ma. However, the samples for the green foyaite have massive amounts of excess argon, where no isochron solution was achieved. Further analysis would be required to decipher if the green foyaite did indeed intrude at 953.58 Ma or if it is recording a reversal event at that date.

The Pilanesberg dykes have previously published ages of 1290 ± 80 Ma, 1302 ± 80 Ma, 1310 ± 80 Ma (Robynson dyke) and 1330 ± 80 Ma (Gemspost, Venterspost Mine) (All from Rb-Sr on biotite, Van

Niekerk, 1962., Emerman, 1991). The ages achieved in his study, on the red syenite dyke at 1268 ± 10 Ma, 1219 ± 7 Ma and the grey syenite dyke at 1140 ±18 Ma are younger than the published dates. The error analysis is substantially lower so these dates are close to the real age of the dyke swarms intrusion. Further work would be required to achieve an overlapping error analysis to confirm the validity of the dates proposed.

The grey dyke intruded later than the rest of the southern dyke swarm at it is ~ 66 Ma to 73 Ma ± 12 Ma younger than the age of the red syenite dyke. Records indicate multiple intrusion episodes in the northern dyke swarm where the syenite dykes intrude the dolerite dykes to form a composite dyke of syenite encase in dolerite (Emerman, 1991). Hansen et al. (2006) reported the multistage composite dykes extending down to the gold reef in the southern dyke swarm, indicating that this dyke swarm is also a multistage intrusion event. It is likely that the grey dyke is another episode intruding at a later stage in the southern dyke swarm history. Even though the dykes intrude in different phases, the general trend for the southern dyke swarm remains oriented north-south as the dykes intrude along a weakness zone from the Mesoproterozoic intraplate extension event (Michell and Liferovich, 2006; Retief, 1963).

The Pilanesberg Complex published ages are between 1260 ± 50 Ma (K-Ar, Olivo and Williams-Jones, 1999) and 1397 ± 47 Ma (U-Pb on titanate, Hansen et al., 2006). Those dates suggested that the Pilanesberg Complex was the first intrusion event of the Alkaline Province, which was followed by the Leeuwfontein Complex and Spitskop Complex (1341 ± 37 Ma, Cawthorn et al., 2012). The date achieved for the Complex in this study is 1602 ± 39 Ma, which agrees with the hypothesis that the Pilanesberg Complex was the first intrusion. However, this age is considerably older than the published dates for the Complex, suggesting that the Complex is significantly older than initially estimated.

6.2 CONCLUSION AND SUGGESTIONS FOR FURTHER WORK

The circular 625 km^2 Mesoproterozoic Pilanesberg Complex is the world's largest alkaline intrusion forming part of a larger alkaline system called the Pilanesberg Province with previous ages ranging from 1200 Ma to 1450 Ma (Harmer R., 1992; Hansen et al., 2006). The Pilanesberg Province intrusions include two dyke swarms radiating out to the north-west and south of the Pilanesberg Complex, known as the Pilanesberg dyke System (1290 ± 80 Ma and 1330 ± 80 Ma (Van Niekerk, 1962)), and smaller circular clinopyroxenite intrusions throughout the Bushveld Complex. One of the smaller circular clinopyroxenite bodies is 1207 ± 200 Ma (Cawthorn et al., 2012) and situated in the centre of the Bushveld granites. The Pilanesberg dyke System and the circular clinopyroxenite intrusions are reversely magnetised (-150 to -320 nT) compared to the normally magnetised (166.5 to 330 nT) Pilanesberg Complex, suggesting that a magnetic reversal occurred during emplacement of the Province. The aeromagnetic map of South Africa illustrates the difference in magnetic polarity between the Pilanesberg Complex and the Pilanesberg dyke System.

The 28 km diameter Pilanesberg Complex has surface field relationships that suggest an internal dipping structure; however, the dip relationship of the Pilanesberg Complex is unknown regarding the internal structure and with relation to the host-rock at depth. The 2D gravity profile models of the Pilanesberg Complex assist with determining the emplacement relationship with the host rock. The 2D and 2.5D gravity models suggest that an internal dipping model has the best lowest misfit of 10.16% with the gravity data along the west-east profile. These models agree with Lurie's (1986) proposed inward dipping geometric models. The host rocks accommodation of the large Pilanesberg Complex was unknown. Cawthorn (2015) suggests that the Pilanesberg Complex intrusion did not displace the Bushveld Complex, as there is no evidence seen to the north and south of the Pilanesberg Complex along his gravity profile. Lurie (1986) proposed that the Pilanesberg Complex intruded as a cone sheet geometry and an axis tilted to the south. Cawthorn (2015) disputed this due to the volume and space conundrum where he states that the Bushveld is undisturbed to the north and south of the Pilanesberg Complex. The displaced portion of the Western Bushveld Complex to the west of the Pilanesberg Complex is evidence in support of Lurie's (1986) model of the Pilanesberg's intrusion. The displaced Bushveld rocks also fit the Bouguer gravity data when modelled west of the Pilanesberg Complex in both the 2D and the 3D forward models. The geological map also indicates that some of the Bushveld Complex Main Zone shifted to the west of the Pilanesberg Complex upon emplacement. The structural lineation is from the East African Rift, which have made the area structurally weak, and may be the reason that the Pilanesberg Complex was able displace some of the Bushveld Western limb. The Bushveld Complex would have already faulted the country rock on its emplacement providing a weakened zone ideal for the Pilanesberg Complex to intrude.

The Pilanesberg Complex's unknown 3D geometry below the known surface relationships was examined using 2D, 3D forward and inversion modelling of the gravity and magnetic datasets to form a 3D

geological model of the Complex. Modelling of the Pilanesberg Complex has confirmed that the inward dipping structure does have an overall southward dipping axis, i.e. the Pilanesberg Complex dips to the north. Ground measurements by Lurie (1986) indicated that the north of the Pilanesberg Complex dips outward from the centre and the University of British Columbia (UBC) 3D inversion model was able to confirm that the Pilanesberg Complex northern edge does dip outward to the north. The 3D magnetic inversions of the Pilanesberg Complex indicate an overall inward dipping structure, which correlates with the west-east orientated 2.5D profiles and 3D forward models, where test models of outward dipping and cylindrical bodies were unable to account for the Bouguer gravity signal over the Pilanesberg Complex. The PyGMI 3D forward model showed a good correlation with the UBC 3D inversion for the gravity along the outward dipping northern contact and inward dipping edges elsewhere. The contact depth, Euler deconvolution solutions and 3D magnetic voxel inversion indicate that the Pilanesberg Complex northern block is closer to the surface than the deeper southern block where the depth to fresh bedrock is approximately 1 km deep. The 3D voxel inversion indicated a correlation between the bisecting Vlakfontein fault and the change in depth to bedrock between the northern and southern block. The magnetic voxel inversion data displays the break in the 'C' Shape plug and the depth change between the northern and southern block of the Pilanesberg Complex. The Pilanesberg Complex central 'C' shaped plug forms a central anomaly on both the gravity and magnetic models.

The results of the geophysical modelling produced a schematic sequence of events describing the geological mechanisms and intrusion sequence for the Pilanesberg Complex. The Pilanesberg Complex intruded through pipes and vents in an extensional zone along a fault network weakness point on the edge of the Bushveld Western limb. A tuff and breccia layer capped the Pilanesberg Complex magma on the surface forming the top boundary for the ring structure to form below and allowing the Complex to expand laterally with each new layer. The layers intruded from the outer red syenite, the central red foyaite and then the white and green foyaite that use caldera magma subsidence to intrude between the red foyaite and red syenite. The Complex dips to the north due to a trap door graben subsidence that included rotation and block movement with the help of the internal Vlakfontein fault and a fault on the southern edge. Complicated faulting and movement of the Bushveld Complex have accommodated for the ~28 km Pilanesberg Complex in the Bushveld Western limb. The fractures and block movement are substantially more complicated with factors such as uplift, extensional environment and erosion making up for aspects required for the simple illustration to be possible

The minimum depth extent for the Pilanesberg Complex is 5 km, which is the minimum allowed depth for the 3D forward PyGMI gravity modelling to provide a potential data match. A maximum possible depth extent is more complicated as the Euler deconvolution solutions are possibly referring to the contact with the Bushveld Complex. The Euler deconvolution solutions provide depth estimates between ~ 12 km, 8 km and 10 km on the western edge and ~ 7 km, 15 km and 8 km on the west-east profiles. The Euler deconvolution solutions indicate that the northern contact does dip out to the north to a depth of 12 km (profile 4, Figure 3.19). The modelled 45° outward dipping northern contact has a positive

correlation with the gravity data when modelled with the 3D forward PyGMI gravity model (Figure 4.26 – 4.30).

The internal structure of the Pilanesberg Complex was also examined with magnetic and gravity image processing which were able to identify 2-3 ring-like structures around a central plug on the magnetic maps. The magnetic maps also showed that the Pilanesberg Complex has been cross-cut by the northern Pilanesberg dyke swarm as well as the unrelated east-west dyke swarm.

Geochronology of the Pilanesberg Complex attained ages of 1602 ± 39 Ma and 15834± 11 Ma for the white foyaite (samples 6 and 7 using amphibole spectrum analysis). The age is considerably older than the previously published dates, which ranged between 1200 Ma and 1450 Ma. The dyke samples are dated at 1160 ± 9 Ma on amphiboles using inverse isochron analysis on the grey dyke from site 1 and at 1219 ± 7 Ma and 1268 ± 10 Ma on feldspars using spectrum analysis of the red syenite dyke from sites 3 and 4. The age dates for the southern Pilanesberg dyke swarm are younger than the previous ages for the dykes, which were between 1290 Ma and 1330 Ma. The age dating has made it possible to distinguish between different episodes of dyke intrusion, namely the red syenite dyke is older and the younger grey syenite dyke occurred as a later episode in the intrusion sequence.

In cases when the Pilanesberg rocks appear to be highly altered, the feldspar age results apear to be unrealistically young, however dating of the amphibole grains produced reliable data with smaller errors between 7 Ma and 61 Ma with a standard deviation of 14 Ma. Magnetite in the samples was associated with the amphibole thus producing consistently competent ages from the amphibole analysis.

The Pilanesberg Complex is chemically and spatially associated with the Pilanesberg dyke system and the other intrusions in the Pilanesberg Province. The first event of the intrusions from the samples in this study is the white foyaite of the Pilanesberg Complex followed by the younger red syenite dyke and the younger still grey syenite dyke. The Pilanesberg Complex age dates of 1602 ± 39 Ma and 1584± 11 Ma make the Pilanesberg Complex substantially older than the rest of the Pilanesberg Province, which has dates of 1207 ± 200 Ma at Elandskraal Volcano (Cawthorn et al., 2012) and 1374 ± 10 Ma at Leeuwfontein Complex (Hansen et al., 2006).

Suggestions for continued work that were beyond the scope of this project should include geochronology being done on each of the Pilanesberg Complex lithologies to determine the age from the inner ring to the exterior ring of the structure. The age and difference of the northern dyke swarm should also be compared with the other intrusions from the Pilanesberg Province in a large scale study.

REFERENCES

Blakely, R.J. (1995). Potential Theory in Gravity and Magnetic Applications. Cambridge University Press, Cambridge; P55-61; P200-201; P350-351.

Burns, C. (2012). Introduction of VOXI Earth Modeling technology: Accessible 3D modelling technology advances exploration geophysics for improved drill targeting. *Technology*. March 9, 2012. http://www.earthexplorer.com/2012/ Introduction _ of_VOXI_Earth_Modelling_technology.asp

Butler, R.F., (1992). Paleomagnetism: magnetic domains to geological terranes. Blackwell Scientific, Boston; P. 238.

Cawthorn, G.R. (2015). The geometry and emplacement of the Pilanesberg Complex, South Africa. *Geological Magazine:* Cambridge University Press: P. 1-11.

Cawthorn, G.R., Ellam, R.M., Ashwala, L.D., Webb, S.J. (2012). A clinopyroxenite intrusion from the Pilanesberg Alkaline Province, South Africa. *Precambrian Research*. P. 25– 36 and 198– 199...

Cawthorn, R. G. (2009). *Emplacement geometry of the Pilanesberg Complex*. Out of Africa Conference 2009, University of the Witwatersrand, Johannesburg, South Africa. Abstract, P. 22.

Cawthorn, G.R., Eales, H.V., Walraven, F., Uken, R., Watkeys, M.K. (2006). *The Bushveld Complex*. In: Johnson, M.R., Anhaeusser, C.R., and Thomas, R.J. (Eds.), the Geology of South Africa. Geological Society of South Africa, Johannesburg/Council for Geoscience, Pretoria, P. 261-279.

Cawthorn, R.G. (1988). The Geology of the Pilanesberg, Information Series 1. National Parks Board of Bophuthatswana, Mafikeng. P. 8-13

Cole, P. (2012). Development of a 3D potential field forward modelling system in Python. IN43A-1505. AGU fall meeting, San-Fransisco 2012. ePoster: fallmeeting.agu.org/2012/files/2012/11/3DModelling_PCole1.pdf

Cooper, G.R.J. (2014). The automatic determination of the location, depth, and dip of contacts from aeromagnetic data. *Geophysics*, V. 79, No. 3. P. J34-J41.

Cooper G.R.J. (2011). Grav2Dc – gravity modelling and inversion, Version 2.06. Johannesburg, University of the Witwatersrand. Visited June 2011: http://www.wits.ac.za/academic/science/geosciences/research/geophysics/gordoncooper/6511/software.html,

Cooper G.R.J. (2004). Euler Deconvolution applied to Potential Field Gradients. *Exploration Geophysics*, V. 35, P. 165–170.

Coomber, S.J. (2008). Gravity modelling in the Western Bushveld Complex, South Africa, using integrated geophysical data. M.Sc. Thesis, University of the Witwatersrand, Johannesburg, South Africa.

Emerman, S.H. (1991). Correlation of a dyke swarm in southeastern Botswana with the Pilanesberg dyke swarm South Africa. *Journal of African Earth Sciences*, V. 12, No. 4, P. 525-531.

Ferguson, J. (1973). The Pilanesberg Alkaline Igneous Complex. Trans. Geol. Soc. S.A., V. 76; P. 249-270.

Fowler C.M.R. (1990). *The solid Earth, an introduction to global geophysics*. Cambridge University Press, United Kingdom; P. 206-207.

Gose, W.A., Hansen, R.E., Harmer, R.E., Seidel, E.K. (2013). Reconnaissance paleomagnetic studies of Mesoproterozoic alkaline igneous complexes in the Kaapvaal Craton, South Africa. *Journal of African Earth Science*, V. 85, P. 22-30.

Gose, W.A., Johnston, S.T., Thomas, R.J. (2004). Age of magnetization of Mesoproterozoic rocks from the Natal sector of the Namaqua–Natal belt, South Africa. *Journal of African Earth Sciences*, V. 40, P. 137–145.

Gough, D.I. (1958). A study of the Paleomagnetism of the Pilanesberg dykes. *Geophysics Journal International*, V. 7, No. 54, P. 196-213.

Hansen, R.E., Harmer, R.E., Blenkinsop, T.G., Bullen, D.S., Dalziel, I.W. D., Gose, W.A., Hall, R.P., Kampunzu, A.B., Key, R.M., Mukwakwami, J., Munyanyiwa, H., Pancake, J.A., Seidel, E.K., Ward, S.E. (2006). Mesoproterozoic intraplate magmatism in the Kalahari Craton: A review. *Journal of African Earth Sciences*, V. 46, P. 141-167.

Hinze, W.J., Aiken, C., Brozena, J., Coakley, B., Dater, D., Flanagan, G., Forsberg, R., Hildenbrand, T., Kaller, G.R., Kellogg, J., Kucks, R., Li, X., Mainville, A., Moring, R., Pilkington, M., Plouff, D., Ravat, D., Roman, D., Urrutia-Fucugauchi, J., Véronneau, M., Webring, M., Winester, D. (2005). New standards for reducing gravity data: the North American gravity database. *Geophysics*, V. 70, P. J25-J32.

Harmer, R.E. (1999). The petrogenetic association of carbonatite and alkaline magmatism: constraints from the Spitskop Complex, South Africa. *Journal of Petrology*, V. 40, P. 525–548.

Humphrey, A.W. (1914). The geology of the Pilanesberg and the surrounding country. Union of South Africa, Mines Department, Geology Survey. *Report of the Geological Survey of South Africa*, 1911(3); P.75.

Jansen, D. (1977). *The Geology of the country of Pretoria: An explanation of sheets 2527DA, DB, DC, DD and 2528CA, CB, CC, CD.* Department of Mines, Geological Survey. The Government Printer, Pretoria

Jarvis, A., Reuter, H. I., Nelson, A., Guevara, E. (2008). Hole-filled SRTM for the globe Version 4, available from the CGIAR-CSI SRTM 90m Database, (http://srtm.csi.cgiar.org).

Kuiper, Y. D. (2002). The interpretation of inverse isochron diagrams in 40Ar/ 39Ar geochronology. *Earth and Planetary Science Letters*, V. 203, I. 1, P. 499-506.

Letts, S.A. (2007), The Paleomagnetic significance of the Bushveld Complex and related 2 GA magmatic rocks in ancient continental entities, University of the Witwatersrand, Johannesburg, South Africa.

Liferovich, R.P., Michell, R.H. (2006). Appetite-group minerals from Nepheline syenite, Pilanesberg Alkaline Complex, South Africa. *Mineral Magazine*, October 2006, V. 70 (5); P. 463-484.

Lurie, J. (1986). Mineralisation of the Pilanesberg Alkaline Complex. In Mineral Deposits of South Africa 2 (C. R. Anhaeusser and S. Maske, eds.). The Geological Society of South Africa, Johannesburg, South Africa. P. 2215-2228.

MacKenzie, W.S., Adams, A.E. (1994). *The colour atlas of rock and minerals in Thin Section.* Manson Publishing, London, P. 67-98.

McCaffrey, L.P. (1993). Geohydrology of the Pilanesberg. M.Sc. Dissertation, University of the Witwatersrand.

Michell, R.H., Liferovich, R.P. (2006). Sub-solidus deuteric/hydrothermal alteration of eudialyte in lujavrite from the Pilanesberg Alkaline Complex, South Africa. *Lithos*, V. 91; P. 352-371.

Molengraff, G.A.F. (1905). Preliminary Note on the Geology of the Pilandsberg and a Portion of the Rustenburg District. *Trans. Geol. Soc. S.A.*, V. 8; P. 914-923.

Olivo, G.R., Williams-Jones, A.E. (1999). Hydrothermal REE Rich Eudialyte from the Pilanesberg Complex, South Africa. *The Canadian Mineralogist*, V. 37; P.673-663.

Pantshi, B. (2006). The red syenite of the Pilanesberg Complex as a Nepheline source for the South African ceramics and glass industry. M.Sc. Dissertation, University of Pretoria.

Renne, P.R., Karner, D.B., Ludwig, K.R. (1998). Absolute Ages Aren't Exactly, *Science*, V. 282; P. 1840.

Retief, E.A., (1963). Petrological and Mineralogical Studies in the Southern Part of the Pilanesberg Complex, Transvaal, South Africa. Ph.D. thesis, Univ. of Oxford, Oxford, UK.

Rodriguez, E., C.S. Morris, J.E. Belz, E.C. Chapin, J.M. Martin, W. Daffer, S. Hensley, (2005). An assessment of the SRTM topographic products. *Jet Propulsion Laboratory*, Technical Report JPL D-31639, Pasadena, California, P. 143.

Rollinson, H. R. (1993). *Using geochemical data: Evaluation, Presentation, Interpretation*. Pearson Prentice Hall, Harlow - England.

Shand, S.J. (1923). The alkaline rocks of the Franspoort Line, Pretoria District. *Transaction Geological Society South Africa*, V. 24; P. 81–100.

Shand, S.J. (1928). The Geology of Pilanesberg (Pilanesberg) in the Western. Transvaal: A study of Alkaline Rocks and Ring intrusions. *Transvaal Geological Society South Africa*, V. 31; P. 97-156.

Stettler, E.H., Fourie, C.J.S., Bühmann, J.R., Hattingh, E., Cole, P., Kleywegt, R.J., Wolmarans, L.G., Cloete, A.J., (1999). Magnetics, South African Geophysical Atlas vol. 2 (CD-ROM). Council for Geoscience, South Africa.

Talwani, M., Ewing, M. (1960). Rapid computation of gravitational attraction of three-dimensional bodies of arbitrary shape. *Geophysics,* V. 25, P.203-225.

Thomson, D.T., (1982). EULDPTH: A new technique for making computer-assisted depth estimates from magnetic data: *Geophysics*, V. 47, P. 31–37.

Van Niekerk, C.B. (1962). The Age of the Gemspost dyke from the Venterspost Gold Mine. *Trans. Geol. Soc. S.Aft.,* V. 65, P. 105-111.

Verwoerd, W.J., Weder, E.E.W., Harmer, R.E. (1993). The Stukpan carbonatite in the Orange Free State goldfield. *South African Journal of Geology*, V. 96, P. 108–118.

Webb, S.J., Cawthorn, G.R., Nguuri, T., James, D. (2004). Gravity modelling of Bushveld Complex connectivity supported by Southern African Seismic Experiment results. *South African Journal of Geology*, V. 107, P. 207-218.

Webb, S.J., Ngobeni, D., Jones, M.W.Q, Abiye, T., Lee, M., Devkurran, N., Goba, R., Burrows, D., Ashwal, L. D., Pellerin, L., (2011).Hydrogeophysical investigation for groundwater at the Dayspring Children's Village, South Africa. *The Leading Edge*, April 2011. P. 936-940.

Welraven, F., Du Plessis, S. J. P., Iuris B. (1981). 2526 Rustenburg 1:250 000 geological series. Department of Mineral and Energy Affairs. *Spec. Pub. Geol. Soc. S. Afr*., V. 1, P. 242-265. Republic of South Africa.

2526 Rustenburg. 1981. Compiled by Walraven, F. From mapping by personnel of the University of Pretoria (1977), Young, D.R., Vermaak, C.F., Coertze, F.J., Retief, E.A., Walraven, F., Andrew, G.F., Verwoerd, W.J., Strauss, C.A., Crocker, I.T., MacCaskie, D.R., Clubley-Armstrong, A.R., Prevost, X.M., Davies, G.R., Morgan, R.P.E., Durr, K.W., Von Backström, J.W., Loubser, P.J., Snyman, A.A., Blom, L.W.R., Visser, H.N. and personnel of the University of the Witwatersrand (subdivision of the Dolomite). Explanation by Walraven, F., P. 37.

APPENDIX A

CONFERENCE ABSTRACT – SAGA 2013

The 2013 Saga abstract introduces the Pilanesberg Province and the areas of interest with in it. The intrusions that are examined are the Pilanesberg Complex and the Pilanesberg dyke System. How these intrusions relate is not known and differences in their magnetic field responses are examined. The intrusions relationships of the Pilanesberg Province will only become clear once there is a good understanding of the main intrusion; the Pilanesberg Complex. The Pilanesberg Complex is thus examined for geometry and lithological contact relationships to better understand its origin.

A 3D potential field model of the Pilanesberg Complex shape and structure.

S-A. Lee[1], S.J. Webb[1], M.Q.W Jones[1], R.J. Durrheim[1, 2], M. Ganerød[3]

1. University of the Witwatersrand, South Africa
2. CSIR Centre for Mining Innovation
3. Geological Survey of Norway (NGU)

The Mesoproterozoic Pilanesberg Complex, South Africa, is the world's largest alkaline intrusion. While surface field relationships suggest an inward dipping structure. It is unclear how these dips extend to depth, and what is the 3D geometry of the Pilanesberg Complex. 2D and 3D forward and inversion modelling of gravity and magnetic data is used to set limits on the 3D shape of the Complex.

Based on age and chemical affinity, it is known that the Pilanesberg Complex forms part of a larger system of alkaline intrusions that includes two radiating dyke swarms to the north-west and south of the Complex as well as smaller circular clinopyroxene intrusions throughout the Bushveld Complex.

The Pilanesberg dyke swarms and the clinopyroxenite circular intrusions have a reversed magnetism to that of the Pilanesberg Complex suggesting that a magnetic reversal occurred during emplacement of the system.

Key words: Pilanesberg Complex, 3D modelling, ring dyke, magnetic reversal

ABSTRACT

INTRODUCTION

The Pilanesberg Complex, with a diameter of 28 km, is the world's largest alkaline intrusion (Figure 1). The intrusion is located on the Kaapvaal Craton within the Rustenburg layered suit gabbronorite and red granite of the Lebowa Granite Suite on the western limb of the Bushveld Complex, South Africa (Hansen et al., 2006). The Pilanesberg Complex intruded between 1200 and 1450 Ma in the Mesoproterozoic era during an intraplate extension event. The pyroclastic and lava flow sequences resulted in an inward dipping structure around a preserved central core and plug (Olivo and Williams-Jones, 1999; Michell and Liferovich, 2006).

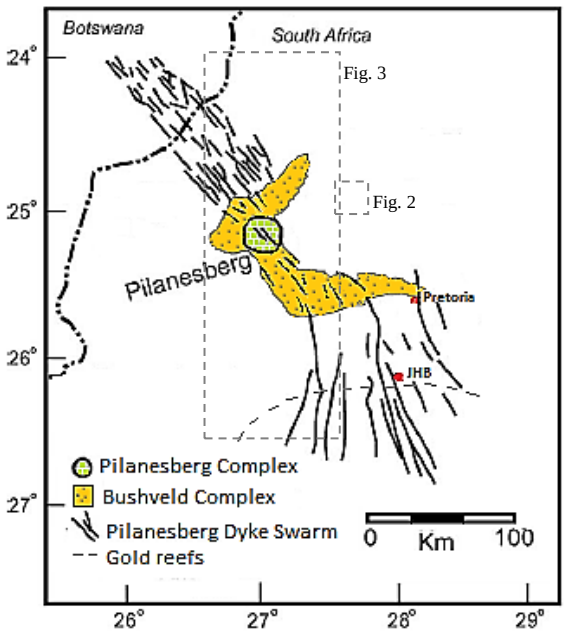

Figure 1. Regional setting of the Pilanesberg Complex and dyke swarms with the western Bushveld complex, modified from Emerman (1991), Cawthorn et al. (2006).

The Pilanesberg Complex is associated with a number of other intrusions including the compositionally associated Pilanesberg syenite dykes (Figure 1). Recent work by Cawthorn et al. (2012) reveals clinopyroxene circular intrusions approximately 8 km wide in the middle of the Bushveld Complex (Figure 2) aged at 1207 ± 200 Ma. The intrusions have a composition affinity to alkaline intrusions similar to Phalabora and thus proposed to be related to the Pilanesberg system (Cawthorn et al., 2012).

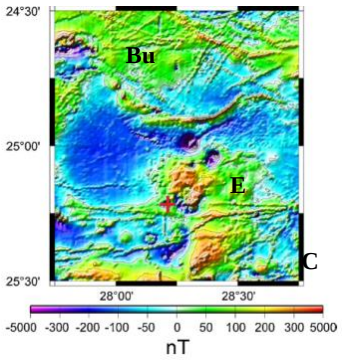

Figure 2. The occurrence of circular intrusions related to the Pilanesberg Complex. Bu-Buffleskraal, E-Elandskraal, C-Cullinan kimberlite (Cawthorn et al., 2012)

One swarm of syenite dykes extends in a north-westerly direction into Botswana: while the second swarm, oriented north-south, can be traced by composition and by magnetic correlation to the south of the Complex and into the Johannesburg Dome (Emerman, 1991).

The dyke swarms are named as Pilanesberg dykes from the comparable compositions as well as the similar age range with the Pilanesberg Complex (Cawthorn et al., 2012). However, the airborne magnetic data of the dykes indicates strong negative anomalies opposite to that of the Complex itself (Figure 3).

The dyke's composition is generally tholeiitic but varies from the composite dolerite-syenite dykes 225 km south of the Complex, exposed in gold mines along the gold reef line in (Figure 1), to the more common syenite dykes occurring across most of the dyke swarm. Gough (1958) examined five Pilanesberg-aged dykes south of the Complex using paleomagnetism and concluded that the dykes carried remnant magnetisation. A strong iso-remnant magnetisation component is recorded from lightning strikes on surface outcrop; thus, rock samples are collected from deep mines or quarries to avoid the surface effect. The samples from the Johannesburg dome gold mines indicated a correlating mean direction for a north-seeking magnetic pole (Gough, 1958). Dykes sampled include the composite dykes (syenite encased in dolerite), on Libanon and Venterspost Gold Mines; the basic dyke at Robinson Deep and East Geduld Gold Mines and syenite at the Simmer and Jack Gold Mine. The mines are found along the gold reef line in Figure 1.

Dykes of both swarms were correlated with a double peak reversed anomaly that is identifiable with a magnetic high peak in the south. This double peaked magnetic anomaly is due to a two staged emplacement dated at 1310 ±60 Ma (Emerman, 1991), where-by the dolerite dykes were intruded by a syenite dyke before the package cooled, forming a composite dyke with a syenite centre surrounded by dolerite (Emerman, 1991).

Airborne magnetic data over South Africa indicates that the Pilanesberg Complex carries a strongly induced magnetisation that produces an anomaly with an amplitude of 325 nT above the background magnetic signature of the country rock into which it intruded. The compositionally associated Pilanesberg dykes are remanently magnetized and have a negative magnetic anomaly of 315 nT with respect to the survey flight height of 150 m (Figure 3). The Pilanesberg Complex does not indicate a well-defined dipole suggesting it carries some remnant magnetisation unless the Pilanesberg dipole low is interfering with the strong low of the Bushveld Complex main zone.

Dating the Complex and the dykes produces large error estimates that are able to define a possible range of the intrusion age but not an exact age. The Complex hosts a large quantity of zirconium and rare earth elements (REE). The zirconium is carried by eudialyte, which makes up 20% of the green nepheline syenite. The zirconium is in an element form within the eudialyte and not in zircon crystals (Olivo and Williams-Jines, 1999).

The age dating on the Complex was obtained using K-Ar and U-Pb titanite methods, giving dates of 1250 ±50 Ma and 1397 ±47 Ma respectively (Pantshi, 2006). These methods produce dates that are not well defined with the Pilanesberg Complex's age ranging from 1450 to 1200 Ma (Cawthorn et al., 2006). The range in ages maybe due to the dating techniques used, since closed system behaviour of the K-Ar method cannot be

tested (e.g. Ar-loss or excess), while the titanite U-Pb method is less retentive of radiogenic lead, such that the ages obtained are possible minimum ages.

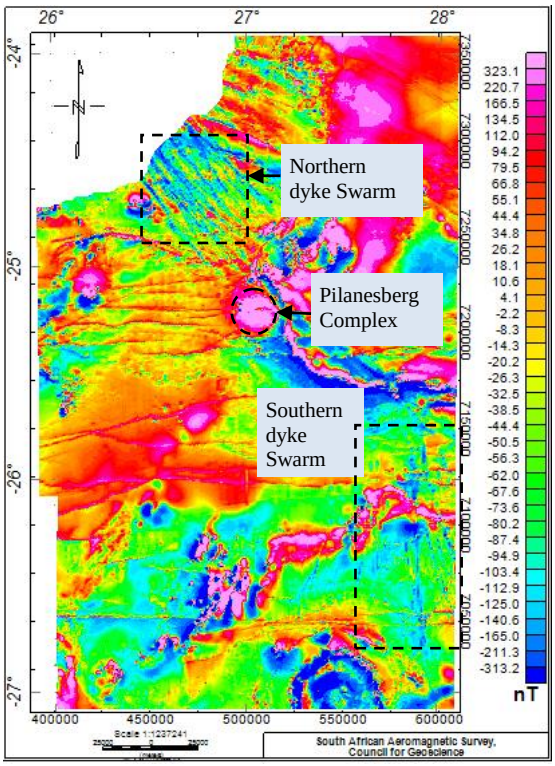

Figure 3. Magnetic data indicating the signature of the Pilanesberg Complex (positive 325 nT signature) and that of the Pilanesberg dykes (negative 315 nT signature) seen in blue, 1:50 000 magnetic maps of South Africa 2426, 2526, 2626 (Council for Geoscience).

The Pilanesberg dykes are dated at 1302 ± 80 and 1290 ± 80 Ma `from Rb-Sr biotite dating which fits into the age range of the Complex (Hansen et al., 2006). The smaller circular intrusions in the Bushveld area also fit in to the age range of the Pilanesberg Province aged at 1207 ± 200Ma (Sm-Nd dating) and 1341 ± 37 Ma at Spitskop further east (Cawthorn et al., 2012).

The age data on the Alkaline Province helps to constrain the emplacement range of the Complex, which is believed to have intruded from the outer ring to the central plug in several stages around the time that magnetic reversal and the dyke swarms intruded. This is examined from existing structural geology and potential field modelling. While the parallel orientation of the dykes is due to a series of normal faults that are directly related to extensional tectonics and alkaline magmatism (Hansen et al., 2006).

Geometry of the Pilanesberg Complex

The geometry of the Pilanesberg Complex at depth has been suggested to be a series of ring dykes or alternately cone sheets are emplaced horizontally and followed by centripetal subsidence (Cawthorn, 2009; Lurie, 1986).

Cawthorn (2009) proposed several models to account for the space required for the 28 km^2 intrusion of the Pilanesberg Complex and how the host rock would accommodate it. The examples in Figure 4 indicate the host rock shifts according to the geometry and manner of intrusion. No depth scale is represented.

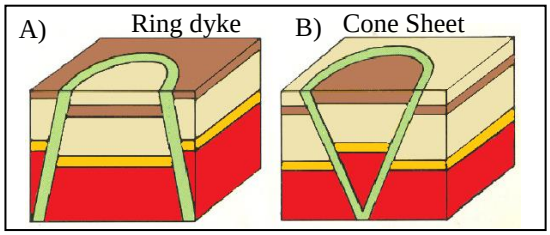

Figure 4. Two possible geometries to explain the host rock space problem for the intrusion of the Pilanesberg Complex. A ring dyke would form either with subsidence of the host rock (left), or the formation of a cone sheet (right), modified from Cawthorn (2009).

Lurie (1986) has proposed a geological model of the Pilanesberg Complex using the dip of the volcanic rocks from surface observation (Figure 5). The model indicates a cone formed by inward-dipping ring dykes around a central plug with the vertical axis leaning to the southeast. Lurie (1986) describes the Complex as being composed of centripally dipping faulted blocks resultant of a collapsed caldera formation with approximate angles of 35° in the south to 50° in the west and 45° in the east. The rocks in the north, however, appear to dip at a 35° angle towards the north (Figure 5).

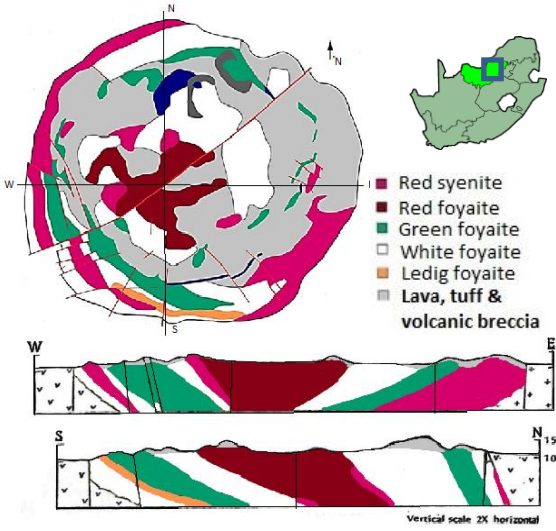

Figure 5. A schematic representation of the geology of the Pilanesberg Complex geology, modified from Lurie (1986), Cawthorn et al. (2006).

The national gravity grid indicates that the Pilanesberg Complex has a negative density difference compared with the Bushveld Complex granite. This will make gravity modelling possible to test the shape of the Complex below the surface relationships using the gravity profile in Figure 6. The data also indicates a change in the gravity signal within the ring structure, which may allow for some modelling of the Complex's internal structure.

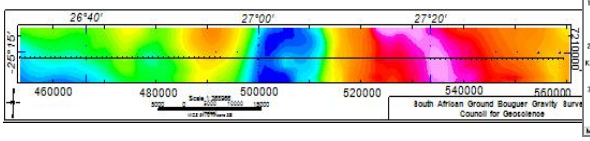

Figure 6. West East Bouguer Gravity Profile over the Pilanesberg complex (Blue) and the Bushveld Complex (Red)

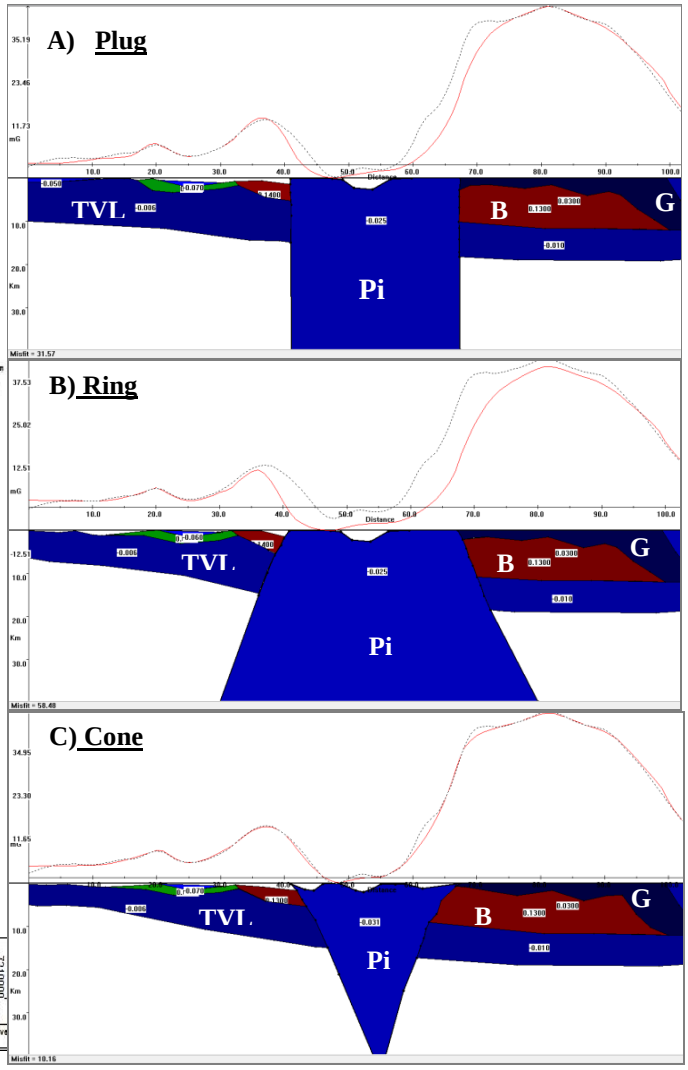

Figure 7. Preliminary modelling the west-east Pilanesberg profile from data in figure 4 showing different Pilanesberg models (Pi) in the host rock, TVL- Transvaal with Magaliesburg quartzite (green), B-Western Bushveld complex, G- granite. The geology is matched to the surface geology (A) Model with vertical contacts produces a poor fit to the field data. (B) An outward dipping Complex has a worse fit than the plug model; however, the inward dipping model in C) is able to match the gravity data better.

METHOD AND RESULTS

The shape of the Pilanesberg Complex is unknown below the measured surface relationship on outcrop apart from the internal structure dipping inward (Lurie, 1986). We test the shape of the Complex using gravity data over the area. The west-east profiles through the middle of the Pilanesberg are modelled (Figure 7) to investigate how the shape of the Complex relates to the calculated field using 2D profile models (from Figure 6) based on the idea in Figure 4+5.

Modelling of the west-east profile over the Pilanesberg Complex indicates that a body with vertical or outward-dipping contacts does not match the gravitational data over the area. However, a body with inward-dipping contacts provides a better fit with the potential field data.

Using the Magnetic data over the Pilanesberg, a 3D Voxi model is inverted for the body and

internal structure (Figure 8). The solution defines the structure as reducing in size with depth and agrees with the 2D inward dipping model from the gravity data set.

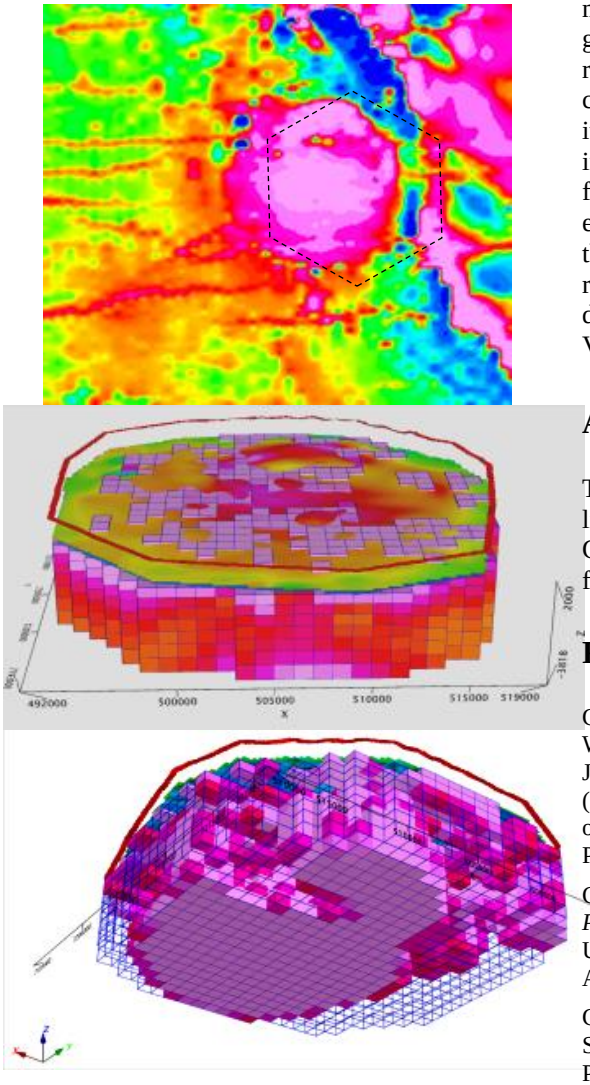

Figure 8. A) The magnetic data over the Pilanesberg complex indicated as a (325 nT) positive anomaly. (B) A preliminary inversion of the Pilanesberg magnetic data into a 3D Voxi model using a 50x50-cell inversion. (C) View from below showing how the Complex decreases in size from the surface to depth

CONCLUSIONS

The Pilanesberg Complex is the world largest alkaline intrusion and forms part of a suite of intrusions with ages ranging from 1450 to 1200 Ma including smaller clinopyroxene bodies in the Bushveld area as well as two dyke swarms of similar age and composition, which have undergone a magnetic reversal.

The Pilanesberg Complex is examined in 2D gravity profiles to determine the emplacement relationship with the host rock. These 2D gravity models suggest an inward dipping model fits the gravity data best and concurs with the field relationships. The space problem of how the country rock accommodated such a large body and its shape, does not appear to be an issue as the intrusion of the Bushveld Complex appears to have fractured the country rock enough to leave it weak enough to accommodate the intrusion as seen in the disturbed Magaliesburg rocks and Bushveld rocks to the west of the Pilanesberg. The inward dipping model is supported by the preliminary 3D Voxi model, which decreases diameter with depth.

ACKNOWLEDGMENTS

Thanks Geosoft for providing software and licences for making processing possible and to the Council for Geoscience for providing the Potential field data.

REFERENCES

Cawthorn, G. R., Eales, H. V., Walraven, F., Uken, R., Watkeys, M. K. (2006). *The Bushveld Complex*. In: Johnson, M.R., Anhaeusser, C. R. and Thomas, R.J. (Eds.), the Geology of South Africa. Geological Society of South Africa, Johannesburg/Council for Geoscience, Pretoria, 261-279.

Cawthorn, R. G. (2009). *Emplacement geometry of the Pilanesberg Complex*. Out of Africa Conference 2009, University of the Witwatersrand, Johannesburg, South Africa. Abstract, P22.

Cawthorn, G. R., Ellam, R. M., Ashwala, L. D., Webb, S. J. (2012). A clinopyroxenite intrusion from the Pilanesberg Alkaline Province, South Africa. *Precambrian Research*. 198– 199. 25– 36.

Emerman, S. H. (1991). Correlation of a dyke swarm in south eastern Botswana with the Pilanesberg dyke swarm South Africa. *Journal of African Earth Sciences*, v. 12, n. 4, p. 525-531.

Gough, D. I. (1958). A study of the Paleomagnetism of the Pilanesberg dykes. *Geophysics Journal International*, V. 7, No. 54, P. 196-213.

Hansen, R. E., Harmer, R. E., Blenkinsop, T. G., Bullen, D. S., Dalziel, I. W. D., Gose, W. A., Hall, R. P., Kampunzu, A. B., Key, R. M., Mukwakwami, J., Munyanyiwa, H., Pancake, J.A., Seidel, E. K., Ward, S. E. (2006). Mesoproterozoic intraplate magmatism in the Kalahari Craton: A review. *Journal of African Earth Sciences*, v. 46, p. 141-167.

Lurie, J. (1986). Mineralization of the Pilanesberg Alkaline Complex. In Mineral Deposits of South Africa 2 (C. R. Anhaeusser and S. Maske, eds.). The

Geological Society of South Africa, Johannesburg, South Africa. p. 2215-2228.

Michell, R. H. and Liferovich, R. P. (2006). Subsolidus deuteric/hydrothermal alteration of eudialyteinlujavrite from the Pilanesberg Alkaline Complex, South Africa. *Lithos*, v.91; p. 352-371.

Olivo, G. R. and Williams-Jones, A. E. (1999). Hydrothermal REE Rich Eudialyte from the Pilanesberg Complex, South Africa. *The Canadian Mineralogist*, v. 37; p.673-663.

Pantshi, B. (2006). *The red syenite of the Pilanesberg Complex as a Nepheline source for the South African ceramics and glass industry*. M.Sc. Dissertation, University of Pretoria

APPENDIX B

WORKSHOP ABSTRACT – AFRICA ARRAY 2015

Geophysical investigations into the geometry and age of the Pilanesberg Complex, South Africa

Sally-Anne LEE[1], Susan J. Webb[1], Morgan Ganerød[2], M. Q. W. Jones[1] and R. J. Durrheim[1,3]

1. School of Geosciences, University of the Witwatersrand, Private Bag 3, WITS, 2050, South Africa
2. Geological Survey of Norway, Leiv Eirikssonsvei 39, N7491 Trondheim, Norway
3. CSIR Centre for Mining Innovation, South Africa

Email: sally-anne.lee@hotmail.com

The Mesoproterozoic Pilanesberg Complex is one of the world's largest alkaline intrusions. Here we present 2D and 3D models of gravity and magnetic data to set limits on the poorly known 3D geometry with respect to dips and depth extent.

In the past, the age data and chemical affinity have been used to suggest the Complex is part of a larger system of alkaline intrusions, which include two dyke swarms radiate to the north-west and south of the Complex, as well as circular clinopyroxene intrusions in the centre of the Bushveld Complex.

The dyke swarms and the clinopyroxenite intrusions are reversely magnetised with IGRF corrected values ranging between -150 to -320 nT compared to the normally magnetised 166 to 330 nT Pilanesberg Complex, suggesting a magnetic reversal occurred between the emplacement of the Pilanesberg Complex and the dykes.

The grey syenite dyke from the southern dyke swarm is dated at 1139.7 ± 18.3 Ma using amphiboles and inverse isochron analysis. While feldspar grains used with spectrum analysis are dated at 1219.4 ± 6.5 and 1268.3 ± 10.3 Ma for the pink Pilanesberg syenite dyke.

The age of the Pilanesberg Complex as determined from the white nepheline syenite using amphibole spectrum analysis is 1602.42 ± 38.9 and 1583.9 ± 10.8 Ma. This is the first well-constrained age for the Pilanesberg and it demonstrates that it is significantly different from the dykes and clinopyroxene circles.

Keywords: Pilanesberg Complex, 3D modelling, Paleomagnetism, Geochronology

APPENDIX C

CONFERENCE ABSTRACT – SAGA 2015

The Pilanesberg Province is composed of Mesoproterozoic syenite intrusions. Within the Province, the intrusions are separated into those that are positively magnetized and those that are negatively magnetized. This separation is investigated with questions including a possible magnetic reversal for the cause. The geochronology indicated that Pilanesberg Complex is considerably older than the Pilanesberg dyke Swarm, which widens the interpretation of the Provinces origin possibilities.

Potential magnetic reversal of the South African Pilanesberg Complex and Pilanesberg dyke System using paleomagnetism and geochronology.

S-A. Lee1, S.J. Webb1, M. Ganerød 2, M.Q.W. Jones1

1. University of the Witwatersrand, South Africa, sally-anne.lee@hotmail.com; susan.webb@wits.ac.za

2. Norges Geologiske Undersøkelse, Norway.

BIOGRAPHY

Sally-Anne Lee is a master's candidate at Wits University in potential field geophysics looking at the geology, geometry and paleomagnetics of the South African Pilanesberg Complex and related dyke System. The Pilanesberg analysis includes 2D, 3D potential field modelling as well as 3D inversions for the geometry as well as paleomagnetism and geochronology included here.

SUMMARY

The Pilanesberg Complex forms part of a larger system of alkaline intrusions, known as the Pilanesberg Alkaline Province. This Province includes two dyke swarms that radiate north-west and south of the Complex, as well as smaller circular clinopyroxenite intrusions throughout the Bushveld Complex.

The Pilanesberg dyke System and the clinopyroxenite intrusions are reversely magnetised with IGRF corrected values between -150 to -320 nT compared to the normally magnetised 166 to 330 nT Pilanesberg Complex. Paleomagnetism and age dating is used to test the hypothesis that a magnetic reversal occurred between the emplacement of the Pilanesberg Complex and the Pilanesberg dyke System.

The Complex dates at 1602.42 ± 38.9 Ma and 1583.9 ± 10.8 Ma, based on the analyses of white foyaite samples from the southern edge of the Complex (using amphibole spectrum analysis). These ages are vastly different from previously reported ages between 1200 Ma and 1450 Ma. Ages of the Pilanesberg dyke Swarms of 1139.7 ± 18.3 Ma obtained for the grey syenite dyke (using amphiboles inverse isochron analysis), and of 1219.4 ± 6.5 to 1268.3 ± 10.3 Ma on two red syenite dyke samples (using feldspars spectrum analysis) are significantly younger. The significantly different age data and opposite paleomagnetism poles of the Complex and dyke System suggest that reversed magnetisation of the dykes is the result of a magnetic reversal between the emplacement of the Complex and the dyke System.

Key words: Pilanesberg Complex, Pilanesberg dyke System, Pilanesberg Province, magnetic reversal, Pilanesberg age.

INTRODUCTION

The Mesoproterozoic Pilanesberg Complex, South Africa, is the world's largest alkaline intrusive complex. Surface field relationships suggest the Complex

Based on age data and chemical affinity, the Pilanesberg Complex formed part of a larger system of alkaline intrusions, known as the Pilanesberg Alkaline Province.

The Pilanesberg dyke System (Jansen, 1977) is compositionally associated with the intrusions in the Pilanesberg Province. One swarm of syenite dykes trends in the north-west- south-easterly direction extending to the northwest of Pilanesberg into Botswana. The second swarm, trending north-south, is traced by composition and magnetic correlation from the south of the Pilanesberg Complex into the Johannesburg Dome (Emerman, 1991) (Figure 1).

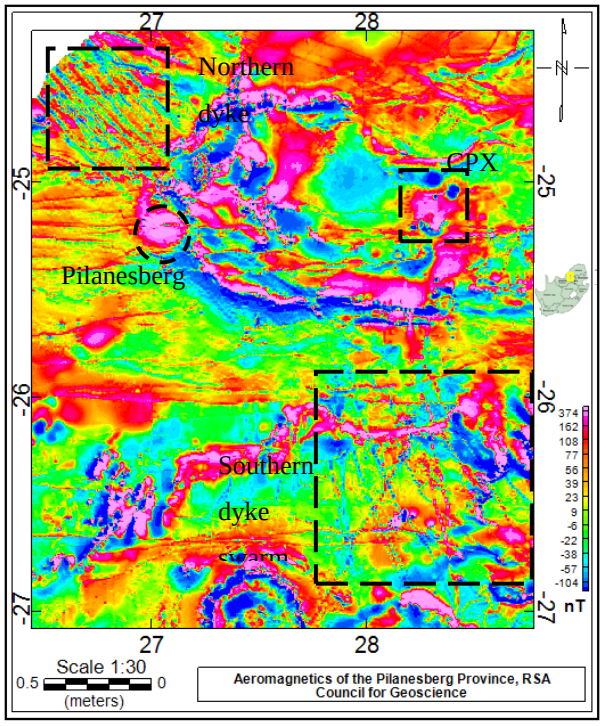

Figure 1. Magnetic data over the Pilanesberg Complex and Pilanesberg dyke swarms, from the Council for Geoscience. The magnetic map compares the positive anomaly of the Pilanesberg Complex with the negative anomalies from the dyke swarms. The southern swarm is difficult to image as it is orientated north-south and the flight lines are north-south.

The two dyke swarms have similar double-peaked reversed magnetic anomalies (Gough, 1958). The double peaked anomaly results from a two-staged emplacement dated at 1310 ±60 Ma (Emerman, 1991). First, a dolerite dyke intrudes followed by a syenite dyke through the centre. The package cooled to form a composite dyke with a syenite centre surrounded by dolerite (Emerman, 1991. C. R. Anhaeusser, pers. Comm, 2012). The double-peaked magnetic anomalies are also observed in the northern dyke swarm in the south-east of Botswana (Figure 1.7). The composite dolerite-syenite dykes also extend 225 km south of the Pilanesberg Complex and are exposed in the Wits Central Rand Gold mines along the gold reef (Hansen et al., 2006). The compositions of the Pilanesberg dolerite dykes from the southern dyke swarm are tholeiitic and are comparable to basalts that are abundant in iron and silica with less aluminium (Hansen et al., 2006). Across both the dyke swarms, the most common composition is that of the syenite dykes, which are identifiable by a single magnetic anomaly.

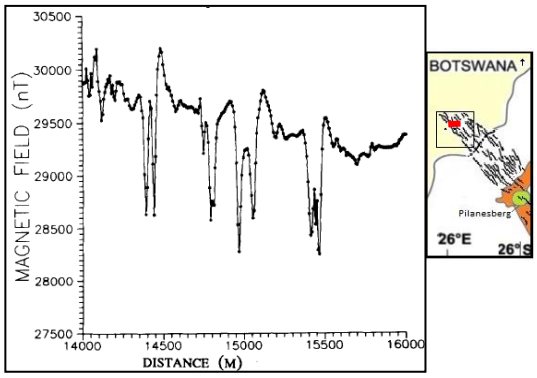

Figure 2 A profiles in Botswana of the total magnetic field across dykes of the northern dyke swarm, located south of the Monametsana River (Emerman, 1991). Each double-peak anomaly indicates a Pilanesberg dyke.

Previous Paleomagnetism Data:

Early paleomagnetism studies were conducted by Gough (1958) on the southern dyke swarm using samples from deep mines or fresh quarries, thus avoiding iso-remnant magnetisation of the rocks due to lightning strikes. Gough (1958) sampled five Pilanesberg-aged dykes from the Central Rand Gold mines. The dykes sampled include the composite syenite-dolerite dykes from Libanon and Venterspost Gold Mines, the basic dykes at Robinson Deep and East Geduld Gold Mines, and a syenite dyke at the Simmer and Jack Gold Mine. Gough concluded that the dykes carried remnant magnetisation. There are some non-Pilanesberg normally magnetised dykes in the area (the 1120 ±45 Ma East Rand dykes), which are not related to the Pilanesberg Complex but are associated with the younger weakness zones. They should not be confused with the Pilanesberg dykes (Emerman, 1991).

The dyke samples were used to calculate the mean magnetic pole orientation, which indicated that the dykes carried remnant magnetisation and a mean pole

direction that defines a north-seeking magnetic pole. The paleomagnetic results indicated a correlation in the mean direction for a north-seeking magnetic pole with an inclination +69.3° and azimuth N 24.0° E (Gough, 1958). Gough's mean north magnetic pole has a latitude of 7.5° N and longitude of 42.5° E and represents the pole position at the time of their emplacement. The accuracy of the pole assumes the rocks did not receive thermo-remnant magnetisation by a geocentric dipole field (Gough, 1958).

The Pilanesberg dyke System has an age range of between 1290 ± 80 and 1330 ± 80 Ma (Van Niekerk, 1962; Emerman, 1991), which is comparable to dates previously obtained in the Pilanesberg Province. The Pilanesberg Complex has dates ranging from 1250 ± 50 Ma (Olivo and William-Jones, 1999) to 1397 ± 47 Ma (Hansen et al., 2006; Cawthorn et al., 2012). While available age data the Pilanesberg Complex and dykes in the same period, the airborne magnetic data associated with the dykes indicate strong negative anomalies that are opposite to the positive anomaly over the Pilanesberg Complex (Figure 1). This suggests that a magnetic reversal occurred between the emplacement of the Pilanesberg Complex and the dykes, which has been tested through the paleomagnetism and geochronology to follow.

METHOD AND RESULTS

Samples were collected from two dykes, which form part of the southern dyke swarm. The dykes were situated ~ 400 m apart with one dyke composed of red syenite and the other of grey syenite. The sample locations from the Complex include the white foyaite from a quarry on the south-western edge and the green foyaite from the southern edge of the Complex. The whole rock samples were collected for the paleomagnetism study. The samples are oriented to strike and dip before they are removed from the outcrop. The core samples were drilled out of the whole rock in the lab, where the dip and strike of the whole rock are maintained on each core sample in order for paleomagnetism orientations to be correctly used during demagnetisation. The core samples were sent to Norway Geological Survey (NGU), for paleomagnetism and geochronology. The samples collection information is documented in Table 1.

No	Strike, Dip° and direction	UTM- Easting Northing (m)	Elev. (m)
1	285 °, 80 °, N	35J - 545252 -7134121	1452
2	196 °,65°, W	35J - 545257-7134102	1449
5	266°,5°, NW	35J - 545047-7136294	1502
3	203°,52°, W	35J - 545856-7135710	1475
4	23 °,5 ° E	35J - 545808-7135811	1468
6	110°,76°,SW	35J - 498638-7197097	1146
7	41 °, 85 °	35J - 498650-7197128	1154
8	218 °, 84°	35J - 506485-7196666	1114
9	298 °, 27 °	35J - 506487-7196665	1096

Table 1. Paleomagnetism sample collection and location information. Sample 1, 2 and 5 are from the grey syenite dyke, sample 3 and 4 from the red syenite dyke. The Complex samples include 6 and 7 from the white foyaite and 8 and 9 from the green foyaite.

The samples from the dykes and the Complex were tested with alternating field (AF) demagnetisation and thermal demagnetisation, where possible. Sample 1.1 (Figure 3) is a good example of a sample that completely demagnetises.

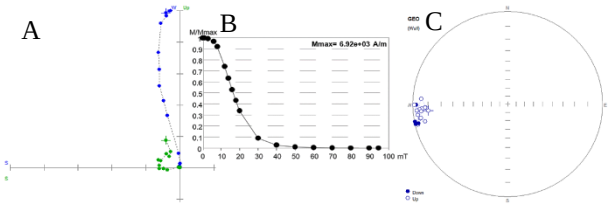

Figure 3. Grey syenite dyke sample 1.1. A) The vertical and horizontal components demagnetise with an extraction component and two components towards zero. B) The sample completely demagnetises using the AF method. C) Demagnetisation steps plot in a good cluster on the spherical projection.

The site 3 and 4 samples are the red syenite dyke (Figure 4), which is less hydrous than the grey syenite dyke as the samples were competent to demagnetise completely using thermal demagnetisation (Figure 5) without and exploding samples.

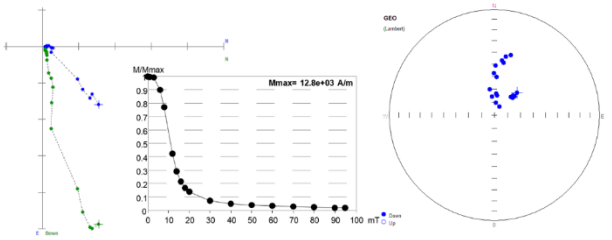

Figure 4. Sample 3.2 AF Demagnetisation of the red syenite dyke.

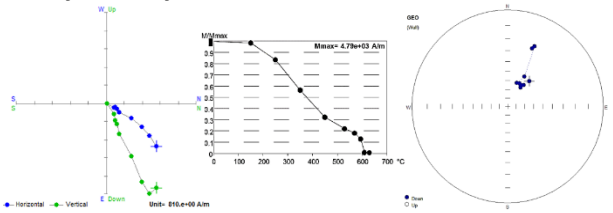

Figure 5. Sample 3.4 Thermal demagnetisation of the red syenite dyke

The dyke samples correlate along the dykes but when compared with the other dyke; they produce a different result, which suggests the grey dyke may have a normal magnetisation.

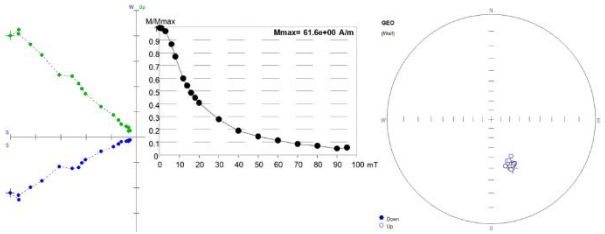

Figure 6. Sample 7.2 AF demagnetisation of the white foyaite from the Pilanesberg Complex.

The paleomagnetism AF results for the majority of the dyke samples were demagnetised with two components. Some samples were unable to demagnetise 100% indicating a component of hematite that resists full AF demagnetisation. In samples of sound quality, these resistant samples were completely demagnetised by thermal demagnetisation. Unfortunately, this process was not consistent with all the samples as some weathering affects caused the samples to explode with thermal demagnetisation. The demagnetisation of the complex samples produced complicated results with the high stability components tending to wonder on spherical projections.

The mean for all the samples from the Complex are compared with all the samples from the dykes then they appear to plot 180º apart. When tested with McFadden and Lowes (1981) null hypothesis, the samples transpose within the 95% confidence error and thus have experienced a reversal (Figure 7).

The paleomagnetic data does indicate that at least one reversal occurred between the emplacement of the Pilanesberg Complex and the Pilanesberg dyke System. Only dykes from the southern dyke swarm were tested, but the entire dyke System has a negative magnetic anomaly, so the assumption is plausible that the reversal occurred before both dyke swarms intruded. There is some evidence on the magnetic map and an indication in the paleomagnetic data that another reversal may

have taken place during the emplacement of the southern dyke swarm. A reversal occurring during the span in which the southern dyke swarm intruded, would assist to explain why two dykes that are a few mere kilometres apart would be chemically so different along the length of the dyke. This would also help to explain why samples from the various dykes behave so differently during the paleomagnetism analysis.

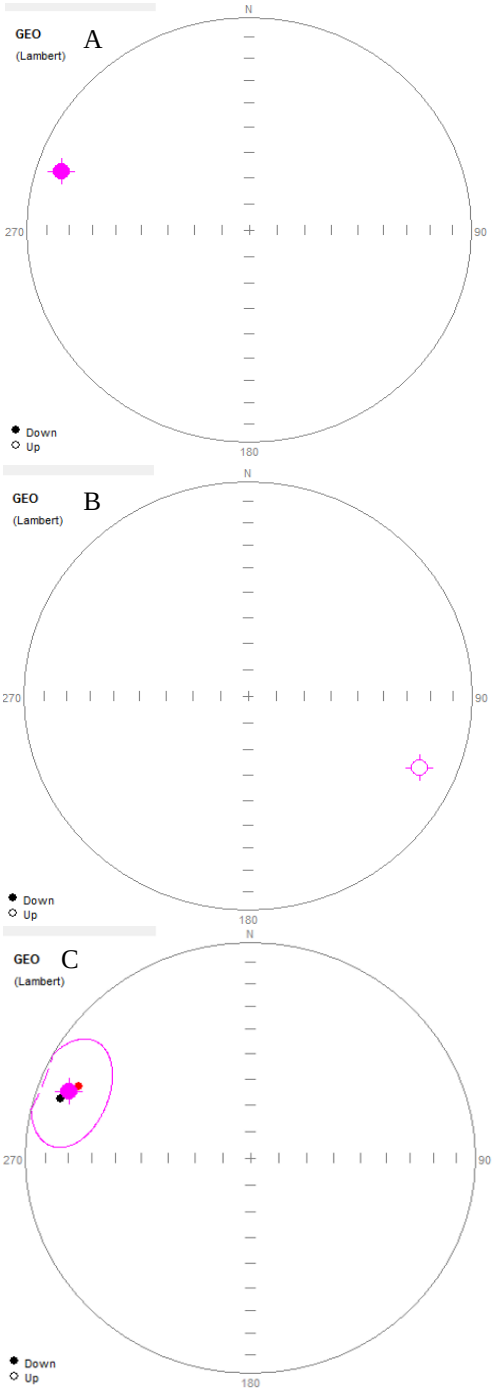

Figure 7. A) The mean pole position for the Pilanesberg dykes which plots 172° apart from the mean pole position of the Pilanesberg Complex in B). C) The Complex mean pole transposed, falls within the 95% confidence of the dykes.

The reversal data indicated a reversal occurred between the emplacement of the Pilanesberg Complex and the Pilanesberg dyke swarms. A poorly identified reversal occurred between the emplacement of the red and the grey syenite dyke such that the grey dyke has a positive magnetisation. Overall, the Pilanesberg dyke System has a negative magnetism; however, on closer inspection some of the dykes have positive signatures that indicate a reversal during the emplacement of the very first dykes.

Geochronology:

Some of the previously recorded dates for the Pilanesberg Province have been recorder in Figure 7. The Pilanesberg Complex, Pilanesberg dyke system and other intrusions in the Province all plot between 1200 Ma and 1400 Ma.

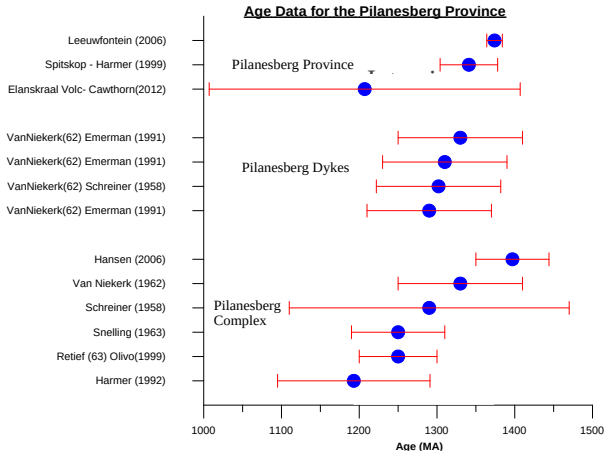

Figure 8. Published ages for intrusions in the Pilanesberg Province including ages for the Pilanesberg Complex and the Pilanesberg dyke System.

The samples have some alteration and any zirconium in the samples is associated with eudialyte, so the Ar^{40}/Ar^{39} igneous and metamorphic method is used

instead of zircon dating. The Ar^{40}/Ar^{39} geochronology is an important igneous rock dating method as it assumes that all the Ar^{40} remains after cooling past the closing temperature for that rock (Renne et al., 1998).

The samples were crushed and sieved to isolate grains of 180-250 µm at the Norwegian Geological Survey, NGU. Visual inspection with a binocular microscope showed a moderate degree of alteration in most samples. The samples were washed in $5HNO^3$ for 5 minutes at room temperature in an ultrasonic bath to remove carbonate and light surface alteration, and subsequently washed ultrasonically with distilled water several times.

The k^{39}(n, p)Ar^{39} transformation takes place during irradiation in the Institute for Energiteknikk (IFE, Kjeller, Norway). Samples were calculated against the Hb3gr hornblende standard (1080.4 ± 1.1 Ma), which is calibrated directly to the U-Pb system (Renne et al., 1998). The samples were step heated using a resistance furnace (Heine type). The gases extracted were swiped over getters for 2 minutes (SAES AP-10), then in a separate part of the extraction line for 9 minutes (SAES AP-10 getters). The peaks are determined by peak hopping (at least eight cycles) on masses Ar^{41} to Ar^{35} on Balzers electron multiplier on a MAP 215-50 mass spectrometer. Data from unknowns were corrected for blank prior to being reduced with the AgeMonster software package (written by M. Ganerød), that implements the equations in McDougall and Harrison (1999) using the decay constants of Renne et al. (1998) and the trapped Ar^{40}/Ar^{36} ratio of 298.56 ± 0.31 of Lee et al. (2006). Data reduction in AgeMonster incorporates corrections for mass discrimination, decay of Ar^{37} andAr^{39}, interfering isotopes produced during irradiation. A plateau is defined according to the following requirements: at least three consecutive steps, each within 95% confidence level, comprising at least 50% of total Ar^{39} and mean square of weighted deviates (MSWD) less than the two-tailed Student T critical value. We calculated a weighted mean plateau age (WMPA), weighting by the inverse of the variance. The weighted York-2 method computes the inverse isochron results, where a valid isochron has an MSWD value less than the two-tailed F-test critical value. All uncertainties (apart from the total fusion ages) are expanded by the square root (MSWD) if MSWD > 1.

The results of the geochronology for each intrusion are presented as follows starting with the grey syenite dyke, which achieved an age of 1160 ± 9.1 Ma (Figure 9).

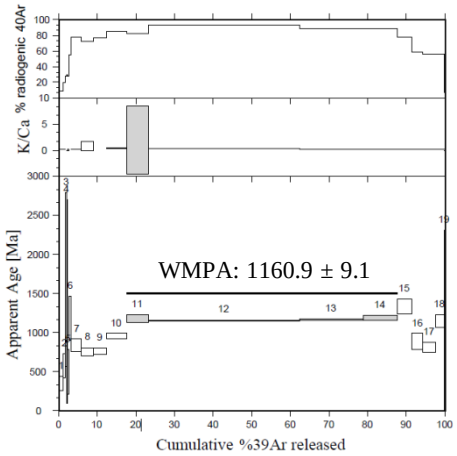

Figure 9. Sample 1 indicates an amphibole age for the grey dyke of 1160 ± 9.1 Ma using spectrum analysis and a plateau between steps 11 and 14.

The red syenite dyke achieved an age of 1219 ± 6.5 Ma for sample 3 (Figure 10) and an age of 1268 ± 10.2 Ma for sample 4 (Figure 11). Both of these ages were achieved from using feldspar grains.

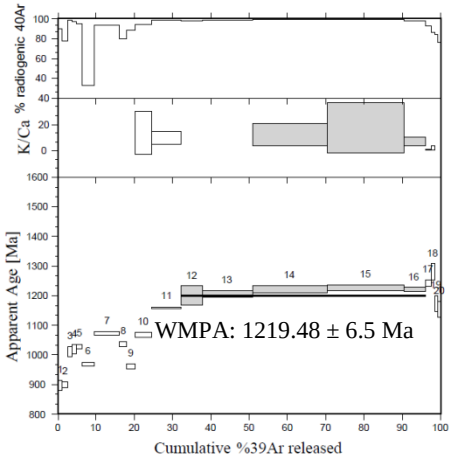

Figure 10. Sample 3 feldspar reliable age is 1219.48 ± 6.5 Ma with spectrum analysis between 12 and 16.

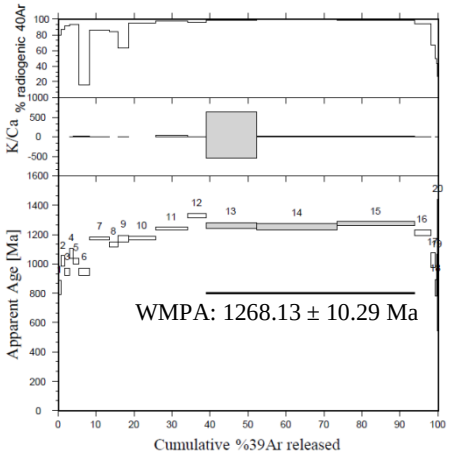

Figure 10. Sample 4 Feldspar ages of 1268.13 ± 10.29 Ma with spectrum analysis.

The white foyaite from the Pilanesberg Complex achieved ages of 1602 ± 38 Ma for sample 6 and 1583 ± 10 Ma for sample 7 (Figure 11).

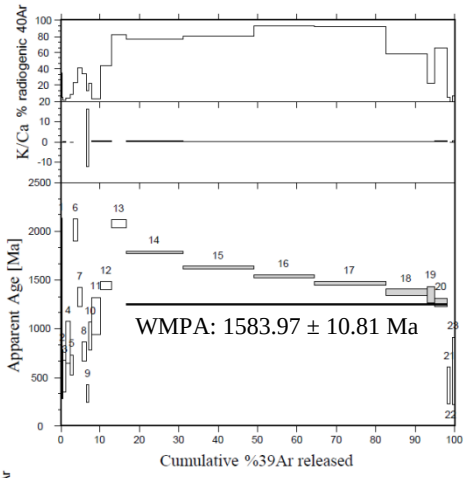

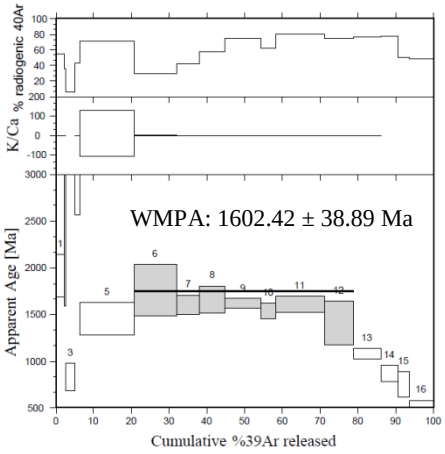

Figure 11. The spectrum analysis of amphibole grains results for sample 6 (A) and sample 7 (B) from the Pilanesberg Complex.

The geochronology results are summarised in Table 2. Sample 1 is from the grey syenite dyke; sample 3 and 4 from the red dyke and sample 6 and 7 are from the Pilanesberg Complex white foyaite.

Table 2. Ar^{40}/Ar^{39} Spectrum analysis results for furnace step heating experiments with the ages reported in Ma. Uncertainties are taken as analytical errors at 1.96 σ. The superscript under column sample denotes mineral used (F = feldspar, A = amphibole).

The age ranges achieved for the southern Pilanesberg dyke swarm is relative to previously published dates. However, the dates achieved for the Pilanesberg Complex (Figure 12) are considerably older than expected ages.

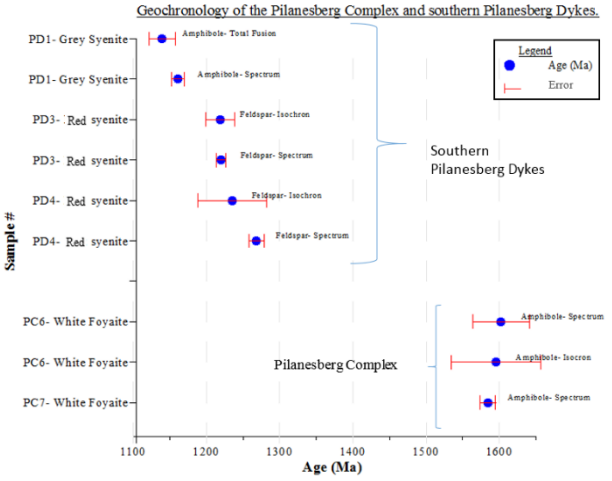

Figure 12. The ages for grey and red Pilanesberg dykes range between 1160 Ma and 1268 Ma while the Pilanesberg Complex is dated between 1583 and 1613 Ma.

CONCLUSIONS

The Pilanesberg dyke System and the circular clinopyroxenite intrusions are reversely magnetised with values ranging between -150 to -320 nT compared to the normally magnetised 166.5 - 330 nT Pilanesberg Complex, proposing that a magnetic reversal occurred during emplacement of the system. The different magnetic polarities of the Pilanesberg Complex compared with the Pilanesberg dyke System seen on the aeromagnetic map of South Africa.

No	Steps (n)	%39 Ar	Age ±1.96 σ	MSWD (P)	TFA ±1.96 σ	K/Ca ±1.96 σ
1 A	11-15 (4)	69.91	1160 ± 9.10	2.233 (0.082)	1098 ±9.85	0.071 ±0.003
3 F	12-16 (5)	63.62	1219 ± 6.51	2.341 (0.053)	1167 ±3.9	8.1 ± 6.2
4 F	13-15 (3)	54.9	1268 ± 10.2	1.136 (0.321)	1219 ±6.26	6.1 ± 9.2
6 A	7-14 (7)	58.29	1602 ±38.8	1.335 (0.237)	1490 ±47.8	0.17 ±0.02
7 A	15-21 (7)	81.61	1583 ± 10.8	258.30 (0.0)	1512 ± 9.9	0.36 ±0.032

Specific geochronology from the Pilanesberg Complex attained ages of 1602.42 ± 38.89 Ma and 1583.97± 10.81 Ma for the white foyaite samples 6 and 7 using amphibole Spectrum Analysis. This age is considerably older than the previously published dates, which ranged

between 1200 Ma and 1450 Ma. Paleomagnetism samples analysed indicated a magnetic reversal between the Complex and the southern dyke swarm, which is dated at 1139.71 ± 18.30 Ma on amphiboles using inverse isochron analysis of the first dyke from site 1 and at 1219.48 ± 6.51 Ma and 1268.13 ± 10.29 Ma on feldspars spectrum analysis of the second syenite dyke from site 3 and 4.

The Pilanesberg rocks are generally highly altered which produced some unrealistic dates from the feldspar grains, however dating of the amphibole grains produced reliable data with reasonable errors between 6.51 Ma and 61.47 Ma with a standard deviation of 14.94 Ma. The age dates for the southern Pilanesberg dyke swarm are younger than the previous ages for the dykes, which were between 1290 Ma and 1330 Ma.

The paleomagnetism study of the dykes and the Complex indicates that the dykes have a distinct positive pole while the Complex plots roughly 180° away. The transposed pole for the Pilanesberg Complex falls within the 95% confidence of the pole for the southern dykes such that it passes the null hypothesis reversal test. The positive reversal test indicates that at least one reversal of the Earth's magnetic field occurred after the emplacement of the Pilanesberg Complex and the subsequent intrusion of the Pilanesberg dyke Swarms.

The Pilanesberg Complex has been chemically and spatially associated with the Pilanesberg dyke System and the other intrusions in the Pilanesberg Province. The age dates for the Pilanesberg Complex, of 1602.42 ± 38.89 Ma and 1583.97± 10.81 Ma, makes the Complex substantially older than the rest of the Pilanesberg Province which has dates of 1207 ± 200 Ma at Elandskraal Volcano and 1374 ± 10 Ma at Leeuwfontein Complex. The age, size, small chemical difference and magnetic intensity all suggest that the Pilanesberg Complex could be an independent occurrence that should be classified separately from the rest of the intrusions in the Pilanesberg Province.

ACKNOWLEDGMENTS

Thanks to the Norwegian Geological Survey, NGU, for processing the paleomagnetism and geochronology data.

REFERENCES

Cawthorn, G.R., Ellam, R.M., Ashwal, L.D., Webb, S.J., 2012, A clinopyroxenite intrusion from the Pilanesberg Alkaline Province, South Africa: Precambrian Research, 25– 36 and 198– 199.

Emerman, S.H., 1991, Correlation of a dyke swarm in southeastern Botswana with the Pilanesberg dyke swarm South Africa: Journal of African Earth Sciences, 12, 4, 525-531.

Gough, D.I., 1958, A study of the Paleomagnetism of the Pilanesberg dykes: Geophysics Journal International, 7, 54, 196-213.

Hansen, R.E., Harmer, R.E., Blenkinsop, T.G., Bullen, D.S., Dalziel, I.W.D., Gose, W.A., Hall, R.P., Kampunzu, A.B., Key, R.M., Mukwakwami, J., Munyanyiwa, H., Pancake, J.A., Seidel, E.K., Ward, S.E., 2006, Mesoproterozoic intraplate magmatism in the Kalahari Craton: A review: Journal of African Earth Sciences, 46, 141-167.

Jansen, D., 1977, The Geology of the country of Pretoria: An explanation of sheets 2527DA, DB, DC, DD and 2528CA, CB, CC, CD: Department of Mines, Geological Survey: The Government Printer, Pretoria.

McFadden, P.L. and Lowes, F.J., 1981, The discrimination of mean directions drawn from Fisher distributions: Geophysical Journal of The Royal Astronomical Society, 67, 19-33.

Olivo, G.R., Williams-Jones, A.E., 1999, Hydrothermal REE Rich Eudialyte from the Pilanesberg Complex, South Africa: The Canadian Mineralogist, 37, 673-663.

Retief, E.A., 1963, Petrological and Mineralogical Studies in the Southern Part of the Pilanesberg Complex, Transvaal, South Africa: Ph.D. thesis, Univ. of Oxford, Oxford, UK.

Van Niekerk, C.B., 1962, The Age of the Gemspost dyke from the Venterspost Gold Mine: Trans. Geol. Soc. S.Aft., 65, 105-111.

APPENDIX D

PHYSICAL PROPERTY MEASUREMENTS

Table D. Density measurements of samples collected from the grey syenite dyke, the red syenite dyke, the Pilanesberg Complex white foyaite and the Pilanesberg Complex green foyaite. Average densities have been calculated for each lithology as well as for each site from numerous rock measurements per sample. The calculation is done by measuring the weight of the sample in air as well as the weight of the sample when submerged in water.

Pilans Geology	Geology Density	Site Density	Site			Sample type				
	Average Density g.cm-3	Average Density g.cm-3	Dp	1.1		broken r	Ave. den	Density	W air	W water
		Site 1				big	2.62	2.630	1850.37	1146.85
								2.630	1850.36	1146.79
								2.631	1850.35	1146.94
								2.602	1850.35	1139.24
								2.598	1850.34	1138.14
			Dp	1		broken r	Ave. den	Density	W air	W water
						small	2.48	2.470	141.37	84.13
								2.472	141.37	84.18
								2.478	141.38	84.32
		2.57						2.484	141.37	84.46
								2.490	141.38	84.6
			Dp	1.4		broken r	Ave. den	Density	W air	W water
							2.62	2.610	385.72	237.95
								2.617	385.73	238.31
								2.618	385.73	238.39
								2.619	385.72	238.46
								2.620	385.72	238.48
		Site 2	Dp	2.3		broken r	Ave. den	Density	W air	W water
						big	2.63	2.628	1878.6	1163.65
								2.626	1878.59	1163.3
								2.626	1878.58	1163.17
								2.628	1878.57	1163.75
								2.628	1878.57	1163.8
			Dp	2.2		broken r	Ave. den	Density	W air	W water
						small	2.63	2.628	371.12	229.91
		2.63						2.629	371.13	229.94
								2.631	371.14	230.1
								2.633	371.14	230.17
								2.633	371.14	230.2
			Dp	2		broken r	Ave. den	Density	W air	W water
						small	2.63	2.622	242.42	149.97
								2.632	242.41	150.3
								2.633	242.42	150.34
								2.632	242.42	150.33
								2.635	242.41	150.42
		Site 5	Dp	5	Grey	broken r	Ave. den	Density	W air	W water
							2.62	2.614	397.44	245.4
								2.616	397.42	245.48
								2.616	397.43	245.5
								2.617	397.42	245.54
								2.617	397.43	245.56
			Dp	5.3		broken r	Ave. den	Density	W air	W water
						small	2.63	2.633	228.05	141.44
								2.634	228.04	141.45
		2.63						2.634	228.04	141.46
								2.633	228.04	141.44
								2.633	228.05	141.44
			Dp	5.1		broken r	Ave. den	Density	W air	W water
						big	2.65	2.652	1417.67	883.18
								2.652	1417.67	883.13
								2.651	1417.67	882.95
								2.654	1417.64	883.4
								2.652	1417.66	883.14
Grey Dyke	2.61									

	Average	Average	Dp	3	Pink	broken rock	Ave. densit	Density	W air	W water
	Density g.cm-3	Density g.cm-3					2.67	2.670	172.16	107.67
								2.670	172.15	107.68
		Site 3						2.671	172.15	107.7
								2.671	172.16	107.71
								2.672	172.15	107.72
			Dp	3	Pink	broken rock	Ave. densit	Density	W air	W water
							2.67	2.672	228.23	142.83
								2.672	228.23	142.83
								2.673	228.21	142.83
		2.68						2.673	228.22	142.84
								2.675	228.21	142.9
								2.675	228.21	142.91
R			Dp	3	Pink	Core piece	Ave. densit	Density	W air	W water
e							2.73	2.731	54.22	34.37
d								2.733	54.23	34.39
								2.734	54.24	34.4
D								2.734	54.24	34.4
y								2.735	54.24	34.41
k										
e	2.69	Site 4	Dp	4	Pink	broken rock	Ave. densit	Density	W air	W water
							2.68	2.680	190.63	119.51
								2.681	190.63	119.52
								2.682	190.61	119.53
								2.682	190.61	119.55
								2.682	190.62	119.54
			Dp	4	Pink	broken rock	Ave. densit	Density	W air	W water
							2.73	2.730	59.46	37.68
								2.731	59.45	37.68
		2.69						2.731	59.45	37.68
								2.730	59.45	37.67
								2.731	59.45	37.68
			Dp	4	Pink	broken rock	Ave. densit	Density	W air	W water
							2.65	2.648	72.91	45.38
								2.647	72.92	45.37
								2.646	72.93	45.37
								2.646	72.94	45.37
								2.648	72.92	45.38

Pilanesberg White Foyaite	Average	Site 6	Dp	6		broken rock	Ave. densit	Density	W air	W water
	Density	Average				small	2.65	2.650	344.01	214.19
	g.cm-3	Density						2.654	344.02	214.38
		g.cm-3						2.654	344.01	214.4
								2.654	344.01	214.41
								2.654	344.01	214.4
			Dp	6.1	white	broken rock	Ave. densit	Density	W air	W water
		2.65					2.65	2.654	1176.69	733.26
								2.652	1176.68	732.95
								2.652	1176.69	732.96
								2.652	1176.68	732.99
								2.652	1176.69	733.02
		Site 7	Dp	7.2		broken rock	Ave. densit	Density	W air	W water
	2.66						2.66	2.664	777.35	485.52
								2.664	777.35	485.56
								2.664	777.35	485.6
								2.665	777.33	485.63
								2.665	777.33	485.63
		2.66								
			Dp	7	white	broken rock	Ave. densit	Density	W air	W water
							2.66	2.664	811.84	507.08
								2.664	811.83	507.14
								2.665	811.82	507.14
								2.665	811.81	507.16
								2.665	811.82	507.17

Pilanesberg White Foyaite	Average Density g.cm-3	Site 8	Dp	8		broken rock small	Ave. density 3.18	Density 3.178	W air 28.19	W water 19.32
								3.182	28.19	19.33
								3.172	28.2	19.31
								3.182	28.19	19.33
								3.181	28.18	19.32
			Dp	8		broken rock	Ave. density	Density	W air	W water
							3.19	3.182	36.46	25
								3.187	36.46	25.02
								3.187	36.46	25.02
								3.185	36.47	25.02
								3.185	36.47	25.02
			Dp	8		broken rock	Ave. density	Density	W air	W water
							3.10	3.091	40.24	27.22
								3.099	40.23	27.25
		2.99						3.098	40.24	27.25
								3.105	40.24	27.28
								3.103	40.24	27.27
			Dp	8		broken rock	Ave. density	Density	W air	W water
							3.11	3.108	72.84	49.4
								3.108	72.84	49.4
								3.106	72.84	49.39
								3.106	72.83	49.38
								3.107	72.83	49.39
								3.109	72.84	49.41
			Dp	8		broken rock	Ave. density	Density	W air	W water
							3.02	3.018	140.1	93.69
								3.018	140.1	93.7
								3.019	140.1	93.71
								3.020	140.1	93.73
								3.021	140.1	93.74
	2.92	Site 9	Dp	9	weathere	broken rock	Ave. density	Density	W air	W water
		Average Density g.cm-3					2.59	2.588	285.4	175.1
								2.589	285.4	175.14
								2.589	285.4	175.16
								2.590	285.4	175.18
								2.591	285.4	175.22
			Dp	9	weathere	broken rock	Ave. density	Density	W air	W water
							2.67	2.663	148.3	92.59
								2.671	148.3	92.76
								2.675	148.3	92.85
								2.678	148.3	92.9
								2.681	148.3	92.96
			Dp	9	weathere	broken rock	Ave. density	Density	W air	W water
							2.66	2.660	177.7	110.92
								2.662	177.7	110.96
								2.666	177.7	111.07
		2.85						2.668	177.7	111.11
								2.668	177.7	111.13
			Dp	9		broken rock	Ave. density	Density	W air	W water
							3.15	3.136	105.2	71.63
								3.138	105.2	71.65
								3.158	105.2	71.86
								3.161	105.2	71.89
								3.163	105.2	71.91
			Dp	9		broken rock	Ave. density	Density	W air	W water
							3.18	3.177	88.55	60.68
								3.178	88.55	60.69
								3.178	88.55	60.69
								3.174	88.55	60.65
								3.173	88.55	60.64